Nonlinear Dynamics and Far-Infrared Broadband Spectroscopy of $YBa_2Cu_3O_7$ Josephson Junctions for the TESLA Test Facility Linac

Dissertation
zur Erlangung des Doktorgrades
des Fachbereichs Physik
der Universität Hamburg

vorgelegt von
Frank Ludwig
aus Hamburg

Hamburg
2003

Gutachter der Dissertation:	Prof. Dr. U. Merkt Prof. Dr. M. Schilling
Gutachter der Disputation:	Prof. Dr. M. Schilling Prof. Dr. P. Schmüser
Datum der Disputation:	18.07.2003
Vorsitzender des Prüfungsausschusses:	Prof. Dr. D. Fay
Vorsitzender des Promotionsausschusses:	Prof. Dr. R. Wiesendanger
Dekan des Fachbereichs Physik:	Prof. Dr. G. Huber

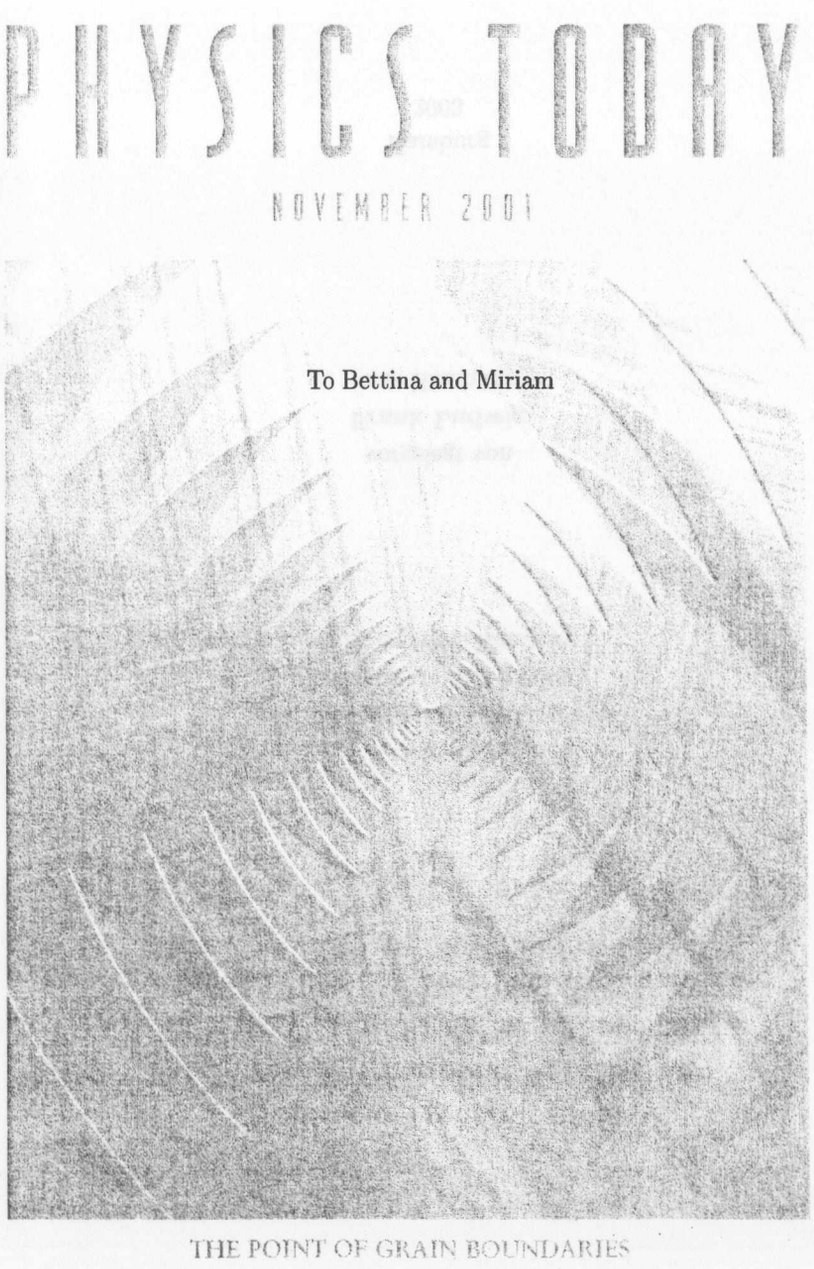

Abstract

In the present work, the longitudinal form factor of picosecond electron bunches at the TESLA-Test-Facility linac is investigated with Hilbert transform spectroscopy by analyzing coherent far-infrared broadband transition radiation with Josephson junctions made of the high temperature superconductor $YBa_2Cu_3O_7$. The investigation of the nonlinear dynamics of a pulsed driven Josephson junction within the Focker-Planck formalism, by introducing a difference recurrence scheme, allows us the consequent derivation of the detectors maximum rf-power ratings beyond the present linear Hilbert theory. Because of the combinatoric of a dense line spectrum an increase of the pulse pause, contrary to a decreasing pulse width in the delta pulse limit, can not be compensated by increasing the rf-power for a constant detector response without reducing the quality of the spectral reconstruction. The frequency dependent spectral decrease of the detectors response limits the detectors dynamic range and prevents a detailed reconstruction of the far-infrared time domain signal. A spectral compensation of the signal before the essential demodulation process is required by using quasioptical components and variation of the junctions critical current by external magnetic flux. To increase the dynamic range and the measuring bandwidth for a single-bunch measurement, measurements of serial arrays of up to 200 Josephson junctions, quasioptical replicator stages of Fabry-Perot interferometers, ultra low-noise broadband amplifiers and analytic spectral correction functions are presented. The generation of well defined pulses produced by quasioptical components for junctions with increased I_cR_n-product are investigated. The next generation Josephson junction arrays, so called rf-dc-SQUIDs, using discrete spectra have been presented. They combine a low-noise signal pickup, high readout bandwidth and voltage biasing of junctions with small normal-state resistances. The sensor is independent of the junctions parameter spread and has the opportunity for high integration. For spectroscopic applications using continuous rf-radiation the sensor offers additional a chopper port, which promises the suppression of all 1/f-noise sources. Measurements of Josephson junctions made of the high temperature superconductor $YBa_2Cu_3O_7$ based on low loss $LaAlO_3$ bicrystal substrates using a far-infrared laser and Josephson self oscillations confirm the detection of monochromatic radiation at least of up to several THz and the successful broadband input coupling with logarithmic periodic antennas. Because of the mixing effects of an arbitrary distribution of Shapiro steps, analytic spectral correction functions are deduced expecting a unique spectral reconstruction beyond the present small signal Hilbert theory. Within the Focker-Planck formalism and stochastic solutions, asymmetric spectra and a phase dependence of the stationary detector response for a high spectral degeneracy are found. This promises a unique time domain reconstruction of the far-infrared signal and the realization of integrated hybrid oscilloscopes of sub-ps resolution with high sensitivity as new applications for Hilbert transform spectroscopy.

Zusammenfassung

In der vorliegenden Arbeit wird der longitudinale Formfaktor von Elektronpaketen mit Picosekunden Länge an dem TESLA-Test-Facility Linearbeschleuniger mittels Hilbert-Transformations-Spektroskopie durch Analyse von kohärenter breitbandiger, ferninfraroter Übergangsstrahlung durch Josephson-Kontakte aus dem Hochtemperatursupraleiter $YBa_2Cu_3O_7$ untersucht. Die Untersuchung der nichtlinearen Dynamik eines gepulst betriebenen Josephson Kontakts mittels der Focker-Planck Methode durch Einführung eines rekursiven Differenzschemas erlaubt die analytische Herleitung der maximalen spektralen Detektorantwort außerhalb der linearen Hilbert-Theorie. Im Gegensatz zu einer Verkleinerung der Pulsbreite im Grenzfall kurzer Pulse, kann aufgrund der Kombinatorik eines dichten Linienspektrums, eine Vergrößerung der Pulspausen hinsichtlich einer konstanten spektralen Detektorantwort bzw. eindeutigen spektralen Rekonstruktion nicht durch eine Erhöhung der Pulsleistung kompensiert werden. Die spektrale Abnahme der Detektorantwort mit zunehmender Frequenz verhindert eine detaillierte Bestimmung der Form des ferninfraroten Zeitsignals und erfordert eine spektrale Anpassung des eingestrahlten Signals vor dem eigentlichen Demodulationsprozeß mittels quasioptischer Komponenten und Veränderung des kritischen Stromes des Josephson-Kontakts über einen externen magnetischen Fluß. Zur Erhöhung des Dynamikbereiches und der Meßbandbreite für eine Einzelpulsmessung der Elektronenpakete werden Messungen an Serienarrays aus bis zu 200 Josephson Kontakten, quasioptische Replikationsstufen mittels Fabry-Perot Interferometern, extrem rauscharme Breitband-Verstärker und analytische spektrale Korrekturfunktionen vorgestellt. Wir diskutieren die Erzeugung von wohldefinierten Pulsfolgen mittels quasioptischer Komponenten für den Einsatz von Josephson-Kontakten mit erhöhtem I_cR_n-Produkt. Die nächste Generation von Serienarrays, so genannte rf-dc-SQUIDs, für die Verwendung von diskreten Spektren werden vorgestellt. Sie kombinieren einen breitbandigen und rauscharmen Signalabgriff für Kontakte mit kleinen normalleitenden Widerständen. Der Sensor ist unabhängig von Parameterstreuungen der Kontakte, hoch integrierbar und bietet einen Choppereingang, was eine vollständige Unterdrückung des 1/f-Rauschens verspricht. Messungen an Josephson Kontakten aus dem Hochtemperatursupraleiter $YBa_2Cu_3O_7$ auf verlustarmen $LaAlO_3$ Bikristallsubstraten mittels eines ferninfraroten Lasers und Josephson-Eigenoszillationen bestätigen den Nachweis von monochromatischer Strahlung bis weit in den THz-Bereich und die erfolgreiche Einkopplung mittels logarithmisch periodischer Antennen. Aufgrund des Mischungsverhaltens beliebiger Shapiro-Stufenverteilungen lassen analytisch abgeleitete Korrekturfunktionen eine eindeutige spektrale Rekonstruktion auch außerhalb des Kleinsignalfalls der Hilbert-Theorie erwarten. Im Rahmen des Focker-Planck Formalismus und stochastischer Lösungen beobachten wir asymmetrische Spektren und eine Phasenabhängigkeit der stationären Detektorantwort für einen spektralen Entartungsgrad. Dieses verspricht eine eindeutige Rekonstruktion des ferninfraroten Zeitsignals und somit die Realisierung eines integrierten hybriden Oszillographen mit sub-ps Auflösung und hoher Empfindlichkeit, welches ein neues Anwendungsfeld für die Hilbert-Transformations-Spektroskopie eröffnet.

Contents

a prediction of mass spectra of different particles for the minimal supergravity szenario, where the breaking of symmetry is transmitted to our eigenworld by gravity [Zer02]. It can be shown, that using supersymmetry, the three Standard Model gauge couplings unify up to a certain accuracy, Fig.1.1(b). The gauge coupling unification determines one of them $\alpha, \sin^2\theta, \alpha_s$ theoretically in good agreement with the measured weak mixing angle. With high precision measurements of a future linear collider different GUT models can be ruled out at shorter distances. However, future data from e^+e^- linear colliders, TESLA in particular, will investigate their mass spectra and couplings with clear signatures and high-precision measurements at a center of mass energy of 500GeV up to 800GeV [TDR01]. Following a long tradition at DESY building accelerating structures for entirely different research fields, the TESLA design includes an X-ray free electron laser (FEL) delivering wavelengths around 1 Å with a high peak brilliance.

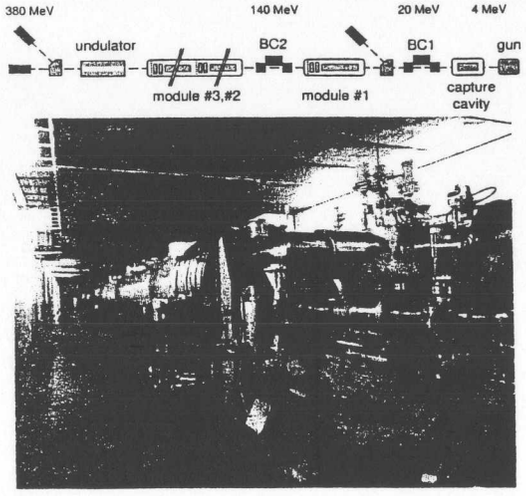

Figure 1.2: *Schematic layout and picture of the TESLA Test Facility (TTF). Module housing of several superconducting accelerating cavities and bunch compressors are seen.*

The TESLA-Test-Facility (TTF) Fig.1.2 has been setup at DESY to provide superconducting standing-wave acceleration structures made of niobium and an ultraviolet Free-Electron-Laser (UV-FEL). Meanwhile, 9-cell cavities reach an acceleration gradient of 25MV/m. The cavities operate at an rf-frequency of 1.3GHz with a quality factor of about $Q_0 \approx 2 \cdot 10^{10}$. Usually the surface resistance increases towards higher gradient fields and the cavities are operated in pulsed mode to reduce the averaged cryogenic load. Electrolytic polishing of the cavity surface combining with several multi-cell cavities, so-called superstructures, promises a gradient of 35MV/m for the TESLA-800GeV [Lie01, Lil01].

At the TTF linac an UV-FEL has been operated to prove the viability of the Self Amplified Spontaneous Emission (SASE) mode of free electron lasers. The requirements on the electron beam quality of such a SASE-FEL are very demanding in terms of small transverse and longitudinal emittances. Especially the requirements for the longitudinal phase space with 1nC of charge concentrated in less than 1ps and with small energy spread are the subject of intense theoretical and experimental studies. To increase the sensitivity and to decrease the statistical errors of the measurements in particle physics, high particle flux and energy are required. Concerning accelerator physics this requires an improved spatial resolution and smaller temporal resolution by shortening the beam pulses up to the sub-millimeter wavelength regime.

In this thesis, the longitudinal charge distribution of electron bunches is determined by measuring coherent transition radiation spectra with Josephson junctions.

1.2 Outline of this thesis

In this thesis, the focus lies on the measurement of coherent transition radiation with Josephson junctions made of a high temperature superconducting material $YBa_2Cu_3O_7$. Contrary to Fourier spectroscopy, Josephson junctions promise a fast method to distinguish different electron bunches propagating within the accelerator providing no complicated synchronization for an operation at highest frequencies [Gro95]. Analyzing frequencies up to the far-infraded regime away from the energy gap of conventional superconductors, requires HTS materials. Providing a frequency selectivity, bolometric detectors, established for imaging applications in radio astronomy require higher order quasioptical filters for spectral measurements. Heterodyn receivers are designed mainly for demodulation of several spectral lines and are not suitable for broadband applications. As depicted in the electromagnetic spectrum Fig.1.3, the choice of high temperature superconducting materials for Josephson junctions is an attractive possibility for detecting far-infrared radiation of the sub-millimeter wavelength range for a precise measurement of the bunch shape.

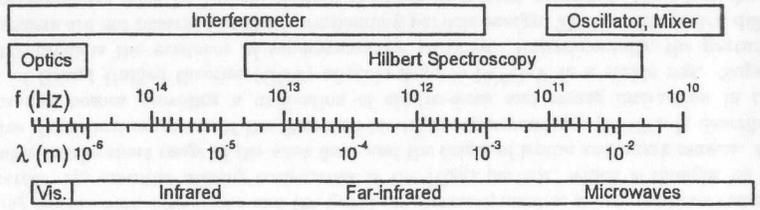

Figure 1.3: *Electromagnetic spectrum and its spectroscopic applications.*

Conventional radio frequency (rf) electronics with their high power consumption meanwhile enter the lower frequency range of Hilbert transform spectroscopy using Josephson junctions. Josephson junctions intrinsically combine the demodulation by using a mixer and local oscillator. As reviewed in chapter 3, measuring the current voltage characteristics of a Josephson junction change caused by the transition spectrum allows its reconstruction by using the Hilbert theory. Unfortunately the so called Hilbert transform spectroscopy is only a linear small signal theory with respect to the irradiated spectral intensity and handles only time unlimited signals. But in fact, the junction is a highly nonlinear device and a fast single-bunch measurement requires limited sampling times.

The Josephson junction is a macroscopic quantum device having a small response. This limits, by noise, the measuring bandwidth according to section 4.6. To increase the measuring bandwidth, the detectors response, respectively its maximum rf-power rating, is analyzed within the Focker-Planck formalism for pulse-type rf-signals and a possibly unique spectral reconstruction as performed in chapter 4. Contrary to a decreasing pulse width, an increasing pulse pause cannot be compensated by increasing the rf-power for a constant detector response. Therefore, according to chapter 6, well defined quasioptical pulse replicator structures are investigated offering a sufficient seperated line spectrum. Several methods to increase the measuring bandwidth are suggested. The most attractive one, so called rf-dc-SQUIDs, possibly the next generation of Josephson junction arrays, are presented in section 6.2. Indeed, the junction remains a frequency selective device and the demodulation process takes time. The spectroscopy of a single pulse can performed by using an rf-filter to provide sufficient interaction

Chapter 1

Introduction

1.1 Motivation

One of the fundamental principles of modern science is the close interaction between theory and the experiment. In the elementary particle physics community there is broad consense, that a linear collider, in particular TESLA (TeV-Energy-Superconducting-Linear-Accelerator), will be needed for precise measurements and for the detailed exploration of new physics to describe the fundamental constituents of matter and their interactions. Despite the great success of the Standard Model, based on the gauge symmetry group $SU(3) \times SU(2) \times SU(1)$ describing electro-weak interaction and the quantum chromodynamics, many questions remain unanswered. An essential missing cornerstone is the Higgs particle, which is thought to be responsible for the short range of the weak force and the origin of lepton and quark masses. An attractive theoretical extension of the Standard Model is supersymmetry (SUSY). It describes fermions and bosons providing a unification of electro-weak and strong interaction in the context of Grand Unified theories (GUT) of scale $\Lambda_{GUT} \approx 10^{16}$GeV in a stable way. Supersymmetry predicts the existence of supersymmetric particles. Experimentally, the particles superpartners are not observed at the corresponding particle energy. Their mass spectra differ and supersymmetry must be broken. Several szenarios have been suggested. Fig.1.1(a) shows

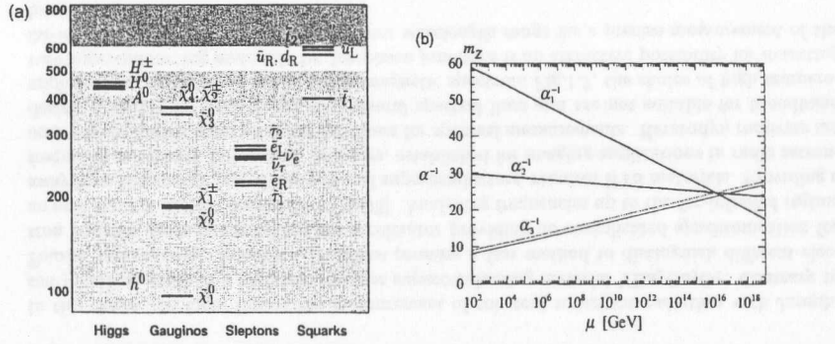

Figure 1.1: *(a) Spectrum of Higgs particles, gauginos and scalar particles in the minimal supergravity szenario, masses in GeV [Zer02]. (b) The renormalization group evolution of three Standard Model gauge coupling constants assuming a simple SU(5) GUT gauge group and a grand desert [Mura98].*

time with radiation, as shown in section 4.4.2. Once understanding from sections 4.5ff, that the maximum rf-power ratings are caused from a high degeneracy of dense spectra, higher order mixing effects are analyzed to provide spectral correction functions for the reconstruction algorithms to increase the measuring bandwidth. Beyond the Hilbert theory, several effects like spectral symmetry breaking or a phase dependence of the stationary detector response might be very useful and promise a unique reconstruction of the time domain rf-signal, while offering an absolute uncritical triggering of the rf-radiation for highest frequencies. Beside one publication, up to now this thesis is unpublished.

For the very fast reader, the propositions marked by vertical lines of sections 4.4 → 4.6 → 4.5 → 5.5 → 6.1.3 → 6.2 → 6.3 should be studied.

Chapter 2

Transition radiation

This chapter provides an overview on the basic properties of transition radiation. Charged particles can emit electromagnetic radiation under various circumstances. Synchrotron radiation is emitted by accelerated particles traveling in vacuum. Čerenkov radiation is only emitted when charged particles move with higher velocity than the speed of light in a medium. When a charged particle passes a dielectric boundary transition radiation is emitted. In principle the emitted transition radiation energy is frequency independent. But considering a finite size of the transition region and diffraction at millimeter wavelength, the transition radiation gets frequency dependent. The focus here lies on far-infrared coherent transition radiation for electron bunchlength measurements.

2.1 Optical transition radiation

If a point charge e is uniformly moving perpendicular to an infinite extended boundary of permittivity change from vacuum to medium ε_r the radiation intensity $d^2W/d\omega d\Omega$ is emitted into the backward hemnisphere and is given by the Ginzburg-Frank equation [Gin79].

$$\frac{d^2W}{d\omega d\Omega} = \frac{e^2\beta^2}{4\pi^3\varepsilon_0 c}\frac{\sin^2\theta\cos^2\theta}{(1-\beta^2\cos^2\theta)^2}\left|\frac{(\varepsilon_r-1)(1-\beta^2+\beta\sqrt{\varepsilon_r-\sin^2\theta})}{(1+\beta\sqrt{\varepsilon_r-\sin^2\theta})(\varepsilon_r\cos\theta+\sqrt{\varepsilon_r-\sin^2\theta})}\right|^2 \tag{2.1}$$

To derive the Ginzburg-Frank equation first of all the electric field carried by a charge distribution in a medium of permittivity ε_r can be determined by solving the inhomogeneous Maxwell's equations in frequency domain resulting in algebraic expressions concerning all transversal coordinates x, y and time t. The radiation field propagating as a plane wave from the boundary has to be solved from the homogeneous wave equation using the boundary condition $\nabla\cdot\mathbf{D}=0$ for the field of charge and the radiation field at both media, where the field of charge is not of interest at infinity. As depicted in Fig.2.1a the emission of backward transition radiation is indicated by the wave vector $\mathbf{k}$ and electric field vector $\mathbf{E}$ under the angle θ. The velocity of the charge is $\beta=v/c$. Supposing a metallic medium with infinite optical density $\epsilon_r\to\infty$ fields cannot penetrate and Eq.2.1 reduces to

$$\frac{d^2W}{d\omega d\Omega} = \frac{e^2\beta^2}{4\pi^3\varepsilon_0 c}\frac{\sin^2\theta}{(1-\beta^2\cos^2\theta)^2} \tag{2.2}$$

The maximum energy of Eq.2.2 $d(d^2W/d\omega d\Omega)/d\theta=0$ is radiated under an angle θ_{max} with the Lorentz factor γ given by

$$\theta_{max}=\frac{1}{\beta\gamma}, \qquad \gamma=(1-\beta^2)^{-1/2} \tag{2.3}$$

The total energy emitted from a metallic screen per unit frequency interval over the angle $d\Omega = \sin\theta d\theta d\phi$ increases with γ values and results to

$$\frac{dW}{d\omega} = \int d\Omega \frac{d^2W}{d\omega d\Omega} = -\frac{e^2\beta^2}{2\pi^2\varepsilon_0 c}\left[4 + \frac{1+\beta^2}{\beta^2}\log\left[\frac{(1-\beta)^2}{(1+\beta)^2}\right]\right]. \tag{2.4}$$

The total emitted energy $W = \int_{opt} dW/d\omega d\omega$ increases with the electron energy. Within the optical wavelength range $\Delta\lambda = 400 - 800nm$ the radiated energy per electron with $\gamma \approx 100$ produce an energy of $0.13eV$. With a photon energy $E_\gamma = \hbar\omega$ of about 2.5eV within the optical frequency approximately 20 electrons are needed to produce one photon. Therefore for a bunch of $5 \cdot 10^{10}$ electrons the generated photons in the visible range are detectable with standard CCD devices. The transition radiator at the TESLA-Test-Facility is a thin 40nm aluminium layer evaporated onto a $25\mu m$ capton foil, which is mounted at an angle of $\psi = \pi/4$ with respect to the accelerator axis for coupling out the backward lobe of transition radiation from the vacuum chamber. As depicted in Fig.2.1b, the oblique incidence for an infinite inclined metallic boundary is discussed in [Ter72]. The angle ψ is defined between the electrons velocity $\mathbf{v}$ and the z-axis. The polar angle θ is between the emitted radiation $\mathbf{k}$ wave vector and negative z-axis. The azimuthal angle ϕ of $\mathbf{k}$ and the xy-plane is defined with respect to the x-axis. The

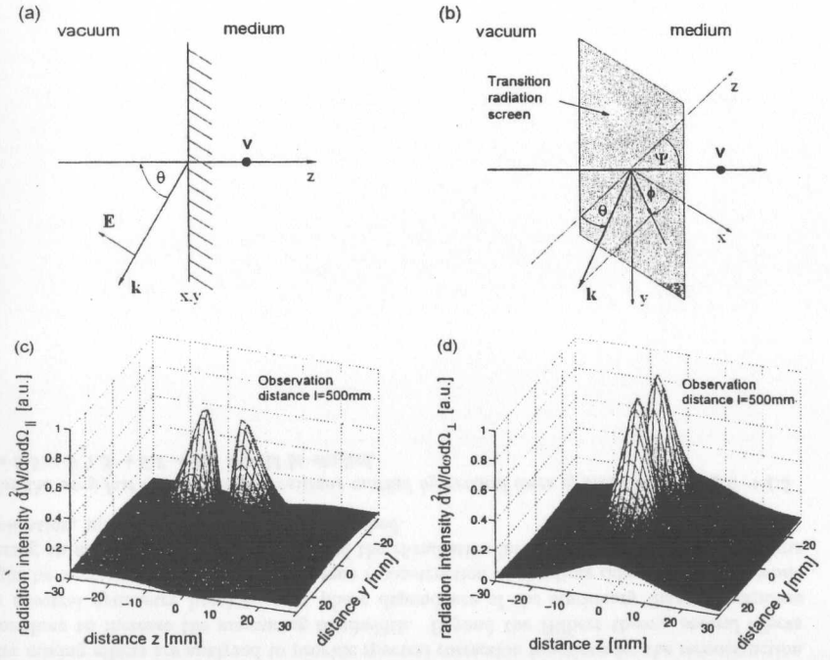

Figure 2.1: *Coordinates for (a) normal and (b) oblique incidence of a charge particle. The xy-plane is choosen to be the foils surface. (c) Parallel $d^2W/d\omega d\Omega_\parallel$ and (d) perpendicular $d^2W/d\omega d\Omega_\perp$ polarized transition radiation detected with an overservation screen located far away from the radiation source.*

emitted transition radiation is polarized parallel and orthogonal to radiation plane, defined by the vectors $\mathbf{k}$ and $\mathbf{v}$, denoted by $E_\parallel$ and $E\perp$ respectively. According to Fig.2.1c,d the transition radiation is detected with a transition monitor located at $y/l = -\phi$, $z/l = \theta + \pi/4$ far away from the radiation origin $y \ll l$, $z \ll l$. The appropriate radiation intensities for a medium with infinite permittivity are given by

$$\frac{d^2W}{d\omega d\Omega_\parallel} = \frac{e^2\beta^2}{4\pi^3\varepsilon_0 c}\left|\frac{\cos\psi(\cos\theta - \beta\cos\phi\sin\psi)}{(1-\beta\sin\theta\cos\phi\sin\psi)^2 - \beta^2\cos^2\theta\cos^2\psi}\right|^2 \tag{2.5}$$

$$\frac{d^2W}{d\omega d\Omega_\perp} = \frac{e^2\beta^2}{4\pi^3\varepsilon_0 c}\left|\frac{\beta\cos\psi\cos\theta\sin\phi\sin\psi)}{(1-\beta\sin\theta\cos\phi\sin\psi)^2 - \beta^2\cos^2\theta\cos^2\psi}\right|^2 \tag{2.6}$$

Eq.2.5,2.6 reduces for normal incidence $\psi = 0$ to the Ginzburg-Frank equation, where the perpendicular field component $d^2W/d\omega d\Omega_\perp$ vanish. For grazing incidence $\psi \to \pi/2$ transition radiation vanish. For a beam incident angle of $\psi = \pi/4$ the backward radiation lobe is strongly directed, centered at $\theta = \psi$ and contributes mostly for small azimuthal angle $\phi = 1/\beta\gamma$ in the radiation plane.

2.2 Source dimension and diffraction of transition radiation

Taking the source dimension of the electric field guided in the TTF's beam pipe of infinite conductivity, radius b and a finite transition radiation screen of diameter d into account, contrary to the Ginzburg-Frank equation, a frequency dependent spectral acceptance function occurs. The projection of the fields carried by the charge distribution onto the transition boundary yields the transverse size of the transition radiation. The fraction of the field components, which are available and contributing to the radiation process can be estimated by a spectral acceptance function

$$D(f) = \int_0^{d/2} dr 2\pi r \tilde{E}_r(k,r) \Big/ \int_0^b dr 2\pi r \tilde{E}_r(k,r) \tag{2.7}$$

using the radial electric field $\tilde{E}_r(k,r)$ of a charge moving in a beam pipe of infinite conductivity. The electric and magnetic fields of a bunch passing the observer $\tilde{E}_z$, $\tilde{E}_r$ and $\tilde{B}_\theta$ within the perfectly conducting beam pipe are derived by solving the Maxwell equations with a Fourier transform of the longitudinal coordinate of wave number $k = 2\pi/\lambda$ for a ring charge distribution of radius a and its Fourier transform $\tilde{\lambda}(k)$ [Schl97].

$$\tilde{E}_z(k,r) = \frac{ik}{2\pi\epsilon_0\gamma^2} q\tilde{\lambda}(k)\left[\begin{Bmatrix} -K_0\left(\frac{ka}{\gamma}\right) I_0\left(\frac{kr}{\gamma}\right), r < a \\ -I_0\left(\frac{ka}{\gamma}\right) K_0\left(\frac{kr}{\gamma}\right), r > a \end{Bmatrix} + I_0\left(\frac{ka}{\gamma}\right)\frac{K_0\left(\frac{kb}{\gamma}\right)}{I_0\left(\frac{kb}{\gamma}\right)} I_0\left(\frac{kr}{\gamma}\right)\right], \tag{2.8}$$

$$\tilde{E}_r(k,r) = \frac{k}{2\pi\epsilon_0\gamma} q\tilde{\lambda}(k)\left[\begin{Bmatrix} -K_0\left(\frac{ka}{\gamma}\right) I_1\left(\frac{kr}{\gamma}\right), r < a \\ I_0\left(\frac{ka}{\gamma}\right) K_1\left(\frac{kr}{\gamma}\right), r > a \end{Bmatrix} + I_0\left(\frac{ka}{\gamma}\right)\frac{K_0\left(\frac{kb}{\gamma}\right)}{I_0\left(\frac{kb}{\gamma}\right)} I_1\left(\frac{kr}{\gamma}\right)\right], \tag{2.9}$$

$$\tilde{B}_\theta(k,r) = \frac{\beta}{c}\tilde{E}_r(k,r). \tag{2.10}$$

Assuming a line charge $a \to 0$, contributions of the vacuum chamber, expressed by the second term of Eq.2.8, Eq.2.9 with $K_0(kb/\gamma)$, are suppressed within the optical range with $k \approx 10^7 m^{-1}$. With $\tilde{E}_z(k,r) \sim \tilde{E}_r(k,r)/\gamma$ and $\tilde{B}_\theta(k,r) = (\beta/c)\tilde{E}_r(k,r)$ the transverse electric

fields components dominate. Well located radial fields on the transition radiation screen at low particle energy emitting high frequency transition radiation produce nearby a flat spectral acceptance function, as shown in Fig.2.2. Estimating the field source dimension R_s with

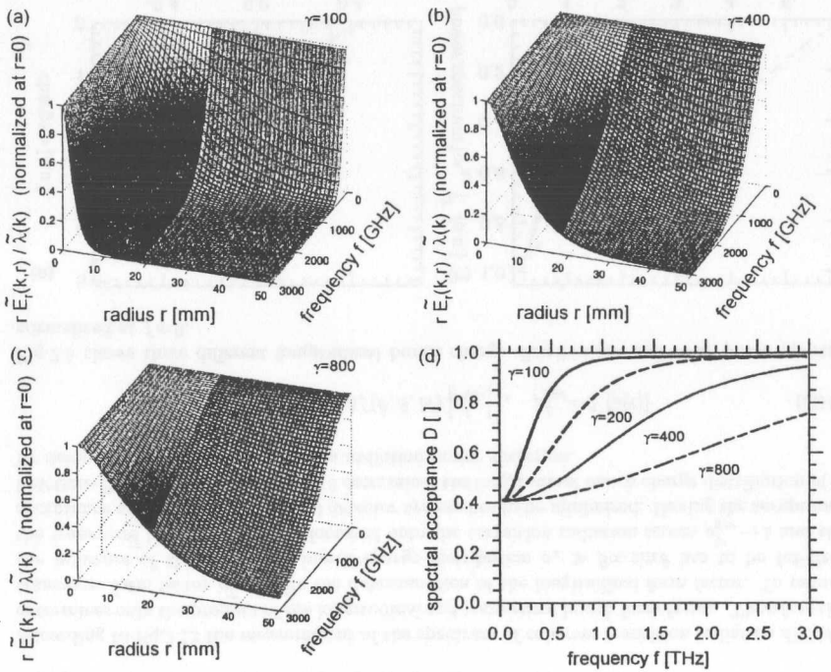

Figure 2.2: *(a)-(c) Fourier components of radial electric field $r\tilde{E}_r(k,r)/\tilde{\lambda}(k)$ of Eq.2.9 normalized at $r=0$ in a beam pipe of infinite conductivity for different frequencies and particle energies. The light gray marked areas miss the transition radiation screen and cannot contribute to the transition radiation. (d) Spectral acceptance function $D(f)$ for different gamma values.*

$R_s\tilde{E}_r(k,R_s) \approx (kR_s/\gamma)K_1(kR_s/\gamma) = 1/e$ at its $1/e$ decay results to $R_s = 0.26c\,\gamma/f$. The source dimension of far-infrared radiation for $f = 300GHz$ at $\gamma = 660$ is about $R_s = 16cm \gg d/2$ and increases towards lower frequencies. Diffraction effects have to be taken into account when measuring transition radiation at millimeter wavelengths. As depicted in Fig.2.3a,b the diffraction of the transition radiation fields at the transition radiation screen boundary shifts the angular maximum of transition distribution to larger angles partly out of the quasioptical detector systems acceptance function resulting in a suppression of low frequency fields. This causes a frequency dependent acceptance function, which can be estimated by the ratio of the radiated field distribution $\tilde{E}^R(k,r)$ from transition radiation, which is available and the collected one from the quasioptical detector system

$$A(f) = \int_{\text{detector system}} dr d\phi 2\pi r \tilde{E}^R(k,r) \Big/ \int_0^\infty \int_0^{2\pi} dr d\phi 2\pi r \tilde{E}^R(k,r). \tag{2.11}$$

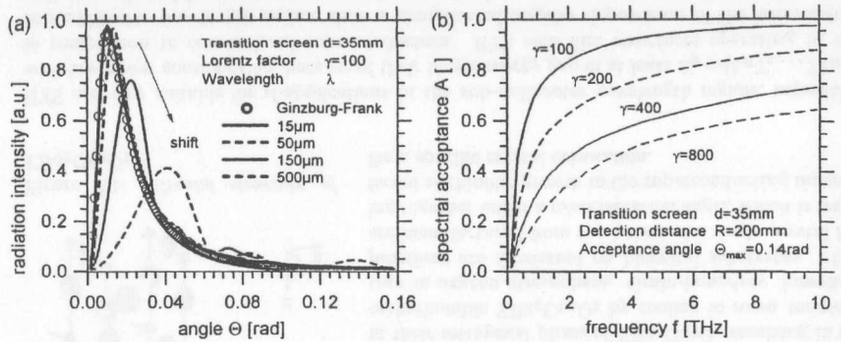

Figure 2.3: *As shown in [Gei99] (a) Computed angular distribution of transition radiation using the Fresnel-Kirchhoff scalar diffraction theory [Hec89] for a finite transition radiation screen including diffraction effects. (b) Diffracted transition radiation power cannot be collected by a parabolic mirror resulting in a decrease of spectral acceptance $A(f)$ for larger wavelengths.*

Instead of using the Ginzburg-Frank equation the radiatied field distribution can be analyzed by computing the angular transition distribution with the Huygens-Fresnel method [Hec89].

2.3 Far-infrared coherent transition radiation

The superposition of transition radiation processes of N particles of a bunch is depicted in Fig.2.4. The far-field approximation of the averaged transition radiation of N particles leads to a dominant coherent part for bunch lengths σ_z larger than the emitted wavelength λ dependent on N^2 and an incoherent part [Han97]. Using the longitudinal $\rho^L(z)$ and transversal $\rho^T(r,\phi)$ charge distribution $\rho(r,\phi,z,t) = \rho^L(z,t)\rho^T(r,\phi)$ for normal incidence of the particle the incoherent transition radiation intensity is given by [Gei99]

$$\frac{d^2W}{d\omega d\Omega} = \frac{N^2}{4\pi^3\varepsilon_0}\frac{\beta^4 c\sin^2\theta}{(1-\beta^2\cos^2\theta)^2}\left|\rho^L_{q,\omega}\right|^2\left|\rho^T_{q,\omega}\right|^2, \tag{2.12}$$

where the form factor $\rho^L_{q,\omega}$ denotes the Fourier transform $\mathcal{F}$ of the longitudinal part of charge distribution with respect to the transversal coordinates r,ϕ and time t, respectively $\rho^T_{q,\omega}$ the transversal charge distribution. Assuming a bunch with gaussian charge distribution yields

$$\rho(r,\phi,z,t) = \frac{Ne}{2\pi\sigma_r}\frac{1}{\sqrt{2\pi}\sigma_z}\exp\left(-\frac{r^2}{2\sigma_r^2}\right)\exp\left(-\frac{(z-vt)^2}{2\sigma_z^2}\right) \tag{2.13}$$

$$\rho^L_{q,\omega}\rho^T_{q,\omega} = \frac{Ne}{v}\exp\left(-\frac{\omega^2\sigma_z^2}{2v^2}\right)\exp\left(-\frac{q^2\sigma_r^2}{2}\right)\exp\left(\frac{i\omega z}{v}\right). \tag{2.14}$$

Using the transversal wavevector of the radiation $q = k\sin\theta$ and its dispersion relation $\omega = ck$ the transition radiation intensity is then given by

$$\frac{d^2W}{d\omega d\Omega} = \frac{N^2e^2}{4\pi\varepsilon c}\frac{\beta^2\sin^2\theta}{(1-\beta^2\cos^2\theta)^2}\exp\left[-\frac{\omega^2}{v^2}\left(\sigma_z^2+\beta^2\sigma_r^2\sin^2\theta\right)\right]. \tag{2.15}$$

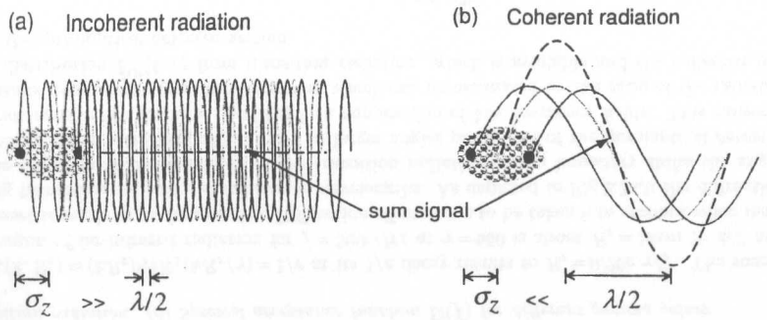

Figure 2.4: *Transition radiation for a bunch of N particles. (a) For $\sigma_z \gg \lambda$ the averaged transition radiation depends linear on N from incoherent emission processes. (b) For $\sigma_z \ll \lambda$ the coherent superposition dominates and averages quadratically with N.*

According to Eq.2.12 the measurement of the spectrum of coherent transition radiation $dW/d\omega$ determines only the product of the longitudinal and transversal bunch form factor. Therefore the transverse form factor $\rho^T_{q,\omega}$ limits the determination of the longitudinal form factor. To reduce the influence of the transverse bunch charge distribution $\sigma_z \gg \beta\sigma_r \sin\theta$ has to be fulfilled, the transverse beam size spot σ_r focussed onto the transition radiation screen $\rho^T_{q,\omega} \to 1$ and the acceptance angle of the quasioptical detector system has to be minimized. Having the acceptance functions Eq.2.7,2.11 in mind Eq.2.15 determines the longitudinal bunch charge distribution $\rho(z)$ by measuring the coherent transition radiation power spectrum.

$$\frac{dW}{d\omega} = D(\omega)A(\omega)f(\theta,\beta,N)\left|\rho^L_{q,\omega}\right|^2, \quad \rho^L_{q,\omega} = \mathcal{F}[\rho(t)] \tag{2.16}$$

Fig.2.5 shows three different longitudinal bunch charge distributions and their power spectra normalized at $f=0$.

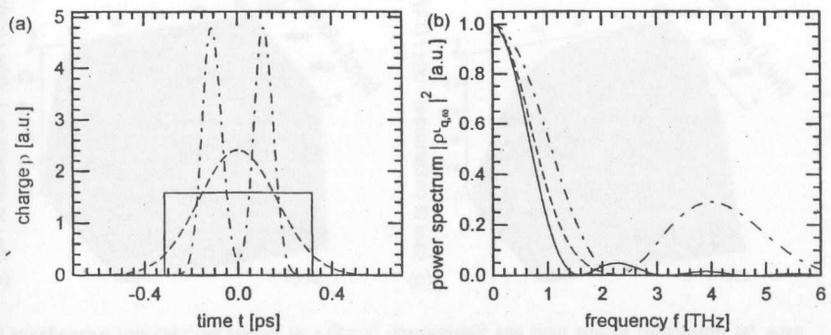

Figure 2.5: *(a) Longitudinal bunch charge distributions and (b) their power spectra.*

Chapter 3

Fundamentals

This chapter reviews basic concepts of a Josephson junction concerning its response on magnetic and radio-frequency (rf) electromagnetic fields. In the latter part a closer view on its noise properties and reconstruction of irradiated monochromatic rf-signals by using the Hilbert transform spectroscopy is presented.

3.1 High temperture superconductors (HTS)

At present, the ceramic compound $YBa_2Cu_3O_{7-\delta}$ is the technologically best controlled and mostly wide used HTS. Depending on the oxygen deficiency δ the transition temperature T_c reaches up to 93K. The crystal structure Fig.3.1 is orthorhombic with lattice constants a=3.82 Å, b=3.88 Å, c=11.68 Å.

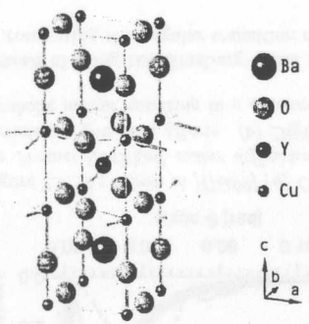

Figure 3.1: *Crystal structure of $YBa_2Cu_3O_7$.*

The coherence length ξ in *ab*-direction is about ξ_{ab} = 1.5nm at zero temperture and an order of magnitude lower in *c*-direction, resulting in a highly anisotropic critical current density. The current transport takes mainly place in the copper-oxygen planes along the *ab*-direction with critical current densities of about $J_c > 10^6 A/cm^2$ at T = 77K. Thin films are epitaxially grown in *c*-axis orientation, deposited at high temperture 750...850°C in their tetragonal phase of $YBa_2Cu_3O_6$ resulting in the orthorhombic $YBa_2Cu_3O_7$ by cooling to room temperature in oxygen atmosphere. Grain-boundary Josephson junctions are fabricated on bicrystal substrates, which are manufactured from two halves of a single-crystal fusing together under a misorientation angle, which is transferred at thinfilm growth to the superconducting material for a specific crystal orientation.

HTS are very suitable for rf-applications in the sub-millimeter wavelength regime, especially with low power consumption, because of their larger energy gap of at least $E_g = 4k_BT_c \ldots 7k_BT_c$ in comparison to conventional superconductors. HTS thin film structures operating in the sub-millimeter wavelength regime show a complicated angular dependence of the transmitted radiation affected by the energy gap anisotropy in d-wave superconductors, anisotropy of the substrate due to birefringence, resonance in the substrate modes, non-homogeneity and the granular structure of HTS films [Tar01]. The influence of the HTS material properties like the

surface resistance, penetration depth and dielectric properties [Kha02] on the electric response properties are negelected in this thesis.

3.2 Josephson effects

A Josephson junction consists of two weakly coupled superconducting electrodes seperated by a non-superconducting barrier for instance a thin insulating layer, acting as a tunnel barrier. If the barrier thickness does not significantly exceed the coherence length ξ, phase coherence appears between the Cooper pair wavefunctions across the barrier. In 1962, B.D. Josephson predicted a supercurrent through the barrier [Jos62]. Cooper pairs tunnel through the insulation and a nondissipative current flows through the junction. Within the macroscopic Ginzburg-Landau (GL) theory a pseudowavefunction Ψ was introduced as a complex order parameter [Gin50]. Gor'kov showed, that the GL theory is derivable as a rigorous limiting case of the microscopic theory, suitable reformulated in terms of Greens functions to treat a spatially inhomogeneous regime. With the help of the Bogoliubov-de Gennes equations the interacting many body system of electrons in the superconductor is represented by a non-interacting system of quasiparticles, namely electrons and holes. Interaction processes are represented by renormalized energies and finite lifetimes of the quasiparticles [Nol92, Chr99]. Using the Bogoliubov-de Gennes equations for inhomogeneous systems is more complicated than the GL theory, which is restricted to temperatures near T_c and to spatial slowly varying Ψ and vector potential $\vec{A}$.

However, for layered superconductors of half-spaces, indexed by (1) and (2), a generalization of the GL free energy density functional can be done [Scha99, Tin96]. Their functional derivation by the vector potential $\vec{A}$ determines the junction current density $j_{1,2}$ in plane $\vec{\varrho} = (x, y)$ with coupling constant η and barrier thickness d to

$$j_{1,2}(\vec{\varrho}, T) = 2e\eta d\frac{2\pi}{\Phi_0}|\Psi_1||\Psi_2|\sin(\varphi_2 - \varphi_1 - \chi_{1,2}) \quad \text{with} \quad \chi_{1,2} = \frac{2e}{\hbar}\int_0^d A_z(\vec{\varrho}, z)dz. \tag{3.1}$$

For a time dependent phase-difference $\varphi = \varphi_2 - \varphi_1 - \chi_{1,2}$ there will be a finite potential difference U over the barrier, independent of material properties. This and Eq.3.1 with the critical current density $j_c(\vec{\varrho}, T)$ is known are the dc- and ac-Josephson effect

$$j_{1,2}(\vec{\varrho}, T) = j_c(\vec{\varrho}, T)\sin(\varphi), \qquad \dot{\varphi}(t) = \frac{2e}{\hbar}U(t). \tag{3.2}$$

3.3 The RCSJ-model

According to the ac-Josephson effect Eq.3.2, not only the supercurrent carried by Cooper pairs of the superconductor contributes to the total current, but also electrons tunnel the barrier. The current is described in the RCSJ-model by the ideal Josephson junction characterized by the critical current I_c and a parallel shunted resistance R_n. Experimentally the biasing of the junction is realized as a current injection with the bias current I_0 and rf-signal I_{rf}, so the contacts are rather described by the phenomenologically RCSJ (Resistively-Capacity-Shunted-Junction)-model than by the microscopic deduced tunnel junction models [Ric97]. The RCSJ-model is useful for a homogeneous current distribution and small junctions with Josephson penetration depth smaller than geometric dimensions. In correspondence with the circuit diagram in Fig.3.2 a displacement current between the superconducting contacts is modeled by

a capacity, that particularly for low-T_c superconductors shows hysteretic modifications of the I-V-characteristic. Localized defect states within the barrier using a normal conductor provide an intrinsically resistive shunt for the quasiparticles suppressing a hysteretic I-V-characteristic. Neglecting the coupling mechanism of the rf-radiation into the Josephson junction, the induced rf-current is realized by a time dependent rf-current source $i_{rf}(\tau)$ without any dc-component.

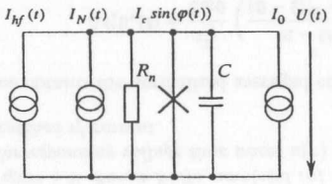

Figure 3.2: *Equivalent circuit diagram for a current biased Josephson junction within the RCSJ-model without external components.*

characteristic frequency	$\omega_c = (2e/\hbar)\, I_c R_n,$
voltages	$\tilde{u} = \omega_j/\omega_c = \bar{U}/I_c R_n$
currents	$i = I/I_c,$
impedance	$r = R/R_n,$
time	$\tau = t\omega_c,$
frequency	$\Omega = \omega_{rf}/\omega_c,$
voltage spectral density	$s_u = S_U\,\omega_c/I_c^2 R_n^2,$
current spectral density	$s_i = S_I\,\omega_c/I_c^2,$
noise rounding parameter	$\Gamma_0 = 2\pi k_B T/\Phi_0 I_c,$
McCumber Parameter	$\beta_c = (2e/\hbar)\, I_c R_n^2 C,$

Table 3.1: *Dimensionless parameters.*

According to Fig.3.2 and the dimensionless parameters in Tab.3.1, the differential equation for the time dependent phase $\varphi(\tau)$ of a current biased Josephson junction without external components results to

$$\sin\varphi(\tau) + \frac{d\varphi(\tau)}{d\tau} + \beta_c\frac{d^2\varphi(\tau)}{d\tau^2} = i_0 + i_{rf}(\tau) + i_N(\tau), \quad i_N(\tau) = i_{th}(\tau) + i_{S_I}(\tau). \tag{3.3}$$

The noise rounding parameter describes the strength of a white noise source $i_N(\tau)$, which consists of thermal current noise $i_{th}(\tau)$ from the normal-state resistance and injected noise $i_{S_i}(\tau)$ from current source. Additional low-frequency fluctuations of the critical current δI_c and normal-state resistance δR_n, caused by stochastic occupation of localized states by electrons in the barrier of the tunnel junction, leads to 1/f-noise, which is well described by a small signal analysis within the RCSJ-model [Mar96].

3.3.1 I-V-characteristic without radiation

In practice, the Josephson junction is driven by the bias current i_0 and the voltage drop $u(\tau)$ over junction, namely its average value $\bar{u}$ is measured. This is because the measuring instruments and voltage pickup at junction has in general low-pass character compared to the Josephson self oscillation frequency. Without any fluctuations $i_N(\tau) = 0$, rf-radiation $i_{rf}(\tau) = 0$ and non-hysteretic contacts $\beta_c \ll 1$ Eq.3.3 reduces to

$$\sin\varphi(\tau) + \frac{d\varphi(\tau)}{d\tau} = i_0, \tag{3.4}$$

and can be solved for $-1 \le i_0 \le 1$ with $\varphi = const$ leading to zero voltage $u(\tau) = 0$, namely the superconducting state. Separation of variables leads for $|i_0| > 1$ to the phase Eq.A.2, respectively voltage Eq.A.4 and taking the time averages over a Josephson oscillation, the I-V-characteristic without rf-radiation follows a hyperbolic formula as shown in Fig.3.3.

$$\bar{u} = \begin{cases} 0 & \forall \quad |i_0| \le 1 \\ \sqrt{i_0^2 - 1} & \forall \quad |i_0| > 1 \end{cases}, \qquad \bar{U} = \begin{cases} 0 & \forall \quad |I_0| \le I_c \\ R_n\sqrt{I_0^2 - I_c^2} & \forall \quad |I_0| > I_c \end{cases} \tag{3.5}$$

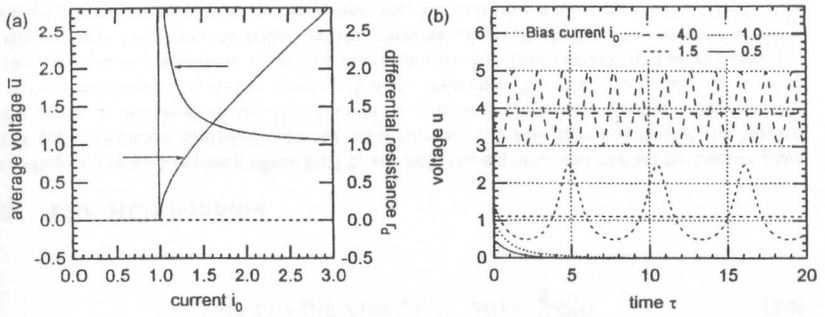

Figure 3.3: *Runge-Kutta simulated (a) V-I-characteristic, differential resistance $r_d = d\bar{u}/di_0$ and (b) voltage time traces of Josephson junction for different bias currents i_0.*

3.3.2 I-V-characteristic with radiation

The I-V-characteristic with monochromatic rf-radiation $i_{rf}(\tau) = i_{rf}\sin(\Omega\tau)$ can be calculated from

$$\sin\varphi(\tau) + \frac{d\varphi(\tau)}{d\tau} = i_0 + i_{rf}\sin(\Omega\tau). \tag{3.6}$$

Under the assumption that the perturbation current i_{rf} is sufficiently smaller than the bias current i_0, the time averaged current change Δi from unperturbated I-V-characteristic, can be obtained by solving Eq.3.6 using the slowly varying phase approximation [Lik96], as outlined in section A.2.2. Under the condition of a constant average voltage $\bar{u} = \overline{\dot{\varphi}(\tau)} = \text{const}$ at bias point $i_0(\bar{u})$ the averaged current change Δi results with the Josephson oscillation $\bar{u} = \omega_j/\omega_c$ for monochromatic rf-radiation in second order perturbation to

$$\Delta i(\bar{u},\Omega) = -\frac{1}{4i_0\,(\Omega^2-\bar{u}^2)}\,i_{rf}^2 \qquad \forall \qquad \bar{u}\neq\Omega \tag{3.7}$$

$$\Delta I(\omega_j,\omega_{rf}) = -\frac{\omega_c^2}{4I_0(\omega_{rf}^2-\omega_j^2)}\,I_{rf}^2 \qquad \forall \qquad \omega_j\neq\omega_{rf},\ \omega_j = \frac{2e}{\hbar}\bar{U}. \tag{3.8}$$

Fig.3.4 shows a simulated V-I-characteristic of a Josephson junction irradiated with monochromatic radiation and corresponding voltage time traces $u(\tau)$ for vanishing noise parameter. The small signal approach Eq.3.7 is only valid for very small rf-currents i_{rf}. In the noiseless case the quadratic behavior of the first order Shapiro step width from induced rf-current is, also for numerical simulations according to Fig.3.5, not realized for bias points at $\bar{u} = \Omega$. The proportionality between current response and rf-power i_{rf}^2 is expressed by the frequency dependent term in Eq.3.7 far away from its divergence. A broadband spectral reconstruction based on Eq.3.7 requires an integral definition excluding the divergence for the noiseless case, namely the Hilbert transform spectroscopy introduced in the next coming sections. Fortunately, due to the damping of intrinsic noise sources the unphysical divergence of Eq.3.7 is not present in real Josephson junctions, as shown in Fig.A.2 for an operation with $\Gamma_0 > 0$. According to Eq.3.5 a noise current causes a voltage drop over the Josephson junction δU, which stochastically modulates the noisefree voltage $\bar{u}$. Under the assumption of a gaussian distributed noise signal $\sigma(\bar{u})$, realized by the following replacement within Eq.3.7

$$\frac{1}{\sqrt{1+\bar{u}^2(\Omega^2-\bar{u}^2)}} \longrightarrow \int_0^\infty \frac{\sigma(\bar{u})}{\sqrt{1+\bar{u}^2(\Omega^2-\bar{u}^2)}}d\bar{u} \tag{3.9}$$

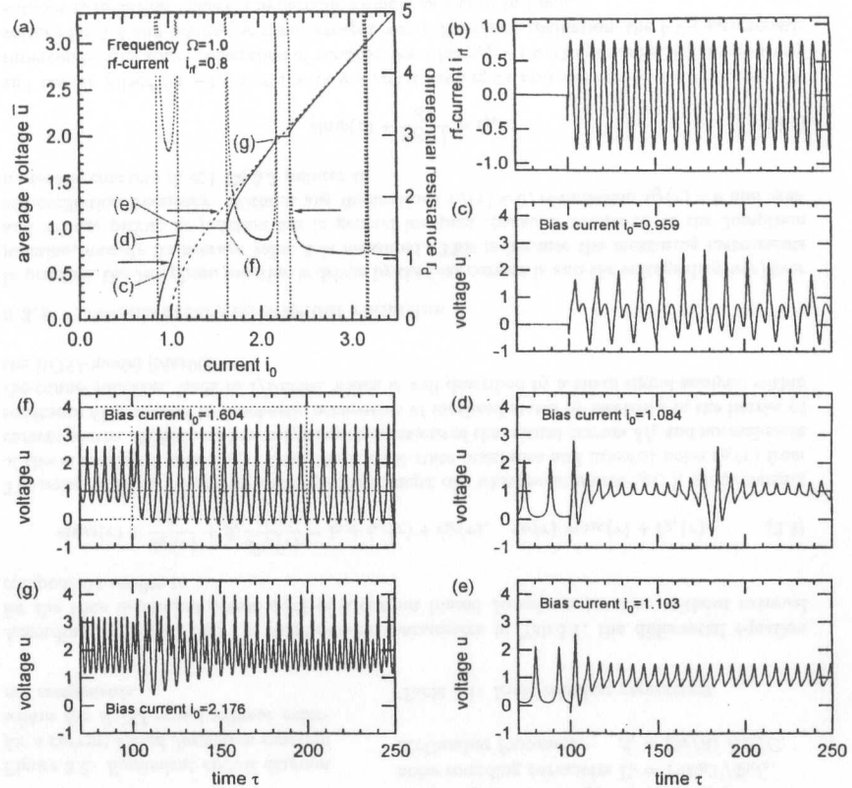

Figure 3.4: *Runge-Kutta simulated (a) V-I-characteristic with monochromatic radiation. (c)-(g) Corresponding voltage time traces $u(\tau)$ for different bias currents i_0 under the influence of a (b) switched rf-current.*

one obtains the normalized averaged current response in the limit of a small signal theory

$$\Delta i(\bar{u},\Omega) = \frac{i_{rf}^2}{8i_0\bar{u}}\left(\frac{\bar{u}-\Omega}{(\bar{u}-\Omega)^2+\Gamma^2} + \frac{\bar{u}+\Omega}{(\bar{u}+\Omega)^2+\Gamma^2}\right) \quad \forall \quad i_{rf}\ll 1, \quad \text{with} \tag{3.10}$$

$$\Gamma(\bar{u},\Gamma_0) = \Gamma_0 r_d^2(\bar{u},\Gamma_0)\left(1+\frac{1}{2i_0^2(\bar{u},\Gamma_0)}\right). \tag{3.11}$$

$\Gamma = \Lambda/\omega_c$ denotes, without any external noise sources, the Josephson self oscillation linewidth, which depends with Eq.3.5 on Nyquist noise of the source resistance R_n for $i_0 \gg 1$, differential resistance R_d and bias current i_0, recognized from the unnormalized linewidth $\Lambda = (2e/\hbar)^2 k_B T(R_d^2/R_n)(1 + I_c^2/2I^2)$ [Lik96]. Eq.3.10 is only valid for small rf-signals. According to Eq.A.21, this is fulfilled for phase deviations $|\Delta\varphi| \cong b_1 i_{rf} < 1$, resulting in

$$i_{rf} \le (i_0-1)\Omega/i_0, \qquad i_{rf} \le (i_0-1)(\Omega\pm\bar{u}). \tag{3.12}$$

Obviously, as depicted in Fig.3.5, driving a monochromatic rf-signal on a curved V-I-characteristic reveals, higher harmonics depending on its amplitude. These higher order Shapiro steps, index by n, occur at multiples of the rf-radiation frequency $\bar{u}=n\Omega$, $n \geq 1$. The 0th order Shapiro step is the suppression of the critical current itself. For lower frequencies $\Omega \ll 1$, respectively high I_cR_n-products, several Shapiro steps are simultaneously activated making broadband spectroscopy difficult.

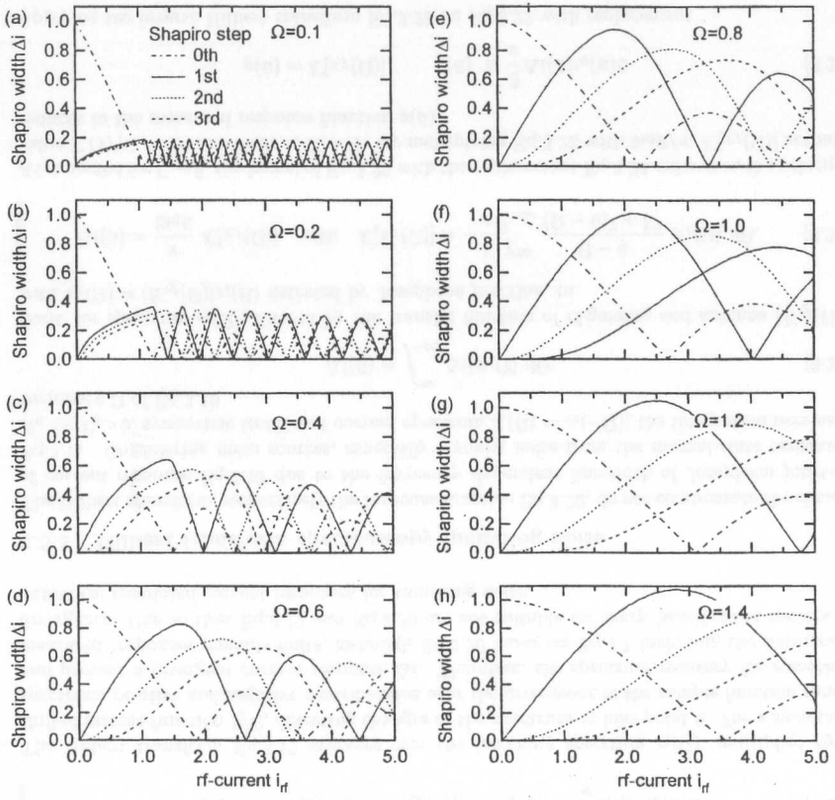

Figure 3.5: *Simulated nth Shapiro step width Δi in dependence of irradiated rf-current i_{rf} for different monochromatic frequencies Ω and noiseless operation.*

3.3.3 Noise in Josephson junctions

• Frequency independent noise

The lower limit of the junction noise operated at temperature $T > 0$ is given by the thermal noise of the normal-state resistance R_n. If the thermal energy is of the order of the Josephson coupling energy $E_J = \hbar I_0/2e$, the noise current temporarily disrupts the phase coupling of the superconducting electrodes, at which the phase slips by a factor of 2π. Thus a voltage

drop occurs and, as depicted in Fig.A.1, the non-zero time averaged voltage drop leads to a noise rounded I-V-characteristic. The degree of noise rounding increases with increasing noise rounding parameter

$$\Gamma_0 = \frac{k_BT}{E_J} = \frac{2\pi k_BT}{\Phi_0 I_c}. \tag{3.13}$$

Additional noise fluctuations from bias current i_0 or reversed impressed current noise sources from voltage readout system can also lead to an increased noise parameter and change the I-V-characteristic. The normal-state resistance provides Nyquist noise with a frequency independent current noise spectral density $S_{I,th}$. The corresponding voltage noise spectral density $S_{U,th}$ of the Josephson junction at frequencies much less than the Josephson frequency is given by [Lik96]

$$s_{i,th} = 4\Gamma_0 \quad , \quad S_{I,th} = 4k_BT\frac{1}{R_n}, \tag{3.14}$$

$$s_{u,th} = 4\Gamma_0 r_d^2\left[1+\frac{1}{2i_0^2}\right], \quad S_{U,th} = 4k_BT\frac{R_d^2}{R_n}\left[1+\frac{1}{2}\left(\frac{I_c}{I_0}\right)^2\right]. \tag{3.15}$$

where the differential resistance results from the noise rounded I-V-characteristic. The term $1/2i_0^2$ accounts for noise contributions at frequencies close to the Josephson frequency, which are mixed down into the low-frequency regime by the inherent non-linearity of the Josephson junction.

• 1/f-noise

Resistance fluctuations δR_n and critical current fluctuations δI_c produce a quadratic increase of the voltage noise spectral density $S_V(f)$ with frequency. Trapping and release of quasiparticles into a high density of localized defect states within the junctions barrier modulate the cooper pair transport, resulting in resistance, respectively current fluctuations. Defining the fluctuation densities $S_R(f)$, $S_I(f)$ and cross fluctuation density $S_{IR}(f)$ the voltage spectral density within a small signal analysis of the RSJ-model is given by [Mar96]

$$S_V(f) = (V-R_dI)^2S_I(f) + V^2S_R(f) + 2C(0)(V-R_dI)VS_{IR}(f) \quad \text{with} \tag{3.16}$$

$$S_R(f) = \left|\frac{\delta R_n}{R_n}\right|^2, \quad S_I(f) = \left|\frac{\delta I_c}{I_c}\right|^2, \quad S_{IR}(f) = \left|\frac{\delta R_n}{R_n}\right|\left|\frac{\delta I_c}{I_c}\right| \tag{3.17}$$

The correlation between resistance and current fluctuations can either be measured and defined in the time domain $C(0)$ or frequency domain $\gamma(f)$ [Lud97]. The correlation definition in frequency domain $\gamma(f)$ determines $C(0)$, reveals much more information and is more suitable for spectroscopy. A comprehensive work on the physical origin, novel correlation measurement techniques for 1/f-noise from Josephson junctions has been discussed earlier [Lud97].

3.3.4 Hilbert transform spectroscopy excluding noise

In the case of a continuous rf-radiation source with normalized current spectral density $s_i(\Omega) = S_I(\omega)\omega_c/I_c^2$, Eq.3.7 generalizes for a symmetric spectrum $s_i(\Omega) = s_i(-\Omega)$ with the replacement and identity

$$i_{rf}^2 \rightarrow \int s_i(\Omega)d\Omega, \qquad \int_0^\infty \frac{s_i(\Omega)2\bar{u}}{\Omega^2-\bar{u}^2}d\Omega = \int_{-\infty}^\infty \frac{s_i(\Omega)}{\Omega-\bar{u}}d\Omega. \tag{3.18}$$

to the Cauchy principle value integral, denoted by $\mathcal{P}$, excluding the pole at $\bar{u}=\Omega$, where $\mathcal{H}$ is actually the Hilbert transform.

$$\Delta i(\bar{u}) = -\frac{\pi}{8i_0\bar{u}}\,\mathcal{H}[s_i(\Omega)] \quad \text{with} \quad \mathcal{H}[s_i(\Omega)] = \frac{1}{\pi}\mathcal{P}\int_{-\infty}^\infty \frac{s_i(\Omega)}{\Omega-\bar{u}}d\Omega. \tag{3.19}$$

Changing to unnormalized units the spectrum $s_i(\Omega)$ identifies as a current spectral density. Therefore Eq.3.19 is strictly only valid for unlimited rf-signals, otherwise the spectral density vanishes. Furthermore the spectrum has to be bandlimited, otherwise the current response is divergent. With Eq.3.19 and the inverse Hilbert transform $\mathcal{H}^{-1}=-\mathcal{H}$, the irradiated spectrum can reconstructed by measuring the voltage dependent change of the current response $\Delta i(\bar{u})$ and I-V-characteristic $i(\bar{u})$ in the small signal limit.

$$s_i(\Omega)=\mathcal{H}^{-1}[g(\bar{u})]=-\mathcal{H}[g(\bar{u})],\qquad g(\bar{u})\equiv\frac{8}{\pi}\Delta i(\bar{u})i_0(\bar{u})\bar{u} \tag{3.20}$$

The Hilbert transform Eq.3.19 averages over the incoming spectrum $s_i(\Omega)$, multiplied by a shifted sample function $1/\Omega$, detecting changes of the spectrum at bias point $\bar{u}$. For a smoothed spectrum, positive and negative contributions near the divergence of the sample function cancel and prevent a divergent current response Δi. Therefore, the spectrum recovery for smoothed measured responses remains finite, although Eq.3.20 bases on Eq.3.7 including the unphysical divergence. Due to this, Eq.3.19 and Eq.3.20 are not suitable for sharp bandlimited spectra or numerical simulated current responses for vanishing noise.

3.3.5 Hilbert transform spectroscopy including noise

The Hilbert transform, respectively the response function Eq.3.20, do not compensate the change of current response Eq.3.10 due to the frequency dependent linewidth of Josephson junction Eq.3.11. Considering noise sources, especially Nyquist noise from the normal-state resistance R_n for $\Gamma_0>0$, symmetric irradiated current spectrum $s_i(\Omega)=s_i(-\Omega)$, the integration over each frequency Ω of Eq.3.10

$$\Delta i(\bar{u})=\int_{-\infty}^{\infty}\Delta i(\bar{u},\Omega)\,d\Omega \tag{3.21}$$

leads, for spectrum $s_i(\Omega)$, filtered by the transfer function of rf-guiding and antenna $|K_{rf}(\Omega)|$, with $s_J(\Omega)=|K_{rf}(\Omega)|s_i(\Omega)$ detected by Josephson junction, to

$$\Delta i(\bar{u})=\frac{\pi}{8i_0\bar{u}}\,\mathcal{K}[s_J(\Omega)]\quad\text{with}\quad\mathcal{K}[s_J(\Omega)]=-\frac{1}{\pi}\int_{-\infty}^{\infty}\frac{\Omega-\bar{u}}{(\Omega-\bar{u})^2+\Gamma^2}\,s_J(\Omega)\,d\Omega. \tag{3.22}$$

As expected for $\Gamma\to 0$, the kernel of Eq.3.22 with the replacement Eq.3.24 reduces to the principle value $\mathcal{P}\,(1/(\Omega-\bar{u}))$ and leads to $\mathcal{K}=\mathcal{H}$. By multiplying Eq.3.22 with $8i_0\bar{u}/\pi$, $\mathcal{K}[s_J(\Omega)]$ actually reduces to the measured response function $g(\bar{u})$.

$$g(\bar{u})=\mathcal{K}[s_J(\Omega)],\qquad g(\bar{u})\equiv\frac{8}{\pi}\Delta i(\bar{u})i_0(\bar{u})\bar{u} \tag{3.23}$$

Applying the inverse Hilbert transform Eq.3.20 on Eq.3.23 with replacement

$$\frac{\Omega-\bar{u}}{(\Omega-\bar{u})^2+\Gamma^2}=\frac{1}{2}\left(\frac{1}{(\Omega-\bar{u})+i\Gamma}+\frac{1}{(\Omega-\bar{u})-i\Gamma}\right) \tag{3.24}$$

yields implicit the spectrum $s_J(\Omega)$ of the measured response function including noise by

$$s_g(\Omega)\equiv\mathcal{H}^{-1}[g(\bar{u})]=\frac{1}{\pi}\int_{-\infty}^{\infty}\frac{\Gamma(\Omega')}{(\Omega-\Omega')^2+\Gamma(\Omega')^2}\,s_J(\Omega')\,d\Omega'. \tag{3.25}$$

Eq.3.25 describes the change of reconstructed spectrum $s_g(\Omega)$ from irradiated spectrum $s_J(\Omega)$ due to the linewidth of Josephson junction. As shown in appendix A.3, unfortunately $-\mathcal{K}\mathcal{K}\neq 1$

is fulfilled. As expected, the spectrum is smoothed out by the Josephson linewidth profile for $\gamma_J(\Omega-\Omega')=\Gamma(\Omega')/((\Omega-\Omega')^2+\Gamma(\Omega')^2)$. The irradiated spectrum $s_J(\Omega)$ can be reconstructed numerically from Eq.3.25 by using a first kind of integral equation solved by the nonlinear method of minimization [Kos02]. Limitation effects from a finite measuring interval of the response function and an enhancement of the spectral resolution, so called supperresolution, can be considered. Using a deconvolution by assuming a frequency independent linewidth is a rather inaccurate approximation near the critical current. To simplify correction factors for broadband and smallband spectra are introduced.

- **Broadband correction factor $\mathbf{k_b(\Omega,\Gamma_0)}$**

For smooth $|K_{rf}(\Omega)|$ and small Γ, compared to the signal bandwidth $\Gamma(\Omega)\ll\Delta B(|K_{rf}(\Omega)|s_i(\Omega))$, according to Eq.3.11 for bias points $i_0\gg 1$, respectively high frequencies and low noise parameters, the measured spectrum $s_g(\Omega)$ is evidently equal to the original spectrum $s_i(\Omega)$. Especially for a nearly constant broadband spectrum $s_J(\Omega)\approx$ const. the correction factor $k_b(\Omega,\Gamma_0)$ of the spectrum results with Eq.3.25, Eq.3.11, $r_d(\Omega)=-(1+\Omega^{-2})^{1/2}$, $i_0=(1+\Omega^2)^{1/2}$ for $\Gamma_0\to 0$ to

$$s_i(\Omega)\approx|K_{rf}(\Omega)|^{-1}\mathcal{H}^{-1}[g(\bar{u})]k_b(\Omega,\Gamma_0)\quad\forall\quad\Gamma(\Omega)\ll\Delta B(|K_{rf}(\Omega)|s_i(\Omega)) \tag{3.26}$$

$$\text{with}\qquad k_b(\Omega,\Gamma_0)=\left[\frac{1}{\pi}\int_{-\infty}^{\infty}\frac{\Gamma_0(1+3/2\Omega'^2)}{(\Omega-\Omega')^2+\Gamma_0^2(1+3/2\Omega'^2)^2}\,d\Omega'\right]^{-1}.$$

The broadband correction factor $k_b(\Omega,\Gamma_0)$ is shown in Fig.3.6b for different noise parameters. The factor has nearly no effect for bias currents $i_0\gg 1$.

- **Smallband correction factor $\mathbf{k_s(\Omega,\Gamma_0)}$**

If $|K_{rf}(\Omega)|$ is a more narrow-band function compared to Josephson oscillation width $\Gamma(\Omega)\gg\Delta B(|K_{rf}(\Omega)|s_i(\Omega))$, Eq.3.25 give the shape of Josephson oscillation. The smallband correction factor $k_s(\Omega,\Gamma_0)$ compensate the change of junction response Eq.3.10 due to the frequency dependent linewidth. For this, we calculate the frequency dependent maximum response for a series of discrete, enough seperated frequencies Ω_n, modulated by a spectrum $|K_{rf}(\Omega)|s_i(\Omega)$,

$$s_J(\Omega)=\sum_n|K_{rf}(\Omega_n)|s_i(\Omega_n)\,\delta(\Omega_n-\Omega)\qquad\forall\qquad\Gamma(\Omega_n)\ll\Omega_n-\Omega_m,n\neq m \tag{3.27}$$

inserted into Eq.3.25 results to

$$s_g(\Omega)=\mathcal{H}^{-1}\,[g(\bar{u})]=\frac{1}{\pi}\sum_n\frac{\Gamma(\Omega_n)}{(\Omega-\Omega_n)^2+\Gamma(\Omega_n)^2}\,|K_{rf}(\Omega_n)|s_i(\Omega_n). \tag{3.28}$$

Under the assumption Eq.3.27 of a non-overlapping spectrum from Josephson junction, the right term of Eq.3.28 dominates for frequencies $\Omega=\Omega_n$, resulting in

$$s_i(\Omega_n)=|K_{rf}(\Omega_n)|^{-1}\mathcal{H}^{-1}\,[g(\bar{u_n})]\,\pi k_s(\Omega_n,\Gamma_0)\quad\forall\quad\Gamma(\Omega)\gg\Delta B(|K_{rf}(\Omega)|s_i(\Omega)) \tag{3.29}$$

$$\text{with}\qquad k_s(\Omega_n,\Gamma_0)=\Gamma(\Omega_n).$$

The smallband correction function $k_s(\Omega_n,\Gamma_0)$ is actually the Josephson self oscillation linewidth and shown in Fig.3.6a. The factor compensates the change of junction response Eq.3.10 due to the frequency dependent linewidth. Fig.3.7a shows the response spectrum $s_g(\Omega)$ for a normalized bandlimited spectrum $[\Omega_1,\Omega_2]$ Sharp structures of the spectrum are smoothed out by the Josephson oscillation linewidth. Fig.3.7b shows the spectral response of an rf-pulse with cutoff according to Eq.3.25. The smooth part of the spectrum is evidently more equal to the original spectrum than its sharped filtered part. Concerning the TTF

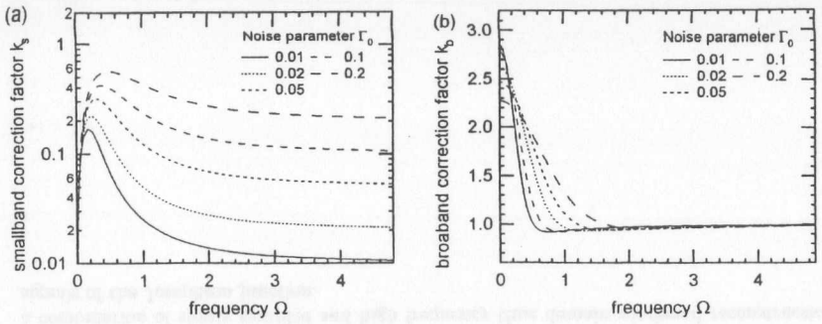

Figure 3.6: *(a) Smallband correction factor k_s and (b) broadband correction factor k_b.*

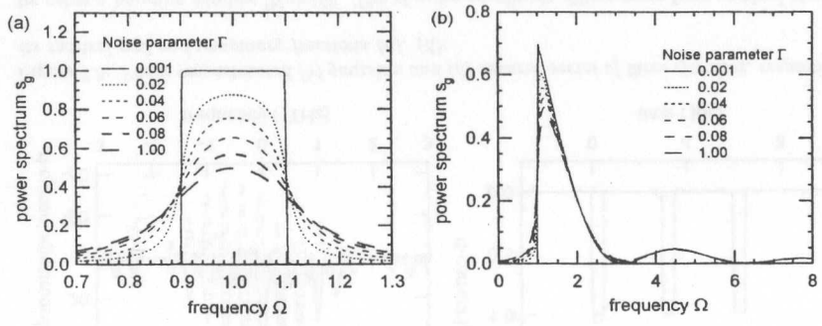

Figure 3.7: *Simulated (a) normalized bandlimited spectrum $[\Omega_l = 0.9, \Omega_2 = 1.1]$ and (b) rf-pulse spectrum with cutoff from Eq.3.25 for different noise parameters Γ.*

application, we are only interested in the single rf-pulse spectral envelope of the discrete distributed frequencies from bunch repetition. Negelecting the intermediate spectral information the system of equations Eq.3.28 has to be solved at discrete frequencies at $\Omega = \Omega_n$ and cutted at finite indicies N, M. The detailed spectral information in the low frequency regime from accurate Eq.3.31 is absolutely neccessary for a realistic time domain signal recovery.

$$s_g(\Omega_m) = \mathcal{H}^{-1}[g(\bar{u}_m)] = \frac{1}{\pi}\sum_{n=-N}^{N} a_{n,m}\, s_i(\Omega_n) = \mathbf{a}\cdot\mathbf{s_i} \tag{3.30}$$

$$\mathbf{s_i} = \mathbf{a}^{-1}\cdot\mathbf{s_g} \quad \text{with} \quad a_{n,m} = \frac{1}{\pi}\frac{\Gamma(\Omega_n)}{(\Omega_m-\Omega_n)^2+\Gamma(\Omega_n)^2}\,|K_{rf}(\Omega_n)| \tag{3.31}$$

3.3.6 Hilbert transform spectroscopy cutoff effects

To calculate the Cauchy principal value integral in the Hilbert transform, usually direct computation or Fast Fourier transfrom techniques are applied. Both of them require a large region of sweeped bias voltage in order to avoid lack of resolution and disturbation of the spectrum. Due to the finite boundaries of the bias voltage Ω_l and Ω_r, correction functions, deduced from

Eq.3.19, are necessary.

$$s_i(\Omega) = -\mathcal{H}[g(\bar{u})] = s_l(\Omega) - \frac{1}{\pi}\mathcal{P}\int_{\Omega_r}^{\Omega_l}\frac{g(\bar{u})}{\Omega-\bar{u}}d\bar{u} + s_r(\Omega) \quad \forall \quad \Omega\in[\Omega_l,\Omega_r] \quad \text{with} \tag{3.32}$$

$$s_l(\Omega) = -\frac{1}{\pi}\mathcal{P}\int_{-\infty}^{\Omega_l}\frac{g_l(\bar{u})}{\Omega-\bar{u}}d\bar{u}, \qquad s_r(\Omega) = -\frac{1}{\pi}\mathcal{P}\int_{\Omega_r}^{+\infty}\frac{g_r(\bar{u})}{\Omega-\bar{u}}d\bar{u} \tag{3.33}$$

To compute contributions from cutoff to negative, respectively positive frequencies $s_l(\Omega)$, $s_r(\Omega)$ we continue the response function Eq.3.20 by the asymptotic behavior of a single Shapiro step response. From Eq.3.10 we obtain in the limit $\bar{u} \gg \Omega, \Gamma$ the asymptotic behaviour of a single Shapiro step as a $1/\bar{u}$ function.

$$g_l(\bar{u}) = \eta_l\frac{1}{\bar{u}} \quad \forall \quad \bar{u}\ll\Omega, \qquad g_r(\bar{u}) = \eta_r\frac{1}{\bar{u}} \quad \forall \quad \bar{u}\gg\Omega \tag{3.34}$$

Here the scaling factors η_r, η_r are introduced. They are determined by the continuity of the measured response function $g(\bar{u})$ and the asymptotic functions $g_l(\Omega_l)$, $g_r(\Omega_r)$ and its derivation at cutoff frequency Ω_l, Ω_r, respectively $\bar{u}_l$, $\bar{u}_r$ for the asymptotic functions.

$$\eta_l = -\frac{g_l(\Omega_l)^2}{g_l'(\Omega_l)}, \quad \bar{u}_l = -\frac{g_l(\Omega_l)}{g_l'(\Omega_l)}, \qquad \eta_r = -\frac{g_r(\Omega_r)^2}{g_r'(\Omega_r)}, \quad \bar{u}_r = -\frac{g_r(\Omega_r)}{g_r'(\Omega_r)} \tag{3.35}$$

The asymptotic correction of the Hilbert transform with cutoff results for the positive asymptotic range $s_r(\Omega)$, and respectively in the same way for the negative asymptotic range $s_l(\Omega)$ to

$$s_l(\Omega) = +\frac{\eta_l}{(\Omega-\Omega_l+\bar{u}_l)}\log\left[\frac{\bar{u}_l}{|\Omega_l-\Omega|}\right] \quad \forall \quad \Omega\gg\Omega_l \tag{3.36}$$

$$s_r(\Omega) = -\frac{\eta_r}{(\Omega-\Omega_r+\bar{u}_r)}\log\left[\frac{\bar{u}_r}{|\Omega_r-\Omega|}\right] \quad \forall \quad \Omega\ll\Omega_r. \tag{3.37}$$

The asymptotic functions Eq.3.34 and therefore the correction spectra Eq.3.36 and Eq.3.37 are strictly valid only for monochromatic radiation spectra based on Eq.3.10. For an unknown coherent broadband spectrum the corrections differ and numerical methods must take into account [Kos02].

3.4 Time domain signal reconstruction

It is obvious, that a time domain signal $i_{rf}(t)$ cannot be reconstructed unique by its power spectrum, respectively spectral density without knowledge of its phase distribution $\psi(\Omega)$.

$$s_i(\Omega) = \lim_{T\to\infty}\frac{1}{2T}\,S^*(\Omega)S(\Omega) \quad \text{with} \quad S(\Omega) = \mathcal{F}[i_{rf}(\tau)] = \xi(\Omega)e^{i\psi(\Omega)} \tag{3.38}$$

However, under the assumption of strictly causality the real and imaginary part depend on each other by the Kramers-Kronig-Relation. For a given symmetric power spectrum $\xi^2(\Omega) = S^*(\Omega)S(\Omega)$ a minimal phase $\psi(\Omega)$ can be given [Schm99, Gei99] resulting in the reconstructed time domain rf-signal $i_{rf}(\tau)$.

$$i_{rf}(\tau) = \mathcal{F}^{-1}[\xi(\Omega)e^{i\psi(\Omega)}], \quad \psi(\Omega) = \frac{2\Omega}{\pi}\,\mathcal{P}\int_0^{\infty}\frac{\ln[\xi(\Omega')/\xi(\Omega)]}{\Omega^2-\Omega'^2}d\Omega' \tag{3.39}$$

Fig.3.8 shows the phase and time domain signal reconstruction of a series of threee gaussian, respectively squared pulses according to Eq.3.39. The inverse Fourier transform is performed

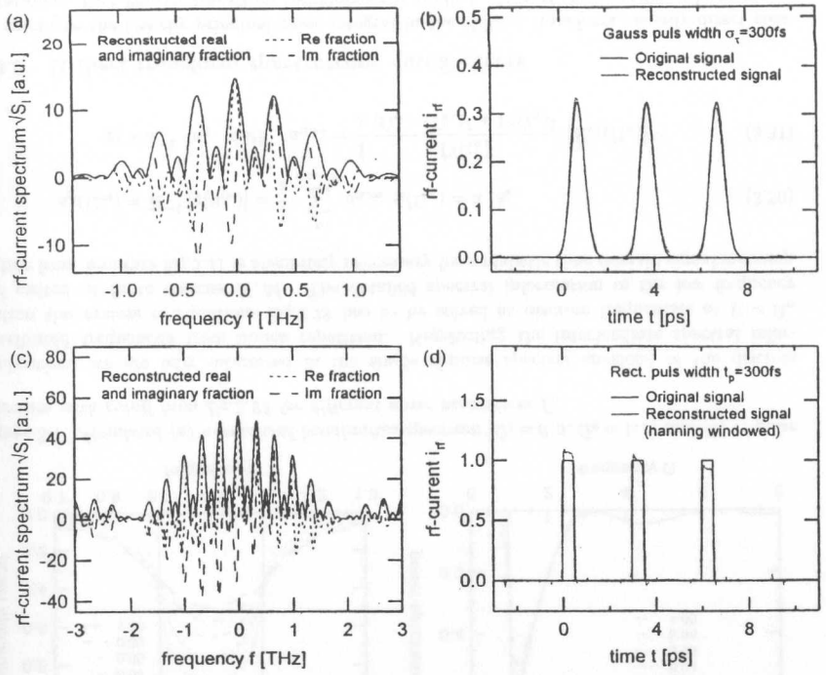

Figure 3.8: *Phase reconstructed (b) gaussian and (d) squared series of three rf-pulses, respectively its spectral real and imaginary fractions (a), (d).*

by using a hanning window [Num00]. The rf-pulse amplitude differs more from original rf-pulse series with increasing signal window. Due to the lower cutoff of the Josephson junction the reconstruction of long tracing rf-signals is limited. Therefore rf-oscilloscope applications requires a combination of slowly sampled and high frequency time domain windowed reconstruction of signals of the Josephson junction.

Chapter 4

Characterization of the spectrometer

In this section the characteristics of the TTF-spectrometer for continuous radiation and pulsed coherent radiation is examined concerning the voltage sensitivity, frequency resolution, temperature behaviour and measuring time. Since the interaction time of radiation with the spectrometer is substantially smaller for pulse-type radiation with long pulse spacing than for continuous radiation, one expects a smaller detector voltage, which limits dramatically the measuring time of the detector. A larger detector voltage can be achieved by increasing the induced rf-current in the Josephson junction, whereby the Hilbert transform spectroscopy looses its validity as small signal theory. The following questions cannot be answered within the Hilbert theory.

- *It is possible to take a spectrum of a single pulse within finite measuring time ?*
- *How are the rf-power maximum ratings defined for a unique spectral reconstruction ?*
- *Is a phase reconstruction of the rf-signal possible ?*

Therefore numerical simulations are investigated and analytic expressions of the voltage expectation value within the Focker-Planck formalism are presented for different types of rf-signals at maximum rf-power ratings by introducing a first order difference recurrence scheme. Because noise sources and the Josephson oscillation dominate the junctions spectral response the Focker-Planck method is an ideal tool to investigate the junction dynamic for broadband rf-signals. Including noise, I derive, that the maximum rf-power ratings for rf-pulses are independent of the pulse period within the delta pulse limit. Contrary, a decrease of rf-pulse width can be compensated by increasing the rf-pulse peak rf-current for a constant voltage response. The maximum peak rf-power rating for pulse-type rf-signals is approximately of the same order as for monochromatic rf-radiation. Furthermore we present analytic correction functions for discrete spectra for multi-harmonic mixing effects and higher order Shapiro steps out of the small signal approach. I reveal ghost spectra and its symmetry breaking mechanism and a phase reconstruction of the incoming rf-signal far away from limits of Hilbert theory.

4.1 Stochastical solution of the RCSJ-model

To ensure a unique reconstruction of the irradiated spectrum, preferentially weak-link type Josephson junctions with non-hysteretic I-V-characteristics are used. The differential equation of the RCSJ-model for the time dependent phase $\varphi(\tau)$

$$\sin\varphi(\tau) + \frac{d\varphi(\tau)}{d\tau} + \beta_c \frac{d^2\varphi(\tau)}{d\tau^2} = i_0 + i_{rf}(\tau) + i_{th}(\tau) + i_{S_I}(\tau) \tag{4.1}$$

is solved by numeric integration methods, as the 4th order Runge-Kutta method. A random number generator generates the noise current $i_{th}(\tau)$ for each time value with step width $\Delta\tau$.

Using a gaussian shaped distribution of the probability density of random numbers, one obtains likewise a gaussian shaped amplitude distribution of currents $i_{th}(\tau)$, whose spectrum is frequency independent up to the frequency $2\pi/\Delta\tau$. After the phase time traces $\varphi(\tau)$ swings out for given initial value and fixed bias point i_0, the voltage time traces $u(\tau)$ can be determined, as well as the expectation value of the voltage $\bar{u}(\tau)$ from Josephson junction by averaging over many periods from rf-signal. Alternatively the averaging process can be performed by a low-pass filter characteristic, representing bond wires, antenna and the rf-amplifier stage.

$$u(\tau, i_0) = \dot{\varphi}(\tau, i_0), \qquad \bar{u}(i_0) = \lim_{T\to\infty} \frac{1}{T} \int_0^T \dot{\varphi}(\tau, i_0) d\tau \tag{4.2}$$

Expecting small detector voltages of pulse-type rf-signals with long pulse spacing and an operation of the TTF-spectrometer at liquid nitrogen temperature near $77K$, the determination of the I-V-characteristics with a Runge-Kutta method is practically not feasible due to the long averaging times. Analytic expressions derived within the Fokker-Planck formalism are more suitable than stochastical models.

4.2 Solution of the Fokker-Planck (FP) Equation

Instead of solving the equation of motion Eq.4.1 stochastically, an ensemble of systems is prepared, which differs by its stochastical quantities. The probability density $W(\varphi, \tau)$ of finding the phase φ at time τ in the interval $[\varphi, \varphi + d\varphi]$ is given by the number of appropriate systems divided by the total number of systems in the ensemble. The Fokker-Planck (FP) equation is the equation of motion for the probability density of macroscopic variables φ, τ. Once having $W(\varphi, \tau)$ expectation values $\langle f(\varphi(\tau))\rangle$ of the system can be determined. A FP equation can be given, if a deterministic equation is additive to a stochastic term with frequency independent spectrum. For non-hysteretic contacts $\beta_c \ll 1$

$$\sin\varphi(\tau) + \frac{d\varphi(\tau)}{d\tau} = i_0 + i_{rf}(\tau) + i_N(\tau), \qquad \langle i_N(\tau)\rangle = 0, \tag{4.3}$$
$$\langle i_N(\tau)\; i_N(\tau')\rangle = 2\Gamma_0 \delta(\tau - \tau'),$$

the FP equation can be given by [Ris96]

$$\frac{\partial}{\partial\tau} W(\varphi, \tau) = L_{FP}\, W(\varphi, \tau) = -\frac{\partial}{\partial\varphi} S(\varphi, \tau), \tag{4.4}$$
$$L_{FP} = \left[\frac{\partial}{\partial\varphi}\left(\sin\varphi - i_0 - i_{rf}(\tau)\right) + \Gamma_0 \frac{\partial^2}{\partial\varphi^2}\right].$$

where $S(\varphi, \tau)$ is a probability currrent. According to Eq.4.3 the averaging of noise over all ensembles for every time vanishes. The normalization of the probability density and the expectation value for the observable $f(\varphi, \tau)$ at time τ is given by

$$\int_{-\infty}^{\infty} W(\varphi, \tau) d\varphi = 1, \quad \langle f(\varphi(\tau))\rangle \equiv \int_{-\infty}^{+\infty} f(\varphi(\tau)) W(\varphi, \tau) d\varphi. \tag{4.5}$$

The voltage response for a switched monochromatic rf-signal, solved by the stochastical and FP method, is shown in Fig.4.1. The voltage response of the FP solutions extract the essential interaction with rf-radiation and by suppressing the Josephson oscillation. To calculate the voltage response of a Josephson junction with arbitrary rf-signals within the FP formalism the ansatz of the probability density with time dependent coefficients $c_n(\tau)$ is presented in detail in

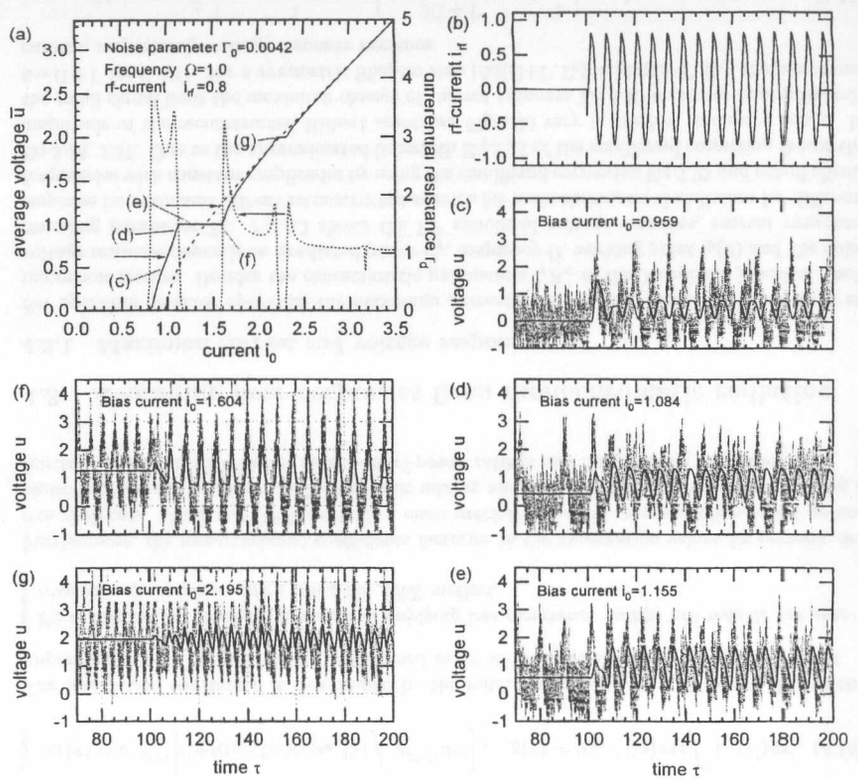

Figure 4.1: *FP simulated (a) V-I-characteristic with monochromatic radiation for noise parameter $\Gamma_0 = 0.0042$. (c)-(g) Corresponding voltage time traces $u(\tau)$ from Runge-Kutta (shadowed) and FP method (thick) for (b) a switched on rf-current.*

the appendix A.7.3. For pulsed-type radiation this ansatz is more efficient, than methods using the Fourier expansion in time, as derived for monochromatic rf-radiation in the appendix A.7.1, A.7.2.

$$W(\varphi, \tau) = \sum_n c_n(\tau)\, e^{in\varphi} \qquad \text{with} \qquad c_n(\tau) = c^*_{-n}(\tau) \tag{4.6}$$

Inserting Eq.4.6 into the FP equation 4.4 a tridiagonal recurrence relation with time dependent coeffients can be given

$$\left(i_0 + i_{rf}(\tau) - \Gamma_0 in - \frac{i}{n}\frac{d}{d\tau}\right) c_n(\tau) + \frac{i}{2}\left(c_{n-1}(\tau) - c_{n+1}(\tau)\right) = 0 \qquad \forall \qquad n \geq 1. \tag{4.7}$$

The normalization of probability density leads for $n = 0$ to $c_0(\tau) = 1/2\pi$. Using its periodicity with respect to the phase φ one can obtain Eq.A.63 the voltage expectation value $\bar{u}(\tau)$ at time τ or averaged expectation value $\bar{u}$ assuming dc-free rf-signals and vanishing noise contributions by averaging over the ensembles.

$$u(\tau) = i_0 + i_{rf}(\tau) + 2\pi \mathrm{Im}\,[c_1(\tau)], \tag{4.8}$$

$$\bar{u} = i_0 + 2\pi \lim_{T\to\infty} \frac{1}{2T}\int_{-T}^{T} \mathrm{Im}\,[c_1(\tau)]\,d\tau \quad \text{with} \quad \overline{i_{rf}(\tau)} = 0,\ \langle i_N(\tau)\rangle = 0 \tag{4.9}$$

Because of the dependencies we laxly call $\bar{u}(\tau)$ the FP 1st order recurrence coefficient, respectively averaged FP 1st order recurrence coefficient. Eq.4.7 is solved by a *2st order* differencing scheme in time leading to a tridiagonal system with constant coefficients. The hierarchy of equations 4.7 read explicitly

$$\begin{pmatrix} 1 & & & 0 \\ +\frac{i}{2} & (i_0 + i_{rf}(\tau) - \Gamma_0 i - i\frac{d}{d\tau}) & -\frac{i}{2} & \\ & +\frac{i}{2} & (i_0 + i_{rf}(\tau) - 2\Gamma_0 i - \frac{i}{2}\frac{d}{d\tau}) & -\frac{i}{2} \\ & & \ddots & \\ 0 & & +\frac{i}{2} \quad (i_0 + i_{rf}(\tau) - n\Gamma_0 i - \frac{i}{n}\frac{d}{d\tau}) & -\frac{i}{2} \end{pmatrix} \cdot \mathbf{c}(\tau) = 0, \quad \mathbf{c}(\tau) = \begin{pmatrix} c_0(\tau) \\ c_1(\tau) \\ c_2(\tau) \\ \vdots \\ c_n(\tau) \end{pmatrix}. \tag{4.10}$$

4.2.1 Difference recurrence relations (DRR)

The rf-signal spectrum is extracted from differences of irradiated and unperturbated I-V-characteristics, respectively their recurrence coefficients. As described by Eq.4.7 and shown in Fig.4.2 a low recurrence cutoff corrects the expectation values from ideal line far away from actual unperturbated I-V-characteristic, indicated by a dashed line. As shown in detail in the appendix A.8.7, a low recurrence cutoff changes the unperturbated I-V-characteristic and produces therefore different scaling and mixing of voltage responses concerning the frequency dependence. For periodic rf-signals without any dc-shift the effect changes only the scaling and justifies the adjustment of higher order effects in the low rf-power regime by the small signal theory, as outlined in section 4.3.3.

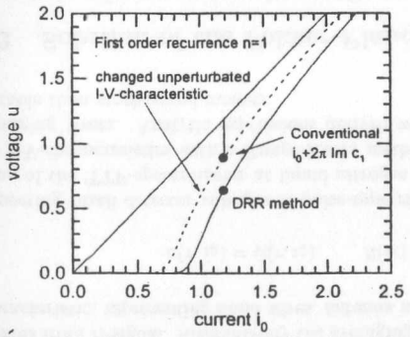

Figure 4.2: *For spectroscopic applications solving of difference recurrence relations gives reliable analytic expressions for a finite cutoff.*

A method is introduced, suitable for spectroscopic applications, by solving Difference Recurrence Relations (DRR) within the FP formalism despite using a low recurrence cutoff implying the knowledge of unperturbated coefficients $c_n(i_0, \Gamma_0)$. Instead of solving the time dependent recurrence relation the FP coefficient $c_n(\tau)$ itself using Eq.4.7, the DRR method handles the change of coefficients $\Delta c_n(\tau) = c_n(\tau) - c_n(0)$ from well known unperturbated coefficients. The essential finite recurrence cutoff at n negelects only coefficient differences $\Delta c_n(\tau) = c_n(\tau) - c_n(0) = 0$, instead of the cutoff coefficient $c_2(\tau) = 0$ itself.

For small voltage responses the coefficient changes remain as well small, as it is the case for the linear theory. As depicted in Fig.4.2, the voltage responses vanish without any rf-signal for the DRR method exactly to the unperturbated I-V-characteristic. Consequently, the difference of the perturbated and unperturbated recurrence relations are solved

$$\begin{matrix} \left(i_0 + i_{rf}(\tau) - \Gamma_0 i n - \frac{i}{n}\frac{d}{d\tau}\right) c_n(\tau) + \frac{i}{2}\left(c_{n-1}(\tau) - c_{n+1}(\tau)\right) = 0 \\ \left(i_0 + \quad -\Gamma_0 i n \quad\right) c_n(0) + \frac{i}{2}\left(c_{n-1}(0) - c_{n+1}(0)\right) = 0 \end{matrix} \tag{4.11}$$

resulting in the DRR equation

$$(i_0 - \Gamma_0 i n)\,\Delta c_n(\tau) + \left(i_{rf}(\tau) - \frac{i}{n}\frac{d}{d\tau}\right) c_n(\tau) + \frac{i}{2}\left(\Delta c_{n-1}(\tau) - \Delta c_{n+1}(\tau)\right) = 0. \tag{4.12}$$

The details for any recurrence order n are explained in the appendix A.8.3 for constant rf-currents. To simplify we truncate Eq.4.12 for $n=1$ neglecting $\Delta c_2(\tau) = c_2(\tau) - c_2(0) = 0$. Taking into account, that $\Delta c_0(\tau) = c_0(\tau) - c_0(0) = 0$ vanishes exactly, one obtains

$$\frac{d}{d\tau} c_1(\tau) + i\,(i_0 + i_{rf}(\tau) - \Gamma_0 i)\,c_1(\tau) = i(i_0 - \Gamma_0 i) c_1(i_0, \Gamma_0), \tag{4.13}$$

solved by the first order DRR equation

$$c_1(\tau) = e^{-g(\tau)}\left[C + i(i_0 - \Gamma_0 i) c_1(i_0, \Gamma_0) \int^{\tau} e^{g(\tau')} d\tau'\right], \quad g(\tau) = i(i_0 - \Gamma_0 i)\tau + i\int^{\tau} i_{rf}(\tau')d\tau'. \tag{4.14}$$

The integration constant C is determined by the initial working point $c_1(0) = c_1(i_0, \Gamma_0)$ of the unperturbated I-V-characteristic. As outlined in detail in appendix A.8.7, we conclude, that

Proposition 2: *Analytic expressions implying low recurrence cutoffs are reliable for spectroscopic applications, when using the DRR method.*

Furthermore, the unperturbated coefficients factorize in the expectation values for periodic dc-free rf-signals. Using the DRR method, a more precisely spectral reconstruction based on analytic expressions, considers multi-harmonic mixing and higher order Shapiro effects causing a junction operation with higher maximum rf-power ratings and finally faster measurements.

4.3 Averaging over responses from monochromatic radiation

4.3.1 Maximum current and voltage response

For optimum detector operation the maximum current response of a Josephson junction is an important feature. Besides the characteristic parameters $I_c R_n$ of the Josephson junction, their voltage response depends on irradiated power i_{rf}^2, frequency Ω, working point $i_0(\bar{u})$ and the noise rounding parameter Γ_0. Fig.4.3 shows the FP simulated voltage response, current response, response function and Hilbert reconstructed spectra for monochromatic rf-radiation for different frequencies with constant amplitudes by using the smallband correction Eq.3.29 and cutoff effects Eq.3.36, 3.37. Due to the approximated linewidth Eq.3.11 of the smallband correction factor the amplitude of the reconstructed Hilbert spectrum Fig.4.3d vary in the low frequency range. In the small signal limit the maximum change of current response Eq.3.10 occurs at approximately $\bar{u} = \Omega \pm \Gamma$ for $\Gamma \ll \Omega$. For a symmetric Shapiro step $|\Delta i(\Omega + \Gamma, \Gamma_0)| \approx |\Delta i(\Omega - \Gamma, \Gamma_0)|$ the maximum current, respectively voltage response becomes

$$\Delta i_{max} = -i_{rf}^2 \frac{1}{8}\frac{1}{(\Omega + \Gamma) i_0(\Omega, \Gamma_0)}\left[\frac{2\Omega + \Gamma}{(2\Omega + \Gamma)^2 + \Gamma^2} + \frac{1}{2\Gamma}\right] \quad \forall \quad i_{rf} \ll 1 \tag{4.15}$$

$$\Delta \bar{u}_{max} \approx -r_d(i_0, \Gamma)\Delta i_{max}, \quad \text{with} \quad \Gamma(\Omega, \Gamma_0) = \Gamma_0 r_d^2(\Omega, \Gamma_0)\left(1 + \frac{1}{2i_0^2(\Omega, \Gamma_0)}\right). \tag{4.16}$$

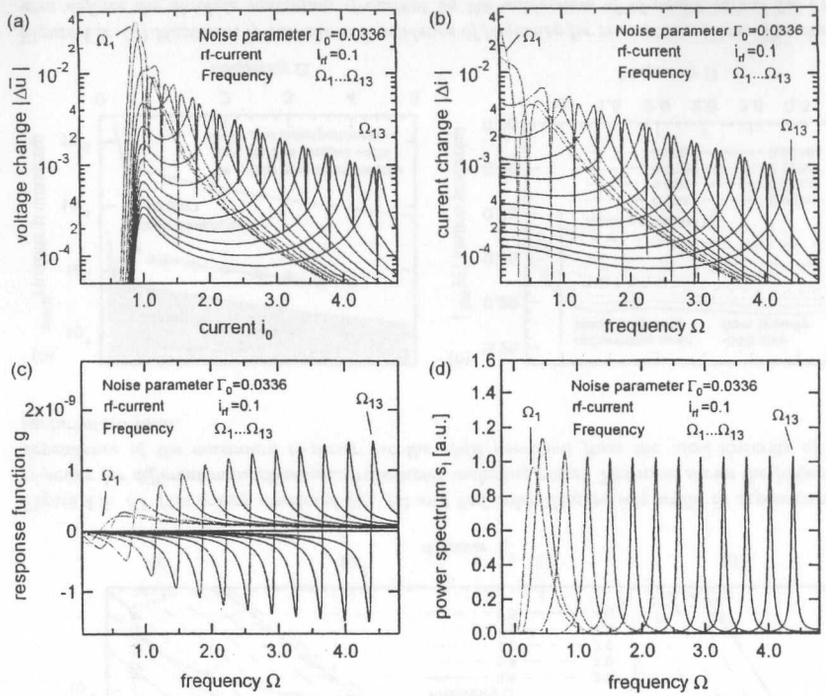

Figure 4.3: *FP (2nd order) simulated (a) voltage response, (b) current response, (c) response function and (d) Hilbert reconstructed spectra for different monochromatic frequencies* $\Omega_n = 0.352n - 0.252$ *with constant amplitude.*

For a smooth spectrum the current response Eq.4.15 is transferred into the measured voltage response Eq.4.16 by the unperturbated differential resistance $r_d(i_0, \Gamma_0)$. The simulated behavior Fig.4.4 is essentially in accordance with measurements of the frequency dependent current response for various noise parameters [Div93]. To find the optimum operation condition for spectroscopy at low-noise operation $\Gamma \to 0$ an analytic expression for maximum current change can be evaluated. With $r_d(i_0, \Gamma_0) \approx r_d(\Gamma_0 \to 0) = -i/\bar{u}$ and $|\bar{u} - \Omega| < \Omega$, the second term in Eq.4.15 dominates and the maximum current, respectively voltage change becomes at $\bar{u} = \Omega + \Gamma$ for $\Gamma \ll \Omega$, $i_0 = \sqrt{1+\Omega^2}$, $r_d = \sqrt{1+\Omega^2}/\Omega$ and monochromatic radiation

$$\Delta i_{max} = \pm \frac{i_{rf}^2}{8\Omega\sqrt{1+\Omega^2}} \frac{1}{2\Gamma} \qquad \forall \quad \Gamma \to 0, \Gamma \ll \Omega, i_{rf} \ll 1 \tag{4.17}$$

$$\Delta i_{max} = -i_{rf}^2 \frac{1}{8} \frac{\Omega}{\sqrt{1+\Omega^2}\,(3+2\Omega^2)} \frac{1}{\Gamma_0}, \quad \Delta \bar{u}_{max} = i_{rf}^2 \frac{1}{8} \frac{1}{(3+2\Omega^2)} \frac{1}{\Gamma_0}. \tag{4.18}$$

The maximum frequency dependent current change Eq.4.18 appears at frequency $\Omega_{opt} = 0.5(\sqrt{13}-1)^{0.5} \approx 0.81$, at somewhat lower frequency compared to the measured results [Div93]. According to Fig.4.4 at low frequencies $\Omega < \Omega_{opt}$ the current response decreases due to the increasing Josephson oscillation linewidth Γ. For higher frequencies $\Omega > \Omega_{opt}$ the

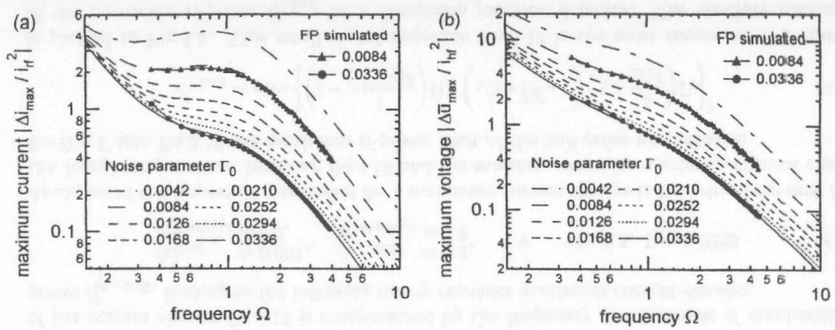

Figure 4.4: *Maximum current (a) and voltage (b) response according to Eq.4.15 for monochromatic rf-radiation* $i_{rf} = 0.1$ *and different noise parameters in the small signal limit.*

response falls inversely proportional to Ω^2.

Proposition 3: *Without any rf-signal compensation discussed in section 6.3, we conclude, that the characteristic frequency of the spectrometer should be nearly equal to the center frequency of expected rf-radiation* $\omega_{rf} \approx \omega_c$.

In the small signal limit and low-noise operation of the spectrometer the unnormalized maximum current and voltage response increase,

$$\Delta I_{max} = -I_{rf}^2 \frac{1}{8} \left(\frac{\hbar}{2e}\right) \frac{\omega_{rf}\omega_c^2}{\sqrt{\omega_c^2 + \omega_{rf}^2}\,(3\omega_c^2 + 2\omega_{rf}^2)} \frac{1}{k_B T} \tag{4.19}$$

$$\Delta \bar{U}_{max} = I_{rf}^2 \frac{1}{8} \left(\frac{\hbar}{2e}\right) \frac{\omega_c^2}{(3\omega_c^2 + 2\omega_{rf}^2)} \frac{R_n}{k_B T}, \tag{4.20}$$

and therefore the measuring time decreases for lower temperature T and higher normal-state resistance R_n of Josephson junction. Because of the frequency dependent acceptance function of the rf-coupling from spectromter, the current response characteristic deviates from Eq.4.18.

4.3.2 Outside the small signal approach

Further the maximum current response of Josephson junction outside the small signal approach is of interest. Especially for the TTF broadband application, a maximum current and voltage change outside the small signal limit is absolute necessary for fast measurements. As expected from small signal theory the current response is proportional to the incident rf-radiation power. This is only valid up to a critical rf-power. To specify this limit, numerical simulations are necessary. We define three different maximum rf-power limits for continuous radiation of the first order Shapiro width characteristic.

$i_{rf,2nd}^2$	- second order perturbation limit from Hilbert theory
$i_{rf,-3dB}^2$	- -3dB deviation from linearity of perturbation limit
$i_{rf,2nd/1st}^2$	- percentual ratio of second/first order Shapiro step width
$i_{rf,absolute}^2$	- limit of uniqueness of rf-power from 1st order Shapiro step width

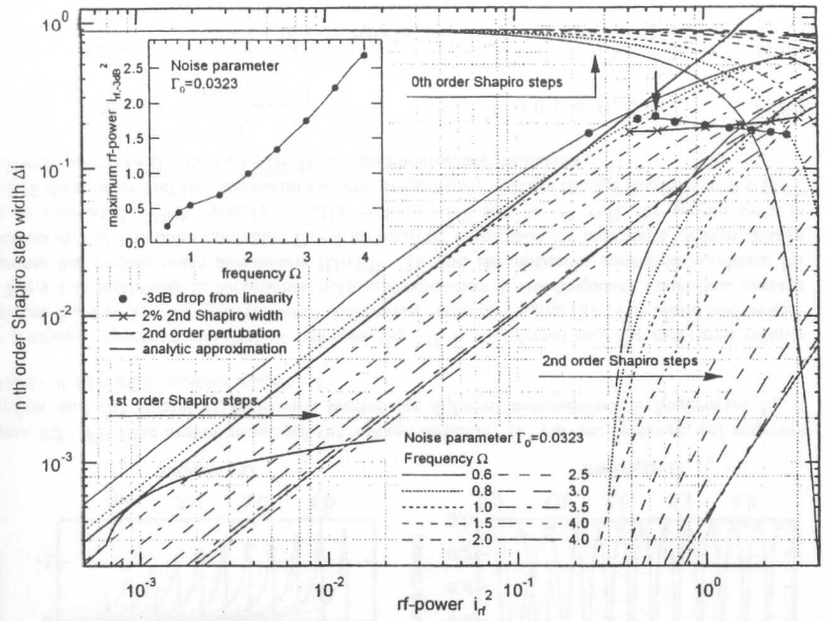

Figure 4.5: *FP (1st order) simulated 0th, 1st and 2nd order Shapiro step width in dependence of rf-power for different monochromatic frequencies including noise. The inset shows the frequency dependence of the maximum rf-power for the -3dB deviation from the ideal linearity of the perturbation limit.*

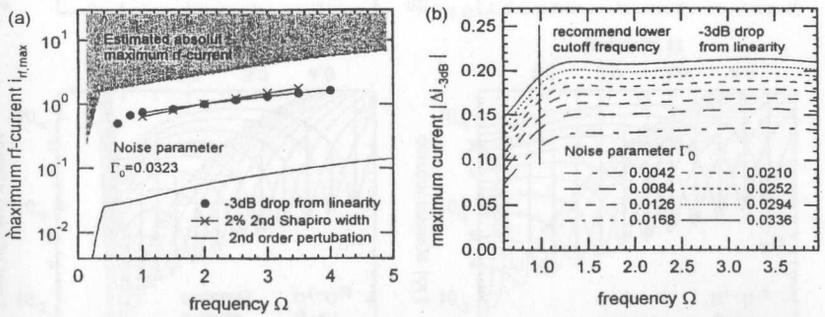

Figure 4.6: *(a) Maximum rf-current in dependence of frequency for several szenarios. The shaded area defines the absolute maximum rf-current by the uniqueness of rf-power versus 1st order Shapiro step width characteristic. (b) Maximum voltage response according to the maximum rf-power limits for monochromatic rf-radiation and different noise parameters.*

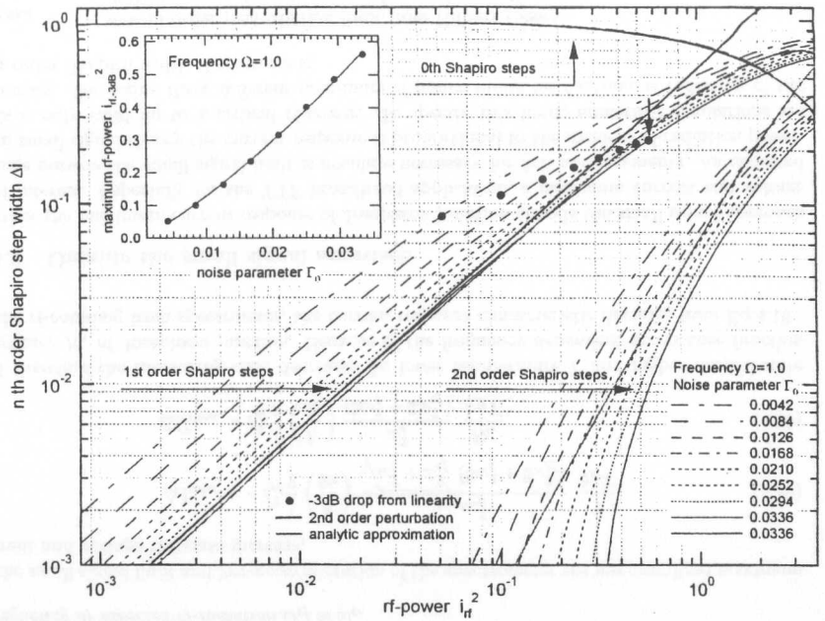

Figure 4.7: *FP (1st order) simulated 0th, 1st and 2nd order Shapiro step width in dependence of rf-power for different noise parameters. The inset shows the frequency dependence of the maximum rf-power for the -3dB deviation from linearity of perturbation limit.*

According to Fig.4.5 several definitions of the maximum rf-power limit lead to nearly frequency independent first order Shapiro step widths. This is evident, because the frequency characteristic of the current change Eq.4.18 is compensated by the frequency characteristic of maximum rf-power $i_{rf,-3dB}^2$, leading to the following nearly constant maximum current changes.

$$\begin{array}{ll} \Delta i_{2nd} \approx 0.001, & \Delta i_{-3dB} \approx 0.2, \\ \Delta i_{2nd/1st} \approx 0.2, & \Delta i_{absolute} \approx 0.8 \end{array} \quad \forall \quad \Omega > 0.5,\ \Gamma_0 = 0.0323 \tag{4.21}$$

As expected the important parameter for a maximum current change is the critical current I_c of the Josephson junction. Inserting Eq.4.18 and the working points for maximum current change $\tilde{u} = \Omega \pm \Gamma$ into Eq.3.12 the maximum rf-power limit of the 2nd order perturbation

$$i_{rf,2nd}^2 = min\left[\left(1 - \frac{1}{\sqrt{1+\Omega^2}}\right)\Omega,\ \left(\sqrt{1+\Omega^2} - 1\right)\left(1 + \frac{3}{2\Omega^2}\right)\Gamma_0\right]^2 \tag{4.22}$$

is plotted in Fig.4.5. This small signal approach Eq.3.12 is the most conservative definition of the maximum rf-power $i_{rf,2nd}^2$ for a Josephson junction detector. The absolute maximum rf-power limit $i_{rf,absolute}^2$ is defined by the uniqueness of rf-power versus 1st order Shapiro step width characteristic. Fig.4.6a summarizes the frequency dependent maximum rf-power limits. According to the inset of Fig.4.5 we find the maximum rf-power $i_{rf,-3dB}^2(\Omega, \Gamma_0{=}0.0323)$ by a smoothed spline in the frequency range $\Omega \in [0.6, 4]$. Inserting this and the temperature

dependence of the maximum rf-power limit $i^2_{rf,-3dB}(\Omega{=}1,\Gamma_0)$ from Fig.4.7 into the rf-current response Eq.4.15, the maximum response of the junction is found, as depicted in Fig.4.6b. Consequently an operation of the detector with a lower cutoff frequency of approximately $\Omega{\approx}1$ is recommended. The expected maximum current change is nearly frequency independent $\Delta i_{-3dB}{\approx}0.2$ for liquid nitrogen cooling of the detector.

Proposition 4: *With an operation at maximum spectral rf-power, we conclude, that the lowest frequency of rf-radiation should be higher than the characteristic frequency of the spectrometer* $\omega_{rf} \geq \omega_c$.

According to the results of the temperature dependent maximum current limit $\Delta i_{-3dB}(\Omega,\Gamma_0)$ of Fig.4.6b, we find the unnormalized maximum current of the Josephson detector.

$$\Delta I_{-3dB} = -I_c\ \Delta i_{-3dB}(\Omega,\Gamma_0), \quad \Delta U_{-3dB} \approx -R_d(\Gamma_0,\omega_{rf},\omega_c)\Delta I_{-3dB} \quad \forall \quad \omega_{rf} \geq \omega_c \tag{4.23}$$

$$\Delta U_{-3dB} = \left(\frac{\hbar}{2e}\right)\omega_c \frac{\sqrt{\omega_{rf}^2+\omega_c^2}}{\omega_{rf}}\ \Delta i_{-3dB}(\Omega,\Gamma_0), \qquad \forall \quad \Gamma_0 \ll 1 \tag{4.24}$$

4.3.3 Low-scale adjustment to Hilbert theory

An analytic approximation outside the small signal theory succeeds by introducing the DRR method, preferable for spectroscopy, within the FP formalism. To simplify we make use of the voltage response from section 4.5 derived within a more generalized description. In detail a single monochromatic frequency is given by

$$\Delta\bar{u} = 2\pi\mathrm{Im}\left[c_1(i_0,\Gamma_0)\left((i_0-\Gamma_0 i)\sum_{n=-\infty}^{\infty}\frac{J_n^2\left(\frac{i_{rf}}{\Omega}\right)}{i_0+n\Omega-\Gamma_0 i}-1\right)\right], \tag{4.25}$$

where n indexed the nth order Shapiro step contribution. The maximum Shapiro step occurs at approximately $\bar{u}^{\pm} = \Omega \pm \Gamma$. The essential 1st order Shapiro step width for small noise parameter dominates for terms with $n{\in}\{-1,0\}$ away from critical current $i_0^{\pm}{\approx}\Omega\pm\Gamma$ for $i_0 \gg 1$, $J_n(x) = (-1)^n J_{-n}(x)$, and

$$\Delta\bar{u}^{\pm} \approx 2\pi\mathrm{Im}\left[c_1(\Omega\pm\Gamma,\Gamma_0)\left((\Omega\pm\Gamma-\Gamma_0 i)\frac{J_1^2\left(\frac{i_{rf}}{\Omega}\right)}{\pm\Gamma-\Gamma_0 i}+J_0^2\left(\frac{i_{rf}}{\Omega}\right)-1\right)\right] \tag{4.26}$$

is given for $\Delta\bar{u}_{max} = \Delta\bar{u}^{+} - \Delta\bar{u}^{-}$ and a smooth spectrum using $\Delta\bar{u}_{max}{\approx}{-}r_d(i_0,\Gamma_0)\Delta i_{max}$ by

$$\Delta i_{max} \approx J_1^2\left(\frac{i_{rf}}{\Omega}\right)\eta_1(\Omega,\Gamma_0) \quad \text{with} \quad \eta_1(\Omega,\Gamma) = \frac{2\pi\mathrm{Im}[c_1(\Omega,\Gamma_0)]}{r_d(\Omega,\Gamma_0)}\,\Omega\,\frac{2\Gamma}{\Gamma^2+\Gamma_0^2}, \tag{4.27}$$

$$\Delta i_{2,max} \approx J_2^2\left(\frac{i_{rf}}{\Omega}\right)\eta_2(\Omega,\Gamma) \quad \text{with} \quad \eta_2 = \eta_1(2\Omega,\Gamma). \tag{4.28}$$

Analyzing dominating terms of Eq.4.26 at $n{\in}\{-2,0\}$ the η_2 parameter derived for a 2nd order current response $\Delta i_{2,max}$ results to $\eta_2 = \eta_1(2\Omega,\Gamma)$. Because the parameter η_1,η_2 depends only on properties of the unperturbate I-V-characteristic and not on rf-power, η_1 separates and can be adjusted to the small signal scaling. Using $J_1^2(x) = (x/2)^2$ for $x \ll 1$ and compare Eq.4.27 with Eq.4.15 we redefine η_1, leading to the maximum onesided 1st, respectively 2nd order current response beyond the small signal limit.

$$\Delta i_{max} = J_1^2\left(\frac{i_{rf}}{\Omega}\right)\tilde{\eta}_1(\Omega,\Gamma) \quad \text{with} \quad \eta_1 \to \tilde{\eta}_1 = \frac{1}{2}\frac{\Omega}{i_0(\Omega,\Gamma)}\frac{1}{\Gamma}, \tag{4.29}$$

$$\Delta i_{2,max} = J_2^2\left(\frac{i_{rf}}{\Omega}\right)\tilde{\eta}_1(2\Omega,\Gamma) \qquad \forall \quad \Gamma \to 0, \Gamma \ll \Omega$$

This small signal adjustment compensates the lack of information from finite recurrence cutoff needed only for the construction of unperturbated V-I-characteristic and not the essential rf-power dependence. Because the induced rf-current is unknown, the 2nd order current response is given by the current response ratio. The ratio is given with $J_2^2(x) = (x/2)^4$ for $x \ll 1$ in the small signal limit by

$$\Delta i_{2,max} = \Delta i_{max}^2\,\frac{\tilde{\eta}_1(2\Omega,\Gamma)}{\tilde{\eta}_1^2(\Omega,\Gamma)} = \Delta i_{max}^2\ 4\Gamma\frac{i_0^2(\Omega,\Gamma)}{\Omega i_0(2\Omega,\Gamma)} \qquad \forall \quad \Gamma \to 0, \Gamma \ll \Omega, i_{rf} \ll 1. \tag{4.30}$$

Using Eq.4.30, higher order spectral contributions can be considered in the rf-signal reconstruction analysis resulting in a higher voltage response and faster measurements. Using a spectrum with constant spectral density, which is not scaled up to the maximum rf-power limits by an rf-signal compensation, the frequency dependent response falls from maximum current change Δi_{-3dB} inversely proportional to Ω^2. The current, respectively voltage change, increases with decreasing operating temperature T due to the increasing temperature dependent critical current $I_c(T)$ and characteristic frequency ω_c. However, to fulfill Eq.4.23 for a given rf-spectrum the characteristic frequency, respectively critical current and therefore the response, is limited.

4.4 Averaging over responses from pulsed coherent radiation

4.4.1 Maximum current and voltage response

In this section we will investigate the maximum possible current response of the Josephson junction for a successful reconstruction of pulse-type rf-signals. Due to the frequency selectivity of the Josephson detector it acts as a smallband filter. Obviously, a constant spectral power density of rf-radiation at fixed frequency should produce a constant response of detector, no matter weather low amplitude and high repetition rate or high amplitude and low repetition rate rf-pulses are applied. For the Josephson detector this should be valid, if the collected spectral power $i^2_{rf,s_i(\Omega)}(\Omega,\Gamma_0)$ from the rf-signal does not exceed the previously defined monchromatic maximum ratings $i^2_{rf,-3dB}(\Omega,\Gamma_0)$ within the detector spectral resolution. This is because the Josephson junction can not distinguish spectral lines within its spectral resolution. A further increase of the incident spectral power beyond the linearity leads to a decrease of the current response. A sufficient condition for the maximum ratings for continuous spectra should be

$$i^2_{rf,-3dB}(\Omega,\Gamma_0) \geq i^2_{rf,s_i(\Omega)}(\Omega,\Gamma_0) \qquad \text{with} \qquad i^2_{rf,s_i(\Omega)}(\Omega,\Gamma_0) = \frac{1}{\pi}\int_{\Omega-\Gamma(\Omega)/2}^{\Omega+\Gamma(\Omega)/2} s_i(\Omega')d\Omega'. \tag{4.31}$$

In this subsection we investigate, if the assumption Eq.4.31 for the maximum ratings is applicable to Josephson junctions. A series of rf-pulses $i_{rf}(\tau)$ with spacing τ_R is given by the convolution of a single pulse $i_{rf,p}(\tau)$ and a series of delta pulses with spacing τ_R. With the repetition rate $\Omega_R = 2\pi/\tau_R$ the Fourier transform $\mathcal{F}$ of the rf-signal is given by

$$i_{rf}(\tau) = \begin{cases} \sum_n \delta(\tau-n\tau_R) * i_{rf,p}(\tau) & \forall\ |\tau| \leq T \\ 0 & \forall\ |\tau| > T \end{cases} \quad \rightleftharpoons \quad \mathcal{F}[i_{rf}(\tau)] = \Omega_R\sum_n \delta(\Omega-n\Omega_R)\mathcal{F}[i_{rf,p}(\tau)]. \tag{4.32}$$

The definition of the spectral density and therefore the Hilbert transform spectroscopy, is limited

to time unlimited signals. For an unlimited rf-pulse series $s_i(\Omega)$ the current spectral density with a single pulse power spectrum $S_p(\Omega)$

$$S_p(\Omega) = |\mathcal{F}[i_{rf,p}(\tau)]|^2\,, \qquad s_i(\Omega) = \lim_{T\to\infty} \frac{1}{2T}\ |\mathcal{F}[i_{rf}(\tau)]|^2 \tag{4.33}$$

results, as derived in the appendix A.4 to Eq.A.55. Inserting this with $|K_{rf}(\Omega)|=1$ into Eq.3.22 the current response results to

$$\Delta i(\bar{u}) = \frac{\pi}{8 i_0 \bar{u}}\ \mathcal{K}[s_R(\Omega)] \quad \text{with} \quad \mathcal{K}[s_R(\Omega)] = -\frac{1}{\pi}\ \frac{1}{2\pi}\ \Omega_R^2 \sum_n \frac{n\Omega_R - \bar{u}}{(n\Omega_R - \bar{u})^2 + \Gamma^2}\ S_p(n\Omega_R). \tag{4.34}$$

Eq.4.34 reduces for $n=\pm 1$ and symmetric spectrum $S_p(\Omega)=S_p(-\Omega)$ to the response of monchromatic radiation Eq.3.10 with amplitude Ω_R. The pulse spectrum $S_p(\Omega)$ must be bandlimited, otherwise the response is divergent. Inserting the current spectral density of a rectangular pulse shape, characterized by pulse width τ_p and peak current i_p,

$$i_{rf,p}(\tau) = \begin{cases} i_p\ \forall\ |\tau| \le \tau_p/2 \\ 0\ \forall\ \text{else} \end{cases} \quad \rightleftharpoons \quad S_p(\Omega) = i_p^2 \tau_p^2 \left| \frac{\sin(\Omega\tau_p/2)}{\Omega\tau_p/2} \right|^2 \tag{4.35}$$

into Eq.4.34, current response for a series of rectangular rf-pulses is given by

$$\Delta i(\bar{u}) = \frac{2\pi}{8 i_0(\bar{u},\Gamma_0)\bar{u}}\ i_p^2 \left(\frac{\tau_p}{\tau_R}\right)^2 \sum_n \frac{n\Omega_R - \bar{u}}{(n\Omega_R - \bar{u})^2 + \Gamma(\bar{u},\Gamma_0)^2} \left| \frac{\sin(n\Omega_R\tau_p/2)}{n\Omega_R\tau_p/2} \right|^2. \tag{4.36}$$

Proposition 5: *As depicted in Fig.4.8 the stationary current response of a Josephson junction driven by an rf-pulse series in the limit of vanishing response structure $\tau_R \gg 2\pi/\Gamma_0$ fall inversely proportional with the pulse pause τ_R. In the limit of non-overlapping responses $\tau_R \ll 2\pi/\Gamma_0$ it falls inversely proportional with τ_R^2.*

As shown in Fig.4.8c the current response fall inversely proportional with Ω^2 for the delta pulse limit $\tau_p \to 0$. The rf-power dependence of the current response for a gaussian rf-pulse series is shown in Fig.4.9. To prevent dc-shifts and a saturation of the junctions response a Butterworth low-pass filter of 10th order with cutoff frequency Ω_F is used for filtering the rf-radiation. Due to the delaying of rf-pulse from filter cutoff, a very high peak rf-current causes the I-V-characteristic to be completely suppressed for high pulse pauses, as shown in Fig.4.8b. Out of the maximum rf-power rating the reconstructed spectra show higher order gaussian spectra at the multiple filter cutoff frequencies, which are referred as ghost spectra. The ghost spectra are asymmetric and described in detail in section 4.5. Fig.4.8b shows the collected power according to Eq.A.73 including overlapping effects in dependence of the pulse pause τ_R for an rf-pulse series at working point near the cutoff frequency. Numerical simulations of the junctions spectral response of a filtered series of rectangular rf-pulses for various repetition rates are shown in Fig.4.10. The information of the essential pulse shape from voltage response Fig.4.10a at higher frequencies fall at least inversely proportional with Ω^2. Acccording to the reconstructed Hilbert spectra Fig.4.10d the responses fall inversely proportional with the pulse pause τ_R, as predicted by Eq.4.36. As derived in the appendix A.6, the maximum peak current ratings for the series of rf-pulses Eq.4.35 with sufficient dense spectrum $\Omega_R \ll \Gamma(\Omega)$ is given by

$$i_p^2(\Omega,\Gamma_0,\tau_p,\tau_R) \le \frac{1}{4\pi}\ \frac{\tau_R}{\tau_p^2}\ \frac{i_{rf,-3dB}^2(\Omega,\Gamma_0)}{\Gamma(\Omega,\Gamma_0)}. \tag{4.37}$$

Experimentally the peak current i_p^2 is adjusted to the maximum average current response of a Josephson junction for a fixed pulse repetition rate. Inserting the maximum peak current

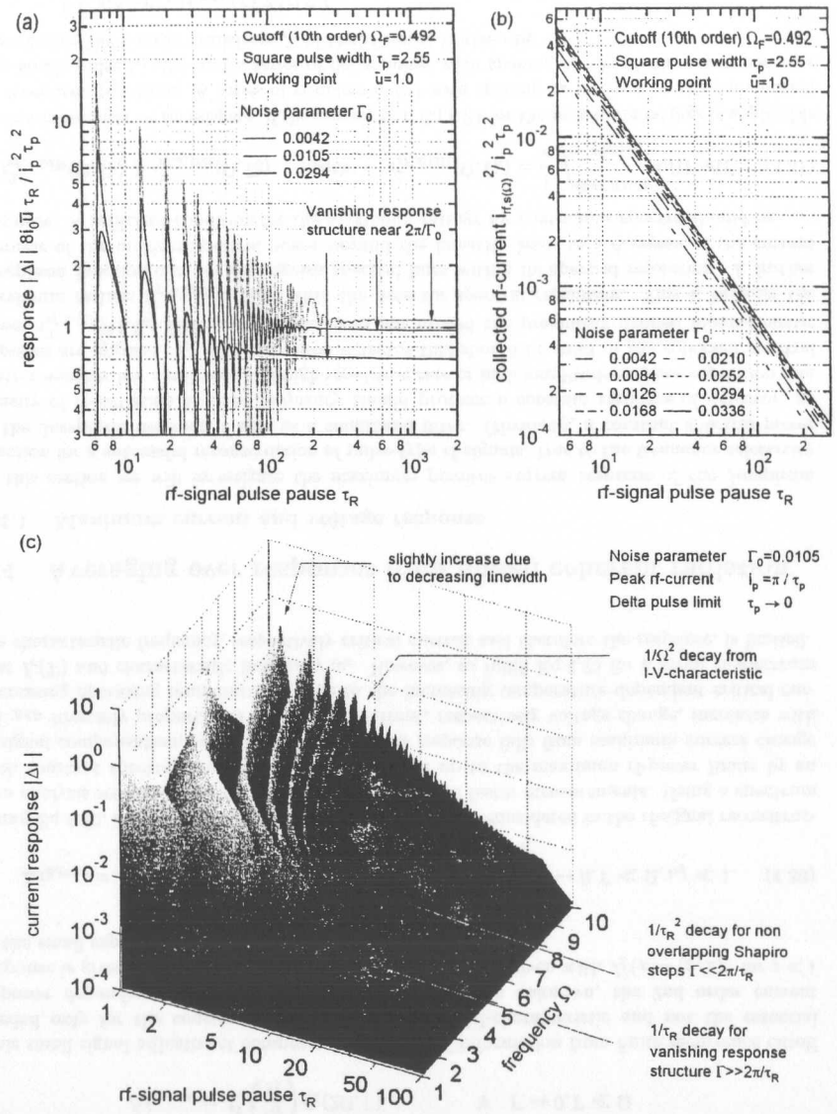

Figure 4.8: *(a) Response function for a series of rf-pulses. (b) Collected power according to Eq.A.73 including overlapping effects in dependence of pulse pause τ_R for a sharp filtered series of rf-pulses at working point near the cutoff frequency. (c) Current response in the delta pulse limit $\tau_p \to 0$.*

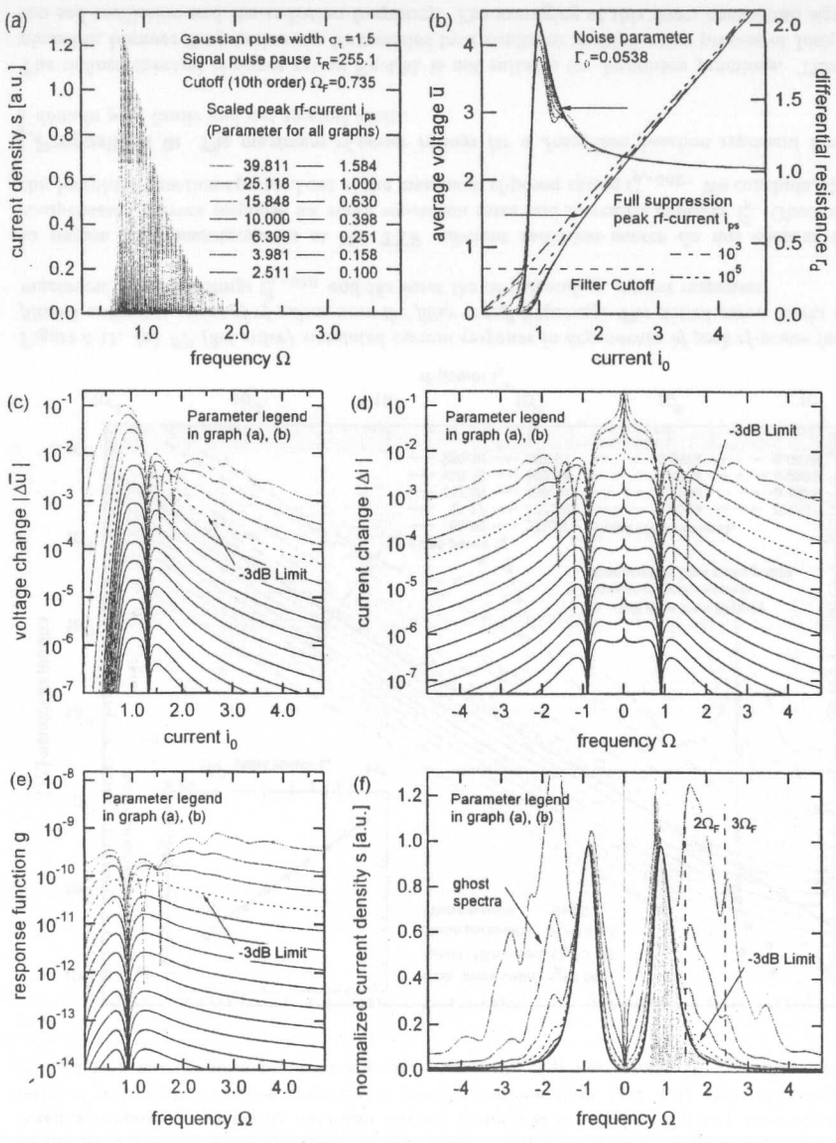

Figure 4.9: *FP (2nd order) simulated power dependence for sharp filtered (a) gaussian rf-pulses (b) I-V-characteristic including the junctions differetial resistance, (c) voltage response, (d) current response, (e) response function and normalized (f) reconstructed Hilbert spectra. The gray marked curve represents the irradiated spectrum.*

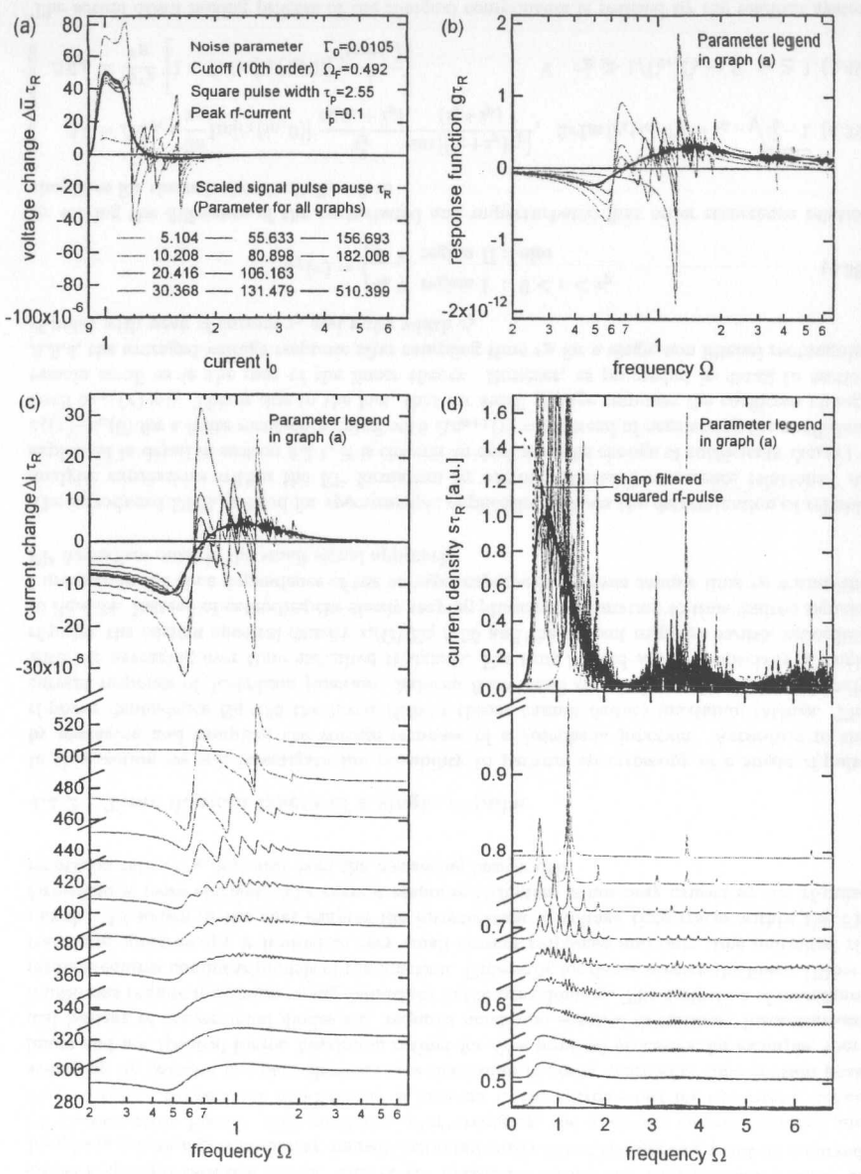

Figure 4.10: *FP (1st order) simulated pulse pause dependence for a sharp filtered squared rf-pulse series (a) voltage response, (b) response function, (c) current response and (d) reconstructed spectra scaled by the pulse pause τ_R.*

Eq.4.37 into the current response Eq.4.36 a pulse pause τ_R independent current response results for a discrete dense spectrum [1]. This result is expected from a linear theory, but the Josephson junction is a highly nonlinear device. Numerical simulations Fig.4.11 for a filtered series of rectangular rf-pulses operating in the structureless limit $\tau_R \gg 1/\Gamma_0$ show in contrary to Eq.4.37 a nearby pulse pause independent maximum rf-power ratings $i^2_{p,-3dB}$. According

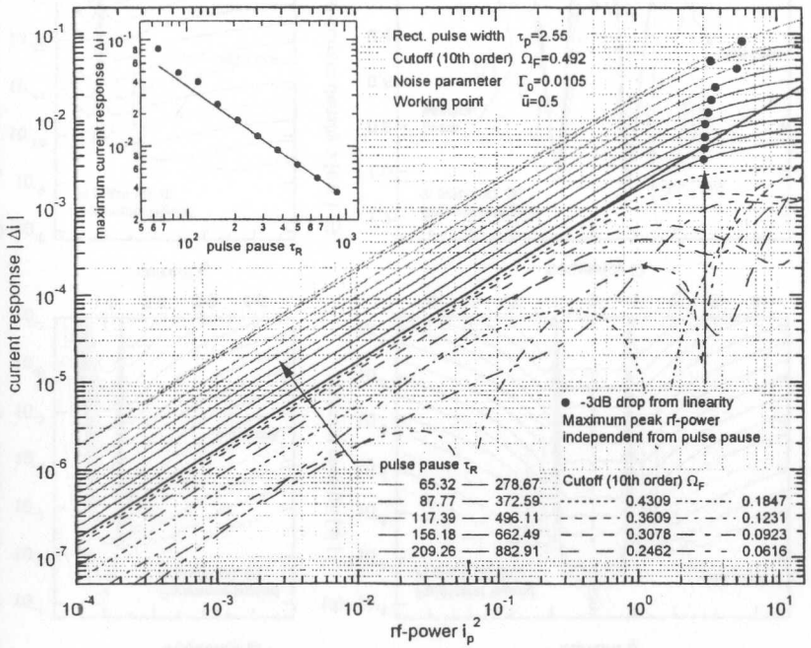

Figure 4.11: *(a) FP (2st order) simulated current response in dependence of peak rf-power for a filtered unlimited series of rf-pulses near the filter cutoff frequency. The dotted curve marks the maximum rf-power ratings $i^2_{p,-3dB}$ and the inset the corresponding current responses.*

to section 5.5.4 measurements at the TTF coherent radiation source do not confirm the compensated current response for small repetition rates and increased rf-power i_p^2. Obviously the Josephson junction operated out of the maximum rf-power rating $i^2_{p,-3dB}$. We conclude, that

Proposition 6: *The maximum rf-power ratings for a Josephson junction represent time domain peak limits and not spectral limits.*

The defined spectral rf-power rating Eq.4.31 is not suitable for Josephson junctions. This is plausible, because the junction can be modeled by a nonlinear multiplication process of Josephson self oscillation and the radiation frequency. The averaging of this down convoluted signal

[1] A more details analysis derived in section A, by taking into account, that neighbouring spectral lines convoluted by the Josephson junction noise produces additional spectral power, results also in a pulse pause independent maximum current response.

makes a spectral sensitive device. Out of the maximum ratings the multiplication process of Josephson junction gets nonlinear, namely instantaneously out of the working point on a curved I-V-characteristic Fig.3.3. This produces, after averaging, the nonlinear current response and Shapiro steps. Because the non-linearity is inherent in the extreme fast multiplication, before averaging by parasite low-pass elements, the maximum rf-power represents time domain peak limits and not spectral limits. Maximum ratings for slow physical processes, for example, thermal heating of conventional diodes etc. requires maximum spectral definitions. Instantaneous limitations require maximum rating definitions in the time domain. The derivation of maximum ratings requires nonlinear models of the junction. Especially for dense spectra the linear Hilbert transform spectroscopy is limited to very small current responses and only time unlimited rf-signals. As shown in the next chapter the investigation of voltage time traces within the FP formalism is more efficient. The current response reduction is not only caused by the rf-pulse repetition rate $1/\tau_R$, but also from the measuring bandwidth.

4.4.2 Time domain traces of a single rf-pulse

In this section we will investigate the possibility to perform spectroscopy of a single rf-pulse by averaging and sampling the voltage response of a Josephson junction. According to the rf-power dependence Eq.4.36 the linear Hilbert theory cannot deduce maximum ratings. The current response of Josephson junction, deduced from small signal theory Eq.A.19 deals only with the averaging over time unlimited rf-signals. For time limited signals, especially a single rf-pulse, the current spectral density $s_i(\Omega)$ Eq.A.55 and the current response vanish, according to Eq.4.34. Instead of extending the slowly varying phase approximation to time limited signals, I investigate the time dependence of the voltage response for a given sample time τ_B within the FP formalism outside the small signal approach.

The introduced DRR method for spectroscopic applications allows the determination of reliable analytic expressions within the FP formalism by solving difference recurrence relations. As explained in detail in section 4.2.1, it is cleverer to deal with the change of coefficients $\Delta c_n(\tau) = c_n(\tau) - c_n(0)$ for a finite recurrence cutoff with $\Delta c_{n+1}(\tau) = 0$ instead of negelecting the coefficient itself $c_{n+1}(\tau) = 0$. This is due to the fact, that for small voltage response the coefficent change remain small as in the case of the linear theory. However, as proceeded in detail in section A.8.4, the averaged voltage response after sampling time τ_B for a single non filtered rectangular rf-pulse with peak rf-current i_p and pulse width τ_p

$$i_{rf}(\tau) = \begin{cases} i_p \;\forall \;\text{region I} : \; 0 < \tau < \tau_p \\ 0 \;\forall \;\text{region II} : \; \text{else} \end{cases} \tag{4.38}$$

by solving the difference of the perturbated and unperturbated first order recurrence relation simplifies for the noisefree limit $\Gamma_0 \to 0$ to

$$\Delta\bar{u} = \Delta\bar{u}_{dc} + \frac{2\pi}{\tau_B}\mathrm{Im}[c_1(i_0,0)]\,\frac{i_p^2}{i_0(i_0+i_p)}\,\frac{\sin[(i_0+i_p)\tau_p]}{(i_0+i_p)}, \quad 2\pi\mathrm{Im}[c_1(i_0,0)] = i_0 - \sqrt{i_0^2-1} \tag{4.39}$$

$$\Delta\bar{u}_{dc} = \frac{i_p\tau_p}{\tau_B}\left[1 + 2\pi\mathrm{Im}[c_1(i_0,0)]\,\frac{1}{(i_0+i_p)}\right] \qquad \forall \;\; \tau_B \gg 1/\Gamma_0,\; \Gamma_0 \to 0,\; i_0 \geq 1. \tag{4.40}$$

The actual down mixing process of the rf-signal components is realized by the readout system transfer function, which has typically low-pass filter characteristic consisting of bond-wires, strip-lines and rf-amplifiers. To simplify, they are modelled by a pure averaging of the voltage response up to the ideal measuring bandwidth $1/\tau_B$, respectively sampling time τ_B. The term

$i_{dc} = i_p \tau_p / \tau_B$ identifies as a pure averaged dc-shift of working point from rf-pulse duration. In accordance with the Hilbert transform theory, the response Eq.4.40 fall inversely proportional with the averaging time τ_B in the limit $\tau_B \gg 1/\Gamma_0$.

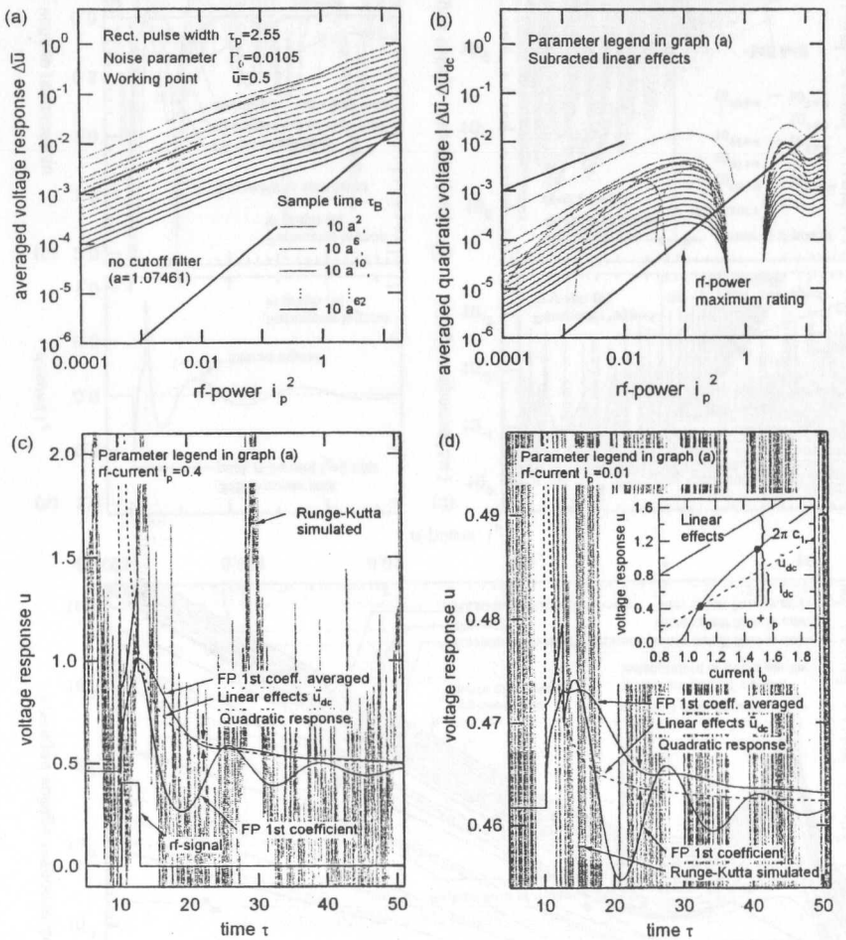

Figure 4.12: *(a) FP (1st order) simulated voltage response in dependence of peak rf-power for an unfiltered single rf-pulse. (b) Response without linear effects. The thick line mark the linear, respectively quadratic rf-power dependence. (c), (d) FP simulated time dependent voltage response for different rf-power.*

Fig.4.12a shows the voltage response Eq.4.39 in dependence of peak rf-power for an unfiltered single rf-pulse. Because there is no rf-filter, linear effects from rf-pulse dc-components i_{dc}

dominates the quadratic detector reponse, which makes spectroscopy impossible. The existance of the quadratic response is shown in Fig.4.12b for subtracted linear effects. Fig.4.12c,d show FP simulated time dependent voltage responses for different rf-currents. The linear effects results from the rf-pulse working point change $\Delta\bar{u}_{dc} = \bar{u}(i_0+i_p, \Gamma_0) - \bar{u}(i_0, \Gamma_0)$ from the junctions I-V-characteristic. The linear voltage effects $\Delta\bar{u}_{dc}$ identifies as the averaged first order dc-shift of rf-pulse. According to Fig.3.5 the linearity between small rf-currents and first order Shapiro width in the noisefree case $\Gamma_0 = 0$ is expressed by the last term in Eq.4.39. The more spectroscopic aspect of the response Eq.4.36 is expressed for increasing noise parameter Γ_0 and the identity $2\sin^2(x) = 1 - \cos(2x)$ by the cos term in Eq.A.144 representing the rf-signal spectral density. Unfortunately, although the noise parameter is increased linear effects from the unfiltered rf-signal, namely its dc-components dominate the quadratic response, as depicted in Fig.4.12a for every sample time. According to Eq.4.39,4.40, this is due to the fact, that both, linear effects $\Delta\bar{u}_{dc}$ and the response fall with the same time dependence, namely inversely proportional to the sample time τ_B. We conclude, that

Proposition 7: *It is not possible to measure a spectrum of a single unfiltered rf-pulse by Hilbert transform spectroscopy without any regulation or detection of the induced averaged voltage response caused from linear effects.*

Detection and compensation of linear effects must be done from other devices and cannot be done by the junction itself, because linear and quadratic voltages both appear only with rf-radiation simultaneously and cannot be separated after the junctions multiplication process. Linear effects can be avoided by suppressing the time dependent rf-pulse dc-components $i_{dc}(\tau_B)$ using a sufficient high-pass filtering in the rf-system.

Fig.4.13a shows the rf-power dependent voltage response by using a high-pass filtering. The maximum rf-power ratings are independent from sample time τ_B in the limit of vanishing response structure in accordance with the results for a series of rf-pulses in Fig.4.11. The FP simulations are carried out by using a butterworth high-pass filter with a sharp filter characteristic and low cutoff frequency Ω_F to prevent a dc-shift of working point, namely $i_{dc}(\tau_B)$. For an ideal sharp filter characteristic in the delta pulse limit the dc-shift from rf-filter is given by

$$i_{dc,HP}(\tau_B) = \frac{1}{\tau_B}\int_0^{\tau_B} i_{rf}(\tau)d\tau \quad \overset{\text{ideal cutoff}}{\longrightarrow} \quad i_{dc,HP}(\tau_B) = i_p\left(1-\frac{2}{\pi}\right)\int_0^{\Omega_F\tau_B}\frac{\sin(\tau')}{\tau'}d\tau'. \qquad (4.41)$$

According to Fig.4.13a, the transition between the linear and quadratic response is clearly seen in the FP simulations for a sampled single rf-pulse. For small sample times, before dc-components from the rf-signal are completely filtered out at sample times τ_B with $i_{dc,HP}(\tau_B) \gg |\Delta\bar{u} - \Delta\bar{u}_{dc}|$, the rf-pulse directly shifts the working point of the amount $i_{dc,HP}$, resulting in a large voltage response. The oscillating filter response results in a time dependent dc-shift of working point, which dominates the quadratic junction response making spectrosopy impossible. Near the maximum rf-power ratings with sufficient long sampling times τ_B with $i_{dc,HP}(\tau_B) \ll |\Delta\bar{u} - \Delta\bar{u}_{dc}|$, where dc-components from rf-pulse are completely filtered out after the prohibit time of the rf-filter is exceeded, respectively effective filtering, spectroscopy is possible. For having an increased voltage response, the single rf-pulse has to be repeated by repetitive delay structures to refresh the voltage response.

Proposition 8: *To perform spectroscopy of a single filtered rf-pulse the sample time τ_B must occur at sufficient small rf-filter oscillations and linear effects compared to the quadratic detector response. For refreshing the voltage response a series of rf-pulses and an efficient high-pass rf-filtering to supress linear effects is of advantage.*

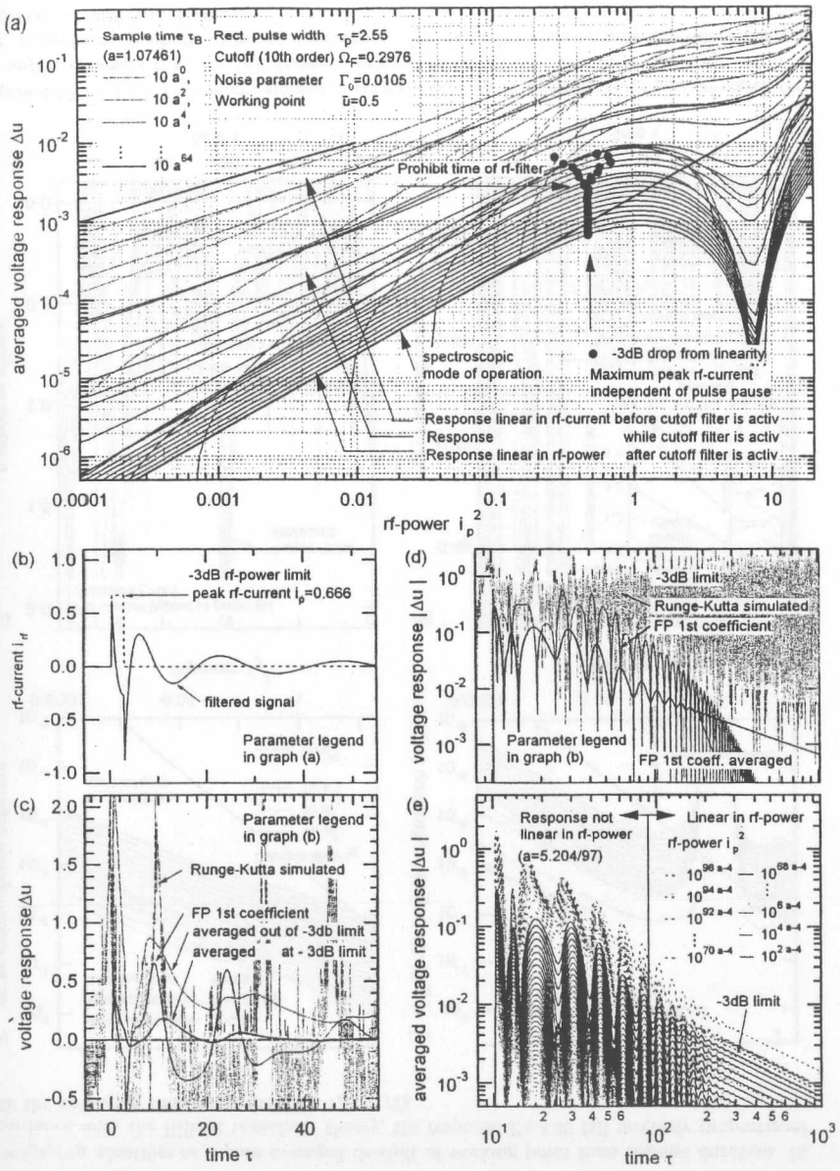

Figure 4.13: *(a) FP (1st order) simulated voltage response in dependence of peak rf-power for a (b) single rf-pulse and different sample times τ_B. (c),(d),(e) Voltage and averaged response deduced from stochastical method and 1st order FP coefficient $c_1(\tau)$ in and out of the -3db limit.*

However, here within the FP formalism, the maximum ratings for the spectroscopic mode of junction operation can be investigated for different noise parameters. To simplify its derivation I make use of the fact, that according the time dependent solution of the FP coefficients $c_1^I(\tau)$, $c_1^{II}(\tau)$ is invariant against $\tilde{Q}_1^+$, $\tilde{Q}_1^-$ from the appendix A.8.2. As proceeded in detail in section A.8.4, the spectroscopic mode of operation of the rf-pulse driven Josephson junction is given in the noisefree limit $\Gamma_0 \to 0$ by

$$\Delta\bar{u} = \frac{\pi}{\tau_B}\mathrm{Im}[c_1(i_0,0)]\,\frac{i_p^2\tau_p^2}{i_0}\left|\frac{\sin[(i_0+i_p)\tau_p/2]}{(i_0+i_p)\tau_p/2}\right|^2, \quad 2\pi\mathrm{Im}[c_1(i_0,0)] = i_0 - \sqrt{i_0^2-1}, \qquad (4.42)$$
$$\tau_B \gg 1/\Gamma_0,\ \Gamma_0 \to 0,\ i_0 \geq 1.$$

According to Fig.4.12, Eq.4.42 is not the strictly derived voltage response of an unfiltered single rf-pulse, but as depicted in Fig.4.13, it describes the spectroscopic properties of a filtered single rf-pulse, especially for long sampling times and small cutoff frequency. In comparision to Eq.4.36, Eq.4.42 contains the quadratic rf-power dependence in the low rf-power region and we pointed out, that we automatically obtain the correct pulse pause dependence, namely $1/\tau_B$ for a structureless response fuuction. Finally, one obtain the important absolute maximum rf-power ratings for a filtered single rf-pulse for the spectroscopic mode of operation in the delta pulse limit $\tau_p \to 0$, while remaining $i_p\tau_p$ constant, from Eq.4.42 to

$$\frac{\partial\Delta\bar{u}}{\partial i_p} = 0 \implies i_p\tau_p = \pi \quad \forall\ \tau_B \gg 1/\Gamma_0,\ \tau_p \to 0,\ \Gamma_0 \to 0. \qquad (4.43)$$

Inserting Eq.4.43 into the current response Eq.4.36 decreased by an increasing pulse pause τ_R reveal the fact, that for an operation at maximum rf-power ratings the response cannot be compensated by increasing the rf-power i_p^2.

Proposition 9: *The maximum response of a pulse driven Josephson junction at maximum rf-power Eq.4.42 differs significantly from the monochromatic driven device with frequency independent rf-power ratings Eq.4.21. Only the voltage response and maxium peak ratings at minimum sampling time are comparable to the monochromatic values.*

4.4.3 Time domain traces of a series of rf-pulses

In this section we will investigate analytical the absolute maximum rf-power ratings for a Josephson junction driven by a series of rf-pulses with pulse width τ_p and pulse pause τ_R. To guarantee a dc-free rf-signal periodic boundary conditions are introduced, which prevent a shift of working point and therefore linear effects in rf-current. As derived in appendix A.8.5 the averaged voltage response in the noisefree limit $\Gamma_0 \to 0$ is given by

$$\Delta\bar{u} = \frac{2\pi}{\tau_R}\mathrm{Im}[c_1(i_0,0)]\,\frac{i_p^2}{i_0(i_0+i_p)}\left[\frac{\sin[(i_0+i_p)\tau_p]}{(i_0+i_p)} - \tau_p\right], \quad 2\pi\mathrm{Im}[c_1(i_0,0)] = i_0 - \sqrt{i_0^2-1}, \qquad (4.44)$$
$$\tau_R \gg 1/\Gamma_0,\ \Gamma_0 \to 0,\ i_0 \geq 1.$$

As expected, the voltage response has no linear effects in the rf-current dependence. For the investigation of the spectroscopic mode of operation of the device, we obtain the same result as Eq.4.42 with $\tau_B \to \tau_R$ for the averaged voltage response. Therefore, the absolute maximum rf-power ratings for a dc-free rf-pulse series in the delta pulse limit is also given by Eq.4.43. According to Fig.4.14b, a refresh, represented by a series of rf-pulses, is needed to prevent a decrease of the voltage response after the first rf-pulse. The corresponding averaged current

response was analyzed in Fig.4.8a. Depending on the rf-filter characteristic, linear effects i_{dc} from rf-pulses are completely filtered out after a few rf-pulses resulting in a stationary voltage response. As depicted in Fig.4.14c an efficient low-pass filtering must occur to suppress the dominant Josephson self oscillation of working point and rf-filter oscillation.

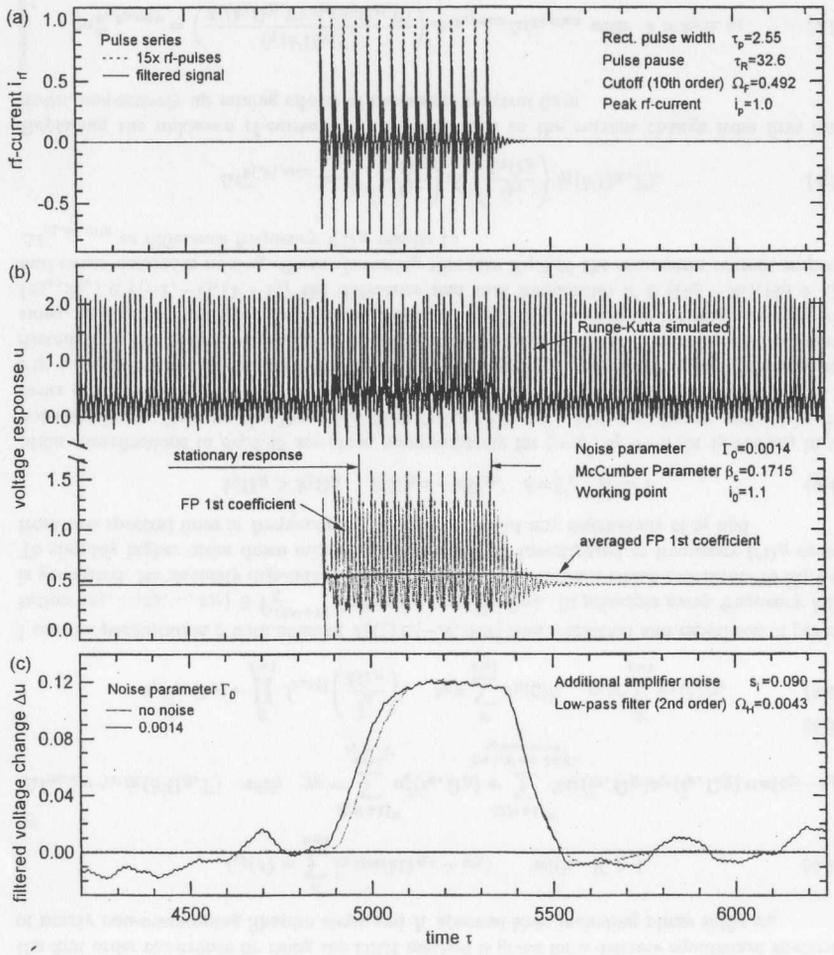

Figure 4.14: *Runge-Kutta and FP simulated (2nd order) (b) voltage response of a (a) sharp filtered rf-pulse series at low-noise operation and its low-pass filtered voltage change.*

As depicted in Fig.4.15, the maximum rf-power ratings of the voltage response for a single rf-pulse with continuously spectrum differs only slightly from the structureless voltage response of the rf-pulse series. Its noise parameter dependence is only weak.

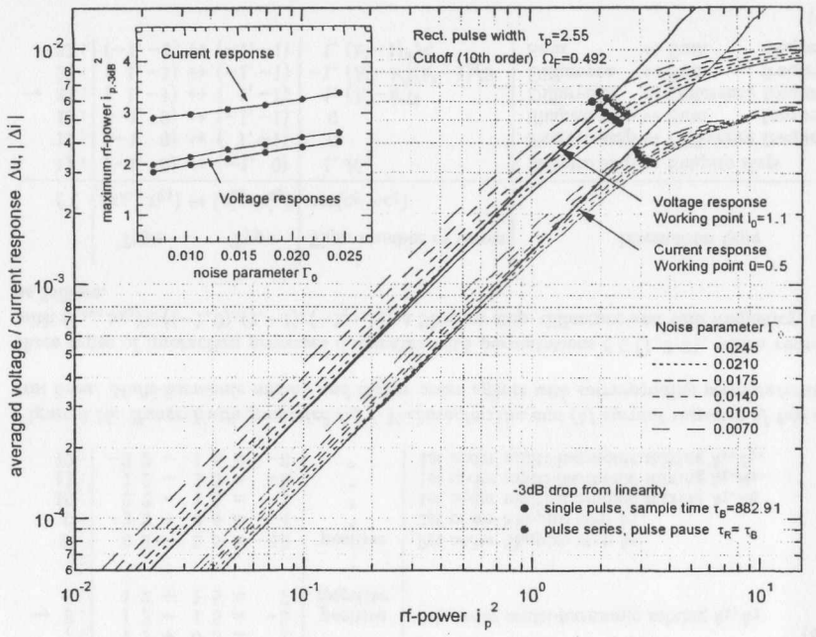

Figure 4.15: *FP simultated (2nd order) voltage response of a sampled single rf-pulse in comparison to a series of rf-pulses in dependence of noise parameter near the filter cutoff. The inset shows corresponding maximum rf-power ratings.*

4.5 Multi-harmonic mixing and higher order effects

Within the linear Hilbert theory, the voltage decrease of response function for rf-pulses with increasing pulse spacing is clearly coming from its spectral density reduction. It seems, that nothing speaks contrary to a compensation by increasing the rf-current. In this section, we will reveal the essential reason for this lack of response compensation concerning the rf-pulse spacing τ_R as the superposition of higher order mixing effects of Shapiro steps. This prevent, preferable for dense spectra, a unique reconstruction of the signal spectrum.

I will present analytical approximations of multi-harmonic mixing effects in first recurrence order, as well as numerical corrections. I will reveal a stationary voltage change from rf-signal phases. We currently observe a broken symmetry on stochastical and Focker-Planck simulated I-V-characteristics under dense spectral irradiation. Furthermore we will investigate iterative methods for the measured current response as a target function. Using a frequency domain rf-signal compensation (FDSC) requires the correction of multi-harmonic mixing effects. Ignoring them causes additional ghost power, preferable in the low frequency range, and falsifies the reconstructed time domain signal. Unfortunately for an equidistant spectrum these effects appear at the same frequencies of the essential spectrum.

4.5.1 Higher order spectral corrections using analytical approximations

Now, I will determine the correction function for an arbitrary distributed disrete spectrum caused from first order mixing effects. As proceed in detail in appendix A.8.6 the current reponse for the first order recurrence by using the DRR method is given for a discrete equidistant spectrum of nearly non-overlapping Shapiro steps and K spectral lines including phase shifts φ_k

$$i_{rf}(\tau) = \sum_{k=1}^{K} \tilde{i}_k \cos(k\Omega_R\tau + \varphi_k) \qquad \text{with} \quad K \geq 1 \tag{4.45}$$

by

$$\Delta i_{max} = \gamma_{k'}\tilde{\eta}_1(k'\Omega_R,\Gamma) \quad \text{with} \quad \gamma_{k'} = \sum_{\substack{\xi=1,\\ b_\xi=-k'}}^{(2N+1)^K} a_\xi^2(\tilde{i}_k,\Omega_R) + \sum_{\substack{\xi=1,\,\xi'=1,\,\xi<\xi',\\ b_\xi=b_{\xi'}=-k'}}^{(2N+1)^K} 2a_\xi(\tilde{i}_k,\Omega_R)a_{\xi'}(\tilde{i}_k,\Omega_R)\cos(c_{\xi'}-c_\xi), \tag{4.46}$$

$$a_\xi(\tilde{i}_k,\Omega_R) = \prod_{k=1}^{K} J_{x_k(\xi)}\left(\frac{\tilde{i}_k}{k\Omega_R}\right), \quad b_\xi = \sum_{k=1}^{K} x_k(\xi)k, \quad c_\xi = \sum_{k=1}^{K} x_k(\xi)\varphi_k. \tag{4.47}$$

I use the permutation ξ with element $x_k(\xi)\in[-N,+N]$ from variation and repetition of permutation $(x_1,...,x_k,...,x_K) \in \tilde{V}_K^{(2N+1)}$ defining $a_\xi = a_\xi(\tilde{i}_k,\Omega_R)$. In principle every frequency $k'\Omega_R$ is generated. Its intensity depends on the number of permutations, which contribute to Eq.4.46. To simplify higher order down mixing contributions are investigated at frequency $k'\Omega_R$ caused from two spectral lines at frequency $k_1\Omega_R$, $k_2\Omega_R$ without any degeneracy of b_ξ and

$$k_2\Omega_R > k_1\Omega_R, \quad b_\xi\Omega_R = -k'\Omega_R, \quad \xi=\xi', \quad N=1 \tag{4.48}$$

Main contributions to Eq.4.46 are given approximately for $\xi=\xi'$, $b_\xi \approx -k$ for $i_0 \ll k'\Omega_R$ in the noiseless limit. Because the Besselfunctions fall rapidly with higher order we restrict to first order effects $x_k(\xi)\in\{-1,0,1\}$. In this case the permutations are listed in the table of Fig.4.16. Fig.4.16a shows the simulated I-V-characteristic and differential resistance of a junction irradiated with two spectral lines and the current change marked by the corresponding permutations, as depicted in Fig.4.16b. The permutations $\xi\in\{5,8\}$, marked by arrows, represent with $(x_{k_1},x_{k_2}) \in \{(-1,-1),(1,-1)\}$ the difference and sum frequencies $k' \in \{(k_2-k_1),(k_2+k_1)\}$ and cause dominant mixing effects. Inserting this into Eq.4.46 the maximum current response $\Delta i^-_{k_1,k_2,mix}$ at difference frequency $k'\Omega_R$ results to

$$\Delta i^-_{k_1,k_2,mix} = J_1^2\left(\frac{\tilde{i}_{k_1}}{k_1\Omega_R}\right) J_1^2\left(\frac{\tilde{i}_{k_2}}{k_2\Omega_R}\right) \tilde{\eta}_1(k'\Omega_R,\Gamma). \tag{4.50}$$

Replacing the unknown rf-currents by Eq.4.27 leads to the current change from first order down, respectively up mixing effects of two single spectral lines.

$$\Delta i^{\pm}_{k_1,k_2,mix} = \left(\frac{\tilde{\eta}_1(k'\Omega_R,\Gamma)}{\tilde{\eta}_1(k_1\Omega_R,\Gamma)\;\tilde{\eta}_1(k_2\Omega_R,\Gamma)}\right)\Delta i_{k_1,max}\Delta i_{k_2,max} \quad \text{with} \quad k'=k_2\pm k_1, \quad k_2>k_1,\; \Delta i_{k',max}=0 \tag{4.51}$$

To correct an arbitrary, broadband and discrete spectral line distribution dominant sum contributions of Eq.4.46 have to be analyzed. By increasing the number of spectral lines, the degeneracy of the summation condition, namely $b_\xi = b'_\xi$, increase rapidly, especially in the low frequency range. To simplify only first order Besselfunctions $N=1$ and a symmetric I-V-characteristic with rf-phases $\varphi_{k_n} = -\pi/2$ for all K spectral lines are analyzed, especially for pulse-type rf-signals. In this case, according to tri- and quadharmonic mixing effects investigated in section A.8.6,

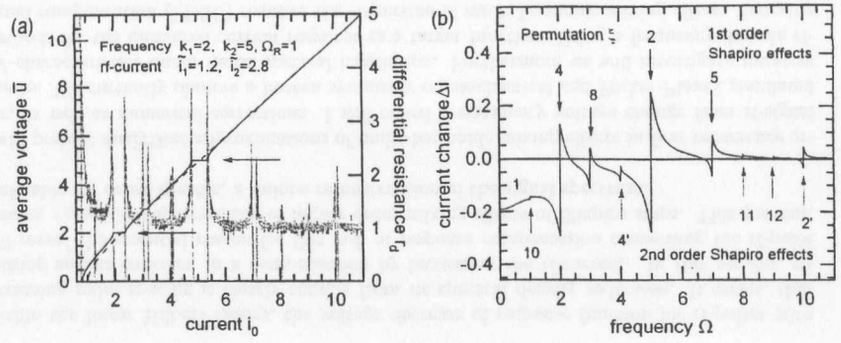

	ξ	$x_2\,k_1 + x_5\,k_2 =$	b_ξ	Range	Type
	1 :	0 2 + 0 5 =	0	neutral	0th order Shapiro step k_1, k_2
	2 :	0 2 − 1 5 =	−5	positive	1st order Shapiro step k_2
	3 :	0 2 + 1 5 =	5	negative	
	4 :	− 1 2 + 0 5 =	−2	positive	1st order Shapiro step k_1
→	5 :	− 1 2 − 1 5 =	−7	"	0th order multi-harmonic mixing k_1, k_2
	6 :	− 1 2 + 1 5 =	3	negative	
	7 :	1 2 + 0 5 =	2	"	
→	8 :	1 2 − 1 5 =	−3	positive	0th order multi-harmonic mixing k_1, k_2
	9 :	1 2 + 1 5 =	7	negative	
	⋮	⋮		⋮	
	2′ :	0 2 − 2 5 =	−10	positive	2st order Shapiro step k_2
	4′ :	−2 2 + 0 5 =	−4	"	2st order Shapiro step k_2
	10 :	2 2 − 1 5 =	−1	"	1st order multi-harmonic mixing k_1, k_2
	11 :	1 2 − 2 5 =	−8	"	1st order multi-harmonic mixing k_1, k_2
	12 :	−2 2 − 1 5 =	−9	"	1st order multi-harmonic mixing k_1, k_2.

(4.49)

Figure 4.16: *Runge-Kutta simulated (a) I-V-characteristic and (b) current response of two spectral lines. Multi-harmonic mixing and higher order effects with corresponding permutations.*

three types of interaction processes dominates with permutations $\xi\in\{1,2,3\}$, which represent with $(x_{k_1},x_{k_2})\in\{(-1,0),(1,-1),(-1,-1)\}$ a Shapiro step, difference and sum frequency, listed as follows.

	$\xi'\xi$	Type $(x_{k_1},x_{k_2}) \leftrightarrow (x'_{k_1},x'_{k_2})$	Type	Sign. number of terms $\cos(c_{\xi'}-c_\xi)$	Interaction type
	11 :	(−1, 0) ↔ (−1, 0)		1, K	Shapiro step ↔ Shapiro step
	12 :	(−1, 0) ↔ (1,−1)		0	Shapiro step ↔ Difference frequency
	13 :	(−1, 0) ↔ (−1,−1)		0	Shapiro step ↔ Sum frequency
→	22 :	(1,−1) ↔ (1,−1)		1, $(K-k')^2$	Difference ↔ Difference frequency
	23 :	(1,−1) ↔ (−1,−1)		-1, $(K-k')(k'-1)/2$	Difference ↔ Sum frequency
	33 :	(−1,−1) ↔ (−1,−1)		1, $(k'-1)^2/4$	Sum ↔ Sum frequency

(4.52)

A Shapiro step $\Delta i_{k',max}$ and a sum or difference frequency $\Delta i^{\pm}_{k_1,k_2,mix}$ simply superpose without any phase dependence. According to Eq.A.188 the summation over all mixing corrections $\Delta i_{k',mix}$ for a given discrete bandlimited spectrum of K spectral lines results to

$$\Delta i_{k',mix} = 2\sum_{k_1=1}^{K-k'}\sum_{k_2=1}^{K-k'}\sqrt{\Delta i^-_{k_1,k'+k_1,mix}\Delta i^-_{k_2,k'+k_2,mix}} \quad \forall\ \varphi_{k_n}=-\frac{\pi}{2}, \qquad (4.53)$$
$$-2\sum_{k_1=1}^{K-k'}\sum_{k_2=1}^{(k'-1)/2}\sqrt{\Delta i^-_{k_1,k'+k_1,mix}\Delta i^+_{k_2,k'-k_2,mix}} \quad 1\le k'\le K,\ K>1.$$
$$+2\sum_{k_1=1}^{(k'-1)/2}\sum_{k_2=1}^{(k'-1)/2}\sqrt{\Delta i^+_{k_1,k'-k_1,mix}\Delta i^+_{k_2,k'-k_2,mix}}.$$

The mixing correction of difference frequencies dominates in the low frequency range. According to section 6.3, supposing a well compensated spectrum, respectively constant spectrum with $\Delta i_{k',max}$ = const., the mixing correction simplifies with $\tilde{\eta}_1(k'\Omega_R,\Gamma)=1/(2\Gamma)$ for $K\gg k'\gg 1$ to $\Delta i_{k',mix}=4\Gamma K^2\Delta i^2_{k',max}$. For a bandlimited rf-signal spectrum ΔB_{eff} the number of spectral lines is given by $\Delta B_{eff}/\Omega_R$ leading to the mixing corrections of a bandlimited constant spectrum

$$\Delta i_{k',mix} = 4\Gamma\left(\frac{\Delta B_{eff}}{\Omega_R}\right)^2\Delta i^2_{k',max}, \qquad \text{with} \qquad K\gg k'\gg 1. \qquad (4.54)$$

The factor $1/\Omega_R^2$ in Eq.4.54 model the high degeneracy of b_ξ expressing the fact, that mixing effects dominates for small repetition rates in the non-overlapping regime of Shapiro steps. According to the current response Eq.4.34 of a series of delta pulses $S_p(\Omega)=i_p^2\tau_p^2\,K_{rf}(\Omega)$

$$\Delta i(\bar{u}) = -\frac{1}{2\pi}\frac{1}{8i_0\bar{u}}\sum_{n=-\infty}^{n=\infty}\frac{n\Omega_R-\bar{u}}{(n\Omega_R-\bar{u})^2+\Gamma^2}\,\Omega_R^2\,i_p^2\tau_p^2\,K_{rf}(n\Omega_R), \qquad (4.55)$$

the maximum current response at frequencies $\bar{u}=k'\Omega_R\pm\Gamma$ for non-overlapping Shapiro steps reduces to

$$\Delta i_{k',max} \approx \frac{1}{16\pi}\frac{1}{\Gamma}\,\Omega_R^2\,i_p^2\tau_p^2, \qquad (4.56)$$

where the spectrum is completely frequency compensated by using an rf-guiding transfer function $K_{rf}(\Omega)$ with $K_{rf}(\bar{u})=i_0\bar{u}$, as discussed in section 6.3. Introducing the quality $\mathcal{Q}$ of the reconstruction algorithm by the ratio of the current change Eq.4.56 and mixing corrections Eq.4.54

$$\frac{1}{\mathcal{Q}}\equiv\frac{\Delta i_{k',mix}}{\Delta i_{k',max}} = 4\Gamma\left(\frac{\Delta B_{eff}}{\Omega_R}\right)^2\Delta i_{k',max} = \frac{1}{4\pi}\,\Delta B_{eff}^2\,i_p^2\tau_p^2, \quad \text{with} \quad K_{rf}(\bar{u})=i_0\bar{u} \qquad (4.63)$$

confirm, that

Proposition 10: *A reduction of the repetition rate Ω_R of rf-pulses decrease the current response and cannot be compensated by increasing the rf-pulse current peak power i_p^2 without disturbing the quality of reconstructing its spectrum.*

Increasing the rf-signal spectral bandwidth ΔB_{eff} reduce the quality of reconstructed spectra, because the number of difference frequencies increase and more disturb the spectrum [2]. Fig.4.17a shows the current response of compensated rf-pulses of width $t_p=0.5ps$. Obviously, when using a frequency compensation with increased high frequency components outside the small signal approach, mixing effects must take into account for a time domain reconstruction. As expected in Fig.4.17a, mixing effects dominates in the low frequency range. By truncating the spectrum

[2] It is more convenient for numerical simulations Fig.6.22 to use another fixing for the frequency compensation $K_{rf}(\bar{u})\Delta B_{eff}^2=i_0\bar{u}$. In this case the current peak power i_p^2 has to be increased for increasing the rf-signal bandwidth.

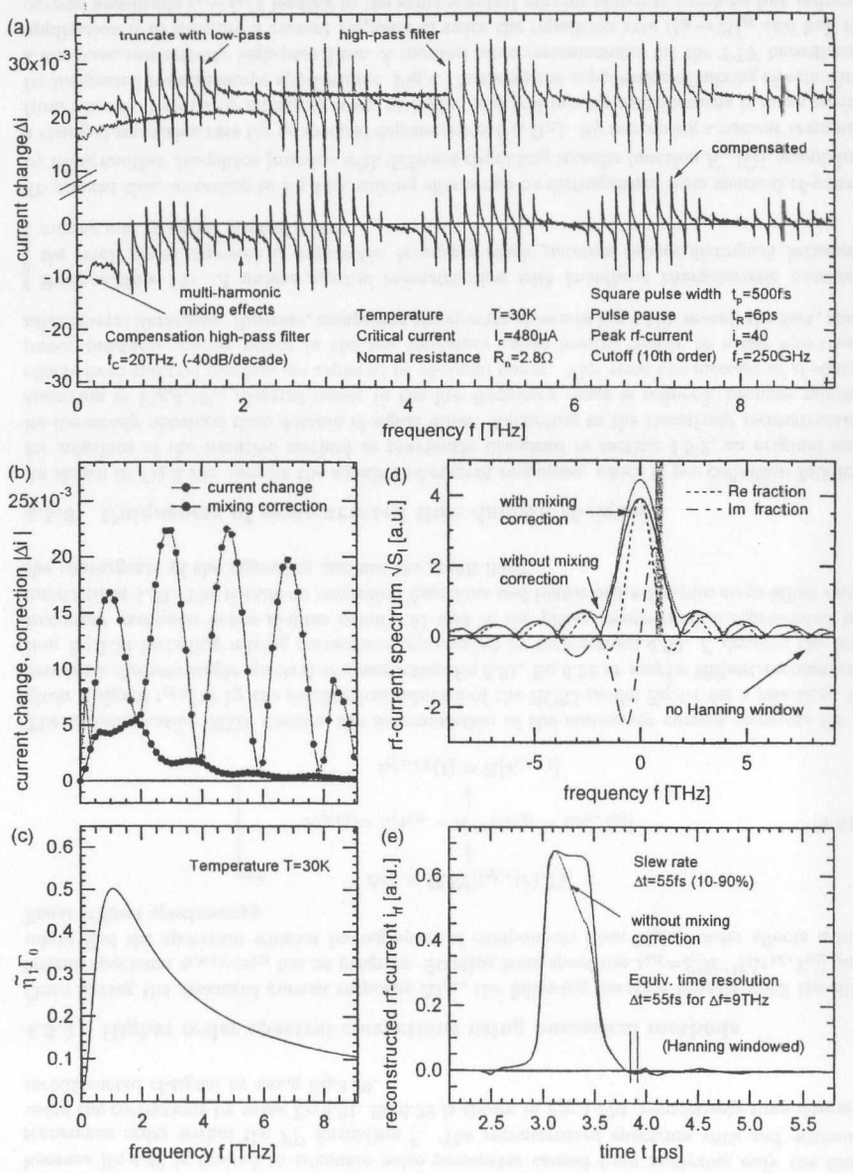

Figure 4.17: *(a) Current response, (b) current correction from Eq.4.55, (c) $\tilde{\eta}_1$ function, reconstructed (d) spectrum and (e) time domain rf-signal for compensated rf-pulses.*

High-pass filtering (Butterworth type) of rf-pulses Eq.4.32 for a frequency compensation K_{rf} (2nd order) and low-frequency cutoff Ω_F (10th order) shown in Fig.6.22b by using a state-space representation of filters [Mat98]:

$$i'_{rf}(\tau) = K_{rf}(\tau) * i_{rf}(\tau) \tag{4.57}$$

↓

Determination of the current response $\Delta i_{k',sim}$ at frequencies $k'\Omega_R$ by the stochastical solution of the RSCJ-model Eq.4.1:

$$\Delta i_{k',sim} = \mathcal{RCSJ}[i'_{rf}(\tau), \Gamma_0] \tag{4.58}$$

↓

Iteratively find irradiated current response $\Delta i_{k',max}$ by using first order mixing corrections Eq.4.51,4.53:

$$\Delta i_{k',sim} = \Delta i_{k',mix}(\Delta i_{k',max}, \tilde{\eta}_1(k'\Omega_R, \Gamma)) \ ? \tag{4.59}$$

↓

Spectral reconstruction for non-overlapping Shapiro steps using Eq.6.21,6.22:

$$s_i(k'\Omega_R) \approx |K_{rf}(k'\Omega_R)|^{-1} \Delta i_{k',max}\ 4k'\Omega_R\ i_0(k'\Omega_R, \Gamma_0)\ 2k_s(k'\Omega_R, \Gamma_0) \tag{4.60}$$

↓

Gaussian extension below cutoff frequency Ω_F with a spectral fit of parameter i_{ps},σ_Ω at the spectrum $s_i(k'\Omega_R)$ in the frequency range $[\Omega_F, \Omega_F{+}3\Omega_R]$ marked by the gray bars in Fig.4.17d:

$$s_i(k'\Omega_R) = \begin{cases} i_{ps}^2 \exp\left(\frac{-(k'\Omega_R)^2}{2\sigma_\Omega^2}\right) & \forall\ k'{=}[0, \Omega_F/\Omega_R] \\ s_i(k'\Omega_R) & \forall\ \text{else} \end{cases} \tag{4.61}$$

↓

Linear interpolation $s_i(k'\Omega_R) \to s_i(\Omega)$, phase reconstruction using Eq.3.39 and an inverse Fourier transformation $\mathcal{F}^{-1}$ using a hanning window [Num00]:

$$i_{rf,p}(\tau) = \mathcal{F}^{-1}[\sqrt{s_i(\Omega)} e^{i\psi(\Omega)}] \quad \text{with} \quad \psi(\Omega) = \frac{2\Omega}{\pi}\, \mathcal{P} \int_0^\infty \frac{\ln\left[\sqrt{s_i(\Omega')/s_i(\Omega)}\right]}{\Omega^2 - \Omega'^2} d\Omega' \tag{4.62}$$

Figure 4.18: *Complete time domain reconstruction algorithm from Eq.4.57 to Eq.4.62 for nearly non-overlapping spectra using mixing corrections derived from FP formalism.*

using high- or low-pass filter it is shown, that mixing effects are caused from interactions of the low and high frequency spectral range. The complete reconstruction algorithm is shown in Fig.4.18 by Eq.4.57-4.62. Fig.4.17b shows the extracted current change and iteratively found mixing correction by using all first order interaction terms of Eq.4.46 for $N = 1$. Considering a limited numbers of measuring points of the junction I-V-characteristic, Shapiro step maxima by using Eq.6.21,6.22 were analyzed instead of Eq.3.29. Our experience show, that it is more convenient for reconstructions at noiseless operation in the limit of non-overlapping Shapiro steps to use the function $\tilde{\eta}_1(\Omega, \Gamma) = 3/(2i_0\Gamma)$ shown in Fig.4.17c instead of Eq.4.30. This is

because Eq.4.46 is limited to adequate noise parameter caused from analyzing only the first recurrence order within the FP formalism [3]. The reconstructed spectrum with and without using the corrections by using Eq.6.21, Eq.6.22 is shown in Fig.4.17d, respectively time domain reconstructed rf-signal by using Eq.3.39.

4.5.2 Higher order spectral corrections using numerical methods

Once having the measured current response Δi_M, the following iteration repeats until the difference spectrum $s_{i,n+1} - s_{i,n}$ has no progress. Starting from spectrum $s_{i,0} = \mathcal{E}[\mathcal{H}^{-1}[\Delta i_M, \Gamma_0]]$ one might find the spectrum without having spectral components from higher order effects using linear Hilbert spectroscopy.

$$\begin{aligned} \Delta i_n &= \mathcal{RCSJ}[i_{rf,n}(\tau), \Gamma_0] \\ &\downarrow \\ s_{i,n+1} &= \mathcal{E}[s_{i,n} - \mathcal{H}^{-1}[\Delta i_M - \Delta i_n, \Gamma_0]] \\ &\downarrow \\ i_{rf.n+1}(t) &= \mathcal{R}[s_{i,n+1}] \end{aligned} \tag{4.64}$$

The transformation $\mathcal{RCSJ}$ denotes the determination of the stationary current response for a given rf-signal $i_{rf,n}(\tau)$ by the stochastical solution of the RCSJ-model Eq.4.1 for a junction. $\mathcal{H}$ denotes a discrete single spectral reconstruction Eq.6.21, Eq.6.22 or maybe Hilbert reconstruction Eq.3.29 including mixing corrections represented by instructions 4.60. $\mathcal{E}$ denotes the low frequency extension below rf-filter cutoff 4.61 and $\mathcal{R}$ the phase reconstruction represented by instructions 4.62. The details on correction functions and higher order Shapiro steps effect only the convergence of the algorithm and not the result itself.

4.5.3 Uniqueness of reconstructed time domain rf-signal

As shown in Fig.4.19c, despite the equality of current responses, which is per definition fulfilled for solutions of the iterative method as previously discussed in section 4.5.2, an original and its iteratively obtained time domain rf-signal differ. According to the iteratively reconstructed spectrum in Fig.4.19b, rf-signal power in the low frequency range is reduced, because mixing effects from spectral maxima are replaced by rf-signal power. Vice versa the increase of rf-signal power produces mixing power in the low frequency range leading finally to a flat spectrum after several iterations. However, comparing the spectra shown in Fig.4.19b reveals the fact, that

Proposition 11: *A unique spectral reconstruction with broadband characteristic outside the small signal approach is impossible, because a single junction cannot distingush between mixing and rf-signal spectral power.*

To prevent this, according to Eq.4.55, mixing effects can be distinguished from spectral rf-power by using another Josephson junction with different rf-guiding transfer function $K'_{rf}(\Omega)$, supplying a changed repetition rate Ω_R or spectral degeneracy $a_\xi(\tilde{i}_k, \Omega_R)$. By measuring a current response from filtered rf-signal by elimating lower or higher spectral mixing contributions is more useful for integrated rf-oscilloscope applications. Fig.4.17a shows the suppression of mixing effects with a low-pass, respectively high-pass filter. A method more recommended for the TTF broadband application is to measure a current response of twice the repetition rate $\Omega_R \to 2\Omega_R$ and half rf-current amplitude $i_p \to i_p/2$ leading to the same spectral current response envelope but reduced

[3] Furthermore the small signal adjustment using the Hilbert transform theory, based on Eq.3.10, is not a good approximation for the noiseless operation $\Gamma_0 = 0$ at adequate rf-power, as depicted in Fig.4.7. A more detailed discussion is performed in section A.8.6.

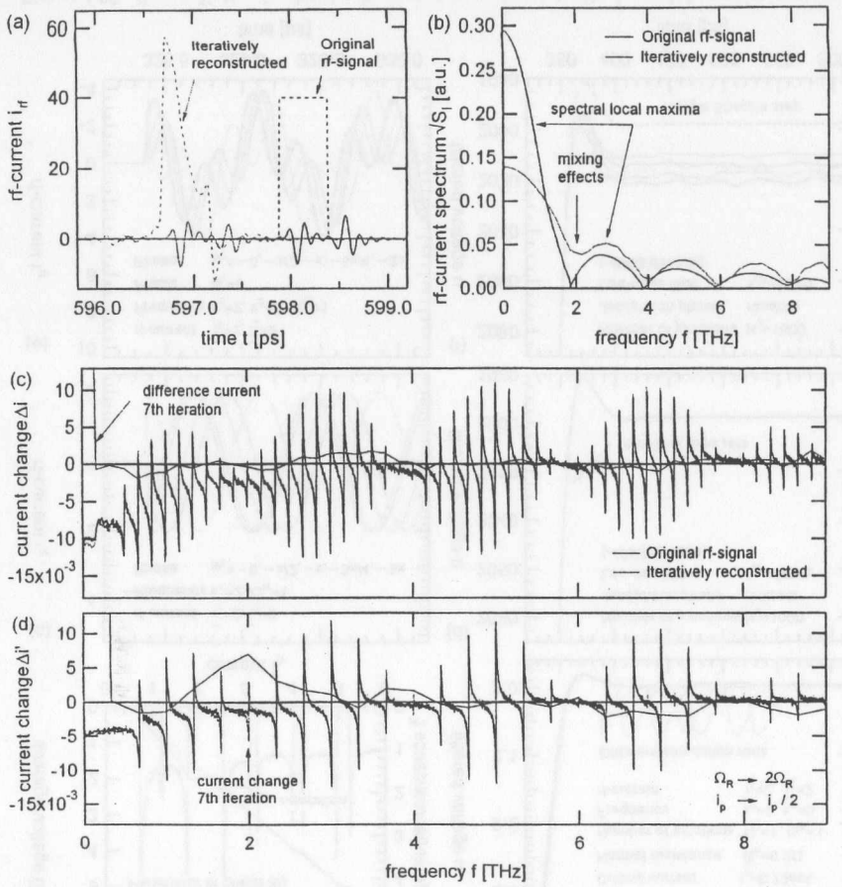

Figure 4.19: *(a) Time domain rf-signal, (b) spectrum and (c),(d) curent responses for an orignal and iteratively reconstructed rf-signal for different rf-guiding transfer functions.*

mixing effects according to Eq.4.54. Taking this into account, the algorithm is extended by another Josephson junction operating with a different rf-guiding transfer function.

$$\begin{aligned} &\Delta i_n = \mathcal{RCSJ}[K_{rf}(\tau) * i_{rf,n}(\tau), \Gamma_0],\ \Delta i'_n = \mathcal{RCSJ}[K'_{rf}(\tau) * i_{rf,n}(\tau), \Gamma_0] \\ &\qquad\qquad \downarrow \\ &s_{i,n+1} = \mathcal{E}[s_{i,n} - \mathcal{H}^{-1}[\mathcal{T}[\Delta i_M, \Delta i_n, \Delta i'_M, \Delta i'_n], \Gamma_0]] \\ &\qquad\qquad \downarrow \\ &i_{rf,n+1}(\tau) = \mathcal{R}[s_{i,n+1}]. \end{aligned} \tag{4.65}$$

$\mathcal{T}$ denotes the essential target criteria for iteration. The function must fulfil $\mathcal{T}=0$ for $\Delta i_M = \Delta i_n$ *and* $\Delta i'_M = \Delta i'_n$ realized by an alternating superposition.

$$\mathcal{T}[\Delta i_M, \Delta i_n, \Delta i'_M, \Delta i'_n] = (\Delta i_M - \Delta i_n) + (-1)^n (\Delta i'_M - \Delta i'_n) \tag{4.66}$$

The iteration repeats until the difference spectrum of both spectral systems $(\Delta i_M - \Delta i_n) = 0$ and $(\Delta i'_M - \Delta i'_n) = 0$ do not change leading to the spectrum $s_{i,n+1} = s_{i,n}$, respectively time domain rf-signal $i_{rf}(\tau)$. Unfortunately the iteration method Eq.4.65 detects mostly only local minima. To prevent this, the method of simulated annealing $\mathcal{SA}$ to find the global minimum is used [Num00]. For vanishing simulation temperature T_n the algorithm simplifies to the downhill simplex method by using the geometrical concept of simplex P including reflections, expansions and contractions in parameter space. The method minimizes the target function $\mathcal{T}$ by changing the discrete current values $i_{rf}(\tau_m)$ at time τ_m. The initial starting simplex is given by a phase reconstructed current trace. Similarly in a solid state the global minimum is found by decreasing the simulation temperature.

$$\begin{aligned} &T_{n+1} = (1-\epsilon) T_n \\ &\qquad \downarrow \\ &i_{rf,n+1}(\tau_m) = \mathcal{SA}[\mathbf{P}, T_n] \quad \forall \quad 0 < m < M. \\ &\qquad \downarrow \\ &\Delta i_n = \mathcal{RCSJ}[K_{rf}(\tau) * i_{rf,n}(\tau), \Gamma_0],\ \Delta i'_n = \mathcal{RCSJ}[K'_{rf}(\tau) * i_{rf,n}(\tau), \Gamma_0] \\ &\qquad \downarrow \\ &\mathcal{T}_{n+1}[\Delta i_M, \Delta i_n, \Delta i'_M, \Delta i'_n] = \mathcal{T}_n \ ? \end{aligned} \tag{4.67}$$

Unfortunately finding the global minimum in the M-dimensional space requires much more computational effort. It seems, that the uniqueness of a spectral reconstrution is guaranteed out of the small signal approach below by using several junctions operating with different rf-guiding transfer functions.

4.5.4 Phase reconstruction, ghost spectra and broken symmetry

Using small averaging times and a single Josephson junction operating in the low-noise regime, the Josephson oscillation must take into account by analyzing the stochastical solutions of the RCSJ-model. Unfortunately, for spectroscopy, all available models handle with averaged expectation values excluding the dominant Josephson oscillation. Consequently

Proposition 12: *To suppress for spectroscopy the Josephson oscillation either a series connection of several mutually decoupled junctions with an incoherent phase addition or a sufficient long measuring time is required for a low-noise operation.*

According to Fig.4.20a,b an operation near Shapiro steps Ω_n causes, similar to a heterodyn receiver, a low IF frequency due to noise sources and requires at least averging times τ_B of about

$$\tau_B \gg \frac{2\pi}{\Omega_n - \bar{u}}, \quad \tau_B = \frac{2\pi}{\Gamma(\bar{u})} \quad \forall \quad \Gamma \ll 1,\ N_J = 1. \tag{4.68}$$

If a sufficient number of N_J junctions are connected in series and mutually decoupled their phases add incoherently and restriction Eq.4.68 is no more valid, because the Josephson oscillation averages out. In this case the voltage response can be described within the FP formalism. The overall Josephson oscillation vanishes and therefore its phase dependencies with rf-signal do also. Despite small oscillation linewidths Γ_0, decoupled junction series arrays allow high measuring bandwidths but reveal no phase relations about the rf-radiation Fig.4.20c,d with respect to the Josephson oscillation. For spectroscopy it is more helpful to study stationary effects of the voltage response from phase shifts between the rf-radiation components itself, not

caused from transient effects from triggering of the rf-radiation appearance and the Josephson oscillation. For a low-noise operation and high measuring bandwidth we use junction arrays described within the FP method. An important phase dependence of the *stationary* voltage response Eq.4.46 is predicted caused from higher order effects, similar to interband modulation effects from nonlinear mixer theory [Gun92].

Proposition 13: *According to Eq.4.46 a stationary voltage change from Josephson junction depends on the rf-radiation phases for a degenerated spectrum $b_\xi = b'_\xi$ and $\xi \neq \xi'$ outside the small signal limit of the Hilbert theory.*

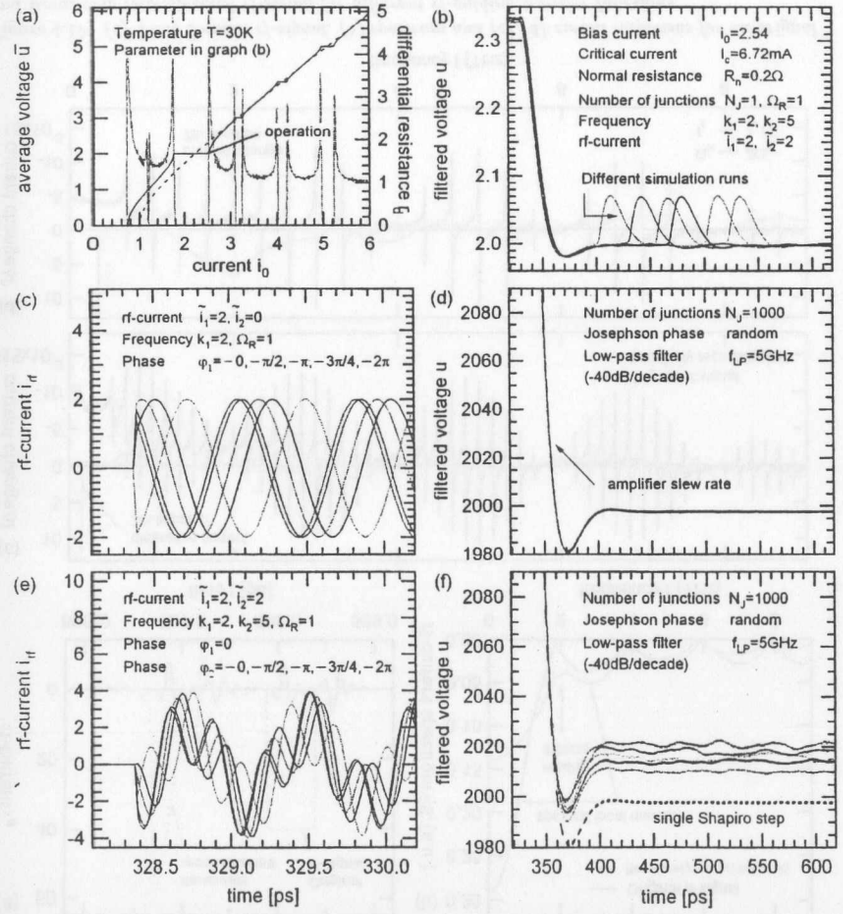

Figure 4.20: *Runge-Kutta simulated voltage response of a mutually decoupled junction series array for varying phase of (c) one and (e) two spectral line(s), respectively filtered voltage transient behaviour (d),(f). (b) Transient voltage response of a single junction for the low-noise operation.*

In detail, analyzing Eq.4.46 for a single spectral line $K = 1$, the allowed permutations for $b_\xi = b_{\xi'}$ simplifies to $\xi = \xi'$ and $c_\xi = c_{\xi'}$ with a vanishing stationary phase dependence, as expected. Considering two spectral lines Fig.4.16, dominant contributions are given for $\xi = \xi'$ leading in first order again to no phase dependence. As depicted in Fig.4.20f, higher orders $x_k(\xi) \in \{-4,-3,-2,-1,0,1,2,3,4\}$ with

ξ	$x_2\,k_1 + x_5\,k_2 = b_\xi$	Range	Type
$\rightarrow$ 40 :	$4\;2\;-\;2\;5 = -2,$	positive	3nd order multi-harmonic mixing k_1, k_2
$\rightarrow$ 41 :	$-1\;2\;+\;0\;5 = -2,$	"	"

(4.69)

reveal several permutations with $b_\xi = b_{\xi'}$ with phase contributions $c_\xi \neq c_{\xi'}$. For this choice of spectral lines the phase dependent stationary voltage change is quite small. A rough estimation of phase dependencies by analyzing Eq.4.46 can be given by the

$$\text{Voltage response: } \Delta\bar{u} \sim \sum_{\xi=1,\xi'=1,b_\xi=b_{\xi'},\xi=\xi'}^{(2N+1)^K} a_\xi(\tilde{i}_k,\Omega_R)a_{\xi'}(\tilde{i}_k,\Omega_R) \quad \text{and} \tag{4.70}$$

$$\text{Phase effect strength: } \Delta\bar{u} \sim \sum_{\xi=1,\xi'=1,b_\xi=b_{\xi'},\xi\neq\xi'}^{(2N+1)^K} \left| a_\xi(\tilde{i}_k,\Omega_R)a_{\xi'}(\tilde{i}_k,\Omega_R) \right|. \tag{4.71}$$

According to Fig.4.21 dominant phase contributions occur, if a down mixed frequency component superposes with a Shapiro step. A more detailed analysis of bi-, tri- and quadharmonic phase effects are derived in section A.8.6. For two spectral lines the phase dependent current change is given by

$$i_{rf}(\tau) = \tilde{i}_{k_1}\cos(k_1\Omega_R\tau) + \tilde{i}_{k_2}\cos(k_2\Omega_R\tau + \varphi_{k_2}) \qquad \text{with} \quad k_2 = 2k_1 \tag{4.73}$$

$$\Delta i^-_{k_1,k_2,phase} = \Delta i_{k_1,max} + \Delta i^-_{k_1,k_2,mix} \pm 2\sqrt{\Delta i_{k_1,max}\Delta i^-_{k_1,k_2,mix}}\;\cos(\varphi_{k_2}). \tag{4.74}$$

and allows a phase reconstruction of the rf-radiation. By using different rf-guiding transfer functions and junctions all currents $\tilde{i}_k$ and rf-phases φ_k can be determined. As depicted in Fig.4.9,4.22 phase effects and a spectral asymmetry of the junction vanish for the small signal theory. As depicted in Fig.4.22d stationary phase contributions outside the small signal limit occur for a high degeneracy of b_ξ by either increasing the number of spectral lines K or the Bessel order N. As shown in Fig.4.22d,e,f an increase of rf-power for a dense spectrum produces additional an asymmetry of the junction response in accordance with FP simulations. The filling up of rf-power below the cutoff frequency is clearly caused from higher order effects. According to Eq.4.74 an asymmetry of the I-V-characteristic in first Bessel order, caused from the interaction of Shapiro steps and down mixed frequencies, vanishes for an rf-pulse series having equal phases $\varphi_k = -\pi/2$. Under the transformation $b'_\xi = -b_\xi$, respectively for permutation elements $x'_k(\xi) = -x_k(\xi)$, the terms b'_ξ, c'_ξ and its degeneracy remain invariant and therefore symmetric. The asymmetry is caused from the identity $J_{x_k(\xi)}(x) = (-1)^{x_k(\xi)}J_{-x_k}(x)$, which changes its symmetry depending on odd or even permutation element x_k leading to an invariant summation contribution $a'_\xi \neq a_\xi$ for $K > 1$.

$$a'_\xi(\tilde{i}_k,\Omega_R) = \prod_{k=1}^{K}(-1)^{x'_k(\xi)}J_{-x'_k(\xi)}\left(\frac{\tilde{i}_k}{k\Omega_R}\right), \quad b'_\xi = \sum_{k=1}^{K}x'_k(\xi)k, \quad c'_\xi = \sum_{k=1}^{K}x'_k(\xi)\varphi_k \tag{4.75}$$

Only for the monochromatic case $K = 1$ out of the small signal limit, $b_\xi = b'_\xi$ is fulfilled for $\xi = \xi'$

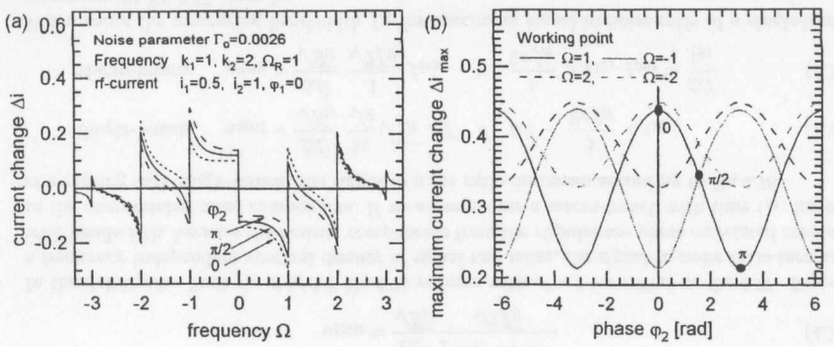

ξ	$x_1\,k_1 + x_2\,k_2 =$	b_ξ	Range	Type
1 :	0 1 + 0 2 =	0,	neutral	0th order Shapiro step k_1, k_2
2 :	0 1 − 1 2 =	−2,	positive	1st order Shapiro step k_2
3 :	0 1 + 1 2 =	2,	negative	
→ 4 :	− 1 1 + 0 2 =	−1,	positive	1st order Shapiro step k_1
5 :	− 1 1 − 1 2 =	−3,	"	0th order multi-harmonic mixing k_1, k_2
6 :	− 1 1 + 1 2 =	1,	negative	
7 :	1 1 + 0 2 =	1,	"	
→ 8 :	1 1 − 1 2 =	−1,	positive	0th order multi-harmonic mixing k_1, k_2
9 :	1 1 + 1 2 =	3,	negative	

(4.72)

Figure 4.21: *Runge-Kutta simulated (a) current response of two spectral lines for different rf-phases and (b) maximum current response at different frequencies. As expected from Eq.4.74 dominant phase effects appear for $k_2 = 2k_1$, if a Shapiro step superposes with a difference frequency. The table lists the available permutations for the first order Besselfunctions $N = 1$.*

and the symmetry of the term a'_ξ has no influence for the product $a'_\xi a'_\xi \geq 0$ without any phase dependence. If the rf-radiation power decreases $i_k \to 0$ dominant summation contributions, beside the 0th Shapiro step, occur for a_ξ consisting of permutations identical to unit vectors $\mathbf{x} = (0, ..., 1, ..., 0)$, namely consisting of one spectral line k. Using unit vectors imply mainly contributions only for $\xi = \xi'$ leading to the symmetric Hilbert small signal theory without phase effects.

Proposition 14: *We recognize, that the spectral asymmetry is inherently connected to the spectral distribution irradiated on the Josephson junction. Therefore phase effects can only be detected outside the small signal approach. To distinguish phase effects with $\xi \neq \xi'$ from higher order mixing effects $\xi = \xi'$ different types of spectral envelopes and junctions biased by the same rf-radiation source have to be used.*

The extension of the phase reconstruction to more complex spectra requires difference equations of Eq.4.46 of the measured current change leading to a nonlinear system of phase equations φ_k. However, a more general theory describing the symmetry breaking mechanism of discrete or continuous spectra predicting the rf-signal phase outside the Hilbert theory have to be investigated in every recurrence order[4].

According to the stochastical description Eq.4.1 the rf-current $i_{rf}(\tau)$ and noise current $i_{th}(\tau)$

[4]For a moment my thoughts connected to elementary particle physics.

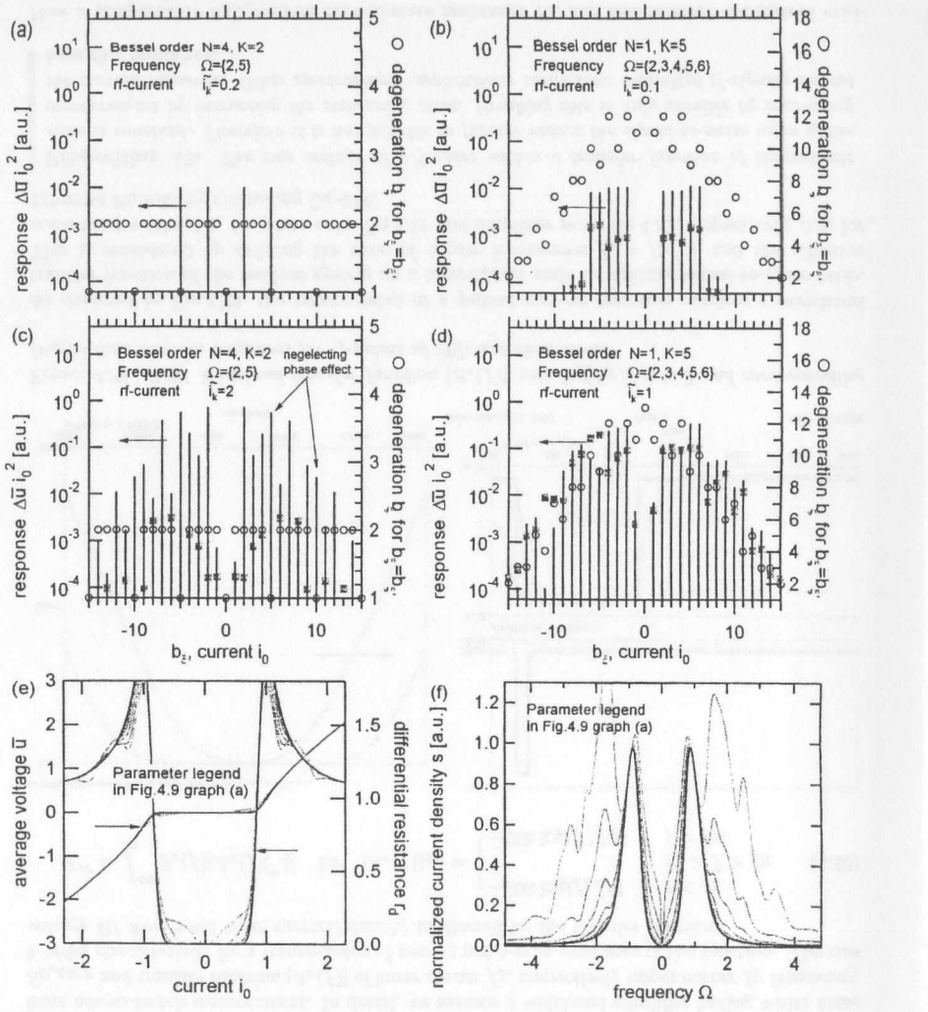

Figure 4.22: *Simulated Eq.4.70 voltage response in dependence of current for (a),(c) two spectral lines and (b),(d) a series of dense spectral lines out of the small signal theory. Gray squares marked contributions to the response Eq.4.71 responsible for phase effects $\xi \neq \xi'$. Because of plotting the response function $\Delta\bar{u}i_0$ the 0th Shapiro step is not shown. (e),(f) FP (2nd order) simulated rf-power dependent rf-pulse spectra using parameters of Fig.4.9.*

have equal significance. Exchanging them, we expect without any rf-radiation the same results Eq.4.46 with vanishing $i_N(\tau) = 0$ and external noise signal $i_{rf}(\tau)$, which can be identified as the junctions intrinsic noise sources. By comparing the exponential phase difference term in

Eq.4.46 with a small signal analysis of 1/f-noise from the junction, reveals its dependence on the autocorrelation spectrum of noise [Lud97], indicating by Eq.24 from appendix B. In other words, the noise correlation spectrum might decided weather the unperturbated I-V-characteristic Fig.1a from appendix B, respectively differential resistance gets symmetric or asymmetric.

4.6 System noise, measuring time and bandwidth

For applications of broadband spectroscopy with Josephson junctions, like the TTF-spectrometer or the proposal of integrated THz oscilloscope, a key feature is the measurement time. In this section we investigate the required time for a spectral measurement with the Josephson detector for pulse-type rf-radiation. Obviously, noise of the detector itself is the limiting quantity for the measurement time of a spectrometer for applications using time limited rf-signals. For rf-pulse spectroscopy only broadband high frequency voltage responses of the detector are important and white noise sources dominate the system noise. We consider Nyquist noise $S_{U,th}$ from normal-state resistance R_n Eq.3.14, 1/f-noise resistance fluctuations of the junction and voltage noise from the first input stage of amplifier $S_{U,AMP}$ or SQUID amplifier readout. We neglect noise from current biasing, flicker noise and input current noise contributions from amplifier.

4.6.1 Averaging over responses from a series of rf-pulses

A single-bunch measurement using replicated rf-pulses requires an averaging over several identical rf-pulses. Due to the small pulse-to-pause duration ratio at the actual TTF timing of about $1ps/1\mu s \approx 10^{-6}$, a macro-bunch measurement using box-car techniques is better to improve the signal-to-noise ratio (SNR) than averaging over the pulse pauses. First of all, the question of the measuring bandwidth for optimal signal-to-noise ratio has to be answered. According to the TTF bunch timing the optimal upper cutoff frequency f_H of measuring bandwidth depends on the replication time ΔT of a single-bunch and is given approximately by $f_H \approx 1/\Delta T$. To show this, we calculate the signal-to-noise ratio of a -20dB/decade filtered squared response, characterized by $\Delta\bar{U}$, ΔT underlying with white noise S_U. We assume a sampling of a single filtered rf-pulse response at $t = \Delta T$, resulting in an signal-to-noise ratio of

$$u_{SNR} = \frac{\Delta\bar{U}}{\sqrt{S_U}} \frac{1 - e^{-2\pi f_H \Delta T}}{\sqrt{2 f_H}} \tag{4.76}$$

In the delta pulse limit $f_H \ll 1/\Delta T$ Eq.4.76 reduces with $e^x = 1 + x + \mathcal{O}(x)$ to Eq.4.77. Despite a frequency independent spectral density of signal and noise, the signal-to-noise ratio increases with bandwidth, because the Fourier components from the rf-pulse are phase correlated contrary to the uncorrelated noise components. If we average over a macro-bunch with time t_M, instead of sampling each single-bunch, the signal-to-noise ratio decreases according to Eq.4.78.

$$\text{Single-bunch:} \quad u_{SNR} = \frac{\Delta\bar{U}}{\sqrt{S_U}} \frac{2\pi}{\sqrt{2}} \sqrt{f_H}\, \Delta T \quad \forall \quad \Delta T < \frac{1}{2\pi f_H} < t_M. \tag{4.77}$$

$$\text{Macro-bunch:} \quad u_{SNR} = \frac{\Delta\bar{U}}{\sqrt{S_U}} \frac{1}{\sqrt{2 f_H}} f_{ave} \quad \forall \quad \frac{1}{2\pi f_H} > t_M,\ f_{ave} = \frac{\Delta T}{t_M} \tag{4.78}$$

When using the measuring bandwidth f_H for maximum signal-to-noise ratio of a single-bunch measurement Eq.4.77 given by

$$\frac{\partial u_{SNR}}{\partial f_H} = 0 \ \rightarrow\ f_H = \frac{1}{4\pi\Delta T} \ \rightarrow\ u_{SNR} \approx \frac{\Delta\bar{U}}{\sqrt{S_U}} \sqrt{\Delta T}, \tag{4.79}$$

only noise voltages are effected by the measuring bandwidth. In this case the signal-to-noise ratio is given by Eq.4.81. Because of 1/f-noise sources from the Josephson junction we employ a bandlimited filtering. A filter characteristic, which does not essentially change the maximum sampled voltage response from rf-pulse is assumed. The rf-pulse replication implies the duration of an rf-pulse series during the complete measuring time ΔT. We pointed out, that the signal-to-noise ratio of a single-bunch measurement Eq.4.81 differs by the tremendous factor f_{ave} from macro-bunch measurement. In detail, we assume a wideband amplifier having white noise $S_{U,AMP}$ and transfer function $|A_v(f)|$ of lower corner f_L, respectively upper corner f_U frequency, k-order characteristic for a transmission of nearby pulse-type responses of the junction. The rms voltage δU from total noise spectral density is effected by the transfer function

$$\delta U^2 = \int_0^\infty S_u(f)|A_v(f)|^2 df \quad \text{for} \quad |A_v(f)|_{dB} = \begin{cases} -20k\log(f_L/f) & \forall\ f < f_L \\ 1 & \forall\ f_L > f > f_H \\ -20k\log(f/f_H) & \forall\ f > f_H. \end{cases} \tag{4.80}$$

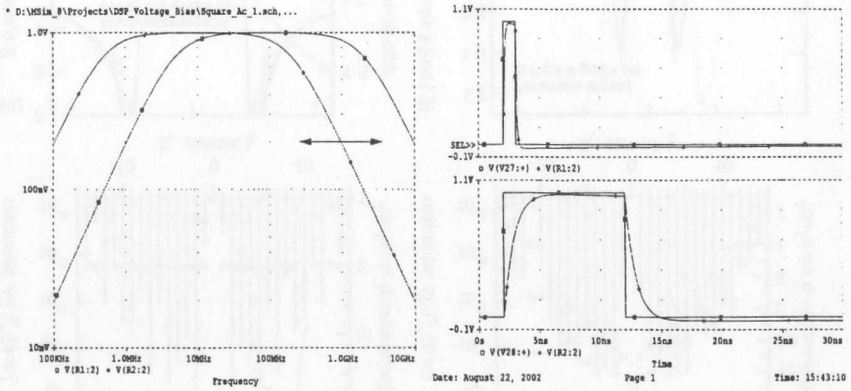

Figure 4.23: *(left) Wideband transfer function $|A_v(f)|$ with $\log[f_H/f_L] \approx 2$ and corresponding (right) time domain responses for rf-pulses of different time scales.*

As depicted in Fig.4.23, the transmission of a pulsed current response requires a wideband transfer function of the readout system on a logarithmic scale for optimal signal-to-noise ratio. This is considered by defining the ratio of corner frequencies $f_p = f_H/f_L$ and the effective noise bandwidths $\Delta\eta_1$ for white noise Eq.4.81 and amplifier noise Eq.4.82, respectively $\Delta\eta_2$ for 1/f-noise Eq.4.85 by evaluating Eq.4.84.

Proposition 15: *The rms voltage of 1/f-noise within a transfer function of logarithmic scale is constant. Therefore it is not possible to further reduce the signal-to-noise ratio of the measurement by increasing the measuring time. Breaking this is only possible by increasing the current response. Other spectroscopic applications using time unlimited rf-signals do not have this limitation.*

Now a temperature independent normal-state resistance R_n and temperature dependent critical current $I_c(T)$ based on measurements of Tab.5.6 for different junctions is assumed. Main contributions to flicker noise in the high frequency range for $I_0 \gg I_c$ comes from resistance fluctuations $S_R = |\delta R_n/R_n|$ caused of intrinsic localized trapping centers within the junctions

barrier [Lud97],[Mar96]. As depicted in Fig.4.24 a series connection of multiple uncoupled and mutually decoupled N_J Josephson junctions is assumed.

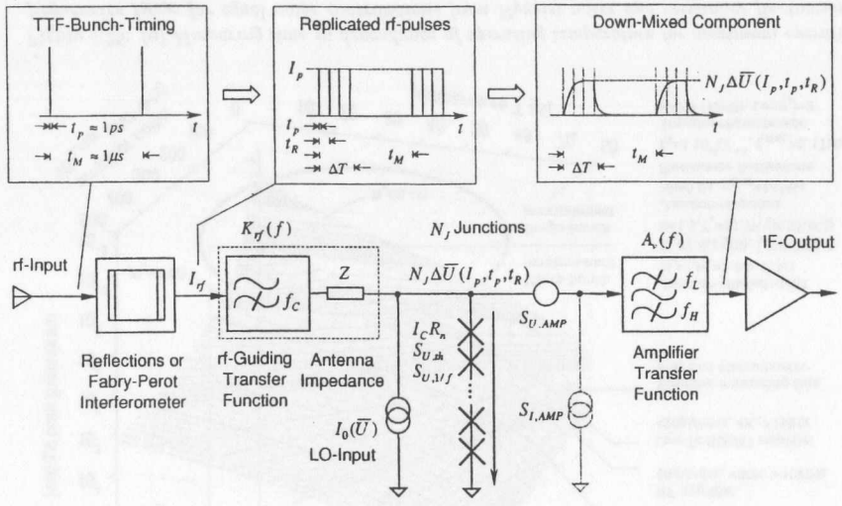

Figure 4.24: *Simplified scheme for the spectral measurement of a series of rf-pulses within the sub-millimeter wavelength regime by using a series connection of Josephson junctions.*

Putting all together, we yield the signal-to-noise ratio of the measurement in unnormalized units

$$u_{SNR} = \frac{N_J U_n(T)\Delta\bar{u}(i_p,\tau_p,\tau_R)}{\sqrt{\delta\bar{U}_R^2 + \delta\bar{U}_{AMP}^2 + \delta\bar{U}_{1/f}^2}} \quad \text{with} \quad \begin{aligned} &U_n(T) = I_c(T)R_n, \\ &I_c(T) = I_c(0)\,(1 - T/T_c)^x,\ \Delta T = nt_R, \end{aligned} \tag{4.81}$$

$$\delta\bar{U}_R^2 = N_J S_{U,th}\Delta\eta_1 = 4k_B T N_J R_n \Delta\eta_1, \quad \Delta\eta_1 = \frac{2k}{2k-1}f_H - \frac{2k}{2k+1}f_L, \tag{4.82}$$

$$\delta\bar{U}_{AMP}^2 = S_{U,AMP}\Delta\eta_1 \quad , \quad f_H = 1/\Delta T,\ f_L = f_H/f_p, \tag{4.83}$$

$$\delta\bar{U}_{1/f}^2 = \left(\frac{h}{2e}\right)^2 f_{rf}^2\, N_J R_n f_R^2\, \Delta\eta_2 \quad , \quad \Delta\eta_2 = \frac{1}{k} + \ln\left[\frac{f_H}{f_L}\right], \tag{4.84}$$

$$S_{U,1/f}(f) = \bar{U}^2(I_0,T)S_R(f) = \left(\frac{h}{2e}\right)^2 f_{rf}^2\, f_R^2 \frac{R_n}{f} \quad \text{with} \quad f_{rf} \le f_{HTSC}, \tag{4.85}$$

where the maximum resistance fluctuations within the measured bandwidth is analyzed by using the maximum operation frequency f_{HTSC} of the Josephson junction. The measuring time for equal Nyquist noise $S_{U,th}$ and resistance fluctuations $S_{U,1/f}$ of operation at maximum frequency f_{HTSC} is shown for a transferred pulsed current response in Fig.4.25a with $k=1$, $\log[f_p]=2$ and given by

$$S_{U,th} = S_{U,1/f} \quad \rightarrow \quad \Delta T = \left(\frac{2e}{h}\right)^2 \frac{4k_B T}{f_{HTSC}^2 f_R^2} \frac{1 - 2/3 f_p}{1 + \ln[f_p]}. \tag{4.86}$$

Flicker noise from resistance fluctuations dominates for a macro-bunch measurement using long averaging times. Contrary, for fast measurements or a single-bunch measurement Nyquist noise dominates. According to Eq.4.81ff the strategy for a single-bunch measurement gets evident.

Proposition 16:

1. *Use high-T_c junctions with high I_cR_n-products operating at low temperature.*
2. *Increase the response $\Delta\bar{u}$ by replication structures and higher order reconstructions.*
3. *Minimize junction resistance R_n low as possible despite an adequate input rf-coupling.*
4. *Use multiple junctions N_J to limit influence of amplifier noise $S_{U,AMP}$.*
5. *Use a fast low-T_c SQUID amplifier pickup for an operation of a single high-T_c junction.*

According to Eq.4.81 and Fig.4.25b the junctions I_cR_n-product and voltage response $\Delta\bar{u}$ mainly influence the measuring time. As depicted in Fig.4.8 the voltage response itself depends strongly on repetition structure. As shown in Fig.4.25b,c a small normal-state resistance R_n, high I_cR_n-products of high-T_c Josephson junctions and low-noise amplification having low-T_c SQUID amplifier readout performances, are neccessary for single-bunch measurements using a single junction. The I_cR_n-products $U_n(T)$ are assumed to be temperature dependent and characterized by the measured ones for bicrystal junction $\#L37$, as shown in Fig.5.6a. The rf-pulse replication limits the measuring time to approximately $\Delta T < 10ns...100ns$ for a single-bunch operation with well defined reflection structures, marked by a circle in Fig.4.25c. This regime requires a high-T_c junction, a wideband ultra low-noise rf-amplifier or low-T_c SQUID amplifier readout, as presented in section C.2.

According to Fig.4.26a the experimental requirements on the amplifier, impedance matching and voltage biasing are more relaxed using a series array of junctions. As depicted in Fig.4.26b,c as a top view of Fig.4.8c, the spectral decay from pulse spectrum limits the dynamic range of the detector requiring a frequency domain rf-signal compensation described in section 6.3. As depicted in Fig.4.17, a frequency domain rf-signal compensation (FDSC) produce at least a constant current response envelope for a successful spectral reconstruction for a series of rf-pulses of about

$$\Delta\bar{u}_{max} = -r_d(i_0,\Gamma)\Delta i_{max}, \quad \Delta\bar{u}_{max} \approx \Delta i_{max} = 0.01 \qquad \forall \quad i_0 \gg 1 \tag{4.87}$$

for the actual implemented reconstruction algorithms. Evaluating the current response for an rf-pulse series Eq.4.36 in the delta pulse limit $S_p(\Omega) = i_p^2\tau_p^2, \tau_p \rightarrow 0$ at maximum rf-power Eq.4.43, we yield for non-overlapping Shapiro steps

$$\Delta i_{max} = \frac{1}{2i_0\bar{u}}\frac{1}{\tau_R^2}\frac{1}{\Gamma(\bar{u})} \qquad \forall \qquad \Gamma \ll \Omega_R. \tag{4.88}$$

According to Fig.4.11 we recognize, that the repetition dependence can not be compensated by a frequency domain rf-signal compensation. But fortunately with increasing I_cRn-product, respectively critical current, the junctions linewidth decrease and overlapping of different Shapiro steps gets less important. According to the dynamic range of the voltage reponse from rf-pulse spectrum Fig.4.27f, we conclude, that

Proposition 17: *Beside using Josephson junctions with increased I_cR_n-product, low normal-state resistance and a series array arrangement, for high freqeuncy spectral measurements of pulsed rf-radiation a frequency domain rf-signal compensation (FDSC) is advantageous, weather using fix rf-filter characteristics or regulations, as discussed in section 6.3.*

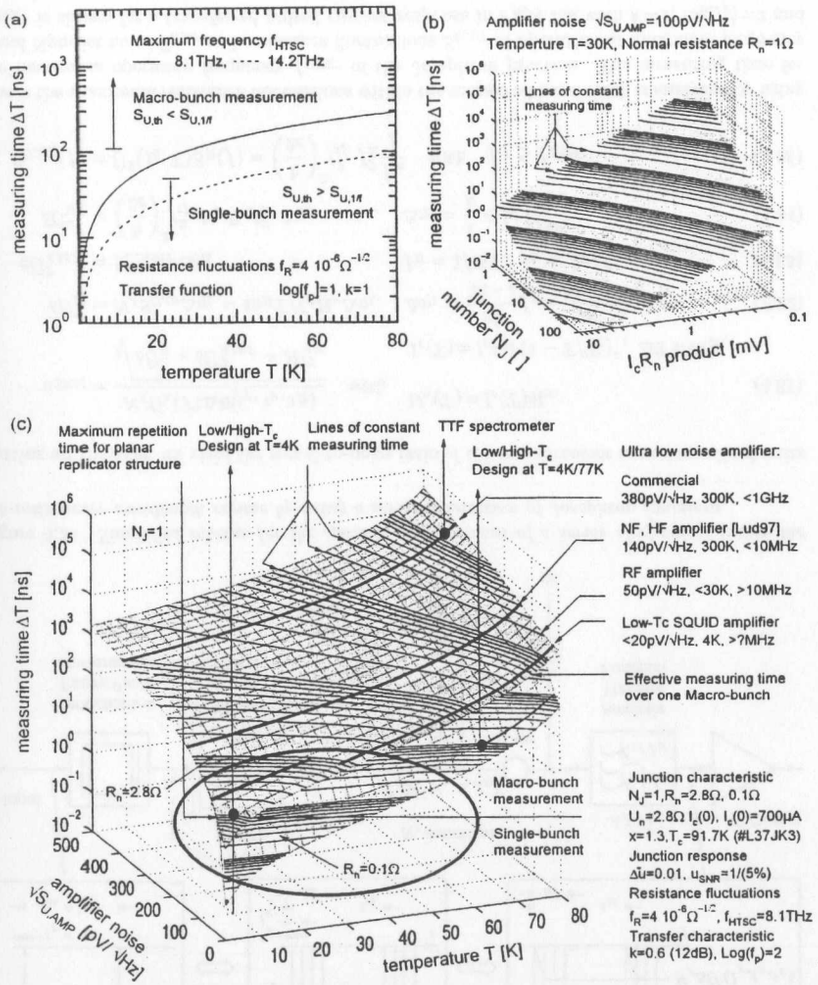

Figure 4.25: *(a) Measuring time in dependence of operating temperature for maximum operating frequencies f_{HTSC} for equal noise contributions from Nyquist noise and resistance fluctuations. Measuring time in dependence (b) of junction number and I_cR_n-product and (c) temperature and noise from voltage pickup for different resistances and amplifiers. The rf-pulse replication limits the measuring time to approximately $\Delta T < 10ns \ldots 100ns$ for a single-bunch operation with well defined reflections, marked by a circle in Fig.4.25c. A fast low-T_c SQUID amplifier pickup is also possible when using a high-T_c Josephson junction with small normal-state resistance R_n.*

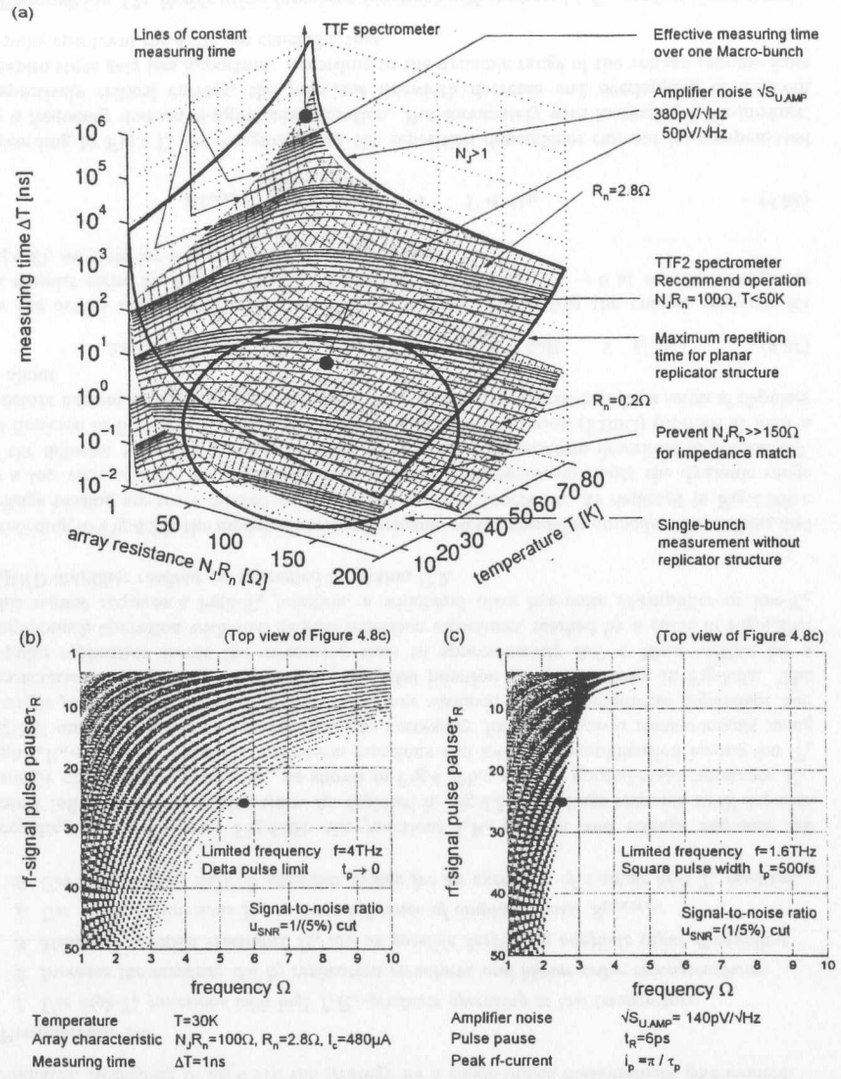

Figure 4.26: *(a) Measuring time in dependence of operating temperature and junction resistance N_JR_n for different resistances and amplifiers. Current response in dependence of pulse pause and freqeuncy for a signal-to-noise ratio of a series of rf-pulses (b) fin the delta pulse limit and (b) finite width. If parameters not listed they are same as in Fig.4.25c.*

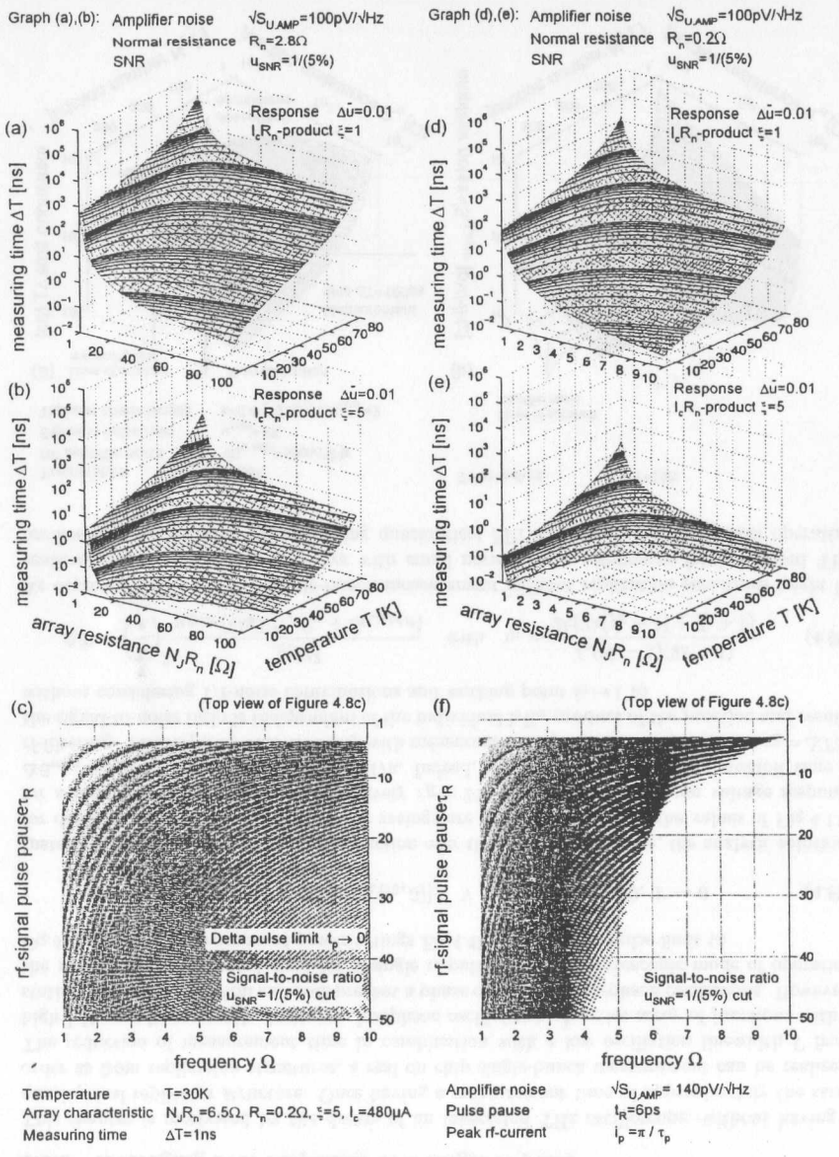

Figure 4.27: *(a),(b),(d),(e) Measuring time for junction types with increased I_cR_n-product, characterized by the parameter ξ. The curves are lines of constant measuring time. Dynamic range of the current response for the (c) delta pulse limit and (f) rf-pulse spectrum.*

The I_cR_n-product of bicrystal junctions have been increased recently by a misorientation of their crystal orientations based on $SrTiO_3$ substrates by a factor of $3 \ldots 5$ [Div02b]. As shown in Fig.4.27, this effect is taken into account by the replacement of critical current $I_c(0) \rightarrow \xi I_c(0)$ characterized by the parameter ξ. Despite using this additional gain of the voltage response from junctions with intrinsically increased I_cR_n-product, the dynamic range of an rf-pulse driven junction is limited and requires a frequency domain rf-signal compensation, as depicted in Fig.4.27f. Fig.4.28 shows the stochastical solution of the voltage response of a compensated rf-pulse driven series array. In accordance with Fig.4.26c lower normal-state resistances increase the signal-to-noise ratio.

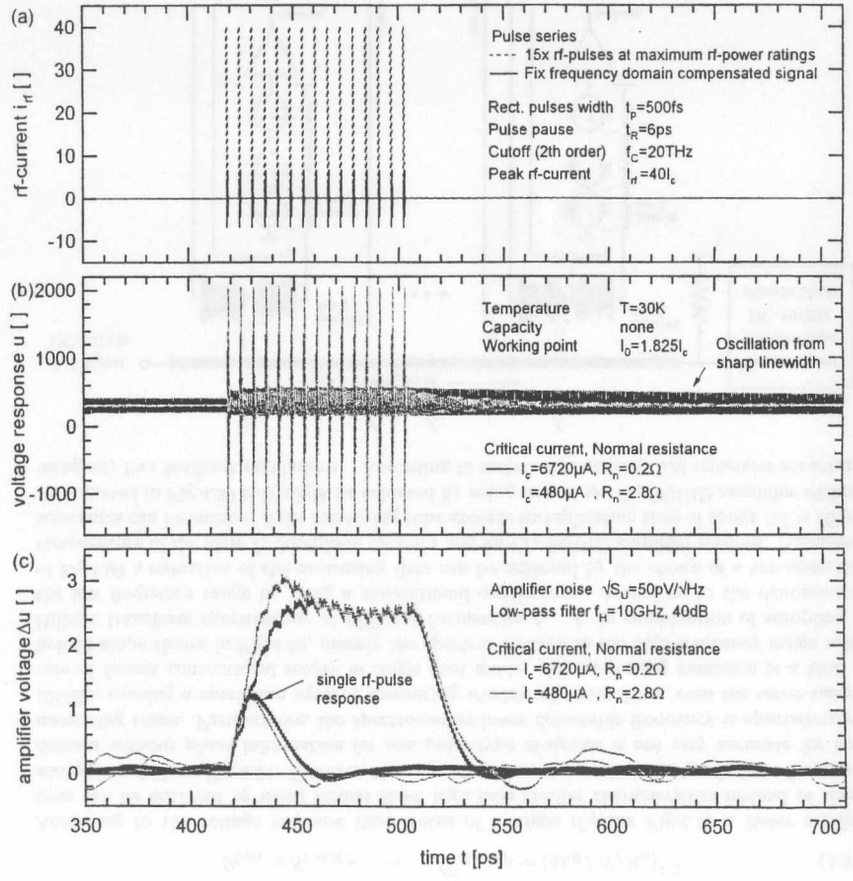

Figure 4.28: *Runge-Kutta simulated response of a second order low-pass compensated filtered (a) rf-pulse series and single rf-pulse with its (b) voltage response for $N = 200$ decoupled Josephson junctions. Figure (c) shows the amplifier filtered responses.*

4.6.2 Averaging over responses of a single rf-pulse

This chapter is motivated by the dream of an integrated THz oscilloscope, without having a quasioptical replicator structure. Once having a measurement time of approximately the same order as from replication structures, a real on chip single-bunch measurement can be realized. The reduction of measurement time in combination with a low oscillation linewidth Γ from high I_cR_n-products reveals dominant Josephson oscillations. A series array of junctions with a statistical spread of critical currents prevent a phase coupling of Josephson oscillations. However, the minimum measurement time for a single rf-pulse for the spectroscopic mode of operation Eq.4.42 results at maximum rf-power ratings Eq.4.43 for the delta pulse limit to

$$\Delta\bar{u}_{max} = \frac{2}{\tau_B}\frac{1}{i_0}\,2\pi\mathrm{Im}[c_1(i_0,0)], \quad \forall \quad i_p\tau_p = \pi,\ \tau_p \to 0,\ \Gamma \to 0 \tag{4.89}$$

Instead of showing a spectrum reconstruction over the full spectral range, the analytic solutions for dense spectra at maximum rf-power ratings are assumed. Inserting the values of Fig.4.17a for a repetition time $t_R = 6ps$, respectively $\tau_R = 24$, we yield the maximum voltage response $\Delta\bar{u}_{max} \approx 0.01$ in accordance with Fig.4.17a. Indeed, the measuring time is the prohibit time of rf-filtering. The response falls inversely with measurement time. After sampling time $\tau_B = \Delta T\omega_c$ the signal-to-noise ratio is *independent* of the individual I_cR_n-product of the junction and results without considering 1/f-noise contributions and working point $i_0 \to 1$ to

$$\Delta T = \left(\frac{\hbar}{e}\right)^2 \frac{\eta_1 N_J^2}{u_{SNR}\,(4k_bTN_JR_n + S_{U,AMP})} \quad \text{with} \quad \eta_1 = \frac{f_p(2k-1)(2k+1)}{2k(2k(f_p-1)+f_p+1)}. \tag{4.90}$$

As depicted in Fig.4.29a, a single-bunch measurement without replication structures might be realized using junction series arrays with small normal-state resistances for integrated THz oscilloscope applications without using quasioptical FPI structures. Once decided operating

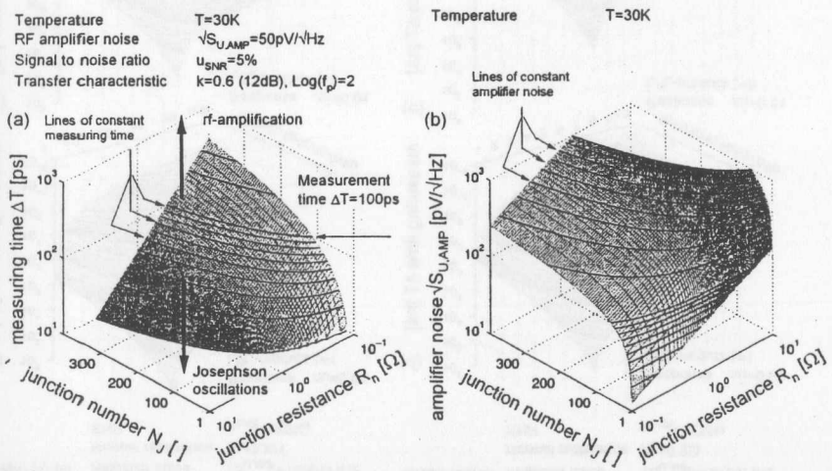

Figure 4.29: *(a) Measuring time in dependence of number of junctions and normal-state resistance for a single rf-pulse at maximum rf-power ratings according to Eq.4.90. (b) Amplifier noise according to Eq.4.91.*

with series junction arrays Fig.4.29b the noise from normal-state resistance should be at least equal the amplifiers noise for a specified operation temperature.

$$S_{U,th} \approx S_{U,AMP} \quad \rightarrow \quad \sqrt{S}_{U,AMP} = (4k_BTN_JR_n)^{1/2} \tag{4.91}$$

According to the voltage response time traces of a single rf-pulse Fig.4.13 a faster settling time can be achieved by using second order high-pass rf-filter characteristics instead of sharp waveguide rf-filters Fig.4.31. However, the reconstruction of time domain signals from frequency domain without phase information for non pulse-type rf-signals is not very accurate for long measuring times. Furthermore, the spectrometers lower detectable frequency is approximately 10GHz, causing a maximum squared measuring window of about 10ps, even the same sample rate of fastest conventional scopes in single shot mode. An interesting extension is a kind of hybrid scope shown in Fig.4.30, namely the spectral analysis in the high frequency range using Hilbert transform spectroscopy at different frequencies $f_1 \ldots f_n$ in combination of sampling in the low frequency range by using a conventional oscilloscope. According to the denominator of Eq.4.90 a reduction of the measuring time can be achieved by the choice of a low operation temperature of the high-T_c Josephson detector and low-T_c SQUID amplifier readout. Replicator structures can be omitted if the measuring time exceeds its replication time of about $\Delta T = 100ps$. As depicted in Fig.4.30 this might be achieved by using several low-T_c SQUID amplifier without using any flux feedback regulations. According to section 6.1, quasioptical replicator structures

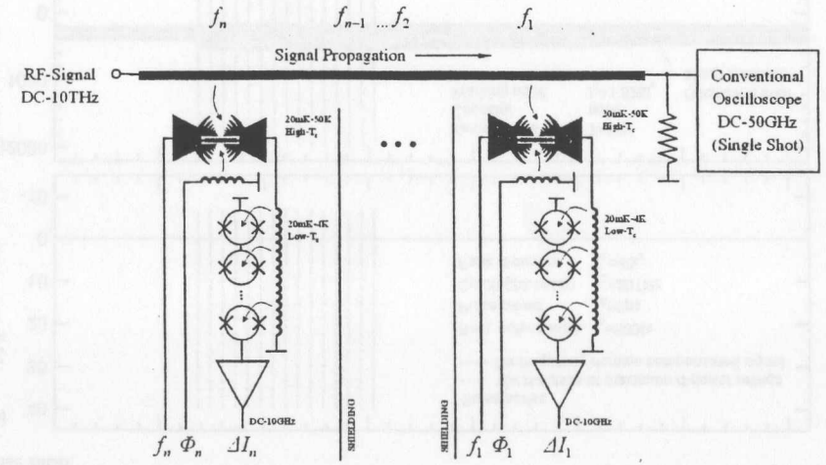

Figure 4.30: *Simplified sketch of an integrated scope for THz signals using a fast SQUID readout.*

consisting of meshes providing a sufficient reflectivity operate up to frequencies of about 4THz, as depicted in Fig.6.1c. According to the I-V-characteristic shown in Fig.5.25, a single pulse measurement far above this frequency without any replication structure might be achieved by using a single high-T_c Josephson junction operating at low temperture and the readout concept of Fig.4.30. As depicted in Fig.4.32, the replacement of Bow-Tie type LC-filter circuit part from LP-antenna by transmission line structures according to Fig.5.17, converts an LP-antenna to a Yagi structure biased by Lecher lines. Now reflections of rf-pulses at mismatched antenna ends occur and the signal-to-noise ratio can be increased. For the current pickup planar rf-transformers [Keh01, AppRF] or a SQUID amplifier can be used. The resolution in the frequency

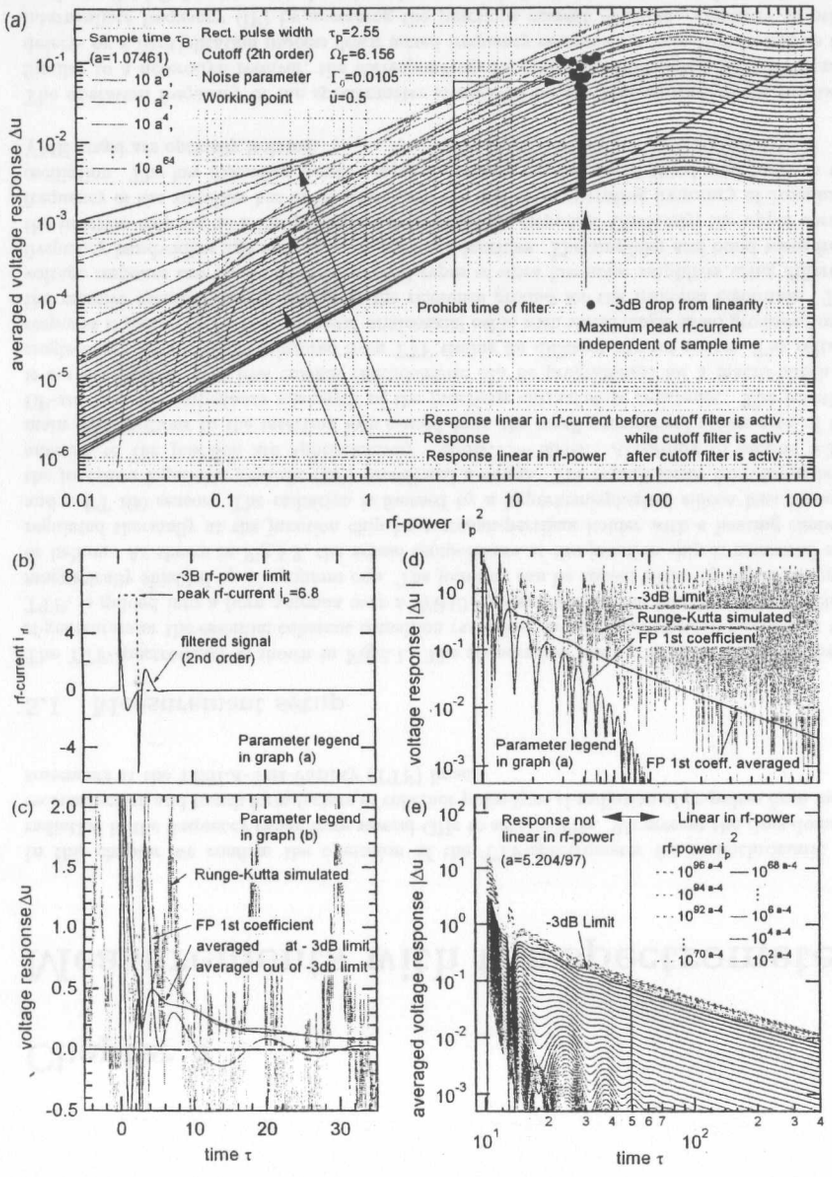

Figure 4.31: *(a) Voltage response in dependence of peak rf-power for a (b) single rf-pulse at different sample times τ_B. (c),(d),(e) Voltage and averaged response deduced from Runge-Kutta method with noise and 1st FP coefficient $c_1(\tau)$ in and out of the -3db rf-power limit.*

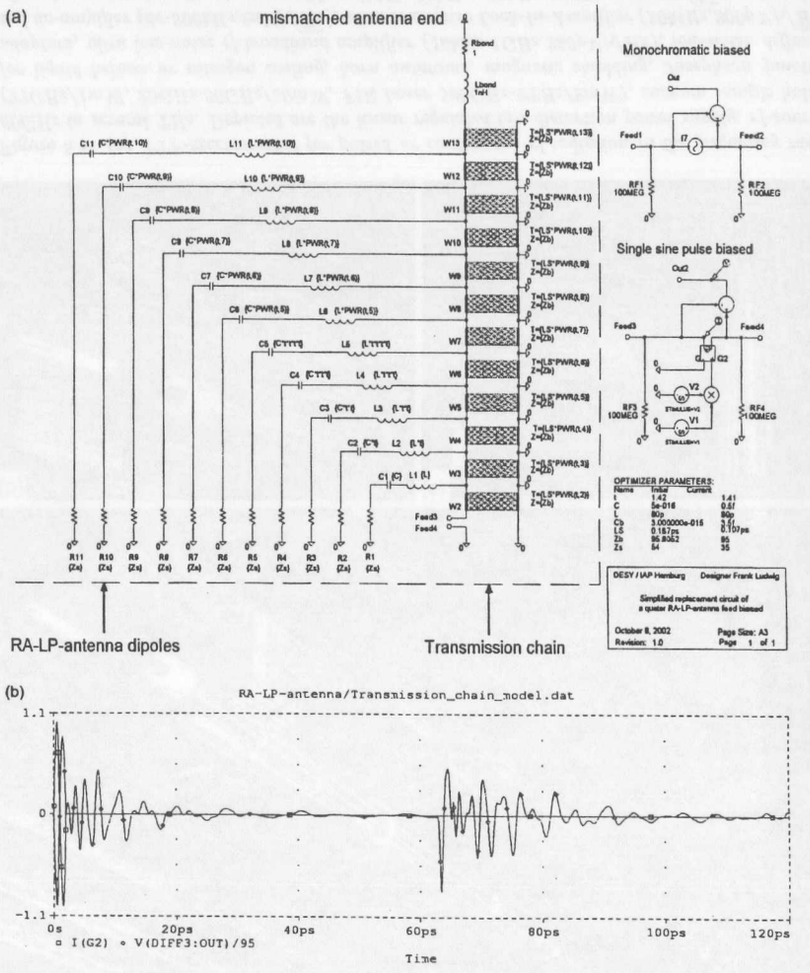

Figure 4.32: *(a) Simplified replacement circuit of an RA-LP-antenna from Fig.5.17 to describe pulse propagation along its dimension including reflections at mismatched antenna ends by using a Yagi structure and Lecher transmission line. (b) PSPICE simulated time response.*

domain is limited by the number of junction arrays. Therefore the time domain rf-signal has to be chopped either by the propagation of the signal by using shielding elements or high-T_c switches by using microbridges under laser irradiation for a successful phase reconstruction. The interesting question of a reliable time reconstruction for arbitrary signals depending on their frequency intersection range of the n windowed detector channels has to be answered.

Chapter 5

Measurements with the spectrometer

In this chapter we confirm the operation of the TTF-spectrometer for monochromatic rf-radiation in the frequency range from several GHz to several THz. We present the time domain reconstruction and bunch form factors of coherent pulse-type rf-radiation of ps-pulses from measurements at the TESLA-Test-Facility (TTF) linac.

5.1 Measurement setup

The TTF-spectrometer is shown in Fig.5.1. The rf-radiation from a far-infrared (FIR) laser, rf-generators or the essential coherent transition radiation, caused from electron bunches at the TTF, is guided into a horn antenna over a WR10 waveguide onto the junction chip, which is magnetically shielded by a cryoperm cup. The junction can be cooled either by liquid nitrogen or helium. As shown in Fig.5.2, the actual temperature at the junction chip is measured and regulated thermally at the junction chip by a stenan-pertinax holder with a heating element and a PT-100 sensor. The radiation is focused by a hyperhemispherical silicon lens through the junctions logarithic periodic (LP) broadband antenna. The overall losses from input horn antenna to the junction are approximately $-50\text{dB}\ldots-60\text{dB}$. According to section 5.3.3, main contributions to the insertion loss caused from the small geometrical active area of the LP-antenna and impedance mismatch of the junctions normal-state resistance. The junction is current biased. The bias current characteristic can be programmed for a macro-bunch or single-bunch measurement triggered from TTF timing for different current ranges. The voltage response is picked up by non magnetic minicoaxial cable with shield single sided grounded onto the massive metallic chassis acting as the reference ground for the frontend electronic. The voltage response can be detected by several types of ultra low-noise amplifiers using different frequency bandwidths and voltage noise spectral densities. The amplifier and bond wires from the junction chip act as a low-pass filter to average the response. Obviously, the upper corner frequency of the amplifier has to be lower than the minimum operating frequency of Josephson oscillation. The low distortion power supply is linearly regulated and the digital ports to the VME crayd are optically isolated.

The operation frequency of the spectrometer is selected by the bias current of the junction. Similar to a heterodyn receiver, the corresponding, so called local oscillator (LO) frequency, detects by a multiplication process down mixed frequency components from rf-radiation as the intermediate frequency (IF) by averaging the junctions current response. Contrary to other methods, the LO frequency can be selected over a wide frequency range very fast without any channelization using different LO sources. The junction implies a voltage-controlled-oscillator as an LO source with multiplier, which gets nonlinear for sufficient high input rf-power.

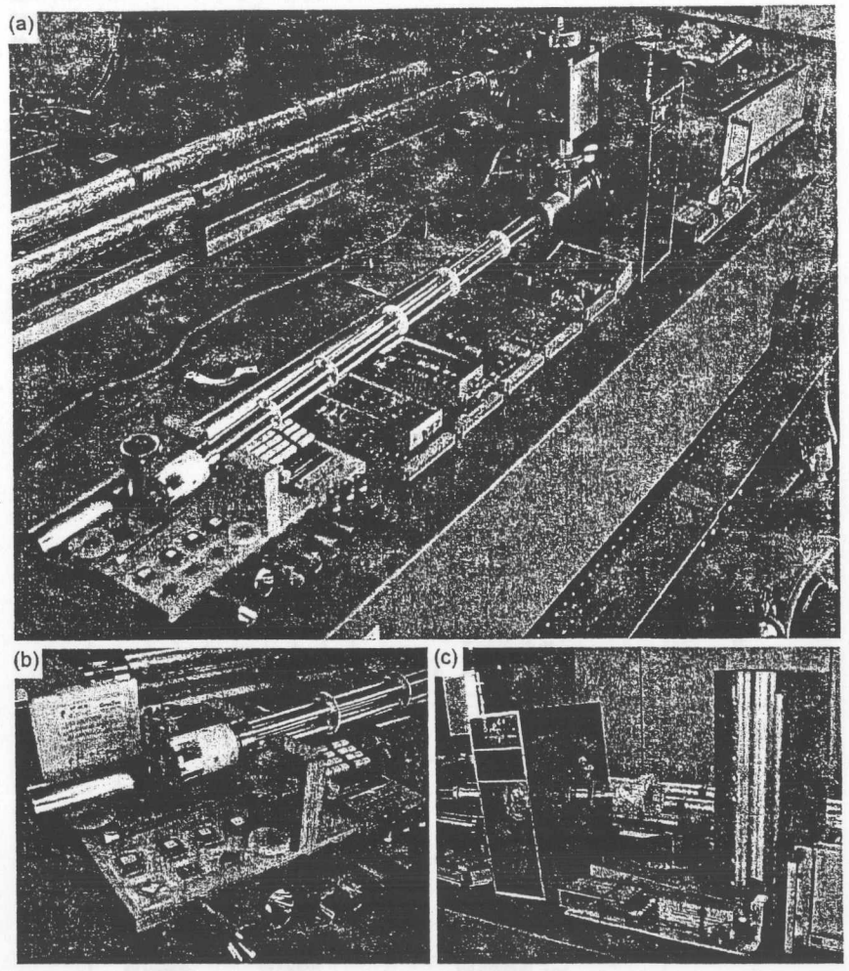

Figure 5.1: *(a) TTF-spectrometer for pulsed or continuous rf-radiation in the frequency range 60GHz to several THz. Depicted are the linear regulated low distortion power supply, rf-sources (77GHz/1mW, 20GHz-60GHz/10mW, FIR Laser 500GHz-2THz/2mW), vacuum sample holder for liquid helium or nitrogen cooling, horn antennas, magnetic shielding, Josephson junction adapters, ultra low-noise rf-broadband amplifier (10kHz-1GHz,380pV/$\sqrt{Hz}$), low-noise differential dc-amplfier (dc-500kHz,2nV/$\sqrt{Hz}$), ultra low-noise Lock-In-Amplifier (10MHz,300pV/$\sqrt{Hz}$), ultra low-noise broadband ac-amplifier (10Hz-20kHz, 10kHz-10MHz,140pV/$\sqrt{Hz}$), ultra low-noise high speed bunch timing matched current source (16Bit resolution, 500kHz, MR 10μA,100μA,1mA,10mA), digital timing adapter and optocoupled isolation for VME crayds. (b) View of the sample holder and (c) rf-input coupling system.*

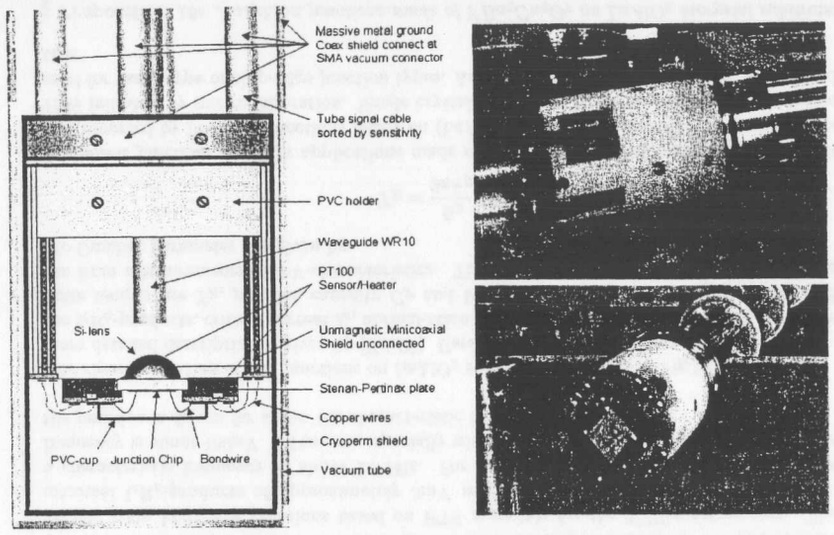

Figure 5.2: *Sketch and picture of the sample holder. The rf-radiation is guided into a horn antenna, coupled to a waveguide onto a hyperhemisphere silicon lens to the junctions LP-antenna. The insertion power loss of the radiation input coupling system is discussed in section 5.3.3.*

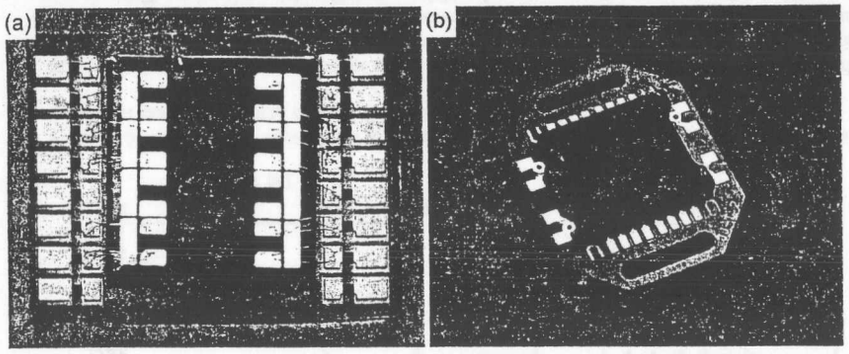

Figure 5.3: *(a) Top view of a chip with four Josephson junctions including LP-antenna bonded in a four-point measurement geometry. (b) Boxed chip. The regulation of the chip temperature is realized by the heat flow from heater to sensor over a sandwiched stenax-pertinax plate.*

5.2 Preparation, substrate material and characterization

The preparation process of Josephson junctions made of high-T_c (HTS) superconductor materials like $YBa_2Cu_3O_7$ is meanwhile a standard process at our institute. We pointed out, that the

Josephson junctions $\#L37$, $\#L40$ operated at the TTF-spectrometer based on $LaAlO_3$ bicrystal substrates and the series-array $\#L45$ with more than 200 Josephson junctions, worked successfully since its first preparation cycle. The Josephson junctions were made on newly introduced $LaAlO_3$ bicrystal substrates with $YBa_2Cu_3O_7$-layers of about 80-160nm thickness and junction widths between 3-6μm for varying critical current I_c and normal-state resistance R_n. The preparation process consists of laser-deposition of $YBa_2Cu_3O_7$ on the substrate, conventional photolithographic structuring and argon-ion etching in a parallel plate reactor as described in detail in [Hei97]. The substrate material have to fulfill several items.

- *To grow $YBa_2Cu_3O_7$ films epitactically in c-axis direction, the lattice constants of the substrate material nearly have to concide with the a- and b-axis of the superconductor $YBa_2Cu_3O_7$.*
- *To prevent thermal twisting during operation and preparation process, the thermal expansion coefficients of the substrate material and $YBa_2Cu_3O_7$ films must be nearly equal.*
- *For THz applications the dielectric constant ε_r and loss coefficient $\tan\delta$ of the substrate in the appropriate frequency range should be small.*

Fig.5.4 shows the temperature dependent dielectric constant and loss coefficient $\tan\delta$ of some substrate materials. According to Fig.5.5 the loss coefficient increases rapidly with increasing frequency.

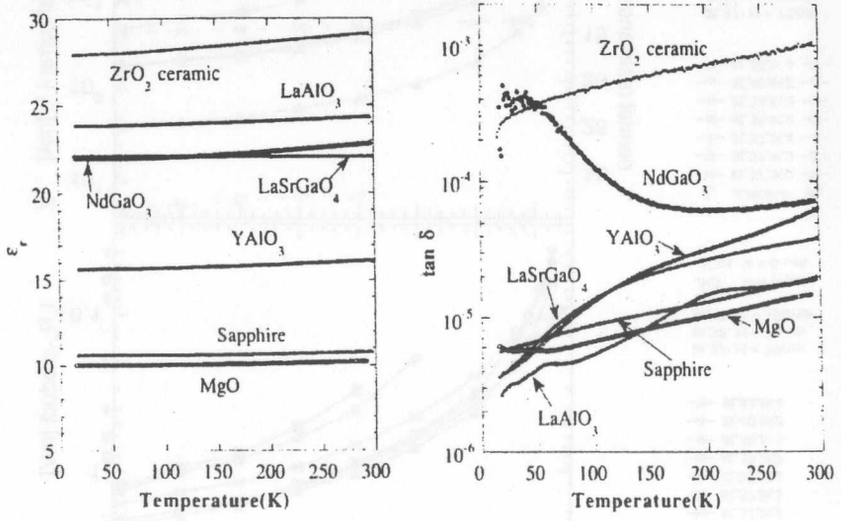

Figure 5.4: *Temperature dependence of dielectric constant ε_r and loss coefficient $\tan\delta$ for different substrate materials from [She94].*

The lattice mismatch from sapphire (Al_2O_3) requires buffer layers between substrate and film of strontium titanate ($SrTiO_3$), magnesium oxide (MgO) or lanthanum aluminate ($LaAlO_3$). The quality of layers is not very satisfying [Phi96]. Silicon reacts chemically with $YBa_2Cu_3O_7$

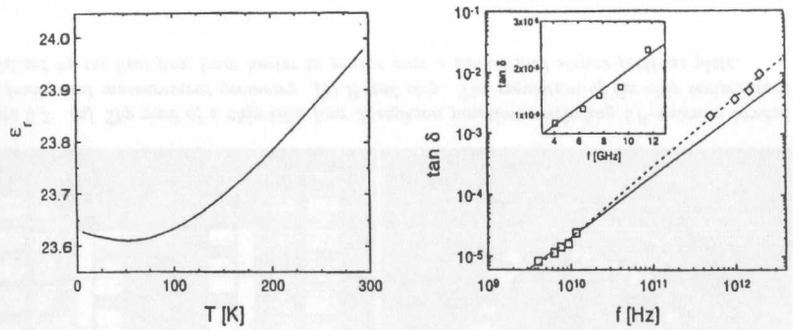

Figure 5.5: *Temperature dependence of dielectric constant ε_r and frequency dependence of loss coefficient* $\tan\delta$ *for* $LaAlO_3$ *crystals from [Zuc97].*

and buffer layers like yttria stabilized zirconia (YSZ) or ceriumoxide (CeO_2) films are required. The intensively investigated substrate material strontiumtitanate ($SrTiO_3$) with $\varepsilon_r = 277$ is not very suitable for high frequency applications with low available rf-power. This concerns not the TTF application with sufficient available rf-power according to section 5.3.3. Whereas neodymiumgalate ($NdGaO_3$), magnesium oxide (MgO) [Che97] and lanthanum aluminate ($LaAlO_3$) are lattice matched and show suitable dielectric coefficients with low losses [Phi96].

Due to the relatively reliable fabrication and excellent RCSJ-performance of I-V-characteristic we use grain boundary junctions based on HTS materials for the TTF-spectrometer. Their maximal I_cR_n-products of approximately 3mV in the low temperature operation results to a characteristic frequency of about 1.5THz. For liquid nitrogen operation the characteristic frequency is about 180μV. Of course, especially when using a frequency rf-signal compensation, the junction is driven far above the characteristic frequency.

The characterization of our junctions on $LaAlO_3$ substrates is shown in Fig.5.6 and Fig.5.7. A more detailed description is given by [Käs00]. Here we focus on the temperature dependence of the I_cR_n-products, critical current I_c, normal-state resistance R_n, noise parameter Γ_0, equivalent noise temperture T_R, junction capacity C_F and McCumber parameter β_c derived from RCSJ fits from measurements of I-V-characteristics. The definitions for the noise temperature and Mc-Cumber parameter are given by

$$T_R = \frac{\Phi_0}{2\pi k_B} I_c \Gamma_0. \tag{5.1}$$

Josephson junctions for THz applications made of MgO bicrystal substrates are investigated and reported by [Vol00]. Junctions based on ($LaAlO_3$) bicrystal substrates are available since 1999 initiated by our collaboration. Single crystal substrates based on $LaAlO_3$ are intensively used for ramp-type or step-edge junction types. According to the following paper, we conclude, that

Proposition 18: *Josephson junctions made of* $YBa_2Cu_3O_7$ *on* $LaAlO_3$ *bicrystal substrates show RCSJ-like I-V-characteristics in a wide temperature range and are well suited for high frequency applications at least up to several THz by using Hilbert transform spectroscopy.*

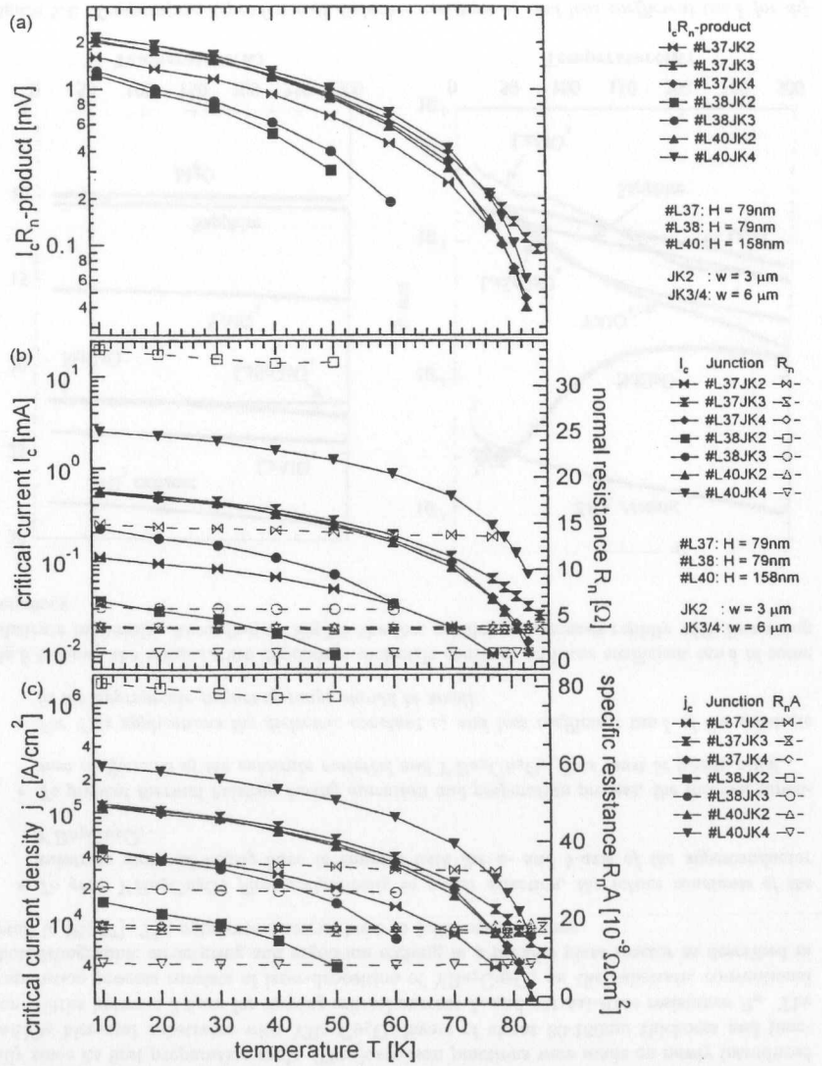

Figure 5.6: *Temperature dependence of (a) I_cR_n-product, (b) critical current, normal-state resistance and (c) critical current density, specific resistance for different bicrystal junction.*

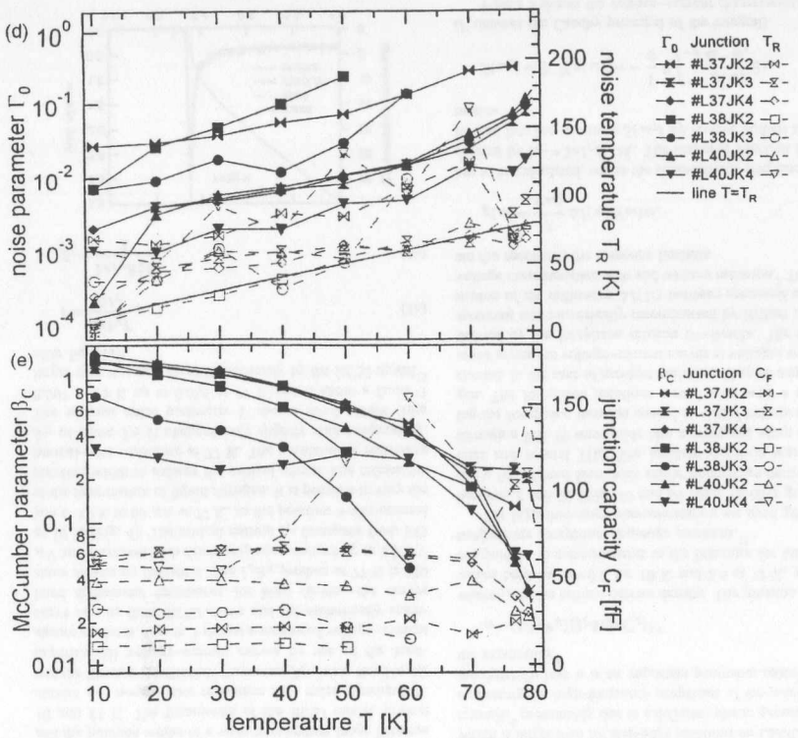

Figure 5.7: *Temperature dependence of (a) noise parameter, noise temperature and (b) McCumber parameter, junction capacity.*

APPLIED PHYSICS LETTERS VOLUME 77, NUMBER 19 6 NOVEMBER 2000

$YBa_2Cu_3O_7$ Josephson junctions on $LaAlO_3$ bicrystals for terahertz-frequency applications

A. Kaestner, M. Volk, F. Ludwig, and M. Schilling[a)]
Institut für Angewandte Physik und Zentrum für Mikrostrukturforschung, Universität Hamburg, Jungiusstraße 11, 20355 Hamburg, Germany

J. Menzel
Deutsches–Elektronen–Synchrotron DESY, Notkestraße 85, 22603 Hamburg, Germany

(Received 30 May 2000; accepted for publication 7 September 2000)

We prepared Josephson junctions made of $YBa_2Cu_3O_7$ on symmetric 24° $LaAlO_3$ bicrystal substrates. For better coupling of high-frequency radiation, we structured the contacts with logarithmic-periodic antennas made of $YBa_2Cu_3O_7$. Characterization was done by measuring the voltage–current characteristics to determine the critical current I_C, the normal-state resistance R_N, the noise parameter Γ, and the Stewart–McCumber parameter β_C as predicted by the resistively and capactively shunted junction model (RCSJ). The junctions showed excellent RCSJ-like behavior with I_CR_N products of up to 2.0 mV at 10 K and 220 μV at 77 K. To demonstrate the possibility to detect high-frequency radiation up to the THz regime, we used the Josephson junction as a detector for radiation from a far-infrared laser and we reconstructed the spectra by Hilbert spectroscopy. © *2000 American Institute of Physics.* [S0003-6951(00)00945-1]

Josephson junctions made of $YBa_2Cu_3O_7$ can be used for high-frequency applications, especially for the realization of mixers and detectors in the frequency domain between 100 GHz and several THz. Therefore, it is necessary to have junctions with adequate properties on suitable substrates. At this time, grain-boundary junctions are commonly used on various substrate materials like $SrTiO_3$,[1] $NdGaO_3$,[2] Si,[3] and MgO.[4] The substrate materials should show low high-frequency losses and a good epitaxial growth of $YBa_2Cu_3O_7$ films.[5] $SrTiO_3$—as state of the art material for superconducting quantum interference devices—is not suitable for high-frequency applications because of its high losses in this frequency range, Si can only be used with buffer layers to grow epitaxial $YBa_2Cu_3O_7$ films.[5] MgO is hydroscopic and $Mg(OH)_2$ is formed in contact with water vapor,[6,7] while $NdGaO_3$ bicrystals are difficult to obtain.

We present results for the bicrystal substrate material $LaAlO_3$, which is well known as a single-crystal substrate for high-quality ramp-edge[8] and step-edge[9] Josephson junctions. $LaAlO_3$ shows low-loss tangents $\tan\delta$ of 5×10^{-6} (Ref. 10) at 8.6 GHz and 77 K, compared to 6×10^{-2} for $SrTiO_3$ and 3×10^{-4} for $NdGaO_3$ (Ref. 5) at 77 K and 5 GHz, and 10^{-4} (Ref. 10) at 100 GHz and 77 K, increasing to 10^{-2} at 3 THz and room temperature.[11] The low relative permittivity ϵ_r of about 24 is almost temperature independent between several kelvin and room temperature and the lowest reststrahl frequency is observed at about 5.5 THz,[10] so usage of $LaAlO_3$ substrates should be possible up to this frequency. We investigated properties of Josephson junctions made of $YBa_2Cu_3O_7$ on this material, such as the resistively and capacitively shunted junction-like (RCSJ) voltage–current curves, temperature dependence of the RCSJ parameters, and functionality at 77 K. We show its suitability for high-frequency applications by detecting radiation up to 1.2 THz with a single Josephson junction using Hilbert spectroscopy.[2]

The Josephson junctions were made on $LaAlO_3$ bicrystal substrates[12] with $YBa_2Cu_3O_7$ layers of about 80–160 nm height and junction widths between 3 and 6 μm to vary critical current I_C and normal-state resistance R_N. We prepared the junctions with logarithmic-periodic antennas to improve coupling of high-frequency radiation[13] into the junction (Fig. 1). The preparation process consisted of laser deposition of $YBa_2Cu_3O_7$ on the substrate, conventional photolithographic structuring, and argon-ion etching in a parallel-plate reactor as described in detail before.[14] The $LaAlO_3$ bicrystal substrates showed no difficulties in the preparation process and the standard parameters for single-crystal preparation could be used.

To characterize the RCSJ behavior of the junctions, we measured the voltage–current characteristics and the differ-

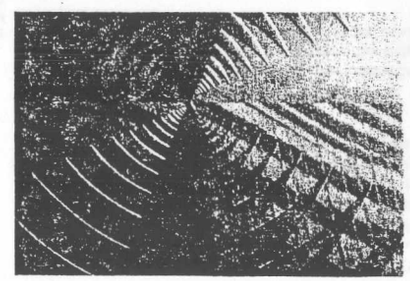

FIG. 1. Phase contrast micrograph of a Josephson junction with a logarithmic-periodic antenna on a $LaAlO_3$ bicrystal substrate, the horizontal grain boundary in the middle of the picture and the twin boundaries in $LaAlO_3$ are clearly seen.

a)Electronic mail: schilling@physnet.uni-hamburg.de

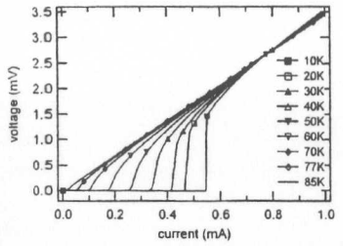

FIG. 2. Current–voltage characteristics of the Josephson junction sample L37 on a 24° $LaAlO_3$ bicrystal with a junction width of 6 μm and a thickness of the $YBa_2Cu_3O_7$ film of 80 nm.

ential resistance dU/dI by lock-in technique in a temperature range between 10 and 85 K. Figure 2 shows the voltage–current characteristics of a Josephson junction on a $LaAlO_3$ bicrystal substrate. The characteristics are RCSJ-like and the junction works in a wide temperature range between 10 and 85 K. The parameters of the RCSJ model, critical current I_C, normal-state resistance R_N, noise parameter Γ, and the Stewart–McCumber parameter β_C, were fitted to the experimental voltage–current curves by use of the least-square methods. Figure 3 shows a measured voltage–current curve and its fitted RCSJ curve and the numerically calculated differential resistances for both curves—the curves show almost no deviation. The I_CR_N product at 77 K is 220 μV and increases with decreasing temperatures up to 2.0 mV at 10 K (Fig. 4). The critical current I_C decreases from 545 μA at 10 K to 63 μA at 77 K, so the junction works optimal at the temperature of liquid nitrogen. It is possible to vary the junction width to enlarge the critical current and reduce the normal-state resistance at 77 K. The normal-state resistance R_N of about 3.6 Ω changes only slightly with temperature. The internal noise parameter Γ shows fitted values from 0.001 at 10 K up to 0.065 at 77 K and is about a factor 2 larger than that calculated theoretically by the RCSJ model[15] after Eq. (1a):

$$\Gamma=\frac{2ek_BT}{\hbar I_C}, \tag{1a}$$

$$\beta_C=\frac{2eI_CR_N^2C}{\hbar}, \tag{1b}$$

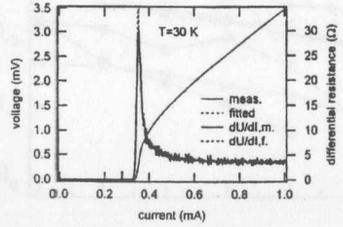

FIG. 3. Fitted voltage–current curves of sample L37 at 30 K, as well as the differential resistances with the corresponding fitted data.

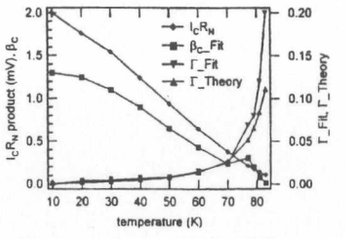

FIG. 4. Fitted I_CR_N products, noise parameter Γ, and Stewart–McCumber parameter β_C of sample L37 at temperatures between 10 and 85 K.

similar to the excess noise observed in other groups.[16] The Stewart–McCumber parameter β_C,[17] calculated by Eq. (1b), ranges between 1.3 at 10 K and 0.2 at 77 K and results in a capacitance of the junction of about 64 ± 3 fF. Therefore, the shunting capacitance per unit area is $C_A=133\pm6$ fF/μm^2, which is larger than for step-edge junctions on $LaAlO_3$ single crystals,[9] presumably due to a different planar geometry. For evaluating the high-frequency properties of the junction, the quasiparticle loss α is an important parameter calculated by the expression[18]

$$\alpha=(1/I_CR_N)(j_C\hbar/2eC_A)^{1/2}, \tag{2}$$

where j_C is the critical current density. The junction showed values between $\alpha=0.8$ for 10 K and 2.6 at 77 K, which is comparable to measurements in the literature for long high-temperature Josephson step-edge junctions.[18]

For high-frequency characterization we used generators between 2 and 20 GHz, 40 and 60 GHz, 76 GHz generator, and a far-infrared laser with single frequencies between 584 GHz and several THz. The incident radiation was guided through a WR-10 waveguide into a cryogenic setup containing the Josephson junction cooled by liquid helium or nitrogen. The Josephson junctions were biased with a constant current. In the case of incident radiation, Shapiro steps occur in the measured voltage–current curves at voltages which are defined by the Josephson relation $U=\hbar\omega/2e$. The incident spectrum was numerically reconstructed by Hilbert transformation of the difference $\Delta I(U)$ between measured current–voltage characteristics with and without radiation.[2] To evaluate the spectrum, the response function

$$g(\omega)=\frac{4}{\pi\omega_C^2}\Delta I(\omega)I(\omega)\omega, \tag{3}$$

has to be calculated, where the characteristic frequency ω_C is defined by $\omega_C=2eI_CR_N/\hbar$. The response function is transformed into the spectrum $S(\omega_S)$ by inverse Hilbert transformation

$$S(\omega_S)=H^{-1}[g(\omega)]=-\frac{1}{\pi}P\int_{-\infty}^{+\infty}\frac{g(\omega)}{\omega-\omega_s}d\omega \tag{4}$$

(P denotes the Cauchy principal of the integral).

Figure 5 shows the voltage–current characteristics $U(I)$ with and without radiation from the far-infrared (FIR) laser at 762 GHz ($\lambda=393$ μm) and the reconstructed spectrum of the laser intensity by Hilbert spectroscopy. The peak in the

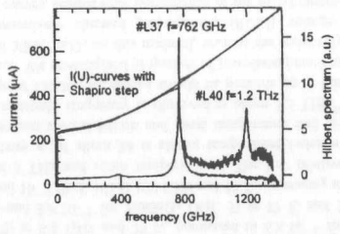

FIG. 5. Measured $I(U)$ curves of the Josephson junction sample L37 at 62 K with and without radiation from a FIR laser at 762 GHz($\lambda=393$ μm) and $P_{FIR}=2.1$ mW. The reconstructed Hilbert spectrum shows a peak at 762 GHz with a linewidth of $\Delta f_{FWHM}=10$ GHz, which is caused by intrinsic thermal noise of the normal-state resistance of the Josephson junction. Also shown is a spectrum at 1.2 THz ($\lambda=251$ μm) for sample L40 at 5 K and $P_{FIR}=0.1$ mW, $S(\upsilon_F)$ with offset and 20 × magnified.

spectrum has a center frequency of 762 GHz with a full width at half maximum (FWHM) linewidth of 11 GHz. It fits well with the theoretical linewidth due to the internal noise of the junction of 10 GHz, which is calculated by[2]

$$\Delta f_{FWHM}=4\pi\left(\frac{2e}{h}\right)^2k_BT\frac{R_d^2}{R_N}\left(1+\frac{I_C^2}{2I^2}\right), \tag{5}$$

where R_d is the differential resistance $R_d=dU/dI$. The resolution ratio is, therefore, 0.013 in the frequency domain at 762 GHz while the noise equivalent power (NEP) is about 7×10^{-14} W/$\sqrt{Hz}$ at 62 K and 762 GHz, which is in accordance with other measurements.[3,19] The linewidth and NEP can be reduced if junctions at lower temperatures or with lower normal-state resistances R_N are used. Also shown in Fig. 5 is our latest measurement at 10 K of a 1.2 THz line of the far-infrared laser detected by a $LaAlO_3$ bicrystal Josephson junction. The linewidth is about 25 GHz while the response is about a factor 20 reduced compared to the 762 GHz measurement with 2.1 mW laser power, which is due to reduced laser power of 0.1 mW at 1.2 THz.

In conclusion, Josephson junctions made of $YBa_2Cu_3O_7$ on $LaAlO_3$ bicrystal substrates show promising properties for high-frequency applications. They can be prepared with standard techniques and show RCSJ-like voltage–current characteristics. They work at temperatures between 10 and 85 K and show I_CR_N products up to 2.0 mV at 10 K. We demonstrated the detection of far-infrared radiation up to 1.2 THz by a single Josephson junction and reconstructed the incident spectrum by Hilbert spectroscopy. Therefore, $LaAlO_3$ bicrystal substrates could become the standard substrate for high-frequency applications with single Josephson junctions at least up to frequencies of 1 THz.

For financial support and interests for their work, the authors thank the Direktorium of the Deutsches–Elektronen–Synchrotron (DESY). Furthermore, the authors thank the CRYSTEC corporation for supplying the $LaAlO_3$ bicrystal substrates.

[1] D. Winkler, Y. M. Zhang, P. A. Nilsson, E. A. Stepantsov, and T. Claeson, Phys. Rev. Lett. **72**, 1260 (1994).
[2] Y. Y. Divin, H. Schulz, U. Poppe, N. Klein and K. Urban, and V. V. Pavlovskii, Appl. Phys. Lett. **68**, 1561 (1996).
[3] J. Chen, E. Kobayashi, K. Nakajima, and T. Yamashita, IEEE Trans. Appl. Supercond. **9**, 4479 (1999).
[4] J. Chen, H. Myoren, K. Nakajima and T. Yamashita, Appl. Phys. Lett. **71**, 707 (1997).
[5] J. Philips, J. Appl. Phys. **79**, 1829 (1996).
[6] W. Langel and M. Parrinello, Phys. Rev. Lett. **73**, 504 (1994).
[7] C. Girardet, P. N. M. Hoang, A. Marmier, and S. Picaud, Phys. Rev. B **57**, 11931 (1998).
[8] Q. X. Jia, F. Yan, C. Mombourquette, and D. Reagor, Appl. Phys. Lett. **72**, 3068 (1998).
[9] H. R. Yi, D. Winkler, and T. Claeson, Appl. Phys. Lett. **66**, 1677 (1995).
[10] C. Zuccaro, M. Winter, N. Klein, and K. Urban, J. Appl. Phys. **82**, 5695 (1997).
[11] D. Grischkowsky and S. Keiding, Appl. Phys. Lett. **57**, 1055 (1990).
[12] The bicrystal substrates were supplied by CrysTec GmbH, Köpenicker Str. 325, D-12555 Berlin, FAX: +49-30 6576 2808.
[13] D. Terpstra, A. J. H. M. Rijnders, F. J. G. Roesthuis, D. H. A. Blank, G. J. Gerritsma, and H. Rogalla, JALCOM **195**, 719 (1993).
[14] J.-K. Heinsohn, D. Reimer, A. Richter, K.-O. Subke, and M. Schilling, Physica C **299**, 99 (1998).
[15] K. K. Likharev, *Dynamics of Josephson Junctions and Circuits* (Gordon and Breach, Amsterdam, 1986).
[16] D. Koelle, R. Kleiner, F. Ludwig, E. Dantsker, and J. Clarke, Rev. Mod. Phys. **71**, 631 (1999).
[17] W. C. Stewart, Appl. Phys. Lett. **12**, 277 (1968); D. E. McCumber, J. Appl. Phys. **39**, 3113 (1968); **39**, 2503 (1968).
[18] Y. M. Zhang, D. Winkler, P. A. Nilsson, and T. Claeson, Phys. Rev. B **51**, 8684 (1995).
[19] M. A. Tarasov, A. Y. Shulman, G. V. Prokopenko, V. P. Koshelets, O. Y. Polyanski, I. L. Lapitskaya, and A. Vystavkin, and E. L. Kosarev, IEEE Trans. Appl. Supercond. **5**, 2686 (1995).

5.3 Characterization of the rf-input coupling system

In this section the rf-guiding transfer function of the rf-input coupling system of the TTF-spectrometer is investigated by simulations and measurements. To simpify the radiation characteristic of the waveguide, the integrated broadband antenna and reflections within the sample holder of the spectrometer are considered.

5.3.1 Logarithmic periodic antenna structures

Antennas provide a well defined coupling to incident rf-radiation. A receiver antenna converts the free propagating electromagnetic wave into an rf-current i_{rf} for the Josephson junction and has to match the vacuum impedance $Z_0 = 377\Omega$ to the junctions normal-state resistance $R_n = 0.1 \ldots 30\Omega$. The antenna acts as a load (emitter antenna) or generator (receiver antenna) and can be described by a frequency dependent complex impedance Z. The reciprocal theorem states, that the impedance for an operation of the antenna as an emitter or receiver is equal [Zin86]. To receive coherent transition radiation over a wide frequency range from 10GHz to several THz a broadband antenna is recommended.

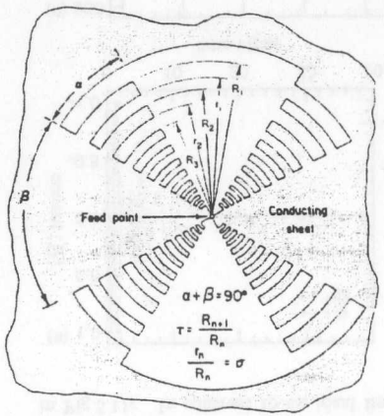

Figure 5.8: *LP-antenna structure to [Duh57].*

A broadband antenna Fig.5.8 is characterized by a constant impedance over a wide frequency range. If the geometry of the broadband antenna is scaled and the wavelength is scaled by the same factor, all properties of the antenna (impedance, polarisation, emitting characteristic...) remain equal. This scaling principle results directly from the Maxwell Equations for dielectrics and conductors without loss and leads to logarithmic periodic antennas (LP-antennas). The LP-antenna features a geometric property, namely a change of scaling maps its form onto itself. In other words, if the infinite antenna structure is described exclusively by angles, their emitting characteristic is equal for all frequencies [Gun92]. This construction scheme of an LP-antenna shows some limitations in practice.

- *The finite size of the antenna breaks the ideal logarithmic-periodic property. The finite antenna size should not significantly change the electric antenna properties. To fulfill this for a fixed wavelength, the current distribution of the infinite LP-antenna has to fall at least with r^{-1} from the feed point [Rum66].*

- *The LP-structure leads to a periodic impedance dependence on the wavelength with periodicity τ. To minimize the impedance change planar antennas must be self complementary. The interchange of the conductor surface with the non-conductor surface and vice versa, leads with an appropriate rotation, to the original antenna. The impedance of such self complementary antenna is given with the vacuum impedance Z_0 by [Rum66]*

$$Z = Z_0/2 = 189\Omega \quad \text{with} \quad Z_0 = \sqrt{\mu_0/\varepsilon_0}. \tag{5.2}$$

Obviously, the upper and lower cutoff frequency of the LP-antenna are limited by the largest and smallest antenna structures. For frequencies above the upper cutoff frequency the antenna should have dipole characteristics. As depicted in Fig.5.9 several antenna geometries, namely the right-angled logarithm periodic antenna (RA-LP-antenna), rounded logarithm periodic antenna (BD-LP-antenna) and the Bow-Tie type antenna are investigated. Now calculations of the frequency

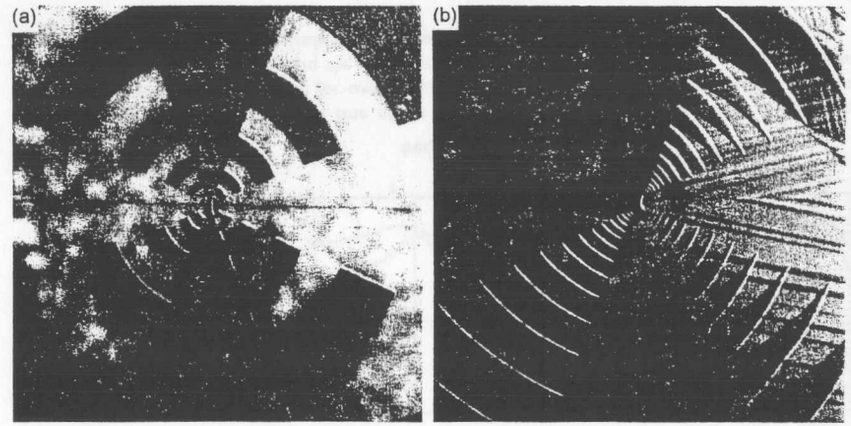

Figure 5.9: *Phase contrast micrograph of Josephson junctions with (a) RA-LP-antenna and (b) BD-LP-antenna on MgO, respectively $LaAlO_3$ substrate material. The grain boundary is visible as a horizontal line in the middle of the Josephson junction. The Josephson junction width is $3\mu m$ for the RA-LP-antenna and $2\mu m$ for the BD-LP-antenna.*

dependent impedance of a RA-LP-antenna using MAFIA (MAxwell's equations using the Finite Integration Algorithm) are presented. Here we follow the more detailed report of [Vol00]. MAFIA solves the Maxwell's equations by the method of finite integration [Wei84, Maf98]. According to Fig.5.10a, the antenna has to be meshed on a lattice of cell size Δx, Δy, Δz smaller

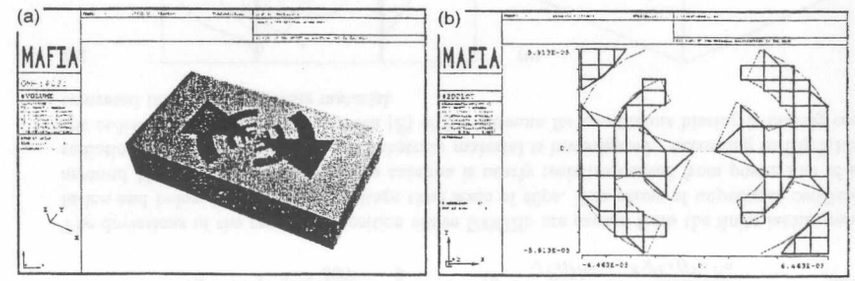

Figure 5.10: *(a) RA-LP-antenna meshed on a lattice by MAFIA. The dimensions of the underlying substrate is 4.1mm×2.3mm×1mm. (b) Zoomed inner part of the current biasing part of the antenna. An ideal conductor for the antenna, isotrop dielectric of substrate material $LaAlO_3$ with $\varepsilon_r = 23$, a single sine pulsed current source and open boundary conditions are assumed.*

than 1/4 the considered wavelength. As depicted in Fig.5.10b, substrate material, antenna properties, electric sources and boundary conditions have to be set for MAFIA's solver. Due to the reciprocal theorem of antennas, the antenna is simulated as an emitting antenna biased by a pulsed current source at their inner ports Fig.5.10b . They act at the same time for the voltage measurement. The antenna impedance is determined by the bias current $I(t)$ and the calculated voltage $U(t)$. Their complex Fourier transforms $\hat{I}(f) = |\hat{I}|e^{i\varphi_I(f)}$, $\hat{U}(f) = |\hat{U}|e^{i\varphi_U(f)}$ define the amplitude and phase of the antenna impedance.

$$|Z(f)| = \frac{\hat{U}}{\hat{I}}, \quad \varphi_Z(f) = \varphi_U(f) - \varphi_I(f) \tag{5.3}$$

Fig.5.11a,b shows the bias current and the simulated voltage time trace of the LP-antenna, respectively its Fourier transforms. The corresponding antenna impedance Eq.5.3 is depicted in Fig.5.11c. In contrast to an ideal frequency independent self complementary LP-antenna,

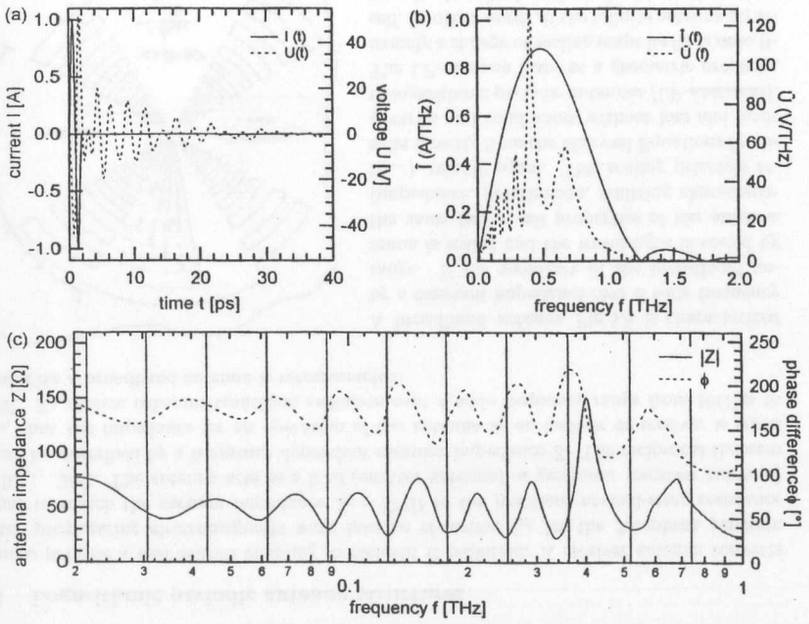

Figure 5.11: *(a) Bias current and simulated voltage time trace of the LP-antenna on $LaAlO_3$ substrate, (b) respectively its Fourier transforms. The vertical lines define the geometric resonance frequencies f_n from Eq.5.4.*

the simulated antenna shows maxima and minima of the impedance. As depicted in Fig.5.11c, the impedance minima can be interpreted by the antennas geometry in the frequency range 50GHz-500GHz. For this we assume, that the antenna effectively emits radiation at a half of the radiation wavelength λ_n from the circular arc u_n with the effective substrate ε_{eff} given by

$$u_n = 2\pi\sqrt{r_n R_n}\,\frac{90°}{360°} = \frac{\lambda_n}{2} \quad \rightarrow \quad f_n = \frac{c}{\sqrt{\varepsilon_{eff}}\lambda_n} = \frac{c}{\pi\sqrt{\varepsilon_{eff} r_n R_n}}. \tag{5.4}$$

The deviations of the resonance position above 500GHz are caused from the finite lattice resolution and below from the finite voltage time scale of 40ps. The phase of impedance oscillates arround 180 degree and therefore the antenna is nearly resistive caused from power loss of irradiation. Now the influence of the substrate material is investigated. According to Fig.5.12a, the radiated electric field distribution $|\vec{E}|$ of the antenna for continuous biasing is mainly concentrated inside the substrate material.

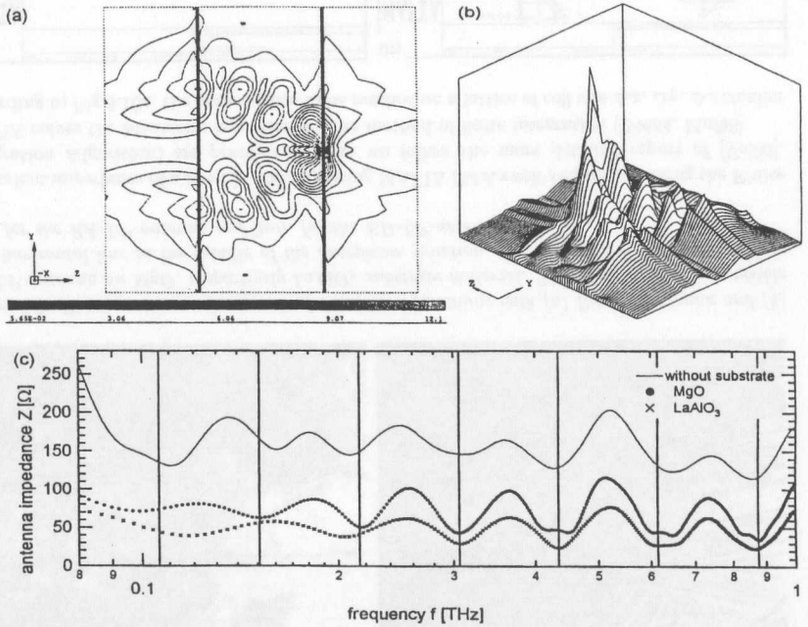

Figure 5.12: *(a) Equipotential line of the (b) electric field distribution shown in Y-Z-plane perpendicular to the substrate for continuously biasing. The substrates are marked by gray lines and the antenna is located on the right surface. (c) LP-antenna impedance without substrate material and different substrate materials with $\varepsilon_{LaAlO_3} = 23$, $\varepsilon_{MgO} = 9.6$.*

The LP-antenna impedance for different substrate materials is shown in Fig.5.12c. The measurements of the LP-antennas self resonances according to section 5.3.2 confirm the assumption, that an effective dielectric constant ε_{eff} of the substrate material can be given by the average of the antennas surrounding dielectric constants of both media.

$$\varepsilon_{eff} = \frac{\varepsilon_{substrate} + \varepsilon_{vacuum}}{2} \quad \text{with} \quad \varepsilon_{vacuum} = 1 \tag{5.5}$$

Inserting the effective dielectric constant into Eq.5.2 leads to the averaged impedance Z of an

LP-antenna with substrate by replacing $\varepsilon_0 \rightarrow \varepsilon_{eff}\varepsilon_0$.

$$Z \approx \frac{189\Omega}{\sqrt{\varepsilon_{eff}}} \tag{5.6}$$

In this MAFIA simulations the dielectric material is assumed to be lossfree. The antenna is assumed to be made of an ideal conductor of infinitesimal thickness. The surface resistance, London penetration depth and critical current of the superconductor are not considered. Furthermore, the interaction of the rf-emitting Josephson junction and antenna is not considered. However, the comparison of the interaction of self emitting radiation from Josephson junction and antenna characteristic is, according to section 5.3.2, essential in accordance with the antennas resonance positions from the simulations.

5.3.2 Josephson self resonances

In this section we show, that the system of Josephson junction and antenna is sensitive to rf-radiation at least up to the THz regime. Because of the ac-Josephson effect, the junction itself emits along its biasing ports rf-radiation. The frequency depends on the averaged voltage drop, respectively current biasing working point. The radiation coupled to the antenna transfer function and its reflected frequency dependent rf-power produces Shapiro steps on the I-V-characteristic. By sweeping the frequency at the antennas feedpoint absorption minima of mismatched antenna dipoles can be detected.

Resonance number	Resonance radius R_n [μm]	Resonance frequency f_n [GHz]	Ratio f_n/f_{n+1}	eff. dielectric constant ε_{eff}
RA-LP-antenna #$L40J2$				
1	22	753	1.42	14.8
2	31	529	1.39	15.1
3	45	380	1.41	13.9
4	64	270	1.38	13.6
5	92	195	1.44	12.6
6	130	135	1.42	13.2
7	184	95	-	13.3
			$\tau_{exp.}=1.41\pm0.02$	$\varepsilon_{eff}=13.8\pm0.8$
BD-LP-antenna #$L37J3$				
1	12.4	1390	1.13	13.6
2	13.8	1230	1.14	14.1
3	15.6	1075	1.12	14.4
4	17.3	960	1.12	14.7
5	19.6	858	1.14	14.3
6	22	751	1.12	14.8
7	25	668	1.13	14.5
8	28	590	1.13	14.8
9	32	520	1.12	14.6
10	35	465	1.13	15.3
11	40	410	1.12	15.1
12	45	367	-	14.9
			$\tau_{exp.}=1.125\pm0.009$	$\varepsilon_{eff}=14.6\pm0.4$

Table 5.1: *Measured resonance frequencies and assigned resonance branch for a RA-LP-antenna and BD-LP-antenna. The resonance frequencies of the RA-LP-antenna agrees with the geometric antenna self resonances.*

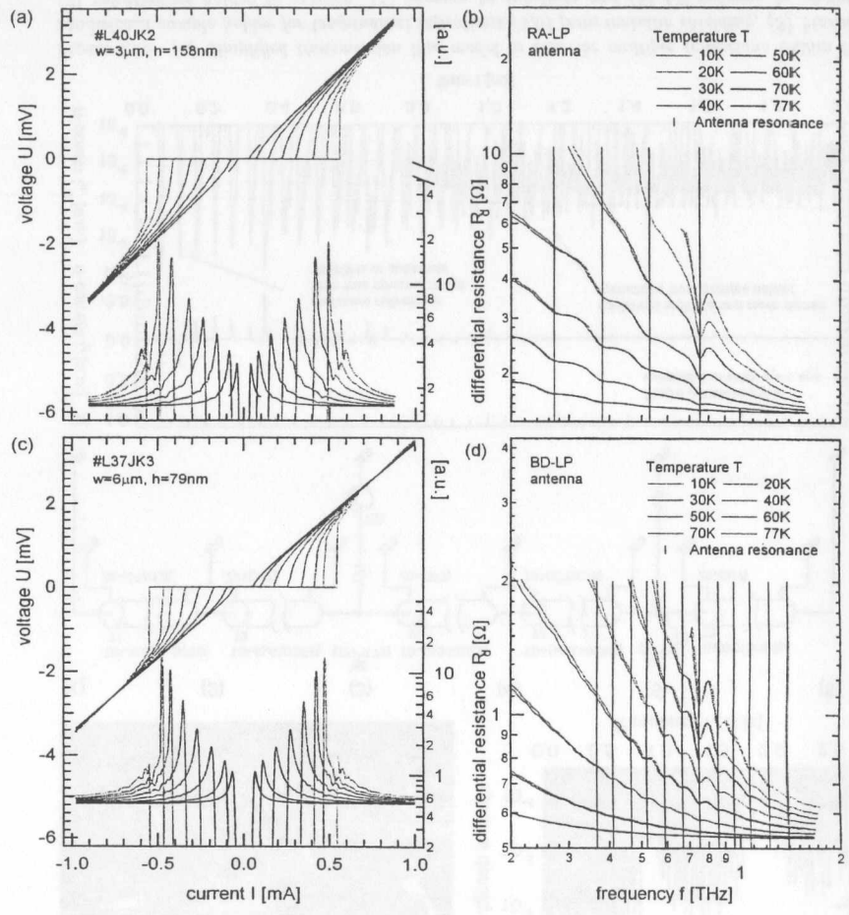

Figure 5.13: *Measured I-V-characteristics and differential resistance of a (a),(b) RA-LP-antenna and (c),(d) BD-LP-antenna for different temperatures. The measured Shapiro steps are caused from reflections of the antennas transfer function of the Josephson self oscillation radiation.*

By measuring the differential resistance R_d of the I-V-characteristic, we compare the resonance positions of the antenna with its geometric resonances Fig.5.13. Indeed, according to Eq.3.22, the induced Shapiro steps get rapidly smaller for higher frequencies. The results are listed in Tab.5.1. For the RA-LP-antenna, respectively BD-LP-antenna, we found, that the measured antenna constant $\tau_{exp.}$ deduced from the resonance frequencies agrees with the geometric antenna constant $\tau_{geo.}=1.42\pm0.01$, respectively $\tau_{geo.}=1.12\pm0.01$. The incoming electromagnetic wave is affected by an effective dielectric constant, consisting of thin $YBa_2Cu_3O_7$-layer, thick (1mm) $LaAlO_3$ bicrystal substrate and vacuum. According to Tab.5.1 the effective dielectric constant

fits quite well to the assumption Eq.5.5.

5.3.3 Waveguide radiation characteristic

Fig.5.14 summarizes roughly the losses of rf-radiation guided into the TTF-spectrometer. In fact, for an rf-power to current response converter the junctions replacement circuit has to replaced by the real equivalent circuit including its environment. Despite rf-power losses from horn antenna input coupling, waveguide, impedance mismatch from vacuum to antenna the main rf-power loss is caused by the spreaded irradiation pattern from waveguide and the geometric antenna structure having broadband characteristic. A hyperhemisphere lens should focus higher frequencies to a minimum spot size for antenna illumination up to the appropriate antenna arms. At the actual TTF-spectrometer an adjustment for optimum focus is not realized.

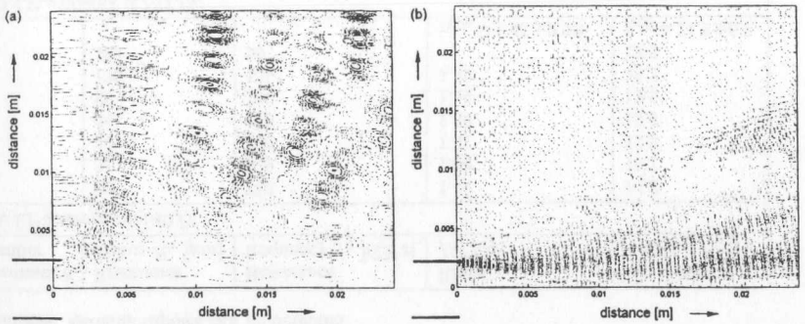

Figure 5.14: *Simulated rf-power density for monochromatic rf-radiation for (a) 76GHz and (b) 500GHz from a waveguide transition of diameter d=5mm to d=48mm for an ideal conductor [Hün01].*

Estimating roughly the effective active area of the antenna for a frequency f_n as the geometrical area of the n.th antenna arm A_n, we get the loss for an illiuminated spot A_s

$$l_a \approx \frac{A_n}{A_s} = \frac{\lambda_n}{2}\frac{\sqrt{\tau_n R_n}(\tau-1)}{A_s} = \frac{c^2(\tau-1)}{2\pi\epsilon_{eff} f_n^2 A_s} \tag{5.7}$$

Supposing a spot size of $A_s = 80\text{mm}^2$, frequency $f_n = 500\text{GHz}$ and $\tau = 1.125$ we get a loss of $l_a = -43\text{dB}$. The availabe peak rf-power of the coherent transition radiation at the TTF linac is about 10MW. As previously shown, the absolute maximum rf-power peak ratings for broadband spectroscopy are roughtly the same as for continuous rf-radiation of about -16dBm, respectively 20μW. FIR-laser measurements at a frequency of $f = 761\text{GHz}$ determine at temperture $T = 62\text{K}$ a noise equivalent power of NEP $= 7 \cdot 10^{-14}\text{W}/\sqrt{\text{Hz}}$ by a loss of -47dB and a junction power consumption of 37nW comparable to other authors [Che99, Tar95]. Therefore approximately twelve decades of rf-power are available for a frequency domain rf-signal compensation (FDSC) and pulse replication structures discussed in detail in section 6.1.

5.3.4 Reflections within the sample holder

The motivation to investigate reflections within the TTF-spectrometer is given by the fact, that our measurements of pulsed type rf-signals at the TTF linac cannot be explained without them.

We describe reflections of rf-radiation in longitudinal direction within the sandwiched sample holder by a transmission line model Fig.5.15a. The simulated response of a single rf-pulse is shown in Fig.5.15c. Dominant replication structures are caused from dielectric substrate, marked

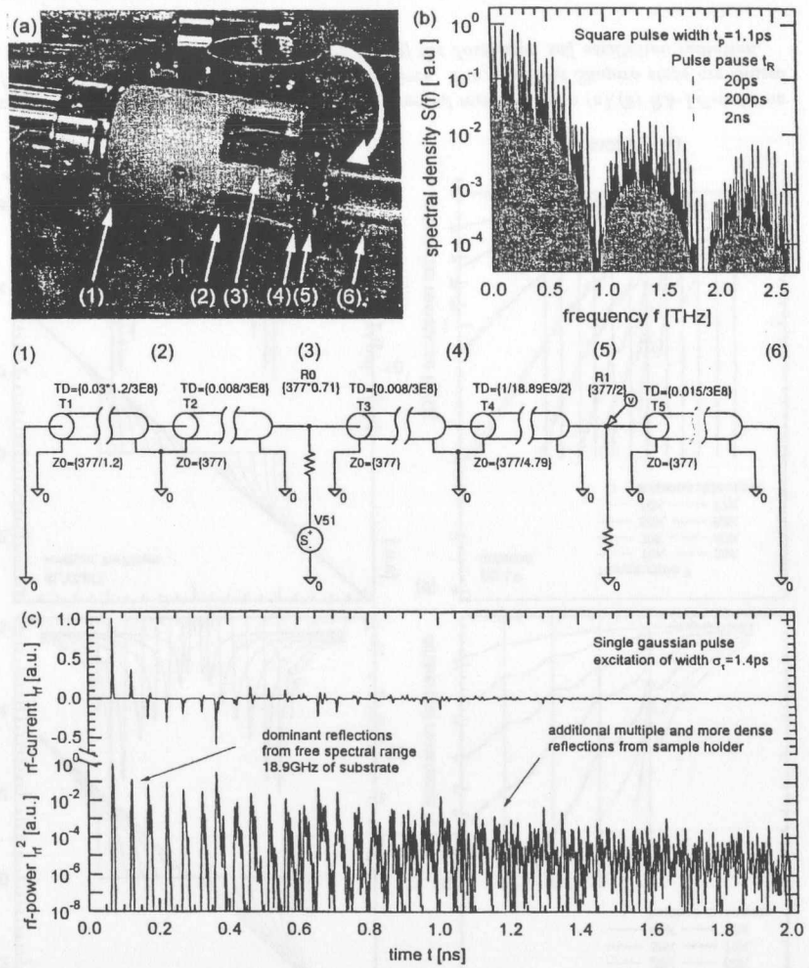

Figure 5.15: *(a) Simplified transmission line model to describe multiple reflections within the sandwiched sample holder for longitudinal reflections (1,6) from metallic shielding, (3) biasing, (2) polyethylene holder to vacuum, (4) vacuum to substrate and (5) LP-antenna to vacuum transition. (b) PSPICE simulated spectral response of an exitation for a (c) single squared rf-pulse for a long measuring time.*

by the numbers (4-5) in the figure and back scattering at metallic shielding (5-6). Screws, cables, waveguide, FR-4 plate, stenan holder and back reflections of attenuation mesh Fig.5.27d are not considered. First replications are caused from the dielectric substrate. After several round trips within the complete transmission structure multiple or quasi randomized decaying replications occur, which decrease rapidly but get more and more dense stabilizing the voltage response. The simulated spectral voltage response Fig.5.15d caused from a single squared rf-pulse exitation essentially infuence its spectrum. As long as the replication structure is a linear system the rf-pulse spectrum is maintained within the frayed spectrum for long pulse pauses, as shown in Fig.5.15b. As depicted in Fig.5.16, measurements of the spectrometers transmittance within the band [40GHz, 60GHz] confirm a high frequency selectivity. According to the measurement

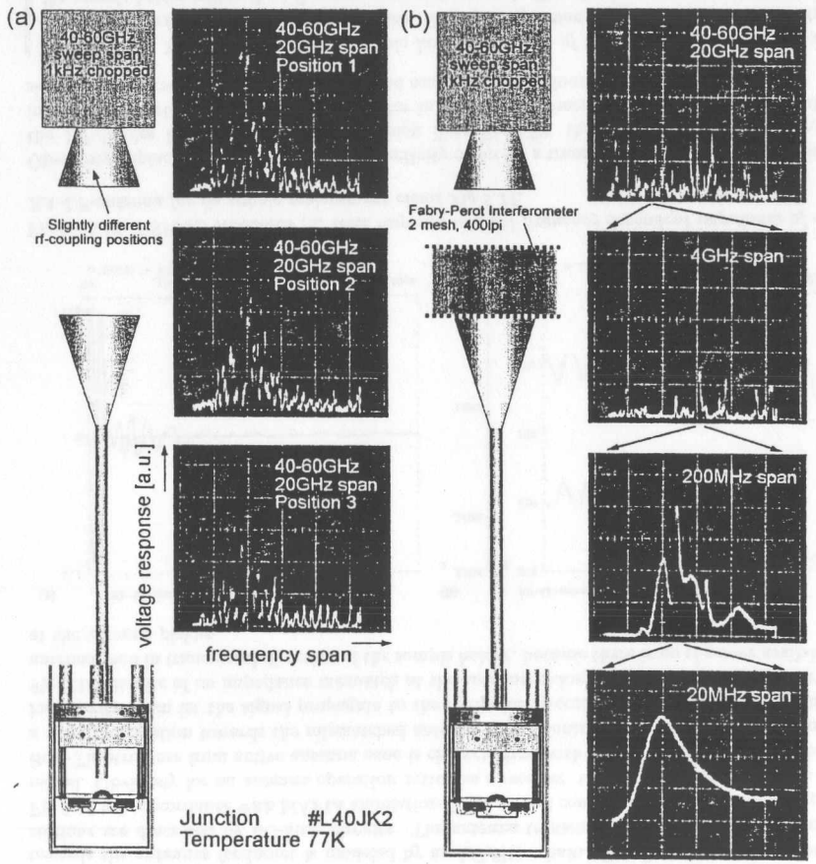

Figure 5.16: *(a) Spectral voltage response of a Josephson junction for different rf-input couplings and (b) using a two mesh Fabry-Perot interferometer within rf-guiding.*

setup Fig.5.19 we sweeped the chopped monochromatic rf-radiation frequency and analyze the junctions voltage response with a Lock-In-Amplifier. Slightly varying the rf-input coupling causes a different spectral transmittance marked by the different positions. The spectral increase near 45GHz is caused from the horn antenna gain. As shown in Fig.5.20b, inserting a two mesh Fabry-Perot interferometer (FPI) into the rf-guiding, spectral power decreases clearly between its fringe spacing. Sharp transmittance peaks indicate a high reflectivity from FPI or metallic shielding implying long replication times up to the 100ns regime. One may ask, if reflections in transversal direction occur propagating along the LP-antenna caused by impedance mismatch at the ends. To answer this, we investigate a more simple equivalent circuit of an RA-LP-antenna Fig.5.17. The antenna arms are modeled by radiation dipoles, each represented by a series LCR-circuit including an appropriate radiation impedance. The propagation of rf-power

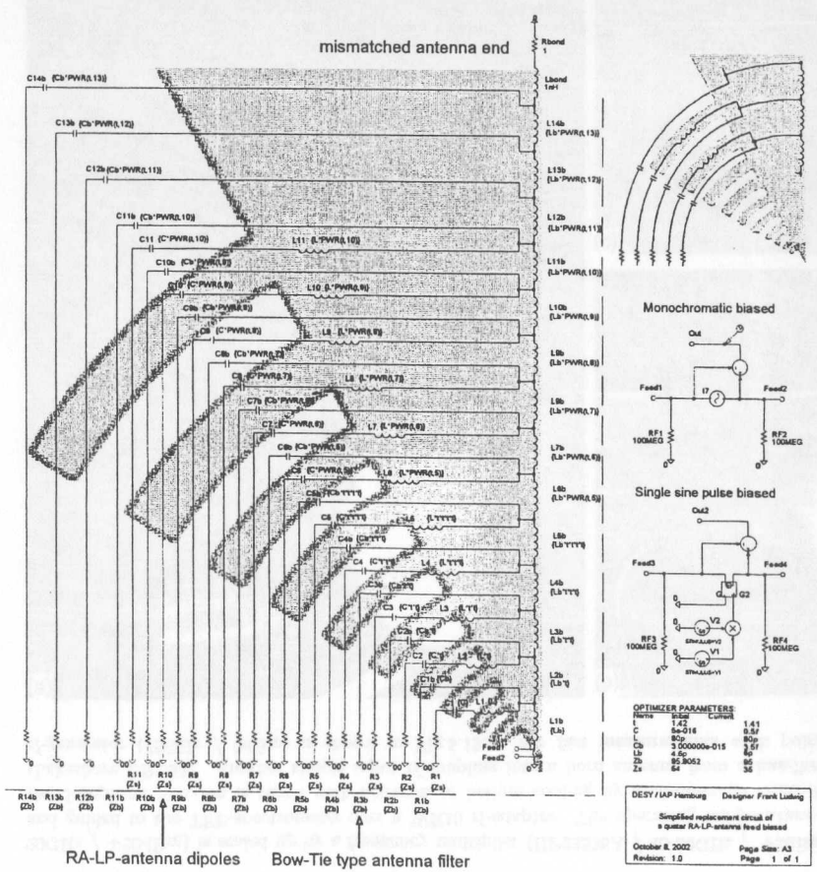

Figure 5.17: *Simplified equivalent circuit of an right-angled LP-antenna.*

towards the antennas feedpoint is modeled by an LC-filter chain. The Bow-Tie type antenna sections are described by LC-filter circuits. The antenna transmittance and rf-pulse response Fig.5.18 is in accordance with MAFIA simulations Fig.5.11 and confirm the validity of the simple model. Obviously for an antenna operation acting as a receiver, the upper inductivity chain of Bow-Tie structure from active antenna zone is characterized with higher impedances and block a wave propagation towards the mismatched antenna ends. Contrary, the inner low impedance inductivity chain let the signal propagate to the feedpoint. According to the rf-pulse response Fig.5.18, despite of an impedance mismatch at the antenna pickup, no reflections occour at the antennas end in transversal direction of the sample holder, because there is no rf-power available at the antenna pickup.

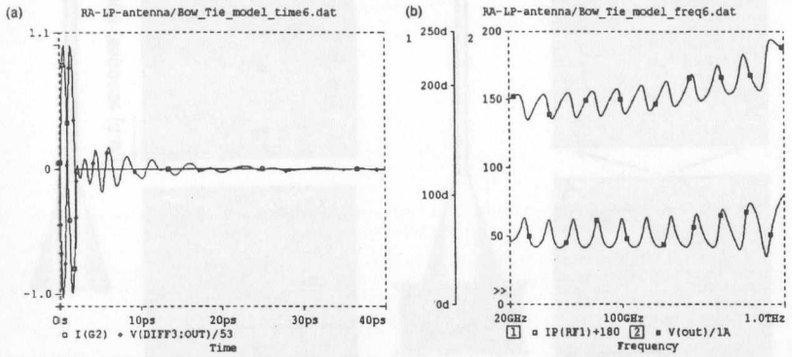

Figure 5.18: *PSPICE simulated (a) time response and (b) frequency dependent impedance of an RA-LP-antenna for its simple replacement cicuit Fig.5.17.*

Obviously, replacing the Bow-Tie type inductivity chain by a transmission structure connecting the LP-dipoles by a mircostrip transmission lines Fig.4.32, the mismatched antenna ends indeed reflects rf-power acting as a resonator in transversal direction. This might increase the signal-to-noise ratio of an intergrated hybrid scope Fig.4.30. However, we conclude

Proposition 19: *The sandwiched sample holder structure of the TTF-spectrometer show longitudinal reflections up to the ns-regime. Multiple reflections propagating transversal to the sample holder within the LP-antenna are not expected. The rf-pulse spectrum is influenced by the complicated replication structure.*

5.4 Characterization with monochromatic rf-sources

In this section we will investigate the response in the I-V-characteristic from rf-radiation at discrete frequencies from a far-infrared laser (FIR-laser) up to the THz regime. Frequency dependent measurements in the range of 40-60GHz render the possibility to investigate partly the transfer function of the TTF-spectrometer.

5.4.1 Measurements with rf-generators

Now we will investigate the response in the I-V-characteristic for lower frequencies. The measurement setup is shown in Fig.5.19a. The rf-radiation from an rf-generator (HP83624B /

20GHz / +20dBm) is scaled up by a frequency multiplier (HP83556A / 40-60GHz / +3dBm) and guided to the TFF-spectrometer over a WR10 rf-adapter. The operating temperature of the Josephson junction is tuned with nitrogen or helium cooling by a commercial controler (Lakeshore DRC93). Another simple input rf-coupling into a horn antenna from a handheld rf-generator (76GHz / 0dBm) is shown in Fig.5.19c. For fast measurements with pulsed

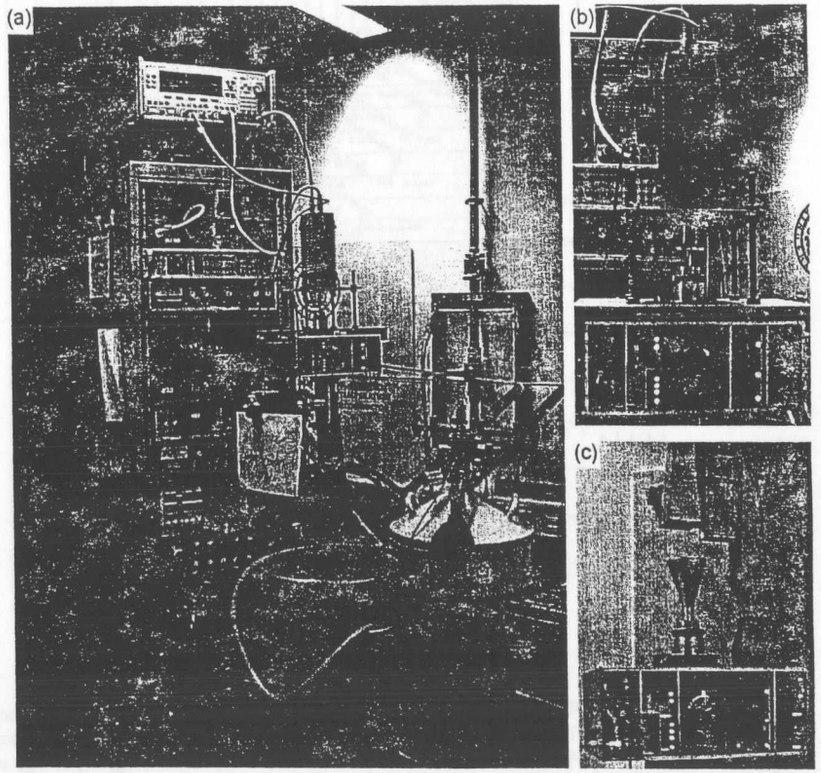

Figure 5.19: *(a), (b) Measurement setup to investigate the voltage response of chopped continuous rf-radiation of 40-60GHz with chopper frequencies up to 10MHz. The TTF-spectrometer is cooled by liquid nitrogen in a dewar. (c) Input rf-coupling into a horn antenna performed by a handheld 76GHz rf-generator.*

rf-radiation the investigation of the voltage response of the system readout Eq.A.139ff in the time domain gets important. The rf-power maximum ratings of the spectrometer and the slew rate of the whole system readout depicted in Fig.5.20b, including bondwires, strip-lines, coaxial lines, rf-amplifiers and matching can be easily investigated by using chopped monochromatic rf-radiation. Experimentally, the following adjustment procedure is recommended for having a maximum voltage response.

Proposition 20:
As depicted in Fig.5.20, by varying the rf-power for a maximum negative voltage response change at fixed bias current I_{max}, a Hilbert reconstruction with negligible higher order effects can be adjusted.

By increasing the rf-power far above this limit the Shapiro step shifts, gets asymmetric according to the unperturbated I-V-characteristic and produces a decrease of the Hilbert spectrum for lower frequencies. The voltage reponse of the spectrometer for the implemented bandlimited rf-amplifier and dc-amplifier is shown in Fig.5.20b. According to Fig.5.28, location *L3*, the TTF-spectrometer was placed in a rough electromagnetic environment for this measurement. In spite of this fact, as depicted in Fig.5.20a, the critical current of the junctions is not suppressed by external magnetic or electric fields. Fig.5.21b [1] shows some I-V-characteristics for a fixed frequency and different rf-power values. Fig.5.22 shows a Hilbert reconstruction using a junction

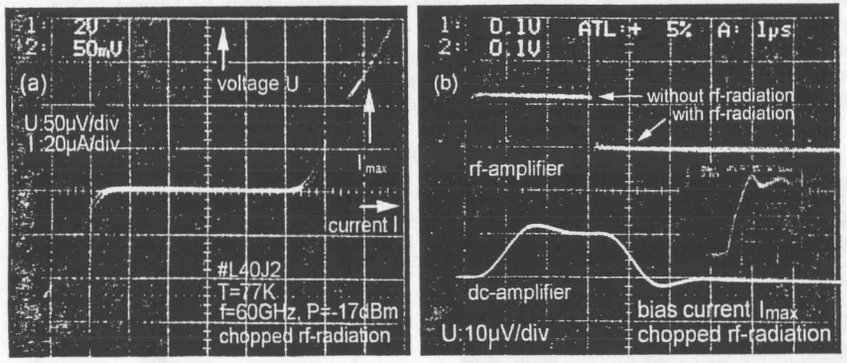

Figure 5.20: *Chopped monochromatic rf-radiation. (a) Measured I-V-characteristic and (b) time dependent voltage response for a fixed bias current I_{max} characterized by the maximum adjustable negative voltage response. The raise time from inset of the rf-amplifier is tuned to 50ns.*

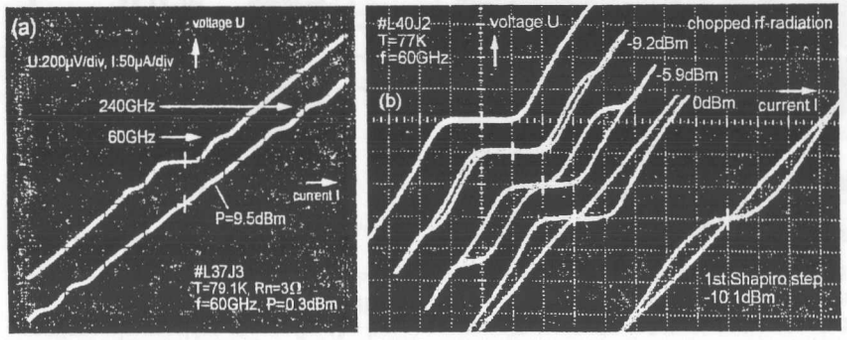

Figure 5.21: *Measured I-V-characteristic taken from oscilloscope screenshots for (a) continuous and (b) chopped monochromatic rf-radiation for fixed frequency and different rf-power.*

[1] Unfortunately the screenshots are taken from a digital scope. This causes measuring points between the radiated and unradiated I-V-characteristic from sampling during the signal raise of the junction response.

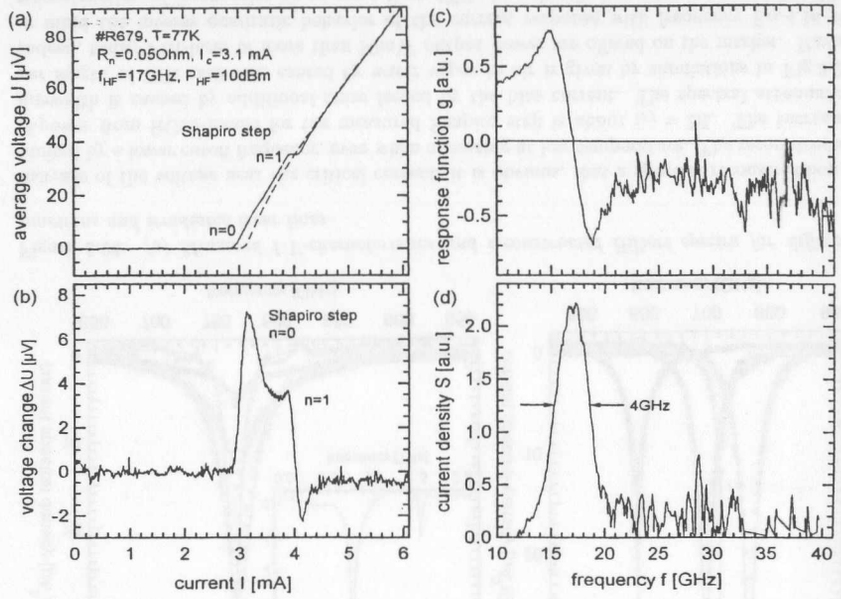

Figure 5.22: *Measured (a) I-V-characteristic (b) voltage change (c) response function and (d) reconstructed spectrum of a junction with small linewidth under monochromatic rf-radiation.*

with small normal-state resistance under monochromatic rf-radiation. Despite the small frequency sweep span of 40-60GHz, we found a maximum of sensitivity of −16.4dBm rf-power at 45GHz. As depicted in Fig.5.16 the transfer function for rf-radiation of the TTF-spectrometer is frequency selective. A quasioptical rf-input coupling system should do not have this characteristic. According to section 6.3, by using a frequency domain rf-signal compensation with sufficient dynamic range in rf-power this failure is compensated.

5.4.2 Measurements with a far-infrared laser

In this section we will show, that our spectrometer based on Josephson junctions on MgO and $LaAlO_3$-substrates operates at least up to the THz regime. A more detailed report is given in [Vol00]. Tab.5.2 lists the dominant available laser lines. Fig.5.23 shows a schematic view of the

Lasermedium	Laserline [μm]	Frequency [THz]	Wavenumber [cm^{-1}]
Methanol	119	2.5228	84
	163	1.8388	61
	251	1.1937	40
Formic acid	393	0.7616	25
	419	0.7172	24
	433	0.6930	23
	513	0.5844	19

Table 5.2: *Summary of the available dominant FIR-laserlines*

FIR-laser. The FIR-laser is an optically pumped gas laser [Hod78]. The medium for the laser is formic acid or methanol. A CO_2-Laser activates rotational- and vibrational transitions and continuously provides energy for the laser process. The variation of the wavelength of the pump laser, lasermedium and the FIR-laser resonator length leads to various discrete lines in the far-infrared spectral range. The available output power is in the mW range. Tab.5.3

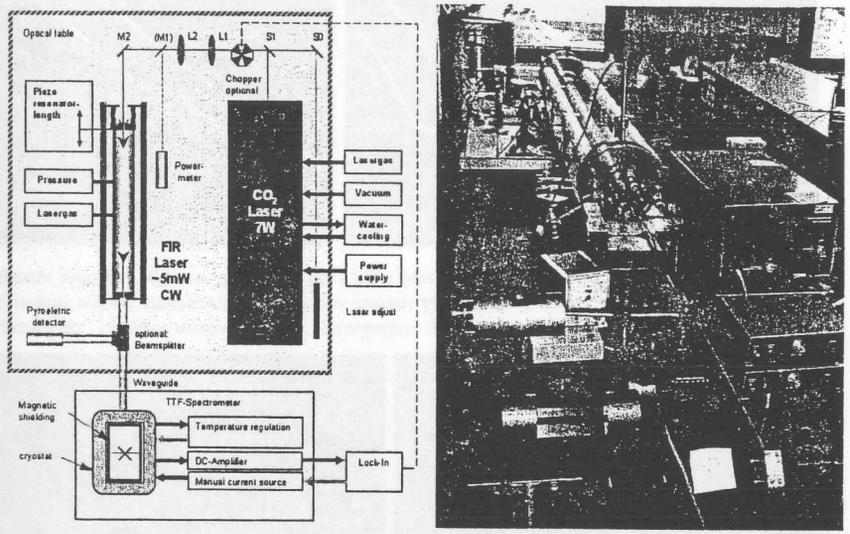

Figure 5.23: *Sketch and picture of the FIR-laser, constructed by Prof.Dr.U.Merkt.*

shows some parameters for different junctions. The rf-radiation frequency f_{rf}, linewidth Δf_{rf} and rf-current I_{rf} are analyzed from gaussian spectral fits of the junctions voltage response. Theoretical predicted linewidth from Eq.3.11 are given in parentheses. P_{rf} denotes the available rf-power at the spectrometers rf-input. P_{JJ} is the rf-power transformed by the junction itself.

Fig.5.24 shows I-V-characteristics and Hilbert reconstructed laser line spectra for different junctions and frequencies. Indicating by the second order Shapiro step, the junction obviously works also at a frequency of 1.5THz. Fig.5.25 show the I-V-characteristic of the junction $\#L40JK2$ operating at low temperature and a reconstructed spectrum. According to the rapid

Junction	Substrate	Antenna	f_{rf} [GHz]	Δf_{rf} [GHz]	I_{rf} [μA]	R_d [Ω]	P_{JJ} [nW]	P_{rf} [mW]	Loss [dB]
L37JK3	$LaAlO_3$	BD-LP	767	30 (16)	94	4.4	19	~ 4	53
"	"	"	721	21 (20)	47	4.7	5.2	$\sim$2.3	56
"	"	"	697	28 (21)	87	4.8	18	$\sim$3.3	53
"	"	"	589	32 (20)	67	5.2	12	$\sim$1.8	52
L37JK2	"	"	769	- (33)	80	20	64	~ 8	51
L40JK2	"	RA-LP	767	50 (6)	76	6.4	10	~ 2	53
"	"	"	1019	30 (3)	12	5.5	0.28	~ 0.2	58
MgO4JK2	MgO	"	764	13 (7)	62	3.6	6.9	~ 7	60

Table 5.3: *Summary of parameters for reconstructed FIR-laserlines.*

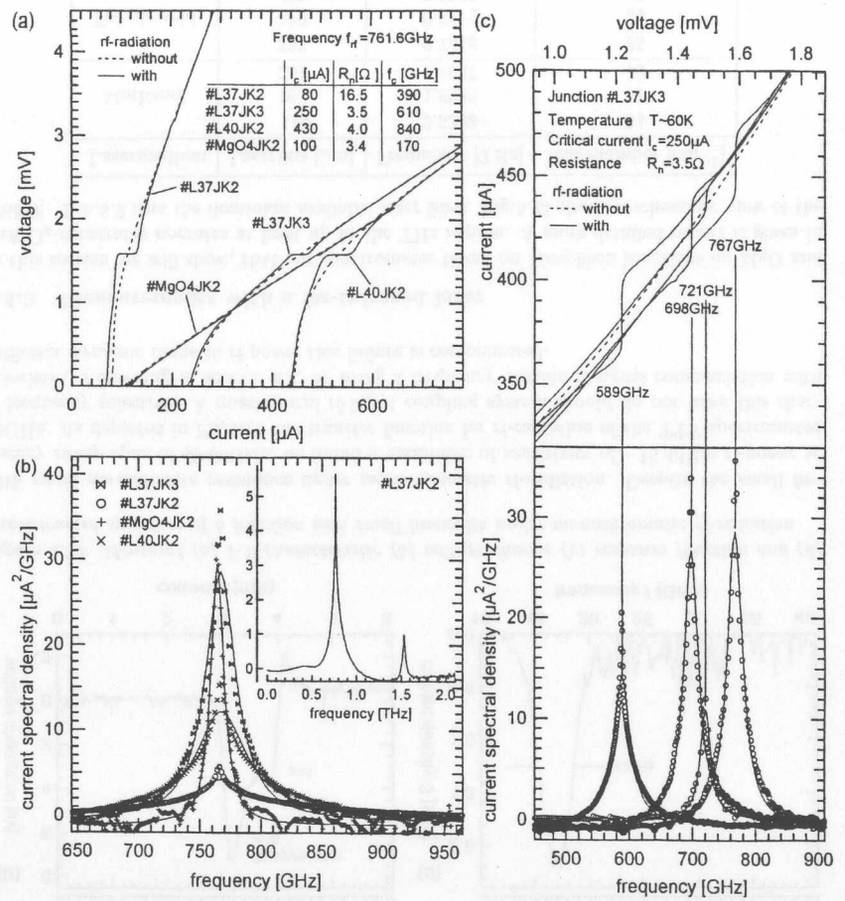

Figure 5.24: *(a) Measured I-V-characteristics and reconstructed Hilbert spectra for different junctions and irradiated laser lines.*

increase of the voltage near the critical current, it is obvious, that a spectral reconstruction is limited by a lower cutoff frequency, even when operating at low temperature. The reconstructed rf-power from RCSJ-model for the measured Shapiro step is about $i_{rf} = 2\%$. The increased linewidth is caused by additional noise feeded by the bias current. The spectral attenuation per length of THz radiation caused by water vapor in air is given by simulations in Fig.5.26. Indeed, today FIR-laser of more than 50mW output power are offered on the market. Having in mind the inverse quadratic behavior of the current response with frequency Eq.4.16 the reconstruction of frequencies up to more than 4THz has already been demonstrated [Div02a]. Mixing experiments of high-T_c Josephson junctions also succeed up to frequencies of 30THz [Gro95].

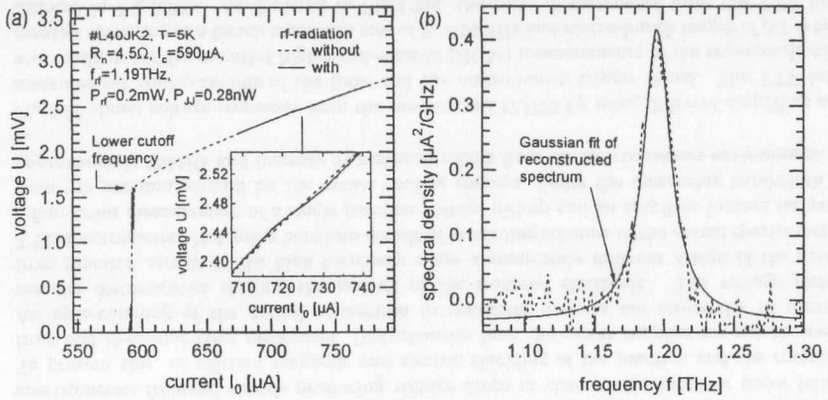

Figure 5.25: *(a) Measured I-V-characteristic of junction #L40JK2 under laser radiation of frequency 1.19THz (252μm laser line) at low temperature and its (b) reconstructed spectrum.*

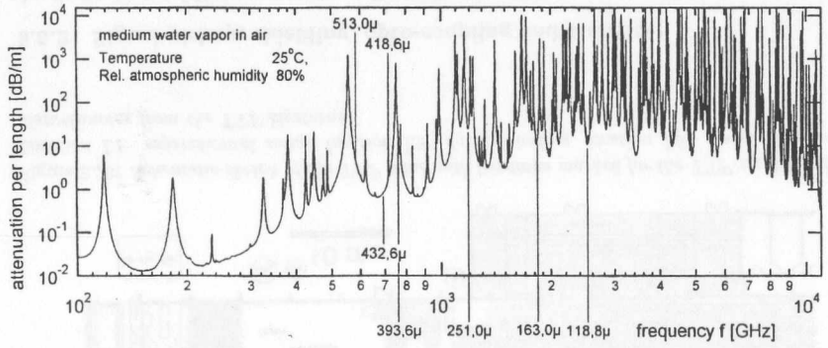

Figure 5.26: *Attenuation of THz radiation caused by water vapor in air. Thanks to Prof.Dr.Karl Jacobs from the radio astronomy group at KOSMA from university of Köln simulation data.*

Proposition 21: *Besides the frequency limit caused from energy gap of the high temperature superconductor $YBa_2Cu_3O_7$, it seems, that the reconstruction of frequencies in the THz regime is only a question of available rf-power.*

5.5 Characterization with coherent rf-sources

5.5.1 Measurement setup

A schematic sketch of the TTF linac with locations used for Hilbert transform spectroscopy is shown Fig.5.28. The measurements are performed at location *L1*, data recording at location *L2* and measurements within the rough environment from TTF klystrons are performed at location

L3. Fig.5.27 shows photographs of different locations and the guiding of transition radiation emitted from the aluminium foil located inside the beam pipe of the accelerator over a grid and two mirrors into the spectrometer, respectively pyroelectric detector. The spectrometer is misaligned from beam axis and attenuated by a mesh to avoid a saturation caused by the high peak rf-power from transition radiation.

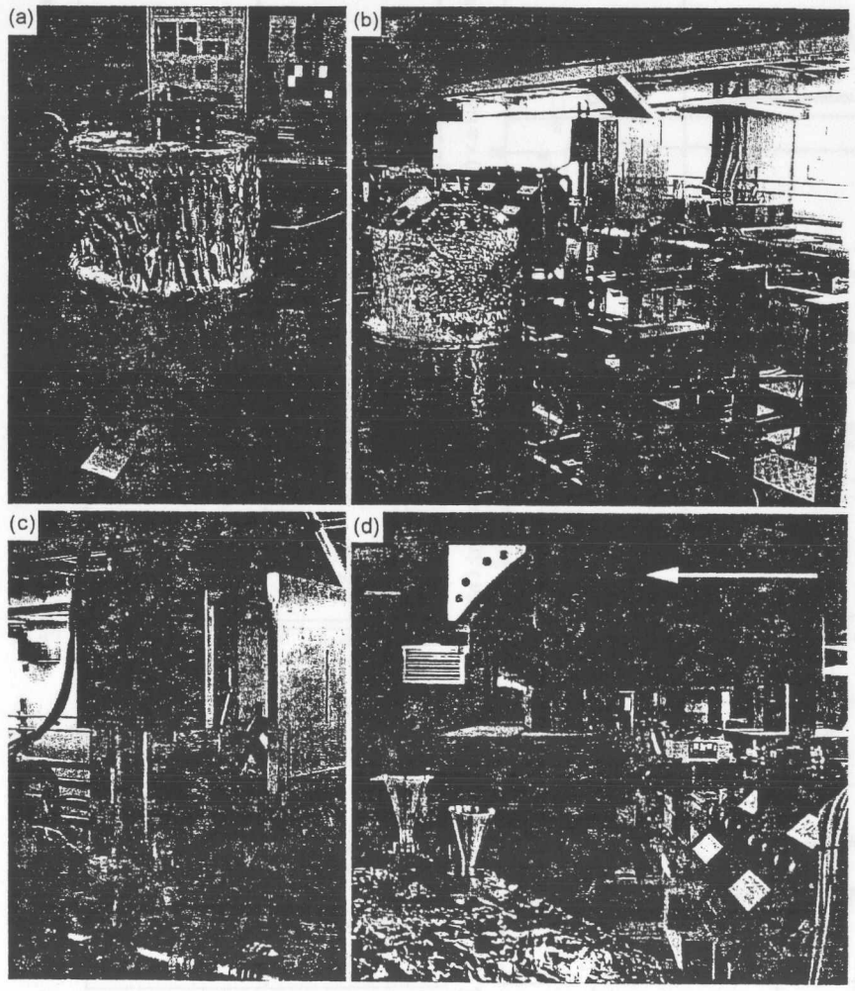

Figure 5.27: *(a) TTF-spectrometer within shielded liquid nitrogen dewar located outside the linac at location L2. (b) Spectrometer completely shielded and located at L1 station ACC3 inside the linac. (c) The transition radiation (quasioptical beam propagation marked by an arrow) is guided over mirrors and grids (d) into the spectrometer (left horn) and pyroelectric detector (right horn).*

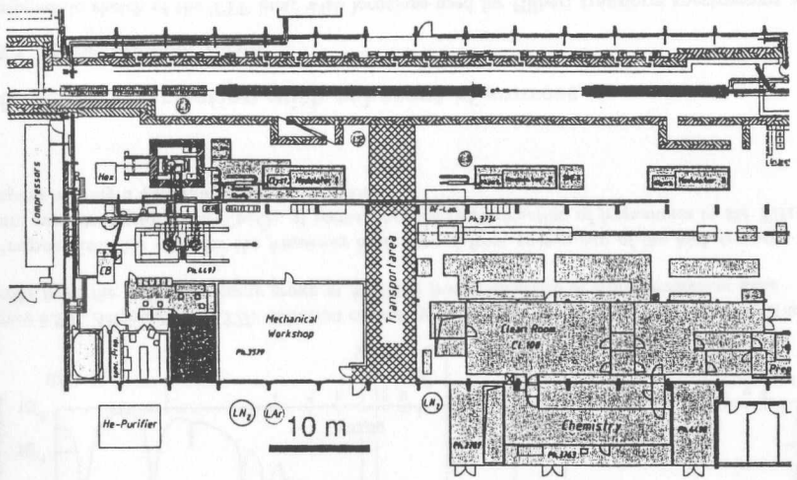

Figure 5.28: *Schematic sketch of the TTF linac with locations marked for the TTF-spectrometer. Location L1: experimental setup, location L2: data recording, location L3: measurements of disturbancies from the TTF klystrons.*

5.5.2 Signal pickup, shielding, opto-coupling and stability

As shown in the I-V-characteristic of Fig.5.20a, the critical current of the junction is not suppressed by continuous external magnetic or electric fields from the TTF environment. Disturbancies are mainly coming from magnetic fields inside the linac caused from station ACC3 and electric crosstalks from high power rf-fields of klystrons, directly acting on the spectrometers frontend chassis producing voltage drops at chassis transitions or screw joints. To prevent this, an efficient magnetic and electric shielding of the junction and the complete front end electronic must performed. Disturbancies from the power supplies are not observed. An opto-coupling of the digital connection to computer systems are essentially to prevent massive disturbancies shifting the ground of the frontend electronic. The voltage pickup from junction reveals in the high frequency range a completely different design of the actual TTF-spectrometer. Not going here into details of grounding schemes of the actual spectrometer, a four-point measurement of a single junction voltage pickup and an amplifier located far away from the junction, caused by the actual cooling concept, limits the measuring bandwidth to approximately 20MHz and increase disturbance effects from the spectrometers environment.

Fig.5.29 shows voltage responses from the junction $\#L37JK3$ by using different amplifiers and measurement configurations of the linac and the macro-bunch trigger signal. The TTF linac was configurated for so-called higher-order-mode (HOM) measurements of the superconducting cavaties operating at a bunch repetition rate of $f_R = 54$MHz and macro-bunch length of $\Delta T = 8\mu s$, denoted in Fig.5.30b. As depicted in Fig.5.29a, the main disturbancies from the TTF linac occurs during the tremendous change of rf-power during the pulse operation for the unshielded spectrometer. The junctions voltage response from coherent transition radiation by averaging over a macrobunch is shown in Fig.5.29c. Switching the junction to the superconducting state,

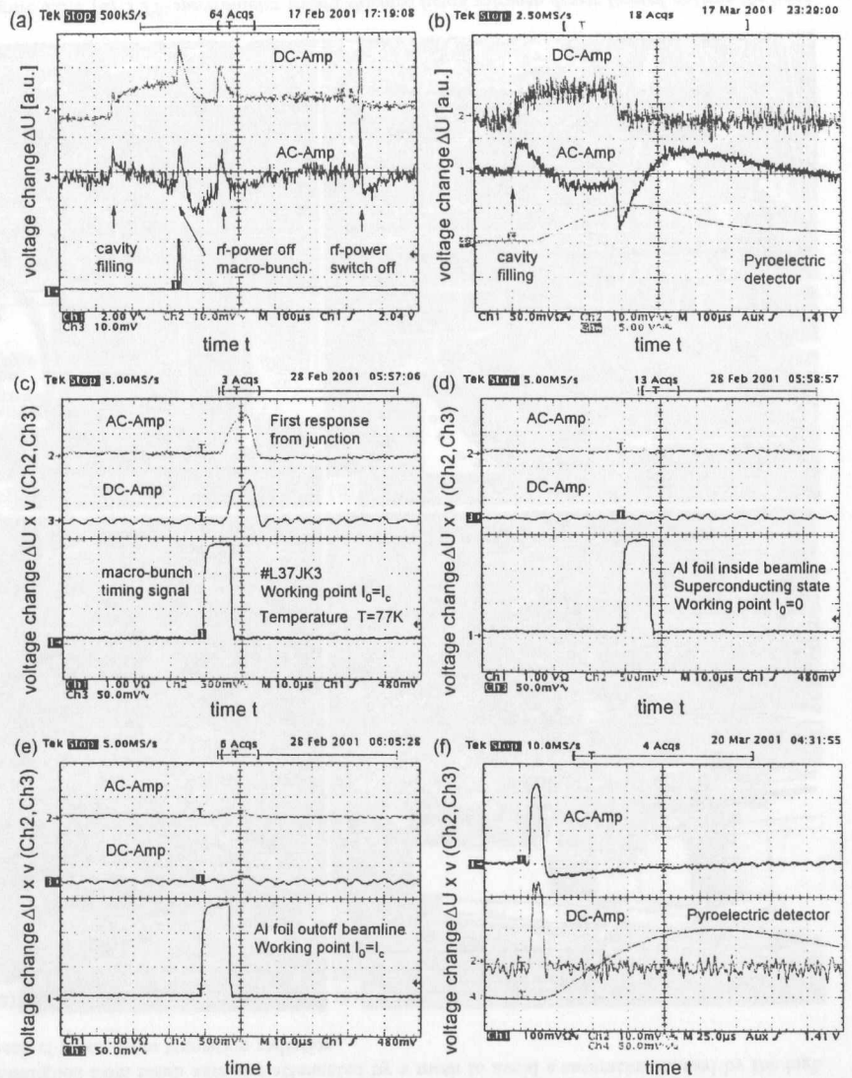

Figure 5.29: *Voltage responses of different amplifiers and measurement configurations of the linac. The dc-amplification was $v = 10^4$, respectively ac-amplification $v = 10^5$. (a) Unshielded and (b) shielded dewar and spectrometer during linac operation. (c) First response from coherent transition radiation by averaging over a macrobunch. (d) Junction at superconducting state $I_0 = 0$. (e) Aluminium foil not inside beamline. (f) Box-car samples of $N = 60$ macro-bunches.*

as depicted in Fig.5.29d, shows no disturbance effects on the shielded spectrometer during the linac pulsed operation. By putting the aluminium foil outside the beamline a small amount of disturbancies or a detection of wake-field rf-radiation shown in Fig.5.29e is detected. For this the junction operates at most sensitive working point near its critical current. To increase the signal-to-noise ratio of the measurement, according to Fig.5.29f, several macro-bunches are box-car sampled. For detecting fluctuations of the transition radition intensity during the linac operation and measurement of the I-V-characteristic, the response of a pyroelectric detector is recorded. According to the measurements Fig.5.30c within the linacs environment during rf-pulse operation reveal at least a minimum of detectable voltage resolution of approximately $\Delta\bar{u} = 50\text{nV}$ for the actual TTF-spectrometer. The junction parameters at linac operation are highly reproducable and stable during the measurement period of approximately 2 weeks for many cooling and warmup cycles. Despite the maximum peak rf-power from TTF linac of about 10MW, -50dB spectrometer attenuation, -20dB mesh attenuation at rf-input, -10dB rf-guiding from linac, the maximum peak rf-power at the junction is estimated to be 100mW, respectively the peak rf-current for the junction $\#L40JK2$ to approximately 200mA. No Josephson junctions were destroyed by peak rf-radiation or other influences.

5.5.3 Averaging, sampling and noise reduction techniques

Box-car techniques, averaging and sampling methods to increase the signal-to-noise ratio of pulsed voltage responses from spectral measurements were previously discussed in section 4.6. All these chopper methods, well established for SQUID amplifier pickups in flux-lock-loop or bias reversal configurations, separating signal from noise by frequency domain shifts cost measurement time, which is, at least for a single-bunch measurement, not feasible.

5.5.4 Measurements with a coherent transition radiation source

In this section coherent transition radiation spectra of electron-bunches and longitudinal form factors measured at the TTF linac for different machine states are presented. Fig.5.30 shows measurements for varying the transition radiation power at constant phase of the bunch compressor, respectively Fig.5.31 vice versa. To guarentee an operation of the Josephson junction below the maximum rf-power ratings the adjustment procedure of linac rf-power described in proposition 20 was applied during the measurements. The TTF linac was configurated for the higher-order-mode (HOM) measurements of the superconducting cavaties operating at a bunch repetition rate of 54MHz and macro-bunch length of $\Delta T = 8\mu\text{s}$, denoted in Fig.5.30b. Fig.5.31a shows the measured unperturbated V-I-characteristic. The measured voltage change $\Delta\bar{U}(I_0)$ is shown in Fig.5.30c. Considering fluctuations of the radiation intensity during linac operation a pyroelectric detector recorded the integrated radiation intensity for correcting the junctions voltage response as shown in Fig.5.30b. The current response $\Delta i(\bar{u})$ is derived numerically by rotating the axis of the measured V-I-characteristic shown in Fig.5.30d. The spectral reconstruction using the method of Hilbert transform spectroscopy and the determination of the rf-pulse shapes using the phase reconstruction of section 3.4 involves a reconstruction algorithm listed in Fig.5.32 by Eq.5.8-5.14. The measurement parameters are given by Eq.4.81 and marked in Fig.4.25 for a single junction $N_J = 1$ and N box-car samples of the actual TTF-spectrometer.

$$u_{S/N} = \sqrt{N}\frac{N_J U_n(T)\Delta\bar{u}(i_p, t_p, t_R)}{\sqrt{\delta\bar{U}_R^2(N_J) + \delta\bar{U}_{AMP}^2 + \delta\bar{U}_{1/f}^2(N_J)}} \tag{5.15}$$

Eq.5.15 reveals, that box-car sampling is not so efficient for the signal-to-noise ratio than using an array of N_J junctions, because an array limits the influence of the pickup noise $\delta\bar{U}_{AMP}$.

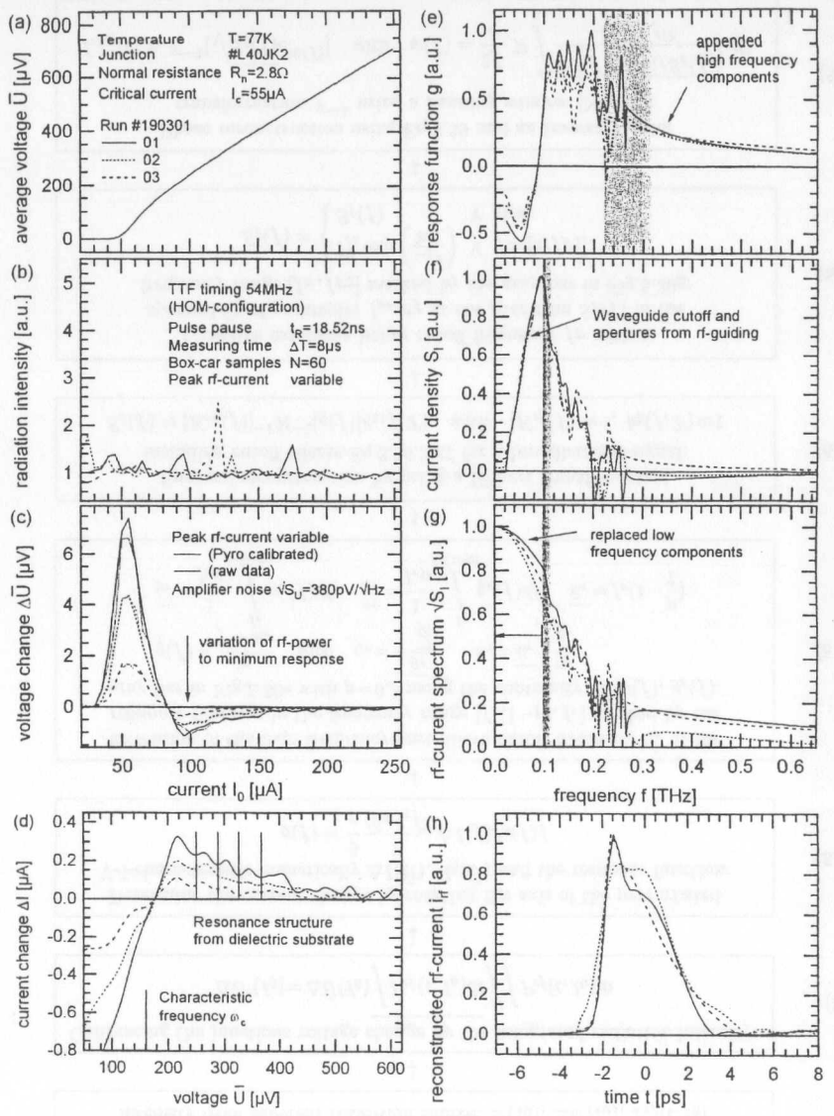

Figure 5.30: *Varying rf-power and constant compression for the higher-order-mode (HOM) configurated linac. Measured (a) V-I-characteristic, (b) radiation intensity from pyroelectric detector, (c) raw data and calibrated voltage reponse and (d) current response. Reconstructed (e) response function with appended high frequencies, (f) rf-current spectral density, (g) current spectrum with a gaussian low frequency extension and (h) time domain rf-current.*

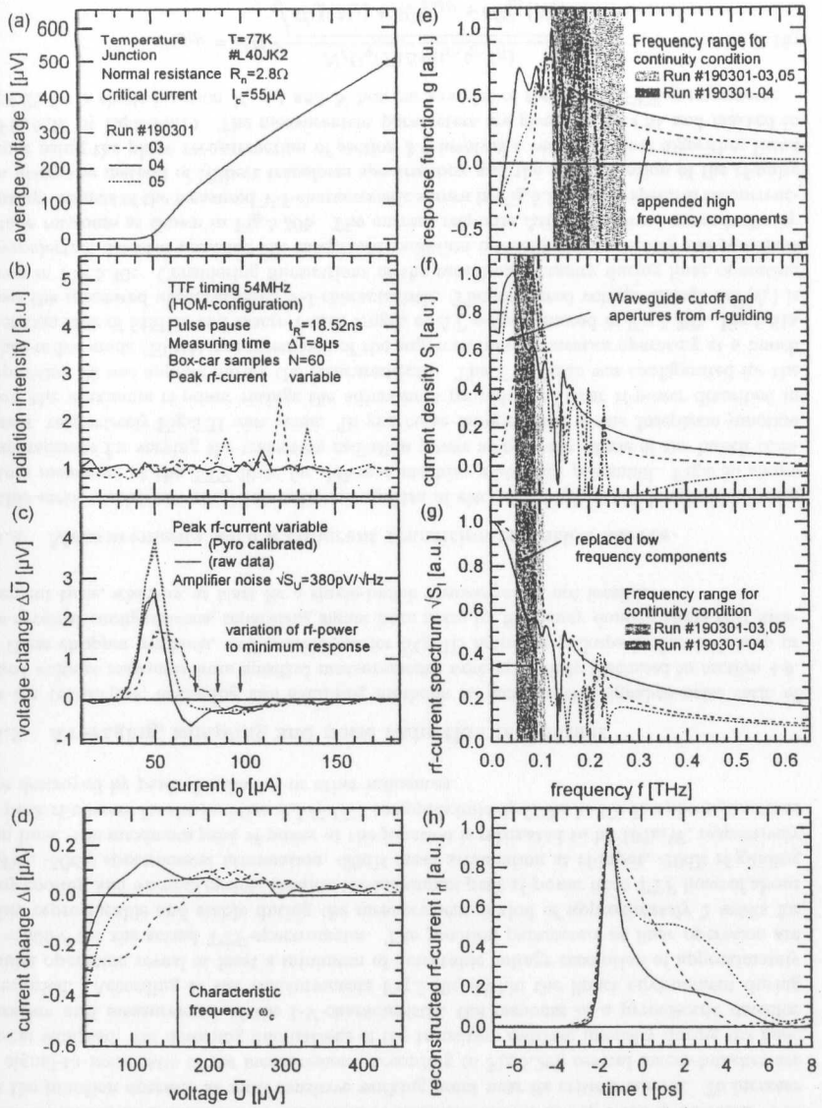

Figure 5.31: *Varying compression with constant rf-power for higher-order-mode (HOM) configurated linac. Measured (a) V-I-characteristic, (b) radiation intensity from pyroelectric detector, (c) raw data and calibrated voltage reponse and (d) current response. Reconstructed (e) response function with appended high frequencies, (f) rf-current spectral density, (g) current spectrum with a gaussian low frequency extension and (h) time domain rf-current.*

Measuring of the junctions I-V-characteristic, voltage change and integrated intensity from coherent transition source: $\bar{U}(I_0)$, $\Delta\bar{U}(I_0)$, $P_{rf}(t, I_0)$ (5.8)

↓

Calibrating the junctions voltage change by the integrated radiation intensity:

$$\Delta\bar{U}'(I_0) = \Delta\bar{U}(I_0) \int \overline{P_{rf}(t, I_0')dt} \Big/ \int P_{rf}(t, I_0)dt \tag{5.9}$$

↓

Determine the current change by rotating the axis of the perturbated V-I-characteristic numerically $\Delta I(\bar{U})$, $I_0(\bar{U})$ and the response function:

$$g(f) = \frac{8}{\pi} \frac{1}{(2\pi f_c)^2} \Delta I(f) I_0(f) f \tag{5.10}$$

↓

Extension of the high frequency part above cutoff frequency f_r of the response function in the frequency range $[f_r(1-p), f_r]$ marked by the gray bar in Fig.5.30e with $p=0.3$ using the continuity of $g_r(f)$, $g_r'(f)$:

$$g(f) = \frac{\eta_r}{f - \kappa_r} \quad \text{with} \quad \eta_r = -\frac{\overline{g_r}^2}{\overline{g_r'}}, \quad \kappa_r = \overline{\bar{u}_r} - \frac{\eta_r}{\overline{g_r}}, \tag{5.11}$$

$$\overline{g_r} = \frac{1}{f_r p} \int_{f_r(1-p)}^{f_r} g_r(f)df, \quad \overline{g_r'} = \frac{1}{f_r p} \int_{f_r(1-p)}^{f_r} g_r'(f)df, \quad \overline{\bar{u}_r} = f_r(1-\frac{p}{2})$$

↓

Spectral reconstruction by using a Hilbert transformation including cutoff effects Eq.3.36,3.37 for a broadband rf-signal:

$$S_I(f) \approx |K_{rf}(f)|^{-1}\mathcal{H}^{-1}[g(f)]k_b(f,T) \quad \text{with} \quad |K_{rf}(f)| \approx 1,\ k_b(f,T) \approx 1 \tag{5.12}$$

↓

Gaussian extension below cutoff frequency f_F with a spectral fit of parameter I_{ps}, σ_f at the spectrum $S_I(f)$ in the frequency range $[f_F, f_{F2}]$ marked by the gray bar in Fig.5.30g:

$$S_I(f) = \begin{cases} I_{ps}^2 \exp\left(\frac{-f^2}{2\sigma_f^2}\right) & \forall\ f = [0, f_{F2}] \\ S_I(f) & \forall \text{ else} \end{cases} \tag{5.13}$$

↓

Phase reconstruction using Eq.3.39 and an inverse Fourier transformation $\mathcal{F}^{-1}$ using a hanning window [Num00]:

$$I_{rf,p}(t) = \mathcal{F}^{-1}[\sqrt{S_I(f)}e^{i\psi(f)}] \quad \text{with} \quad \psi(f) = \frac{2f}{\pi} \mathcal{P} \int_0^\infty \frac{\ln\left[\sqrt{S_I(f')/S_I(f)}\right]}{f^2 - f'^2} df' \tag{5.14}$$

Figure 5.32: *Time domain reconstruction algorithm of coherent transition radiation by measuring the junctions I-V-characteristic $\bar{U}(I_0)$ and voltage change $\Delta\bar{U}(I_0)$ using Hilbert spectroscopy.*

Eq.5.16 lists the parameter resulting from the measurement run #190301-01.

$$\#190301\text{-}01:\quad N_J=1,\ R_n=2.8\Omega,\ I_c=55\mu A,\ U_n=154\mu V,\ \omega_c=467.7s^{-1},\ \Gamma_0=0.0587,\ (5.16)$$
$$i_0=1.74,\ \bar{u}=1.43,\ \Delta i_{max}=0.55\%,\ \Delta\bar{u}=0.65\%,$$
$$\Delta T=8\mu s,\ f_p=100,\ k=1,\ u_{S/N}=1/0.02,\ N=60,$$
$$f_R=3.9\cdot10^{-6}\Omega^{-1/2},\ \delta\bar{U}_{AMP}=108nV,\ \delta\bar{U}_R=38nV,\ \delta\bar{U}_{1/f}=2.5nV$$

By varying the phase of the bunch compressor the electron-bunches can be compressed resulting in different bunch lengths and shapes of the transition radiation pulse. Measurements for different compressions are shown in Fig.5.31. The high frequency extension of the response function is performed by using also 30% of the measured data for the averaged continuity condition.

- *Reliability of the reconstructed spectra:*

  Due to the limited dynamic range of the measurements, high frequency components have to be appended to the response function before applying the Hilbert transformation, as shown in Fig.5.30e. According to the complicated resonance structure near the cutoff frequency $f_r \approx 320$GHz of the measured response function, the high frequency components of the response function Eq.5.11 are extended by using averaged values for the continuity of the response function g_r and its derivation $\overline{g_r'}$ within a given frequency range $[f_r(1-p), f_r]$ marked in Fig.5.30e by a gray bar [2]. The Hilbert transformation using cutoff effects, low frequency extension caused by several apertures within the rf-input coupling system and the phase reconstruction are previously discussed by Eq.4.60ff and do not essentially influence the reconstructed rf-current shape shown in Fig.5.30h [3]. The most critical operation concerning the reliability of the reconstructed rf-pulse shape concerns the high frequency extension of the response function caused by the continuity conditions within a resonance structure. Selecting a frequency range $[f_r(1-p), f_r]$ of about 30% from measured data for analyzing the continuity conditions much larger than a typical single resonance structure, the reconstructed time domain rf-currents shown in Fig.5.30h are nearly the same despite different measurements for varying rf-power and different resonance characteristics.

- *Macro-bunch measurement:*

  As depicted in Fig.5.29c, the voltage response and therefore the time dependent spectral transition radiation intensity during the macro-bunch measurement is not constant. This limits the validity of the measured transition radiation spectra, but vanishes at least for decreasing measuring time or for a single-bnunch measurement.

- *Multiple reflections from sample holder:*

  To explore the measurements using coherent transition radiation a simulation of the experiment is performed and shown in Fig.5.33 for the operation at maximum current change and Fig.5.34 for varying rf-power and rf-pulse shape given by the reconstructed rf-current and parameters Eq.5.16 of the measurement run #190301-01. As depicted in Fig.5.33a the expected maximum current response for the actual TTF timing is by a factor of approximately 20 less than the measured one. Consequently, non equidistant

[2] The frequency range is increased by using $p \to 1.1p$ and Eq.5.11 is evaluated until $\eta_r \overline{g_r} > 0$ is fulfilled.

[3] The lower cutoff frequency f_F is defined at the spectral maximum within the frequency range [10GHz, 100GHz]. The frequency f_{F2} is defined by the maximum negative spectral slope within the cutoff frequency and a 30% level crossing from spectral maximum.

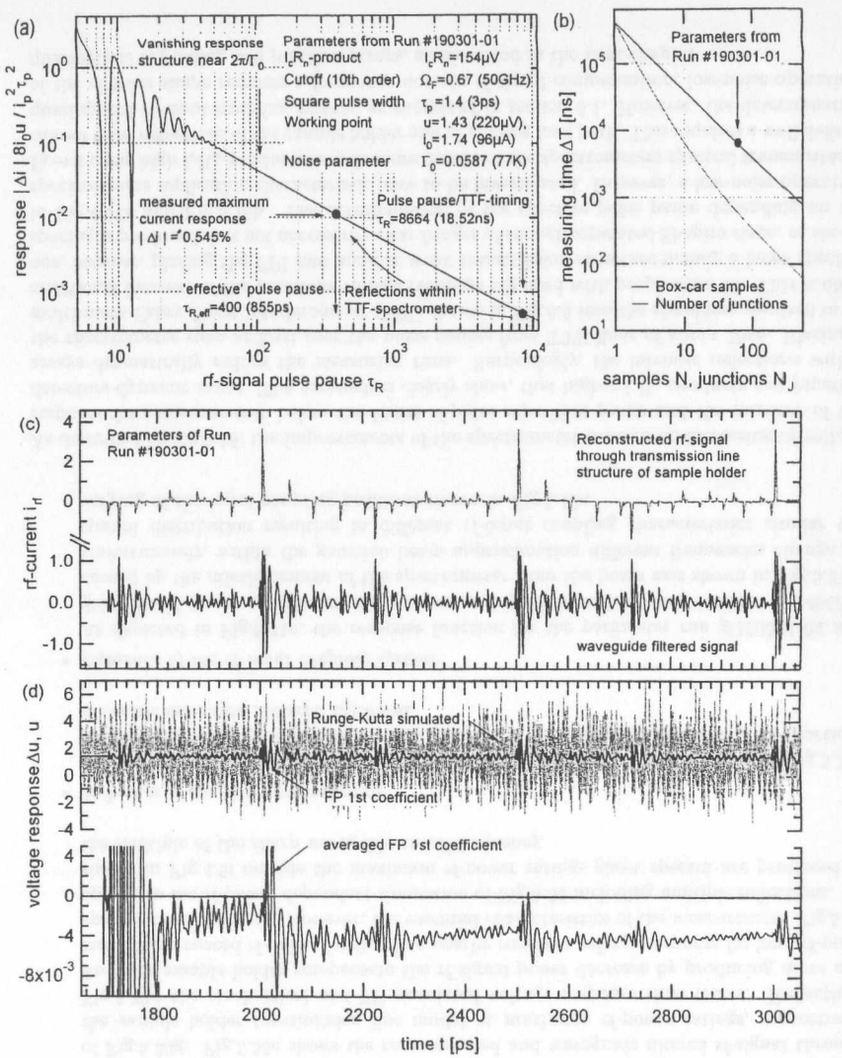

Figure 5.33: *Simulated (a) response function expected from Eq.4.36 for the parameter of the measurement run #190301-01. (b) Measurement time of data #190301-01 for box-car samples and a junction array. Simulated (c) waveguide filtered rf-signal, (d) Runge-Kutta and FP (2nd order) simulated voltage response time traces from reconstructed rf-pulse guided through the sample holder transmission line model at maximum rf-power ratings.*

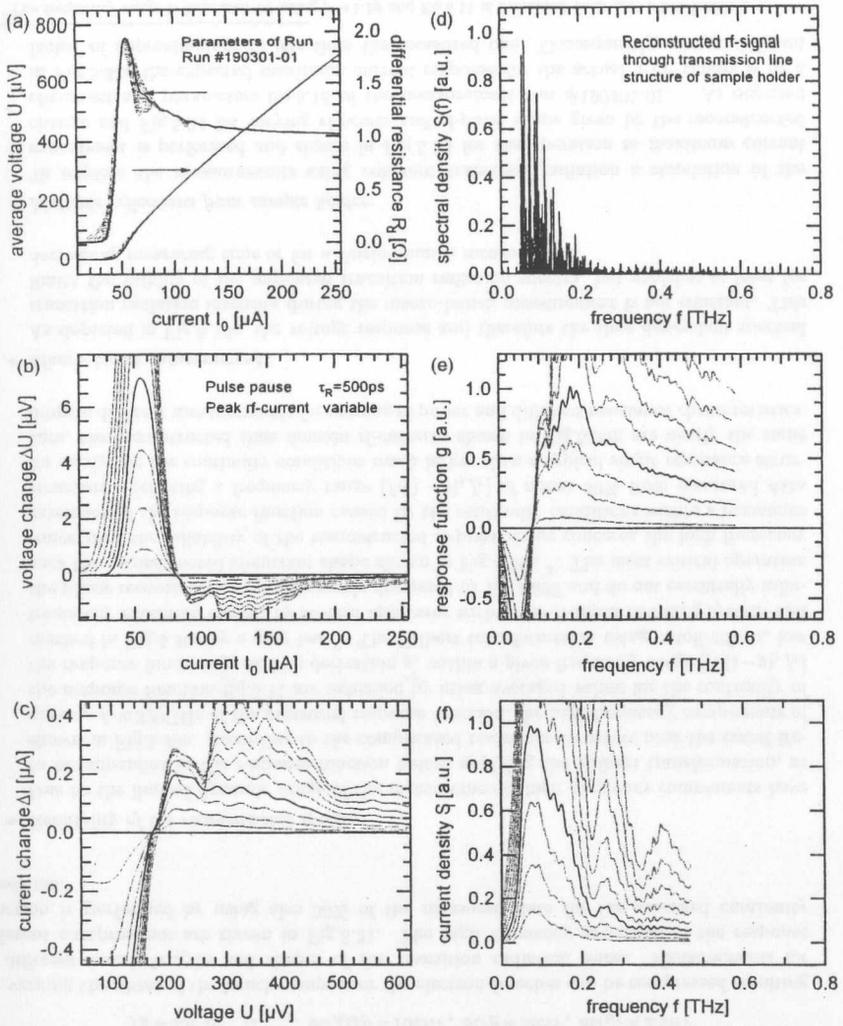

Figure 5.34: *FP (2nd order) simulated spectra for parameters of Eq.5.16 and different rf-power including reflections within the sample holder. (a) I-V-characteristic, differential resistance, (b) voltage response, (c) current response, (d) rf-signal spectrum (e) response function and (f) Hilbert spectrum. The black curves describe measurements of the parameter run #190301-01.*

multiple reflections from sample holder must be assumed by introducing an effective pulse pause $\tau_{R.eff}$. Otherwise, according to Fig.5.34c, the current response for the linacs pulse pause of about 20ns cannot be explain the measurements for an absence of ghost

spectra and operation below the maximum rf-power ratings, which was guaranteed by the adjustment procedure for the linac rf-power of proposition 20. Multiple reflections are described within the transmission line model of Fig.5.15 modelling the sandwiched sample holder of the rf-input coupling system. The simulated irradiated spectrum of Fig.5.34d is in principle in accordance with the spectral resonance structure from the measurements of Fig.5.30g. Fig.5.33c shows the reconstructed and waveguide filtered rf-signal through the sample holder transmission line model at maximum rf-power ratings, respectively Fig.5.33d the stochastical and FP simulated voltage response time traces. Reflections from the sample holder compensate the rf-signal power decrease by producing more and more dense spaced rf-pulses leading to a nearby constant voltage response for long rf-pulse spacing from the linac. However, the essential characteristics of the measurement Fig.5.30 appear in the rf-power dependent simulation of Fig.5.34 including multiple reflections. As shown in Fig.4.9f outside the maximum rf-power ratings ghost spectra are produced at the multiple of the sharp waveguide cutoff frequency.

- *Influence of the dielectric substrate:*
  Comparing the measured and simulated current responses of Fig.5.30d and Fig.5.34c identify its weak spaced fringes as a resonance structure caused from the junctions dielectric substrate material thickness.

- *Influence of the rf-input coupling system:*
  As depicted in Fig.5.31e, the response function for the parameter run #190301-04 and #190301-05 shows a dominant shifted resonance peak from frequency 240GHz to 140GHz caused by the misalignement of the spectrometer from the beam axis shown in Fig.5.27d. Unfortunately, within the gaussian beam approximation different frequencies change its spatial distribution resulting in different rf-input coupling characteristics similar the varying of the input coupling positions shown in Fig.5.16a.

As described by Eq.5.16, the improvements of the spectrometer concern an increasing of voltage response for measurements below the linacs rf-pulse repetition pause and the increase of the detectors dynamic range. The parameters clearly show, that higher I_cR_n-products and junction arrays dramatically reduce the measuring time. Surprisingly, the intrinsic reflections within the spectrometer span at least over the pulse pauses from TTF linac of about 20ns. Placing a multi-mesh Fabry-Perot interferometer (FPI) shown in Fig.6.5 into the rf-guiding resulted in no additional increase of the junctions voltage response adjusted with proposition 20. This is obvious, because, placing the FPI into another weak transmission structure mainly a large spectral spacing is produced, but not necessarily clear fringes of enough seperated Shapiro steps, as shown in Fig.4.17a and Fig.5.16b. The determination of the effective pulse pause depending on the spectrometers replication characteristic have to be investigated. However, a low-noise operation $\Gamma_0 \rightarrow 0$ using high I_cR_n-products reveals more details of the spectrometers spectral transmittance caused from reflections of the sample holder and rf-guiding load path, This requires a well defined quasioptical rf-input coupling system, as suggested in section 6.1. However, the determination of the rf-pulse shape requires a frequency domain rf-signal compensation, low-noise operation, quasioptical rf-guiding and junction arrays, as discussed in the next chapter.

Chapter 6

Conceptual approach to single pulse measurements

A single-bunch measurement with Josephson junctions has not yet been realized. In this chapter, we will suggest improvements for a single rf-pulse measurement. The Josephson junction is a frequency selective device. A frequency component from rf-pulse can be detected by the detector once for a fixed bias current. Indeed, according to section 4.6, intrinsic noise sources due to the normal-state resistance limits the signal-to-noise ratio (SNR) and causes an averaging over many rf-pulses. This prevents a readout with high frequency measuring bandwidth for sampling the junctions voltage response at minimum possible time for single rf-pulses, as discussed in section 4.4.2. Consequently, there are some essential improvements of a spectrometer for a single- or improved macro-bunch measurement.

Proposition 22:

- *Generate a series of rf-pulses from a single rf-pulse by using well defined delay structures.*
- *Increase the voltage reponse by a series connection of several Josephson junctions.*
- *Increase the junctions dynamic range by a frequency domain rf-signal compensation.*
- *Increase the junction I_cR_n-product intrinsically by its preparation processes.*
- *Decrease the operating temperture and use a fast low-T_c SQUID amplifier readout.*

6.1 Pulse repetition

In this chapter we will investigate the production of a series of possibly identical rf-pulses caused from a single rf-pulse. With it, according to Fig.4.6, Shapiro steps increase resulting in an improved signal-to-noise ratio for high readout bandwidth for a single-bunch measurement. Pulse repetitive structures are realized by time delay structures.

Here we investigate, contrary to more open structures with low total rf-power loss, closed quasioptical delay structures, namely Fabry-Perot interferometers (FPI). Many authors, mainly for higher order filtering in the quasioptical frequency range within satellite systems and radio astronomy, investigate interferometers consisting of several impedance grids [Gol98]. Unfortunately, for filtering, they usually discuss only the spectral reflected and transmitted rf-power of the interferometers. For a time domain analysis of an rf-pulse driven FPI, we deduce in the appendix A.9 its impulse response by inverse Fourier transform from the complex transfer function $\tilde{t}$ of its equivalent circuit. Once having the impulse reponse, the time dependent response $r_{i,FPI}(t)$ of an rf-pulse driven n-th order FPI is known.

$$|r_{i,FPI}(t)|^2 = |\mathcal{F}^{-1}[\ \tilde{t}(f, d_i, R, X_g) \cdot \mathcal{F}[i_{rf,p}(t)]\ ]|^2 \qquad (6.1)$$

Within the next sections, several multi-mesh FPIs (MMFPI) are tested for having many output rf-pulses with possibly constant envelope. To prevent a superposition of spectral lines for Hilbert spectroscopy the spectrum of the rf-pulses should be equidistant without disturbing intermediate spectral lines. In contrary to the experimental setup, we investigate the FPIs without any complicated sources and loads.

6.1.1 Transmittance and reflectivity of meshes

Having many output rf-pulses with possibly constant amplitudes, the rf-pulses must stay long in the resonator. This requires high reflection with low material loss grids over a wide frequency range. Various geometries like crosses, tripoles, gridded squares employed as elements of meshes produce each its individual frequency characteristic. According to Fig.6.5a we use electroformed two-dimensional stripline grids acting as a high pass filter operating in the low frequency range.

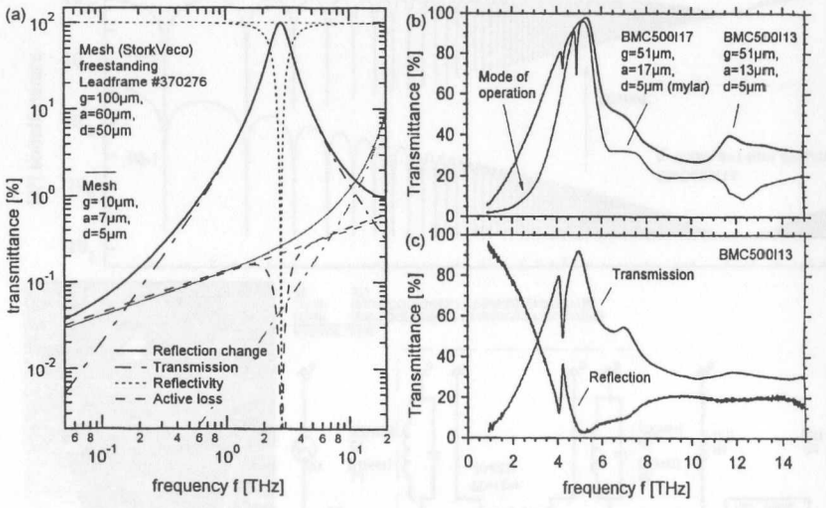

Figure 6.1: *(a) Calculated rf-power transfer functions according to Eq.6.5 from FPI mesh Fig.6.5a of a thick freestanding mesh. (b),(c) Measured rf-power transmission and reflection of two-dimensional nickel wire grids electroformed on a thin mylar sheet using Fourier spectroscopy under vacuum conditions at the MPIfR (For measurement and publication thanks to H.Gemünd and E.Kreysa from submillimeter radio astronomy group.).*

Using the impedance of a stripline grid in the long-wavelength limit $g \ll \lambda$ and the equivalent transmission line impedance of an imperfect conductor [Gol98], the mesh impedance with grid distance g, stripline width a thickness d and conductivity σ for normal incident is given by

$$Z_g = R_l + iX_g \qquad (6.2)$$

$$Y_X = \frac{Z_0}{X_g} = -\left(\frac{\omega}{\omega_0} - \frac{\omega_0}{\omega}\right)\left(\omega_0 \ln \csc\left[\frac{\pi a}{g}\right]\right)^{-1}, \quad \text{with} \quad \omega_0 = 0.93, \omega = \frac{gf}{c} \qquad (6.3)$$

$$Y_R = \frac{Z_0}{R_l} = \frac{2a+2d}{g}\left(\frac{\pi\epsilon_0 f}{\sigma}\right)^{-1/2}. \tag{6.4}$$

The rf-power reflection, transmission and loss results from transmission line methods to

$$|r|^2 = \left|-1\Big/1+2\left(\frac{i}{Y_X}+\frac{1}{Y_R}\right)\right|^2, \quad |t|^2 = \left|1\Big/1+\frac{1}{2\left(\frac{i}{Y_X}+\frac{1}{Y_R}\right)}\right|^2, \quad |l|^2 = 4\frac{|r|^2}{Y_R} \tag{6.5}$$

According to Eq.6.4 the resonance peak shifts to higher frequencies with smaller grid spacing g. Unfortunately, the transmission measurements Fig.6.1b are not performed on freestanding dense meshes Fig.6.5a without dielectric loss. The operation of these meshes are limited of up to approximately 2THz. Today on the market, electroformed meshes are offered down to several μm grid spacing on thin dielectric substrates to increase the reflectivity for higher frequencies or freestanding meshes [1].

6.1.2 Two-mesh Fabry-Perot interferometer (FPI)

In this section the reliability of simple models for time responses of pulse driven FPI's are discussed. Having this, we are able to estimate the number of duplicated rf-pulses for a single pulse measurement. From the equivalent circuit of the two-mesh Fabry-perot interferometer Fig.6.3 we obtain its rf-power transfer function A.223, A.224. Smaller grid spacing shifts the resonance peak for FPI operation possibly up to several THz.

To investigate the response of a pulse driven FPI, we use THz spectroscopy. The setup for measuring the time domain response using a photoconducting dipole antenna is shown in Fig.6.2 and described in detail by [Kha02].

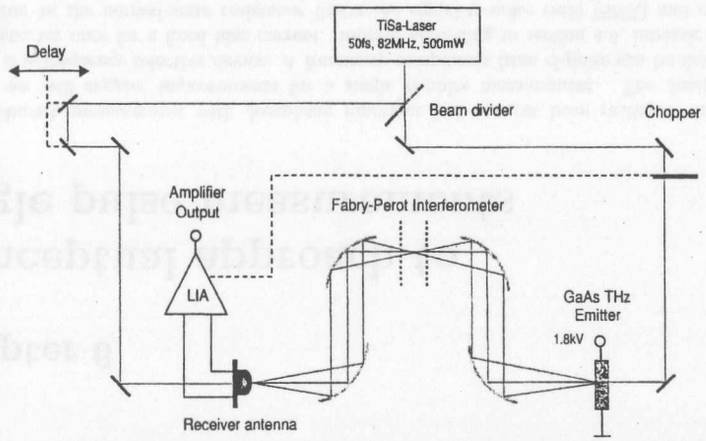

Figure 6.2: *(a) Gated detection scheme for measuring the transmittance using THz spectroscopy. A Fabry-perot interferometer is placed within the quasioptical beam waist.*

[1] Buckbee-Mears/USA, Stork Veco/Netherlands

Optical pulses are generated by a Ti:sapphire laser pumping a gallium arsenide semiconductor producing photocarriers, which are accelerated by an external applied electric field and recombine. The fast change of the photocurrent produce the broadband THz radiation. For measuring the transmittance of the sample the THz radiation is guided over a quasioptical system through a photoconducting dipole antenna. The antenna is gated by the delayed laser pulse generating a bunch of photocarriers. The electric field of the THz pulse serves as a bias for the antenna and is proportional to the photocurrent.

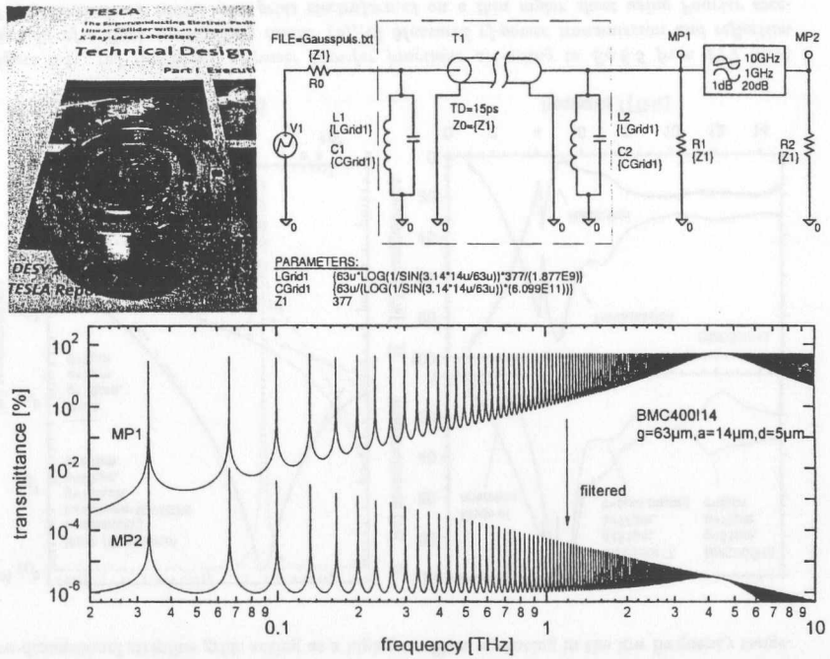

Figure 6.3: *Two-mesh FPI with small aperture of 2.5cm. The meshes are not inserted. Simplified equivalent circuit of the FPI without grid loss and beam walkoff effects. The diagram shows the PSPICE simulated transmittance located at point MP1 of the FPI and MP2. The corresponding time traces are shown in Fig.6.4*

The measured time trace response for a single rf-pulse is shown in Fig.6.4. For a time domain analysis, according to Fig.6.4c, we put the measured free propagating rf-pulse into the simplified equivalent circuit [2] of a two mesh FPI without considering material loss and beam walkoff effects. Walkoff effects from incident beam, lateral offset and beam diffraction itself are more important for long rf-guiding distances. The measured time trace response using an FPI within the beam waist is shown in Fig.6.4b. Beside different noise contributions both time traces agree quite well. As expected, frequencies above several THz with less reflectivity slightly vanishes with increasing

[2] Time trace simulation deduced from frequency methods are numerically limited for infinite small reflections of the FPI in the low frequency range. Analytical descriptions of the FPI's delay lines in state space representation are unpractical, because many coupled differential equations have to be solved. Numerically, the state space ansatz is more convenient and currently implemented by circuit modeling programs.

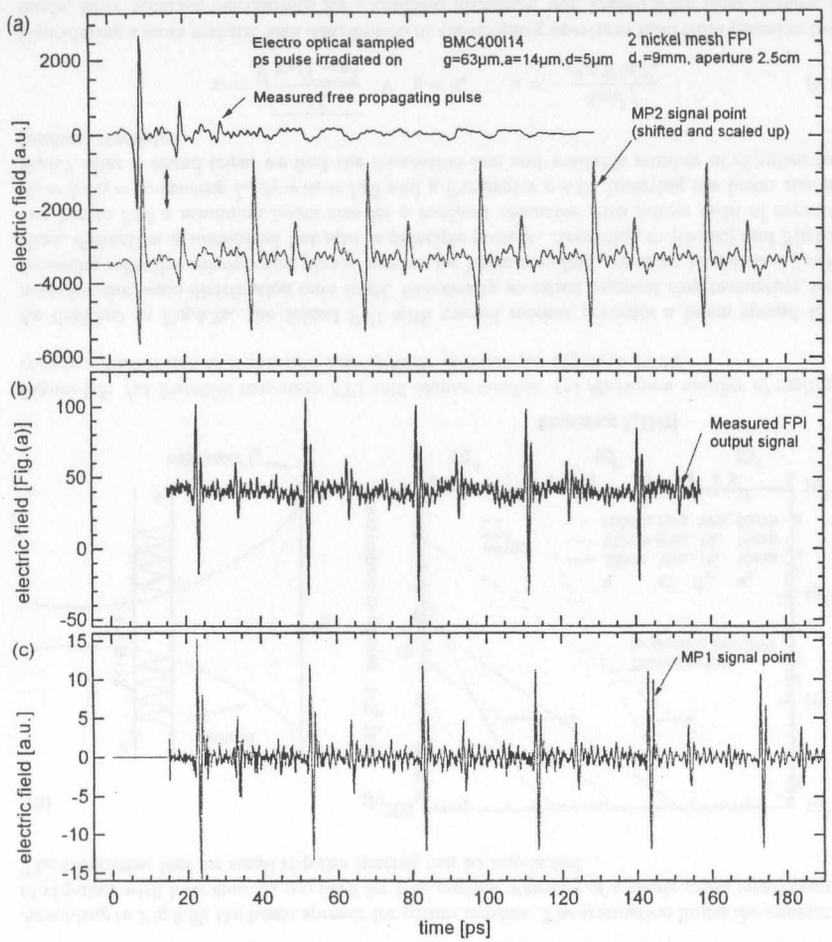

Figure 6.4: *Time domain sampled measurement of (a) a free propagating rf-pulse and (b) replicated rf-pulse series with 30ps delay from the FPI Fig.6.3. (c) PSPICE simulated response of the equivalent circuit of the FPI.*

pulse number. For at least five duplicated rf-pulses, our measurements do not show this effect. However more dense meshes Fig.6.1a should do not have this failure. The ratio of the first rf-pulse to the incoming one determines the rf-power insertion loss of about -35.9dB. The replicated pulse shape differs from the original one, caused by the FPI's transfer function. Filtering with a low-pass filter, complementary to the FPI transfer function, lets the duplicated rf-pulses Fig.6.4a occur appropriate to the measured single rf-pulse. For a high total rf-power transmittance the replacement of one FPI mesh by a nearly complementary grid is more convenient. For pure

inductive and capacitive grids the frequency characteristics compensates with $t + t_c = 1$

$$t_c = -r,\ r_c = -t \quad \rightarrow \quad Y_X^c = 4/Y_X \qquad \forall \quad a \ll g \ll \lambda. \tag{6.6}$$

exactly [Gol98]. Taking the increase of the dynamic range by the rf-signal frequency compensation into account, we actually need the high-pass FPI characteristic Fig.6.3. Compensation, namely low-pass filtering has to be realized in the reconstruction algorithm adjusted by reference measurements from interferometer, blackbody radiation or electro optical sampled rf-pulses. The FPI's sharp filter characteristic should replace the currently installed waveguide.

6.1.3 Multi-mesh (folded) Fabry-Perot interferometer

A multi-mesh FPI (MMFPI) consists of several meshes. Most applications of the far-infrared physics community concern higher order filtering with an improved selectivity for continuous rf-radiation in rf-systems. Higher order filters are realized by several sandwiched meshes with individual element shapes. For modeling MMFPI's beam diffraction, truncation, walkoff effects and absorption of the meshes must be taken into account. According to section 6.2, our collaboration improved the junctions response dramatically by a factor of approximately 14. The requirements on the FPI system simplify dramatically by using several arrays operating at different frequencies. Fig.6.5 shows the spectrometers MMFPI with variable spacing and planar meshes. Once understanding, that diffraction is always present in quasioptical systems, we de-

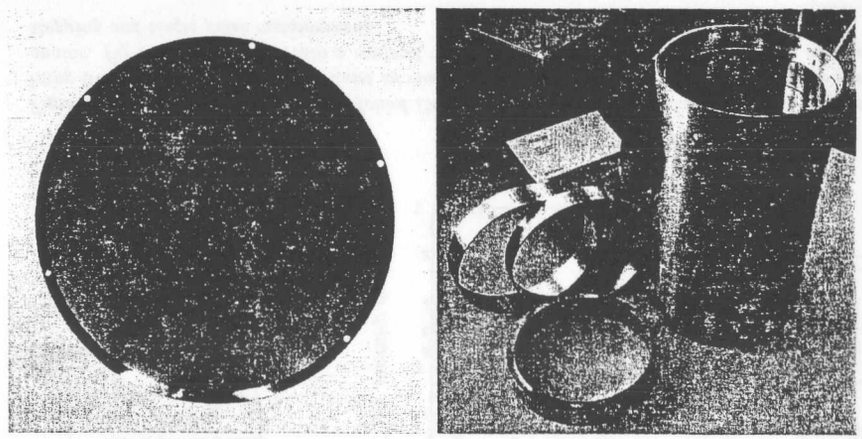

Figure 6.5: *(a) Two-dimensional freestanding planar stripline grids with spacing $g = 100\mu m$, squared hole size $d = 50\mu m$. (b) MMFPI with 20cm aperture, spacer and mesh holder for use on top of the TTF-spectrometer.*

termine the edge taper $T_e(a)$, namely the fractional rf-power loss per pass for a given aperture a and gaussian beam size w. According to the gaussian beam approximation Eq.6.7, diffraction, namely beam truncation from finite quasioptical apertures, limits the production of rf-pulses with long spacing. To show this, we unfold the beam propagation of the previously discussed FPI, with planar mirrors. As depicted in Fig.6.6a the propagation is simply equal to the unperturbated one without diffraction. The beam size spreads w_n after n rf-pulses $z = d(n-1)$ with pulse spacing $d = \Delta T c/2$, beam waist w_0 and frequency $f = c/\lambda$. With the fractional loss per

pass $T_e(a)$ in cylindrical coordinates one finds [Gol98, Sie86]

$$T_e(a) = 1 - F_e(a) = 1 - \int_{r=0}^{r=a} |E(r,z)|^2 \, 2\pi \, r \, dr = e^{-\frac{2a^2}{w^2}} \quad \forall \quad \frac{|E(r,z)|}{|E(0,z)|} = e^{-\frac{r^2}{w^2}} \tag{6.7}$$

$$w_n = w_0 \sqrt{1 + \left(\frac{c^2 \Delta T (2n-1)}{2\pi f w_0^2} \right)^2} \tag{6.8}$$

$$n = \frac{2\pi f w_0^2}{c^2 \Delta T} \sqrt{-\frac{2a^2}{w_0^2 \ln T_e} - 1} + \frac{1}{2} \approx \frac{\sqrt{2}\pi a w_0 f}{c^2 \Delta T \sqrt{-\ln T_e}} \quad \forall \quad n \gg 1. \tag{6.9}$$

According to Fig.6.6b the beam spreads for planar meshes. The truncation limits the generation of rf-pulses with long spacing required for bias current stepping of a single pulse measurement. The truncation loss for small rf-pulse spacing can be negelected.

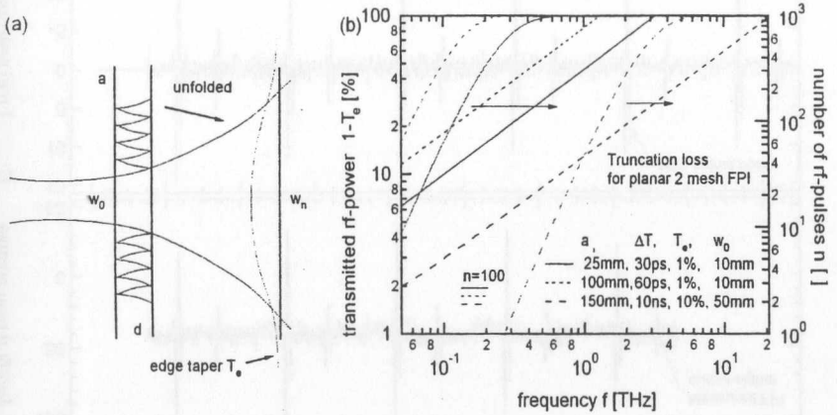

Figure 6.6: *(a) Unfolded two-mesh FPI with planar meshes. (b) Maximum number of replicated rf-pulses limited due to truncation loss of finite aperture for different FPI's.*

As depicted in Fig.6.7a, the folded FPI with curved meshes prevents a beam spread to by mapping the beam distribution onto itself. Practically, so called compact ring resonators, using focussing reflective mirrors and planar meshes for beam coupling are more established [Les90]. Here, diffraction is minimized but also in principle present. According to [Gol98] and Fig.6.7a, one has to find a minimum beam size for a confocal resonator with mirror radii of curvature $R_1 = L, R_2 = L$, spacing L, $d_1 = d_2 = L/2$ and g-Parameter $g = 0$. Inserting the beam size into Eq.6.7 after n round trips, we find the truncation loss and available number of rf-pulses for a confocal resonator.

$$w = \sqrt{\frac{\lambda L}{\pi \sqrt{1-g^2}}} \quad \forall \quad g = 0, \qquad n = -\frac{4\pi a^2 f}{c^2 \Delta T \ln T_e} \tag{6.10}$$

Considering a more realistic field distribution at the coupling apertures than from gaussian beam mode, more accurate calculations for a confocal geometry, well known from laser physics, are given by [Sie86] for n passes

$$T_e = \left[16\pi^2 N_f\right]^{\frac{1}{n}} e^{\frac{-4\pi N_f}{n}}, \quad T_e = \left[1 - (\pi N_f)^2\right]^{\frac{1}{n}}, \quad N_f = \frac{2a^2 f}{c^2 \Delta T} \tag{6.11}$$

$$n = \frac{-4\pi N_f + \ln\left(16\pi^2 N_f\right)}{\ln T_e} \tag{6.12}$$

and plotted for different apertures in Fig.6.7b.

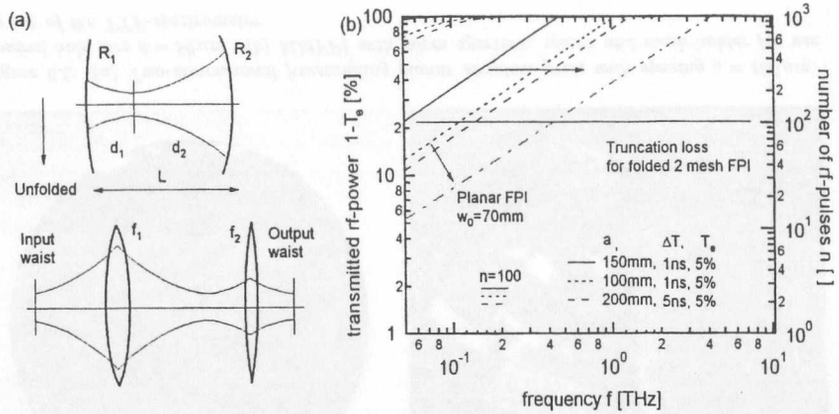

Figure 6.7: *(a) Normal (top) and unfolded (bottom) resonator configurations. The input waist being transformed into an output waist by means of making a complete circuit through the resonator. (b) Pulse replication with a confocal resonator with long pulse spacing for bias current stepping and single pulse measurement.*

Placing dielectric materials for smaller dimensions within the FPI reduces the finesse. Folding the path elimates lateral offsets and walkoff effects. Using longer rf-pulses spacings ΔT requires an increased aperture. Guiding the beam for longer pulse spacing over more focussing reflective mirrors is identical to the unfolded FPI and increases also the truncation loss. Inserting the folded FPI into a waveguide eliminates the truncation loss for the lower frequencies. Instead of using focussing reflective mirrors within a straight-lined waveguide, meshes have to be glued onto a convex dielectric substrate [3]. Fig.6.9c shows a compact approach offering a large aperture.

However, as depicted in Fig.6.8, the freezing out of higher frequencies for increasing replicated rf-pulses can also be taken into account within the reconstruction algorithm. The time domain analysis of the FPI clearly indicates, that depending on the rf-pulse number n, different transfer functions for reconstruction have to be considered. The second rf-pulse simply passes twice the mesh reflectivity characteristic, the nth pulse $2(n-1)$ times. This effect vanishes for a reflectivity small enough in the considered frequency range. Consequently, the measurement of high frequency components has to be done for the first pulses and lower frequencies at last pulses. By multiplying the time dependent decay from diffraction effects of Fig.6.7 truncation effects are included in the simple equivalent circuit. As long as the FPI or quasioptical input coupling system is a LTI system, the Josephson junction sees a well defined transfer function at the selected frequency. Even when we do not distinguish between rf-pulses, as it is the case for averaging from an FPI at fixed bias current. Because the transfer function of meshes and FPI are fixed and can be measured in detail with Fourier spectroscopy or electro optical sampling , considering these effects within the reconstruction algorithm is straightforward.

[3] Care must be taken, that glue does not enter the resonantor.

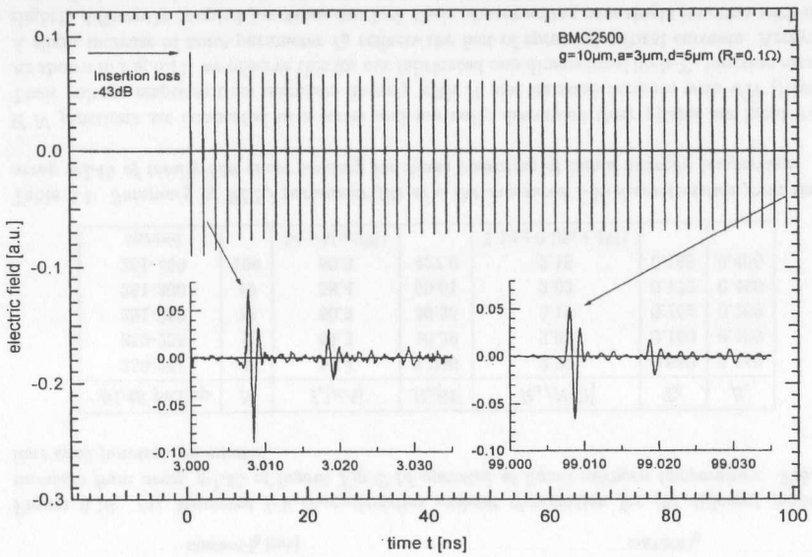

Figure 6.8: *PSPICE simulated two-mesh FPI with long rf-pulse spacing of 2ns. With resistive losses $R_l = 0.1\Omega$ at $f = 100GHz$ the mesh parameter are $g = 10\mu m$, $a = 3\mu m$, $d = 5\mu m$. The inset (same units) shows the freezing out of high frequency components from first rf-pulse $n = 2$ to last rf-pulse $n = 50$.*

In summary, we suggest an optimized quasioptical input coupling system. A time domain analysis of a three-mesh FPI confirms, that reflected pulses from the second FPI bounce back into the first one producing unacceptable difference frequencies and pulse shapes. Furthermore, the insertion loss increases rapidly. As shown in Fig.6.9 a second FPI slightly misaligned from optical axis is advantageous. This prevent back reflections into the folded FPI. The beam displacement from FPI lets the beam running out after several reflections of the junctions focus into an absorber material. This causes, that the actual replicated rf-pulse series finishes after the next long spacing replicated rf-pulse occurs. With it, a strong coupling, as it is the case for the three-mesh FPI in both beam directions exists, occurs only in forward direction. Optional, filters can be placed in front of the junction for a frequency domain rf-signal compensation. For lower insertion loss, reflective mirrors with rank grooves for different propagation delays having no dominant LC-resonant behavior in the transmittance and promise an operation at higher frequencies. Fig.6.9 shows a suggested quasioptical input coupling system with waveguided folded FPI for long pulse spacing and FPI for finite rf-pulse generation. A system of reflective folded mirrors by using ring resonators should also possible. The main features are given by a

Proposition 23:
- *Folded FPI for long pulse spacing with focussing meshes or reflective mirrors.*
- *FPI for small pulse spacing and finite pulse number.*
- *Guiding all quasioptical elements in a waveguide reduce beam truncation.*
- *Reduce back reflections by misalignments.*

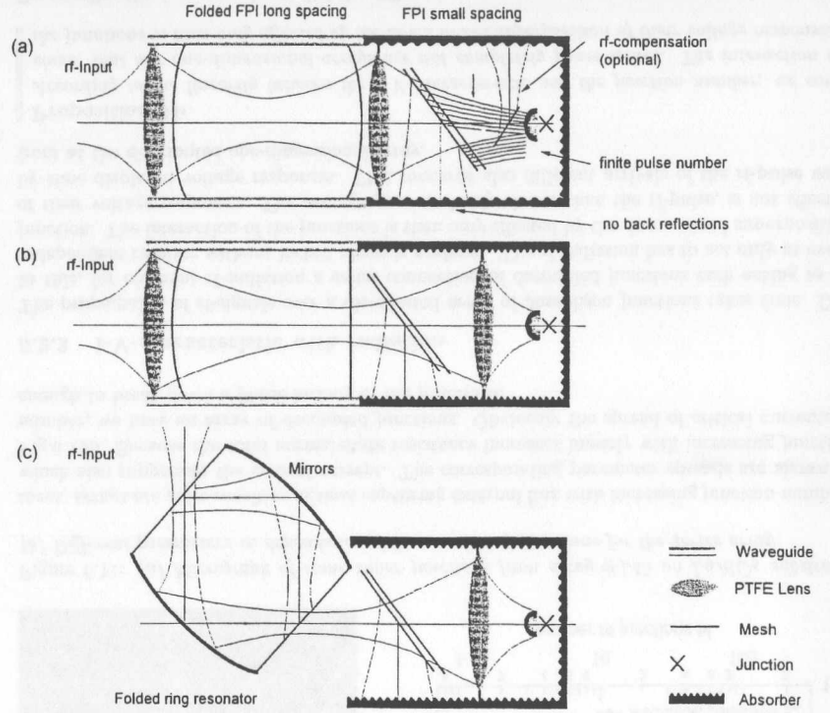

Figure 6.9: *Quasioptical input coupling system for single pulse measurements. (a) Confocal folded FPI for long and FPI for small pulse spacing. (b) Simple configuration for a changeable dewar with liquid helium cooling. (c) Folded ring resonator with curved mirrors and planar meshes without waveguiding.*

6.2 Josephson junction arrays

Josephson junction arrays increase the signal-to-noise ratio (SNR) of voltage responses dramatically. As discussed in section 4.6, the measuring time can be reduced for having a single- or improved macro-bunch measurement. This requires two dimensional arrays or series connection of junctions with almost same normal-state resistance R_n and critical current I_c.

6.2.1 I-V-characteristic without radiation

Fig.6.10 shows I-V-characteristics of a series array of different junction numbers without irradiation. Tab.6.1 lists each junction parameter. A slight increase of noise parameter Γ_0 states the fact of distributed critical currents. The arrays are more sensitive against captured external flux

with increasing junctions number. This also suppresses the critical current. Additional noise contributions are caused from the increased junction resistance divided by the source impedance. Current noise from the input stage of readout amplifier is fed back over the voltage lines due to the increased source impedance and give rise to additional noise.

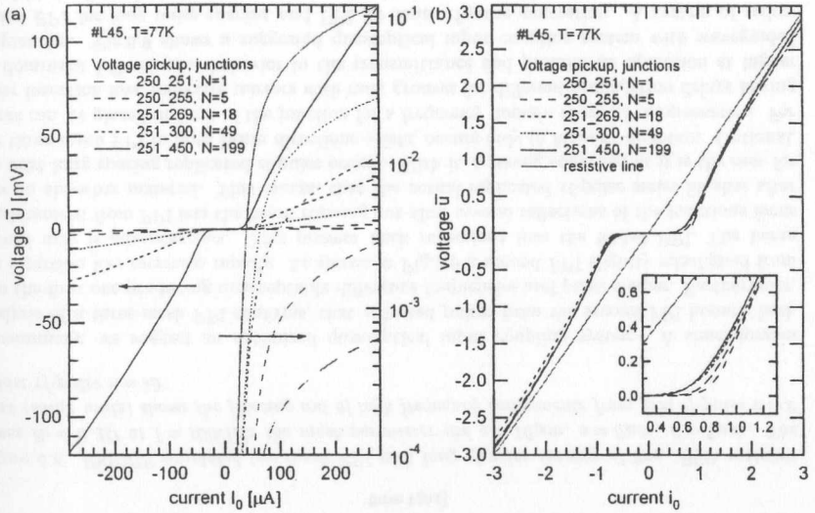

Figure 6.10: *(a) Measured I-V-characteristics without rf-radiation for (b) different junction numbers from array #L45 of layout Fig.C.1d operated at liquid nitrogen temperature. Tab.6.1 lists each junction parameter.*

#L45 pickup	N	$I_c[\mu A]$	$R_n[\Omega]$	$R_n/N[\Omega]$	Γ_0	β_c
250-251	1	53.4	2.266	2.27	0.080	0.144
250-255	5	61.3	10.39	2.08	0.100	0.106
251-269	18	50.3	39.35	2.19	0.164	0.280
251-300	49	58.4	99.61	2.03	0.172	0.460
251-450	199	50.3	427.0	2.15	0.188	0.400
spread		54±5(±9%)		2.14±0.09(±4%)		

Table 6.1: *Summary of RCSJ parameter fits of a the measured I-V-characteristics from series array #L45 of totally 550 grain bondary junctions operating at liquid nitrogen temperture.*

If N junctions are connected in a series and mutually decoupled their phases are incoherent. Their voltage response then increases linearly with N and its noise increase with $\sqrt{N}$ [Kre99]. As shown in Fig.6.11, we observe this for our fabricated one-dimensional high-T_c junction arrays. A slight increase of noise parameter Γ_0 reflects the fact of spreaded critical currents. Arrays of slightly differently coupled junctions can lock their phases acting as a single junction with dramatically improved parameters [Opp97]. Although the junctions are transmission line coupled, a sufficient large spread of the junction parameters R_n and I_c prevent a phase locked coherent state. We have designed different types of arrays. Fig.C.1c shows a one-dimensional series array

of 128 junctions coupled to a fin antenna biased by a LP-antenna. A cut of some inner junctions from #L45 chip is shown in Fig.6.11a. The I-V-characteristic of several voltage pickups of a one-dimensional array with 550 grain boundary junctions Fig.C.1d is shown in Fig.6.10. A slight increase of noise parameter states the fact of spreaded critical currents. Within the measure-

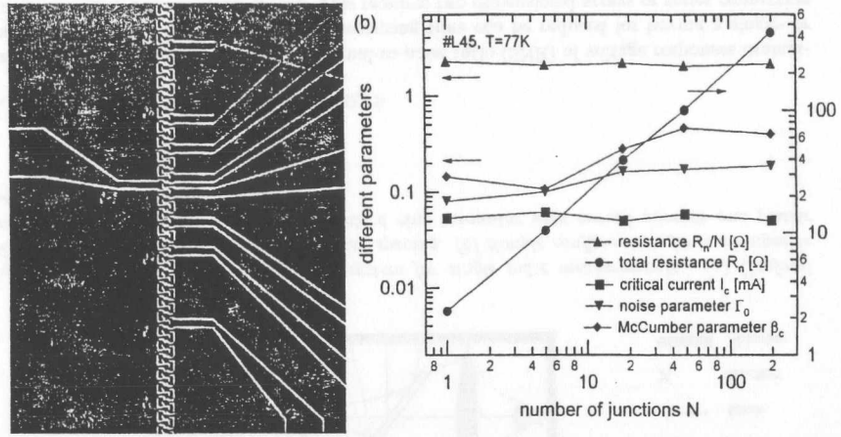

Figure 6.11: *(a) Micrograph of some inner junctions from array #L45 on $LaAlO_3$ substrate. (b) Different parameters in dependence of the number of junctions for the series array.*

ment, arrays are more sensitive against capturing external flux with increasing junction number, which also suppresses the critical current. The corresponding parameter spreads are shown in Fig.6.10b. Because the total normal-state resistance increases linearly with increasing junction number, we have an array of decoupled junctions. Obviously the spread of critical currents is enough to break down a phase locking of the junctions.

6.2.2 I-V-characteristic with radiation

The propagation of rf-signals over a distributed array of Josephson junctions takes time. Due to this, for coherent rf-radiation a series connection of decoupled junctions each acting as an independent receiver without locked phase is prefered. The rf-radiation has to act only at every junction. The interaction of the junctions is then only effected by the down mixed superposition of their voltage responses. The averaging, remarkably slower than the rf-pulse, is not effected by time displaced voltage responses. This concerns also different arrivals of the rf-pulse wave front at the distributed one-dimensional array.

Proposition 24:
According to the linearity between the I-V-characteristic and the junction number, we conclude, that our one-dimensional arrays are not completely phase locked. The interaction of the junctions is then only affected by the down mixed superposition of their voltage responses.

Practically, the junctions have slightly different parameters using a current biasing resulting in a superposition of slightly different rf-characteristics. Therefore, as depicted in Fig.6.12c, Shapiro steps occur not neccessary exactly at the irradiated frequencies and the assumption for spectroscopy $\bar{u} = \Omega$ is not valid, as it is required for the Volt standard. The center frequencies

deviate of about 9% and the linewidths differ by a factor of 3 from the expected ones. Obviously caused by the spread of junction parameters. Especially when using a series of rf-pulses and non-overlapping Shapiro steps, systematic errors concerning the center frequency can be corrected.

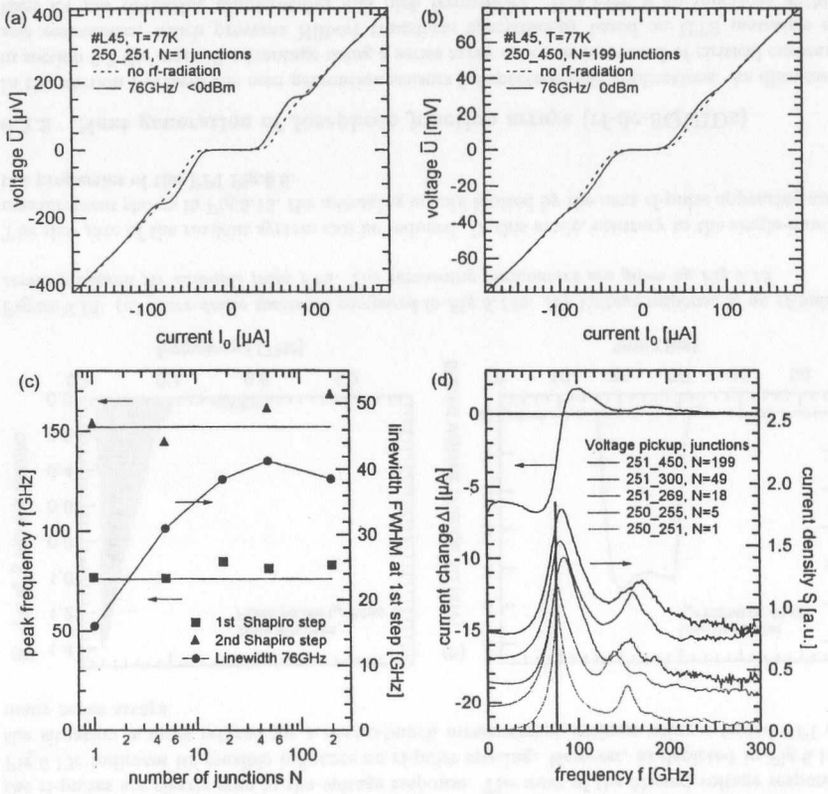

Figure 6.12: *(a),(c) Measured I-V-characteristics with rf-radiation for different junction numbers. (b) Spread of linewidth and center frequency for the 1st and 2nd Shapiro step. (c) Current response and reconstructed normalized Hilbert spectrum.*

The spread of critical currents and normal-state resistances of bicrystal junctions are typically gaussian distributed of about 10%. The spread decreases with decreasing normal-state resistance caused by the stochastical spatial distribution of the junctions grain boundary. In fact, for an operation using small linewidths at low temperature or high frequency the superposition of the junctions responses gets ineffectively. Especially when using a frequency domain rf-signal compensation operating mainly in the resistive part of the junctions I-V-characteristic, the normal-state resistance of each junction within the series array must be adjusted in-situ during or after the preperation process.

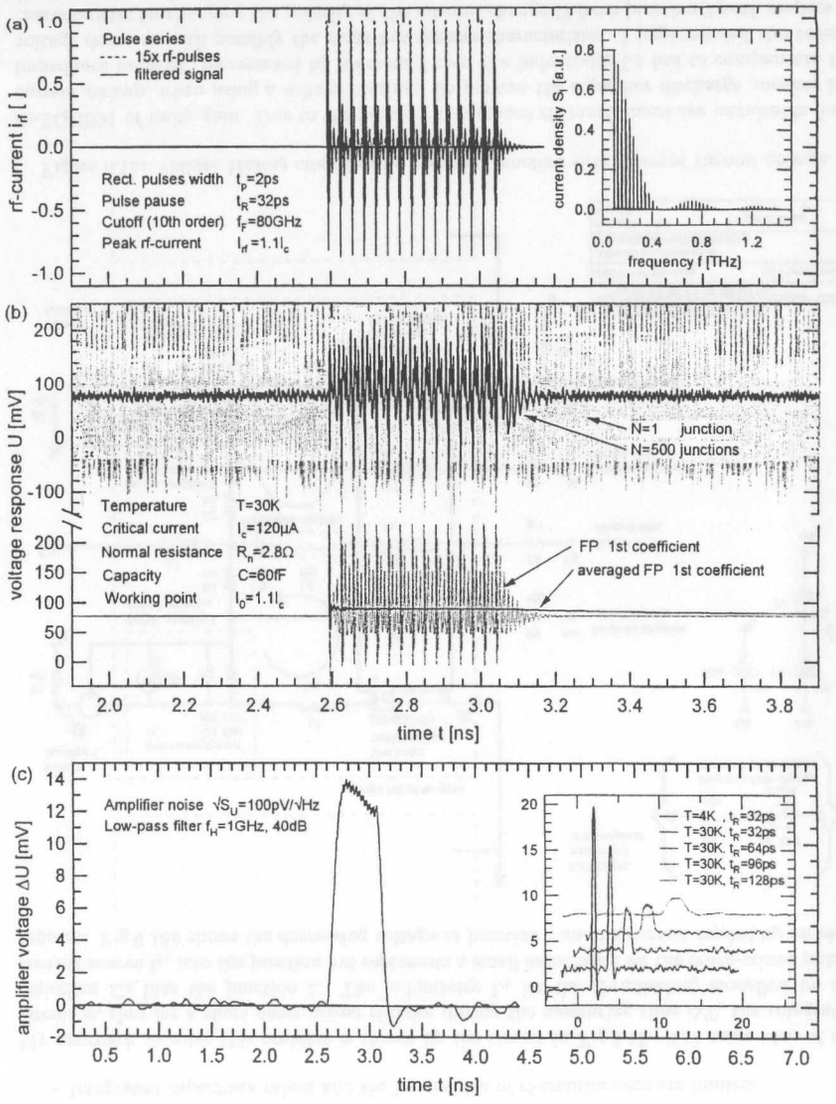

Figure 6.13: *(a) Runge-Kutta and FP simulated (2nd order) voltage response of a low-pass filtered rf-pulse series and its (b) voltage response for N mutually decoupled Josephson junctions. The inset of the (c) amplifier filtered voltage response shows the influence of voltage response from rf-pulse spacing.*

Josephson junction arrays not yet have been measured at the TTF linac. To show the substantial improved signal-to-noise ratio of a series of junctions, its simulated voltage response for completely uncorrelated noise contributions is shown in Fig.6.13. Only a few replicated rf-pulses are sufficient to measure a frequency component at sufficient large temperature and conservative I_cR_n-products, where they should do not show any structure in I-V-characteristic caused from the critical current spread. This should be guaranteed by using a large number of junctions resulting in a symmetric current response. Otherwise its signal-to-noise ratio gain renders the possibility for noise rounding the I-V-characteristic for operation at higher temperatures. The signal-to-noise ratio gain from series array of about $\sqrt{N} \approx 22$ mainly used here for an operation at higher temperature of the spectrometer. The Josephson oscillation averages out and the rf-pulses are clearly seen in the voltage response. The inset of the filtered voltage response Fig.6.13c indicates its sensible influence on rf-pulse spacing. However, as depicted in Fig.6.14, the situation is more relaxed for a macro-bunch measurement without using a folded FPI or many series arrays.

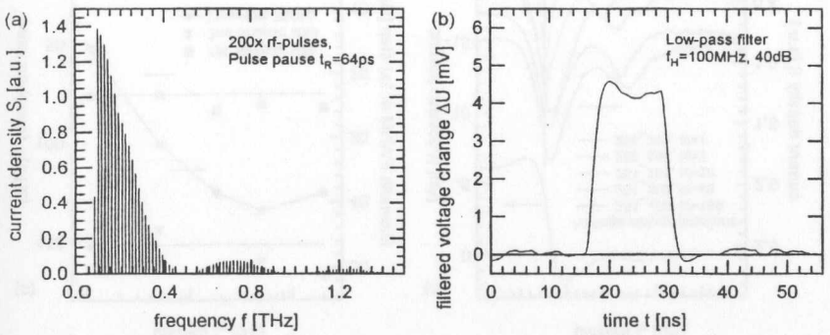

Figure 6.14: *(a) More dense spectrum compared to Fig.6.13a. (b) Voltage response of an rf-pulse series produced for example from FPI. The remaining parameters are given by Fig.6.13.*

The slew rate of the readout system can be reduced. In this mode, contrary to the single-bunch measurement shown in Fig.6.13, the averaging is only limited by the next rf-pulse appearing and the properties of the FPI Fig.6.6.

6.2.3 Next generation of Josephson junction arrays (rf-dc-SQUIDs)

In this section I present the next generation sensors for spectroscopic applications. As discussed in section 6.2 the main disadvantage using a series array concerns its spread of ciritical currents and resistances, which prevents Hilbert transform spectroscopy based on HTS materials at least for low operating temperatures and high frequencies. But even if all junctions within a series array are identical it must be guaranteed, that all junctions get the same rf-power and produce an identical Shapiro step. Experimentally this is difficult to fulfill. Getting independent of the junction parameter spread and the rf-coupling every junction within the series array must be voltage biased $\Delta\bar{u}=0$ and a pickup of the current change Δi must be realized.

A voltage biasing can be either done by a current biased junction using a fast regulation, as discussed in section 6.3 or biasing the junction directly. There are several experimental limitations making a voltage biasing for junctions with small normal-state resistance R_n difficult.

- The voltage source impedance X_S must fulfill $X_S \ll R_n \approx 0.1\Omega$.
- Connections onto the chip involves reactances much higher than X_S.
- Integrated capacitors values and the bandwidth of rf-transformers are limited.

My approach to solve this problem is shown by the circuit in Fig.6.15. The basic idea of the circuit is, that for a short down-mixed rf-pulse during the measuring time ΔT, the integrated capacitor C_3 bias the junction 1. The inductivity L_1 let the rf-radiation, modelled by the current source I_1, into the junction but represents a small inductance for the down-mixed pulsed reponse. Fig.6.16b shows the decreasing voltage at junction 1 and its current readed by an ideal

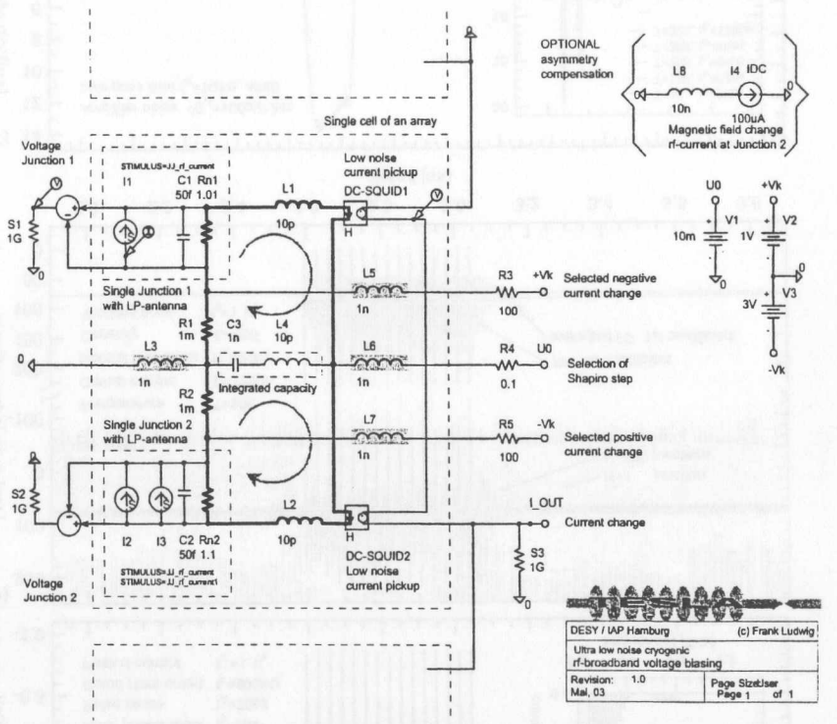

Figure 6.15: *Voltage biasing circuit using a second junction with reversed current change.*

dc-SQUID1 of unity gain. Due to the primary inductance rf-transformers are unsuitable for a current pickup, when using a voltage biasing. To prevent the capacitor discharge another low impedance network, represented by junction 2 over the inductivity L4 has to compensate the voltage decrease with possibly the same but reverse characteristic. I implemented the reverse characteristic by changing the polarity of the current change I2 from junction 2 with respect to I1. According to Fig.6.16b the mirror network improves dramatically the stability of the voltage. The small glitches are caused from the decoupling inductivities L1, L2 and the slew rate of the pulsed currents I1, I2. As depicted in Fig.6.16a the reverse current change is guaranteed by having slightly different voltages within the networks with respect to the Shapiro step. In other

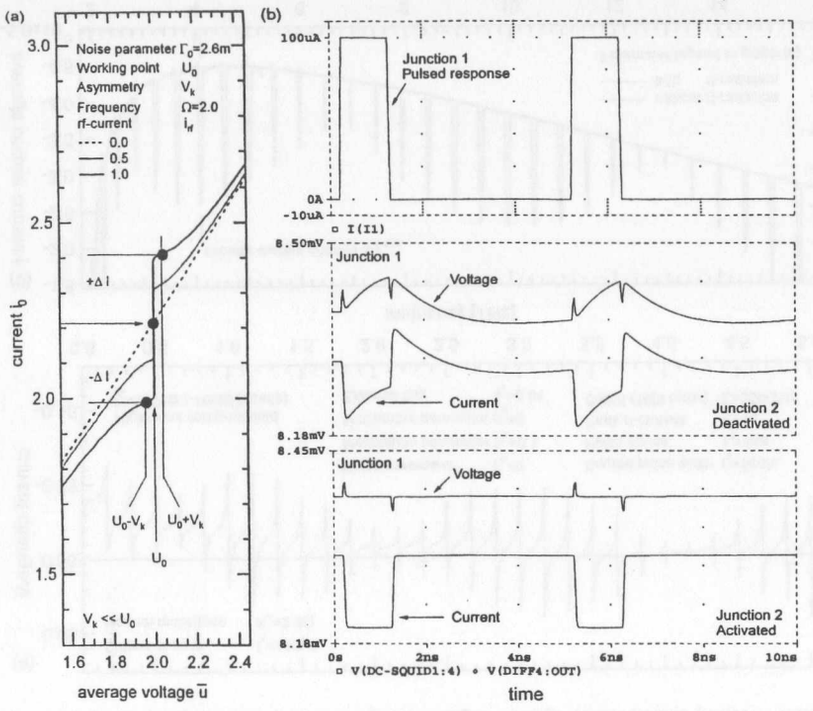

Figure 6.16: *(a) Schematic sketch of a voltage biasing by using a second junction with reversed current change and correction voltages. (b) PSPICE simulated pulsed current reponse I1 from down-mixed rf-radiation, voltage S1 and current time traces of junction 1.*

words, the symmetry breaks by using a voltage drop $\pm V_k$ generated by the resistances R1, R2. The operation is then characterized by

$$\begin{aligned} &\text{Junction 1: } \bar{U}=U_0-V_k,\ -\Delta I=I(U_0-V_k,i_{rf}\neq 0)-I(U_0-V_k,i_{rf}=0)\leq 0\ \ \forall\ V_k,\Gamma_0\to 0 \\ &\text{Junction 2: } \bar{U}=U_0+V_k,\ +\Delta I=I(U_0+V_k,i_{rf}\neq 0)-I(U_0+V_k,i_{rf}=0)\geq 0. \end{aligned} \tag{6.13}$$

The main advantage of this concept is, that the capacitor has to compensate only the difference between the pulsed current responses I1, I2. This is taken into account by using the current source I3. The circuit operates at very low junction resistances and is independent of the junctions parameter spread. If both networks are identical the capacitor C3 can be left. In this case both junctions represent simply a symmetric irradiated dc-SQUID. According to Fig.6.17, I name it rf-dc-SQUID. The phase coherence condition of the Cooper-pair wavefunction of a dc-SQUID is given by

$$\delta_2-\delta_1+\oint \vec{A}d\vec{l}=\delta_2-\delta_1+2\pi\frac{\Phi_t}{\Phi_0}=2\pi n,\quad \text{with}\quad \Phi_t=\Phi_a+LJ+\eta L\frac{I}{2},\ n\in N, \tag{6.14}$$

where the integral defines the collected vector potential $\vec{A}$ from SQUID loop. The total flux Φ_t

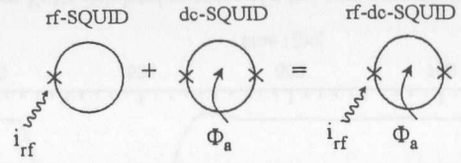

Figure 6.17: *Symbolic definition of an rf-dc-SQUID.*

penetrates the rf-dc-SQUID loop and consists of the external applied flux Φ_a, the self induced flux LJ from circular current and the flux produced from different bias currents I_1, I_2 of the different junction branches. δ_1, respectively δ_2 denotes the junctions phase differences. The current change from rf-radiation should be given in analogy to the circuit Fig.6.15 by the averaged circular current J. In normalized quantities we yield

$$j=\frac{i_1-i_2}{2}=\frac{\delta_1-\delta_2-2\pi\phi_a}{\pi\beta_L}-\eta\frac{i}{2},\qquad i_0=i_1+i_2. \tag{6.15}$$

The modulation depth parameter β_L is defined by $\beta_L=2LI_c/\Phi_0$, where L is the inductivity between both junctions. $\phi_a=\Phi_a/\Phi_0$ denotes the external normalized flux. To simplify I restrict the simulations to a symmetric rf-dc-SQUID with $\eta=0$. Instead of reviewing the formalism of dc-SQUIDs from [Sta95] and its numerical implementations, I proove, that Hilbert transform spectroscopy can be used with rf-dc-SQUIDs. Fig.6.18a shows the simulated response of a symmetric rf-dc-SQUID for monochromatic rf-radiation. Without external flux both junctions

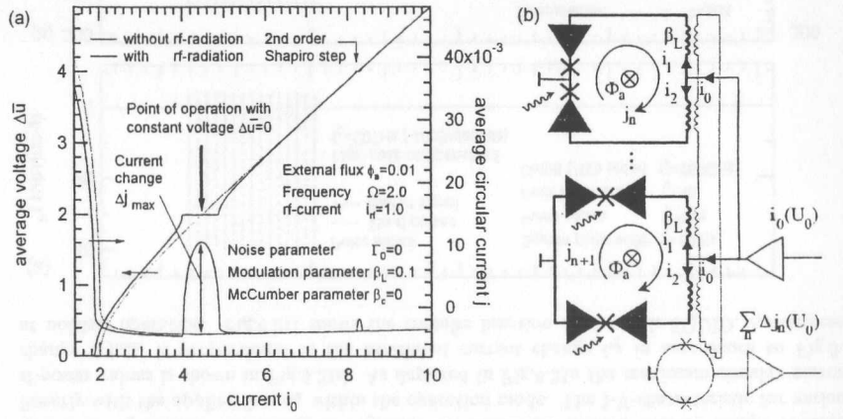

Figure 6.18: *(a) Runge-Kutta simulated I-V-characteristic and circular current response of an rf-dc-SQUID for voltage biased Josephson junctions using monochromatic. (b) Conceptual design for an rf-dc-SQUID series array.*

operates independently and the averaged circular current j vanishes. In contrary to the high frequency circuit shown in Fig.6.16, an rf-dc-SQUID addional fulfill the phase coherence condition of the superconductors. It is obvious, instead of applying a correction voltage, that the symmetry break can be done by using a small external flux. In fact, for $\phi_a\neq 0$ the averaged circular current do not vanishes at the Shapiro step. According to Fig.6.18a the rf-dc-SQUID,

which operates exactly at the crosspoint of the pertubated and unperturbated I-V-characteristic confirms a constant averaged voltage $\Delta\bar{u}=0$ and therefore the operation of the successful voltage biasing. At this working point the circular current gain its maximum, as expected. The simplified measuring setup of an rf-dc-SQUID series array is shown in Fig.6.18b. The circular current change Δj_{max} is detected by a second dc-SQUID. Both junctions are biased by a single LP-antenna. The circular currents are collected from different rf-dc-SQUIDs by using integrated rf-transformers with sufficient broadband characteristic. The main advantage using a superconductive loop is, that the loop inductivity β_L consisting of the antennas and transformers impedance can be dimensioned much larger than it is the case for the high frequency circuit shown in Fig.6.15. This is caused, according to the voltage of a symmetric dc-SQUID

$$v=\frac{1}{2}\frac{d\delta_1}{d\tau}+\frac{1}{2}\frac{d\delta_2}{d\tau} \tag{6.16}$$

by the phase coherence condition Eq.6.14 of the Cooper-pair wavefunction of the dc-SQUID. An asymmetry of the junctions critical currents, resistances or inductivities effects only the shape of the I-V-characteristic, but not the voltage biasing concept. In this case each rf-dc-SQUID has to be biased seperately. The noise rounding of the I-V-characteristic is caused by thermal activated phase jumps, which produce a pulsed output voltage characteristic [Sta95]. Within

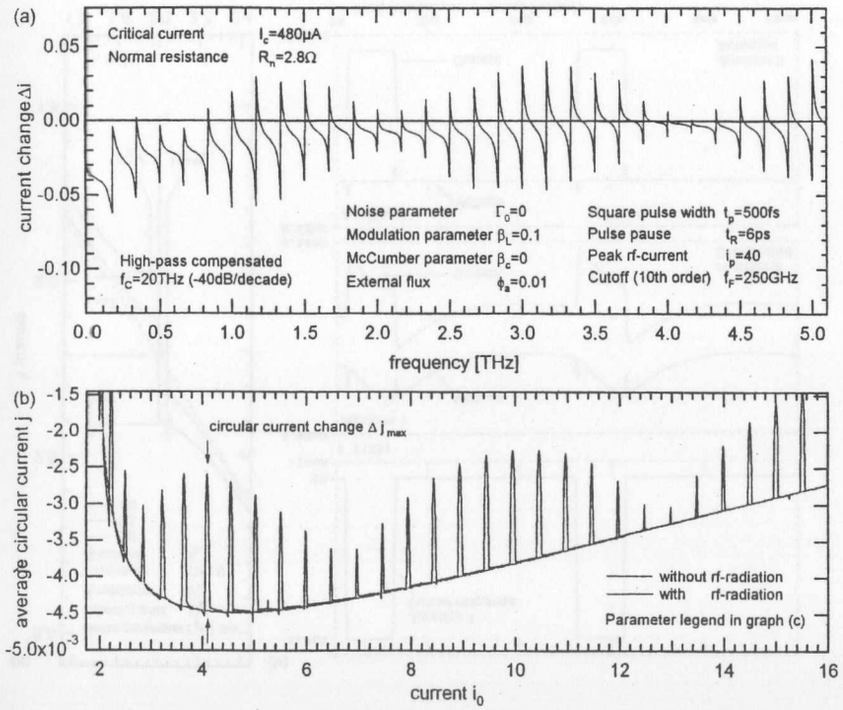

Figure 6.19: *Runge-Kutta simulated averaged (a) current change and (b) circular current response of an rf-dc-SQUID for voltage biased Josephson junctions using coherent rf-radiation.*

an rf-dc-SQUID series array with uncorrelated temperature fluctuations this effect should be negligible. Fig.6.19a,b shows the simulated averaged current and averaged circular current response of an rf-dc-SQUID irradiated with coherent rf-radiation. As expected, according to Fig.6.20, the voltage biasing concept of the junctions using rf-dc-SQUIDs works also for coherent rf-radiation during pulsed operation, especially when using small normal-state resistances. The dependence of the I-V-characteristic and circular current change on the applied flux ϕ_a is shown in Fig.6.21a,b. According to Fig.6.21c the maximum circular current change is scaled linearly with the applied flux ϕ_a within the operation mode. The I-V-characteristic for various rf-power values is shown in Fig.6.21d. As depicted in Fig.6.21e the maximum circular current change Δj_{max} is proportional to the irradiated current change i_{rf} in accordance to Fig.3.5 at noisless operation. Fig.6.21f shows the transfer function of the rf-dc-SQUID. As depicted

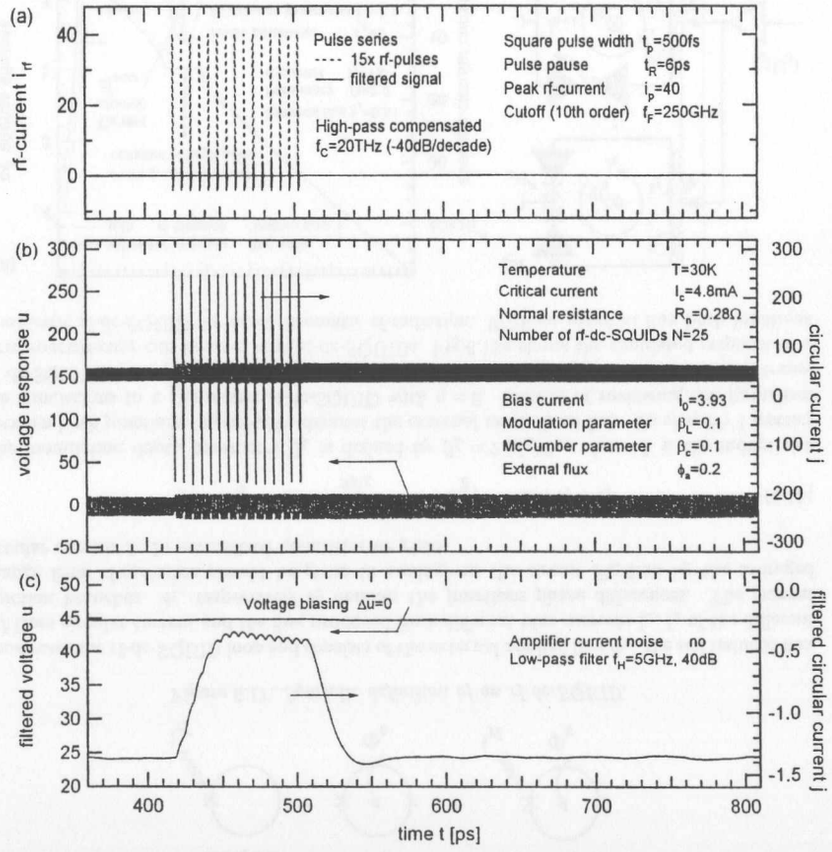

Figure 6.20: *Runge-Kutta simulated response of a low-pass compensated (a) rf-pulse series using a series array of rf-dc-SQUIDs with small normal-state resistances. (b) Corresponding voltage and circular current response after (c) low-pass filtering.*

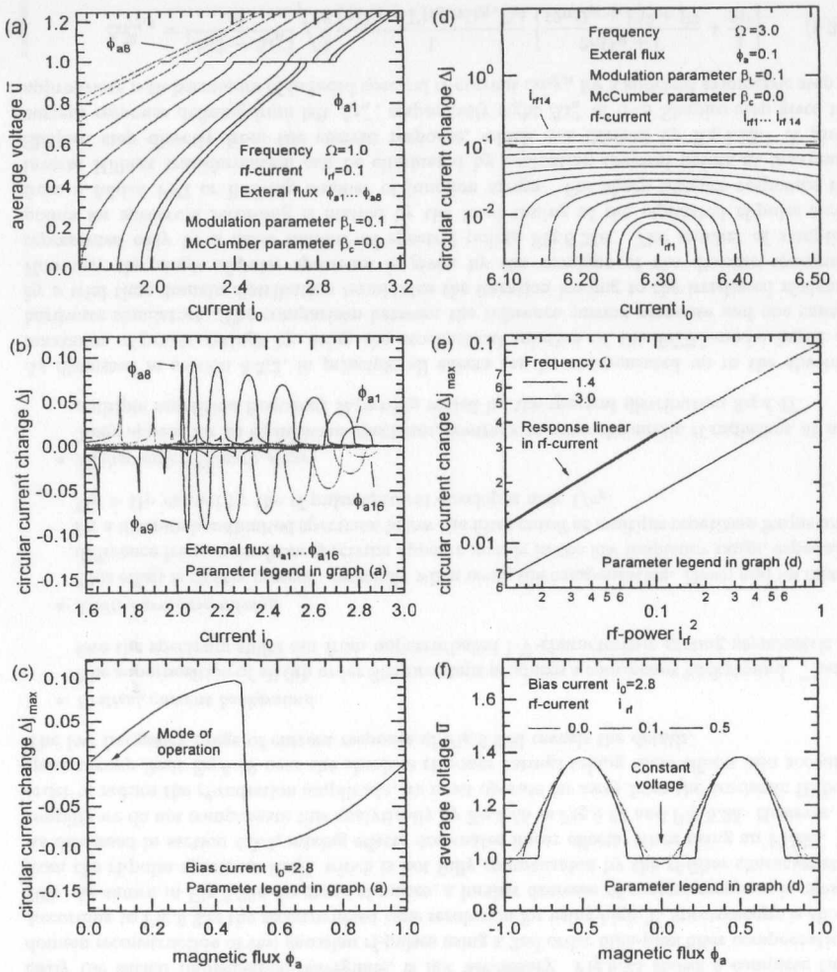

Figure 6.21: *Runge-Kutta simulated (a) I-V-characteristic, (b) circular curent change and its (c) flux dependence for a single Shapiro step irradiated on a symmetric rf-dc-SQUID. The flux is varied by $\phi_{an} = 0.0594n + 0.01$. (d), (e) Circular current in dependence of rf-power for $i_{rfn}^2 = 10^{(4n+40)a-4}$, $a = 5.204/97$ and (f) transfer function of a symmetric rf-dc-SQUID.*

the voltage is constant for a sufficient small applied flux. Therefore the rf-dc-SQUID itself cannot be used to pickup the circular current change. I emphasize, that the current readout is exactly only valid for symmetric Shapiro steps. For analyzing asymmetric Shapiro steps, its shape or continuous spectra the assumption for voltage biasing is no more valid. Similar to the limitations of Hilbert transform spectroscopy, further analytical or numerical calculations

have to be investigated. Here, I consider only the symmetry of a Shapiro step. In fact, the symmetry of the I-V-characteristic itsself can also be useful for generating the current reponse asymmetry. The sensor might play an important role for future rf-applications using continuous rf-radiation, because the external magnetic flux represents an additional chopper port, which promises the suppression of all 1/f-noise sources.

Proposition 25:
The presented rf-dc-SQUID detector combine a very low-noise pickup, high readout bandwidth, voltage biasing of junctions with small normal-state resistances. The detector is independent of the junctions parameter spread and offers the opportunity for high integration without external regulations.

6.3 Frequency domain rf-signal compensation (FDSC)

In this section the most important improvement of the TTF-spectrometer is presented. It strikes that the measured Hilbert spectra, weather for continuous or pulsed rf-radiation, are limited to a relative small bandwidth due to the decreasing signal-to-noise ratio with frequency. This is due to the fact, that the current response Eq.3.22 and Eq.4.36 of the Josephson junction decreases far away from critical current with $1/\Omega^2$ As shown in section 4.6 by Fig.4.27f, although the signal-to-noise ratio gain of approximately 15 from series arrays, 3 from increased I_cR_n-product and 5 from frequency separation of FPI with small rf-pulse spacing, cannot compensates the inverse quadratic decrease of current response for an high frequency operation. To circumvent the current response decrease, the input rf-power for higher frequencies must increased without disturbancies from higher order Shapiro steps of lower frequencies Fig.4.17a. We call this a frequency dependent rf-signal compensation or FDSC. For increasing the dynamic range of the detector several realizations are possible.

6.3.1 Fix frequency dependent compensation by quasioptical components

Far away from critical current, the current response Eq.3.19 decreases with $1/i_0\bar{u} \sim 1/\bar{u}^2$ with increasing frequency $\bar{u}=\omega_j/\omega_c$. The response function Eq.3.20 corrects this by multiplying the inverse. External white noise sources δi, especially from measurement system, also scaled up with increasing frequency by the response function,

$$\Delta i(\bar{u}) = \int_{-\infty}^{\infty} \Delta i(\bar{u}, \Omega)\, d\Omega + \delta i \tag{6.17}$$

resulting in a decreased signal-to-noise ratio. This is typical for reconstructed spectra using Hilbert transform spectroscopy [Schi]. To prevent this, especially for the TTF broadband application, an important improvement is to compensate the signal decrease by increasing the rf-guiding transfer function $|K_{rf}(\Omega)|$ in the high frequency range, respectively decreasing rf-guiding transfer in the low frequency range

$$g(\bar{u}) = \frac{8}{\pi}\,(\Delta i'(\bar{u}) + \delta i)\; i_0(\bar{u})\bar{u}, \quad \forall \quad \Delta i'(\bar{u}) = \frac{\pi}{8 i_0 \bar{u}}\, \mathcal{K}[|K_{rf}(\Omega)|\; s_i(\Omega)] \approx \text{const.}, \tag{6.18}$$

resulting in a more precise recovery of pulse shape. Contrary to astronomy applications at the TTF linac enough rf-power is provided [Gei99]. The voltage response gains dramatically in the high frequency range resulting in a nearly frequency independent signal-to-noise ratio ratio. As mentioned before, a minimum capable rf-pulse spacing increases the voltage response. Especially for non-overlapping spectral lines $\Gamma(\bar{u}) \ll \Omega_R$, the reconstructed spectrum Eq.3.29 is currently derived.

$$s_i(\Omega) = |K_{rf}(\Omega)|^{-1}\mathcal{H}^{-1}(g(\bar{u}))\pi k_s(\Omega,\Gamma_0) \quad \forall \quad k_s(\Omega,\Gamma_0) = \Gamma(\Omega) \tag{6.19}$$

The spectral reconstruction of a series of squared rf-pulses is shown in Fig.6.22 for a second order high-pass compensation filter characteristic $|K_{rf}(\Omega)|$. The reconstruction algorithm is listed in Fig.4.18. The pre-scaling of the rf-spectrum can be realized with quasioptical components like inductive meshes Fig.6.1 for various frequency characteristics. Placing the compensation filters in the rf-guide we have no further increase of noise contributions. Using this method the detectors dynamic range increase dramatically. Furthermore a high order cutoff filter, similarly the actual implemented waveguide, is not neccessary. Fig.6.23 shows a complete time domain reconstruction of two gaussian rf-pulses using a 2nd order high-pass filter compensation. According to Fig.6.23g the reconstructed time resolution for using high-T_c spectroscopy is about 70fs. As shown in Fig.6.23d for small rf-pulses, a further decrease of current response is caused from the rf-pulse spectrum itself, which is not fully compensated by the rf-filter characteristic. As discussed in section 4.5.3, mixing effects dominates linear effects, when using an FDSC. To simplify we do not compensate this analytically by Eq.4.55 in Fig.6.22 and Fig.6.23. However, in order to reduce the rf-radiation amplitude, we must operate far away from the academic Hilbert spectroscopy limit Eq.6.19 near the absolute rf-power ratings taking some effects into account. The low frequency range of current response of Fig.6.22d reveals the details.

- *Critical current background.*
  The superposition of all 0th order Shapiro steps produces a continuous background. Therefore the spectrum shifts out from unperturbated I-V-characteristic getting asymmetric.

- *Multi-harmonic mixing*
  This effect is clearly present, especially when using the compensation. Down and up mixed difference frequencies from spectrum appears mainly in the low frequency range, especially for a discrete bandlimited spectrum below the filter cutoff at multiple repetition frequencies $\Omega_R > \Omega_F$ caused by the rf-pulse spectral envelopes near $1/\tau_p$.

- *Higher order Shapiro steps*
  They appear for an equidistant spectrum, contrary to monochromatic rf-radiation, at *any* multiple repetition frequency $\Omega_n = n\Omega_R$ scaled by the spectral distribution Eq.4.47.

As discussed in section 4.3.2, in principle all effects can be compensated up to the absolute maximum rf-power ratings by using the stochastical solution of the RCSJ-model based on hardware simulators. The comparison between the reference current response and one caused by a trial time domain distribution terminates the iteration leading to the irradiated rf-signal. However, the single rf-pulse spectrum is given by the envelope of the discrete spectrum, represented only by a finite number of spectral points Fig.6.23e. The number of sampling points for spectrum recording is limited by the fixed timing of the replicated rf-pulse series from a folded FPI or limiting number of junction arrays. For sharp Shapiro responses the inverse Hilbert transformation can be eliminated by evaluating spectral points at maximum Shapiro step directly from the current response, which was derived by Eq.4.15. A given current response defining from left Δi_n^-, respectively right Δi_n^+ of n-th Shapiro step gives the appropriate n-th harmonics of induced spectral rf-current $\Delta\tilde{i}_{rf,n}$ for a suffcient symmetric step as

$$\Delta\tilde{i}^2_{rf,n} = \frac{|\Delta i_n^+ - \Delta i_n^-|}{2} \Big/ \frac{1}{8}\frac{1}{(n\Omega_R+\Gamma)i_0(n\Omega_R,\Gamma_0)}\left[\frac{2n\Omega_R+\Gamma}{(2n\Omega_R+\Gamma)^2+\Gamma^2}+\frac{1}{2\Gamma}\right] \tag{6.20}$$

$$\tilde{i}^2_{rf,n} \approx |\Delta i_n^+ - \Delta i_n^-|\; 4n\Omega_R\; i_0(n\Omega_R,\Gamma_0)\; 2k_s(n\Omega_R,\Gamma_0) \quad \forall \quad \Gamma \ll n\Omega_R,\; n>1 \tag{6.21}$$

$$s_i(n\Omega_R) = const.\; |K_{rf}(n\Omega_R)|^{-1}\tilde{i}^2_{rf,n}. \tag{6.22}$$

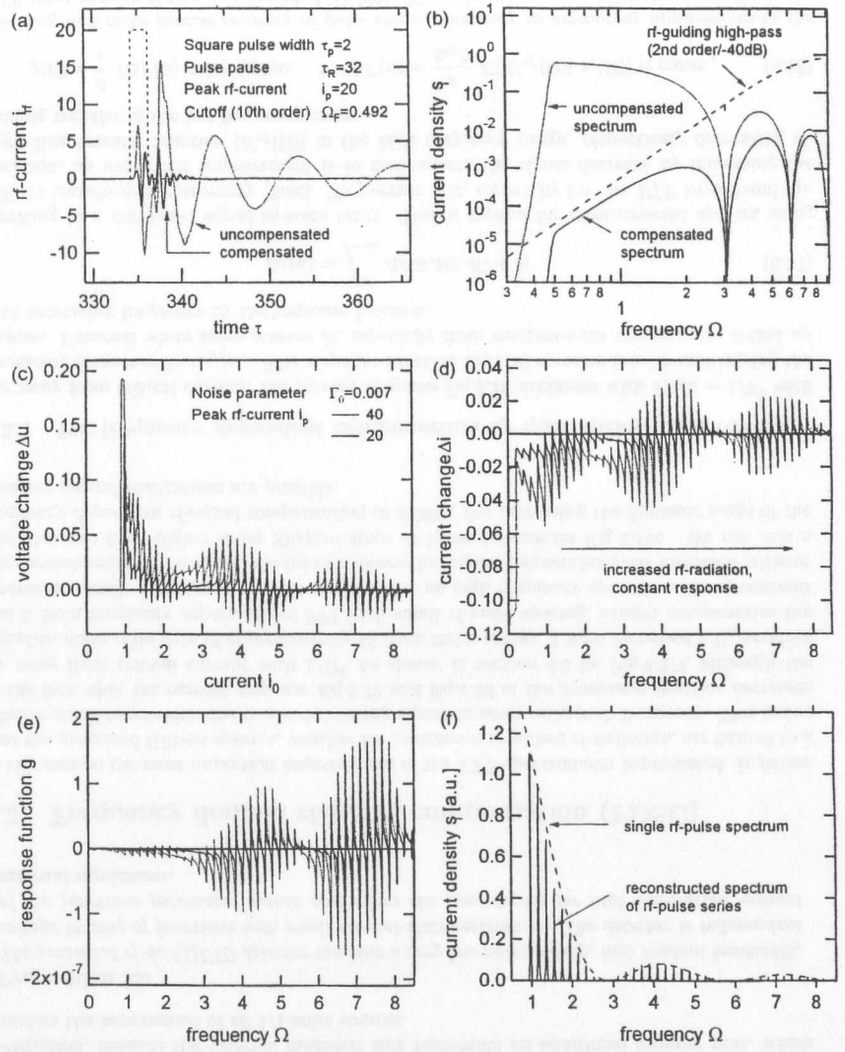

Figure 6.22: *Runge-Kutta simulated frequency dependent rf-signal compensation using a 2nd order high-pass filter of quasioptical components. Appropriate (a) time domain rf-signals, (b) spectra, (c) voltage response, (d) current response, (e) response function and (e) reconstructed Hilbert spectrum using the smallband correction factor k_s.*

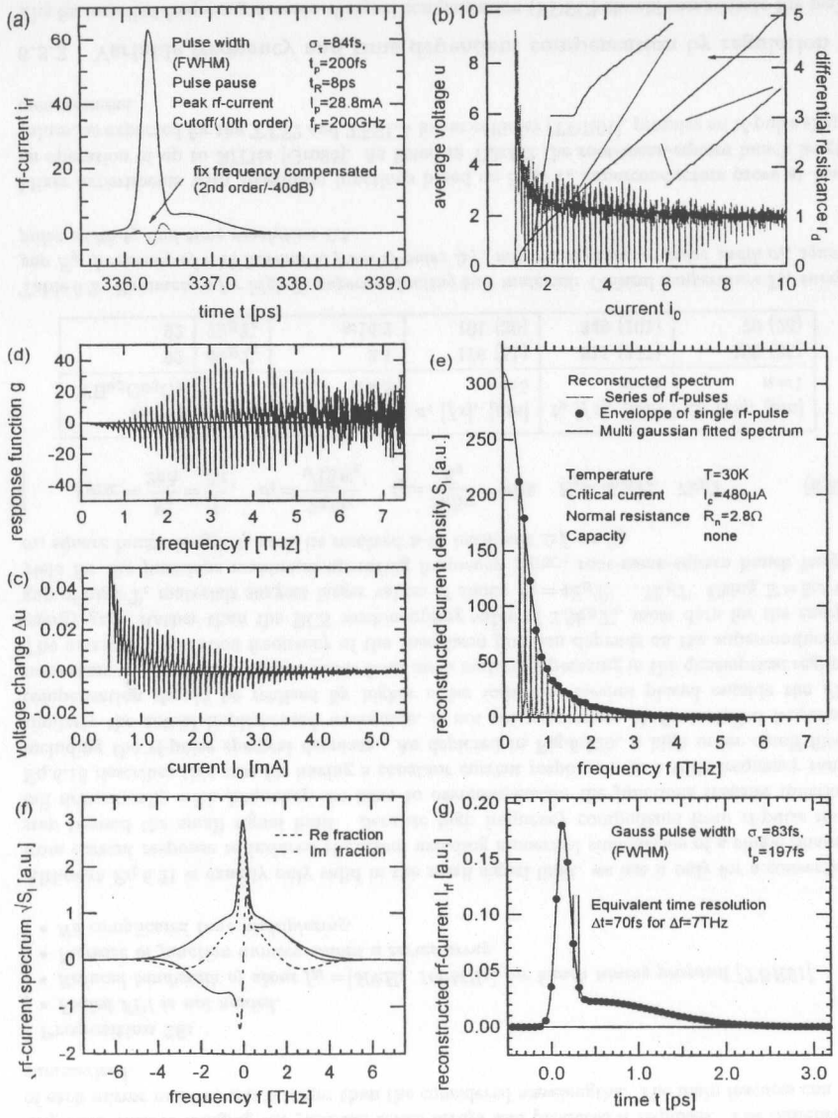

Figure 6.23: *Runge-Kutta simulated Hilbert reconstruction of rf-pulses using a 2nd order high-pass filter compensation pushed to the high-T_c frequency limit. Corresponding (a) rf-signal, (b) I-V-characteristic, (c) voltage response, (d) response function, (e) reconstructed spectrum, (f) phase and (g) time signal reconstruction.*

Analyzing Eq.6.20 by measuring Shapiro steps at $\Delta i_n^+, \Delta i_n^-$, namely simultaneously at different frequencies with $M \times M$ series arrays a simplier concept for a single-bunch measurement using a quasioptical rf-input coupling system is shown in Fig.6.24a. Contrary to Fig.6.9 no time multiplexing or folded FFPI's are needed. The requirements on the high frequency signal pickup are more relaxed with a bandwidth of $f_M = [50\text{kHz}, 100\text{MHz}]$ for the proposed bunch timing [TDR01]. According to the phase dependent current response Eq.4.46 a unique phase reconstruction of the rf-signal consisting of K spectral lines must performed using K different junctions and rf-input characteristics, which vary the parameter $a_\xi(\tilde{i}_k, \Omega_R)$. Fig.6.24b shows a schematic proposal for a single-bunch measurement using reflective delay structures, which promise an operation beyond the frequency limit of FPI structures of approximately 3THz. The beam is defocussed for all frequencies by a curved mirror and partly imaged onto the reflective

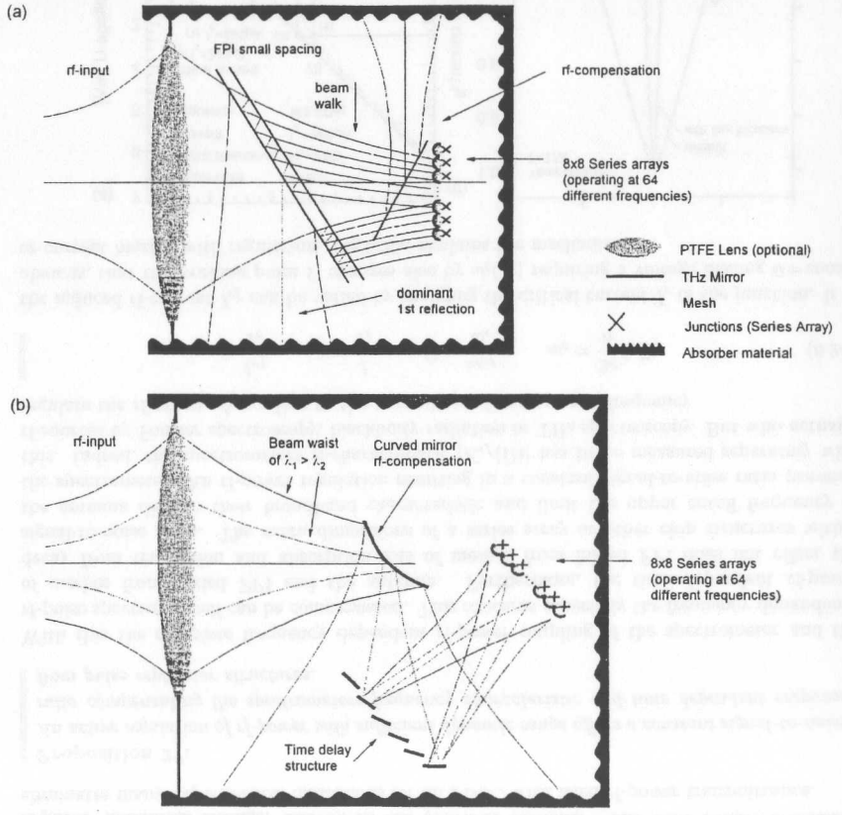

Figure 6.24: *Quasioptical input coupling system for single pulse measurements by using $M \times M$ series arrays operating at different frequencies using (a) FPI pulse replicators or (b) reflective delay structures.*

time delay structure. Depending on the truncation loss, the rf-compensation characteristic can be presicely adjusted by the shape of the curved mirror. The time delay structure consists of n displaced mirrors imaging the junction series arrays and produces n rf-pulses. The dimension of each mirror must be much larger than the considered wavelengths. The main features can be summerized.

Proposition 26:

- *Folded FPI is not needed.*
- *Reduced bandwidth of about $f_M = [50kHz, 100MHz]$ for bunch timing proposal [TDR01].*
- *Increase of junction number within a series array.*
- *No complicated time multiplexing.*

Although Eq.6.21 is exactly only valid in the small signal limit. we use it only for a conversion from current response to induced rf-current avoiding numerical simulations of a single Shapiro step beyond the small signal limit. Because high frequency components from rf-pulse itself fall dramatically with frequency, we have to overcompensate the junctions transfer function. Eq.6.18 describes this case for having a constant current response over a wide frequency range including the rf-pulse spectral decrease. As depicted in Fig.6.22b, a high order cutoff filter, similarly the actual implemented waveguide, is not yet neccessary. A fix installed frequency compensation should be realized by higher order inductive meshes placed outside the FPI resonators to prevent absorption losses from mesh material operating in the quasioptical regime. The maximum operation frequency of the Josephson junction depends on the superconductors energy gap. Rather than the BCS weak-coupling value of $3.5k_BT_c$, most data for the energy gap of high-T_c materials suggest larger values of about $E_g = 4k_BT_c \ldots 7k_BT$. Using $E = \hbar\omega$ we yield for the junctions maximum operating frequency f_{HTSC}, root-mean-square bunch length σ_t, square bunch length t_p with its resolved n-th harmonic $\Delta f = n/t_p$

$$f_{HTSC} = \frac{E_g}{2\pi\hbar} = \frac{1}{\Delta t}, \quad \sigma_t = \frac{2\pi\hbar n}{\sqrt{12}E_g}, \quad t_p = \frac{2\pi\hbar n}{E_g} \quad \text{with} \quad E_g = 4k_BT_c \ldots 7k_BT \tag{6.23}$$

T_c [K] $YBa_2Cu_3O_7$	E_g	f_{HTSC} [THz] $n=5$	σ_t [fs], [μm] $n=5$	t_p [fs], [μm] $n=5$	Δt [fs], [μm] $n=1$
92	$4k_BT_c$	8.1	176 (51)	611 (177)	122 (35)
92	$7k_BT_c$	≈14.2	101 (30)	349 (101)	70 (20)

Table 6.2: *Parameters for high-T_c superconducting bulk material: Critical temperature T_c, energy gap E_g, frequency of n-th harmonic from rf-pulse Δf, minimum gaussian pulse width σ_t, square pulse width t_p and time resolution Δt.*

Mixer experiments with Josephson junctions based on high-T_c superconductors prove at least an operation of up to 30THz [Gro95]. As listed in Tab.6.2 the root-mean-square bunch length values, as expected for the TTF2 and TESLA linear collidier [TDR01], promise an rf-pulse shape measurement.

6.3.2 Variable frequency and time dependent compensation by regulation

The fix installed frequency domain rf-signal compensation (FDSC) should compensate the main rf-power of the junctions characteristic and typical spectra of pulse shapes. Different rf-pulse spectra lead to small deviations from ideal compensation and finally to a worse signal-to-noise ratio for high frequencies. The exact mixing of filter characteristic and rf-power regulation

depends on the dynamic range of the rf-power regulation and on the frequency dependent rf-power maximum ratings, derived in the previous sections. The next simple statement eliminates many experimental limitations for an FDSC with fixed rf-power transmittance.

Proposition 27:

An active regulation of rf-power with sufficient dynamic range offers a constant signal-to-noise ratio compensating the spectrometers frequency characteristic and time dependent response from pulse replicator structures.

With this the complete frequency dependent rf-power coupling of the spectrometer and the rf-pulse spectrum itself can be compensated. This concerns especially the frequency dependence of meshes from folded FPI and the antenna. Furthermore, the time dependent rf-power decay from truncation and absorption loss of meshes from folded FPI does not effect the signal-to-noise ratio. The extra dimensions of a series array or other chip structures within the antenna disturb their broadband characteristic and limit the upper cutoff frequency of the spectrometer. An rf-power regulation resulting in a constant signal-to-noise ratio prevents this. Indeed, the spectrometers rf-characteristic $|K_{rf}(\Omega)|$ has to be measured seperately with rf-sources by Fourier spectroscopy, blackbody radiation or THz spectroscopy. But who actually regulate the rf-power. According to the normalized rf-current and frequency

$$i_{rf} = \frac{I_{rf}}{I_c}, \quad i = \frac{I}{I_c}, \quad \Omega = \frac{\omega_{rf}}{\omega_c}, \quad \omega_c = \frac{2e}{\hbar} I_c R_n \tag{6.24}$$

the induced rf-current I_{rf} can be varied by changing the critical current I_c of the junction. It is obvious, that the working point Ω changes also by $\omega_c(I_c)$ requiring a voltage biasing $\bar{u} = \text{const.}$ or current biasing with regulation. Fig.6.25a explains the mechanism.

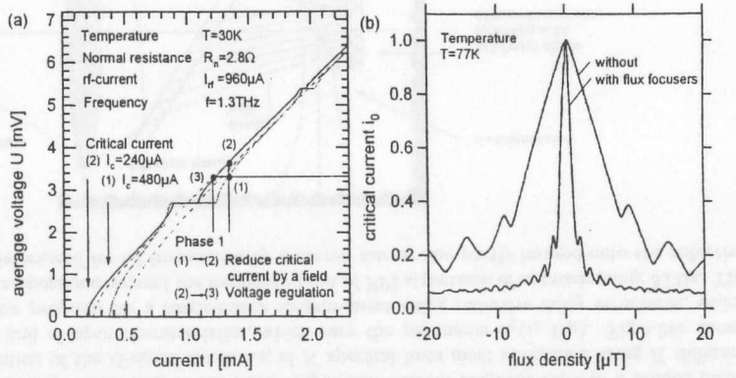

Figure 6.25: *(a) Simulated current change for fixed incoming rf-current by varying the critical current. (b) Measured critical current dependence on flux density of a series array of 105 junctions with flux focusers for higher magnetic sensitivity from [Kre99].*

With this a change of critical current I_c does not change the working point $\bar{u}$ but indeed the rf-power I_{rf} and therefore the voltage change $\Delta\bar{u}(I_{rf})$ with optimized signal-to-noise ratio. Without a regulation the critical current changes also the working point and saturates the high frequency system readout. Because the temperature dependence of the critical current is a slow process, the critical current can be varied by its influence on the magnetic field over the magnetic flux

sensitivity of the junction and its effective area $A_{eff}(T)$ shown in Fig.6.25b. The effective area of a junction depends on the temperature weakly as a consequence of the temperature dependent London penetration depth $\lambda_L(T)$. For the current response Eq.4.19 for monochromatic rf-radiation and voltage Eq.6.25, respectively current driven Eq.6.26 junction and Frauenhofer pattern $I_c(\Phi_y, T)$ Fig.6.25b, we yield

$$\Delta I_{max} = -I_{rf}^2 \frac{1}{8} \left(\frac{\hbar}{2e}\right) \frac{\omega_{rf}\omega_c(I_c(\Phi_y,T))^2}{\sqrt{\omega_c(I_c(\Phi_y,T))^2 + \omega_{rf}^2}\ (3\omega_c(I_c(\Phi_y,T))^2 + 2\omega_{rf}^2)} \frac{1}{k_B T} \tag{6.25}$$

$$\Delta U_{max} = I_{rf}^2 \frac{1}{8} \left(\frac{\hbar}{2e}\right) \frac{\omega_c(I_c(\Phi_y,T))^2}{(3\omega_c(I_c(\Phi_y,T))^2 + 2\omega_{rf}^2)} \frac{R_n}{k_B T} \quad \text{with} \tag{6.26}$$

$$I_c(\Phi_y, T) = I_c(0,T) \left| \frac{\sin(\pi\Phi_y/\Phi_0)}{\pi\Phi_y/\Phi_0} \right|, \qquad \Phi_y = B_y A_{eff}(T). \tag{6.27}$$

The suitable hardware is straightforward and shown in Fig.6.27 for a voltage biased junction. The rf-pulse spacing of about 1ns-5ns from a folded FPI for a single-bunch measurement requires a fast regulation time. For optimized signal-to-noise ratio over a wide frequency range and limited regulation time a two phase measurement with time multiplexing is recommended.

- *Phase 1:* A fast regulation within a shifted quasi single-bunch measurement adjusts and stores the rf-power compensation characteristic with appropriate bias currents $I_{\phi,N}(\bar{u})$ and flux $I_{\phi,N}(\bar{u})$ for every bunch from several macro-bunch measurements.
- *Phase 2:* The stored compensation characteristic $|K_{rf}(\Omega)|$, represented by its bias currents $I_{\phi,N}(\bar{u})$ and flux $I_{\phi,N}(\bar{u})$ for each single-bunch, is recalled in the order of replicated rf-pulses from folded FPI with deactivated regulation for a single-bunch measurement.

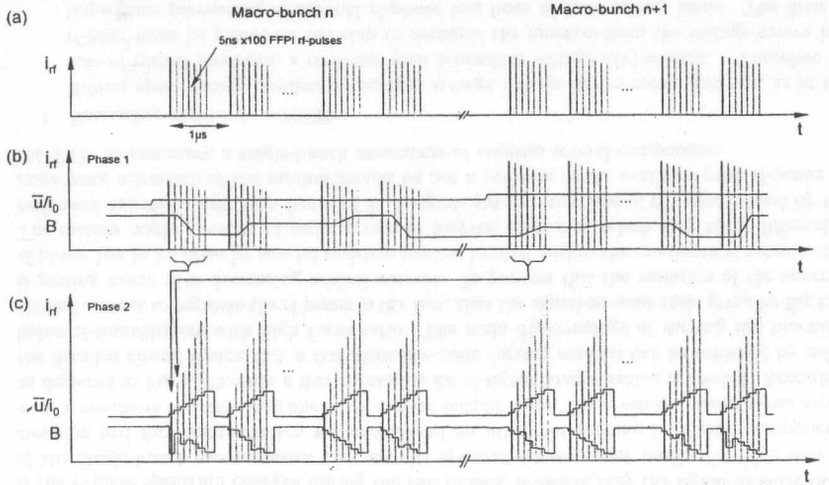

Figure 6.26: *(a) TTF bunch timing. (b) RF adjustment within a shifted quasi single-bunch mesasurement for optimized signal-to-noise ratio. (c) Single-bunch measurement with time multiplexing scheme.*

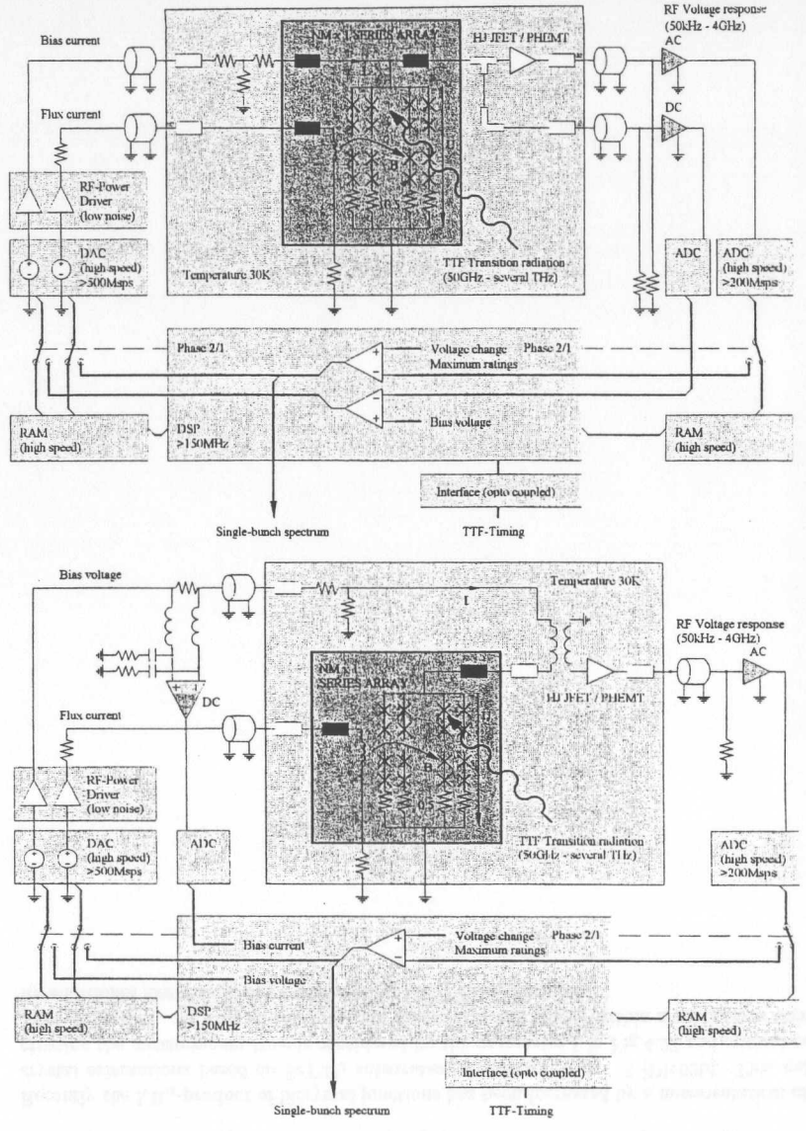

Figure 6.27: *Simplified setup for a single-bunch measurement with a frequency doamin rf-signal compensation using a flux regulation for (a) current and (b) voltage biased junction arrays.*

If the rf-pulse spectrum changes during the two phases, it effects only the signal-to-noise ratio of the single-bunch measurement and not the spectral measurement itself. For bias current stepping and flux compensation we recommend an ultra fast settling by digital components with a minimum of noisy components at current output stage. For a voltage biased series array, as depicted in Fig.6.27b, only a flux regulation for rf-signal compensation is needed. According the detailed circuit design C.2, a fast ultra low-noise current readout can be achieved by using balun rf-transformers with high turns ratio. The main disadvantage of varying the junctions critical current to regulate the rf-power is the fact, that the signal-to-noise ratio given by Eq.4.81 is getting worse with decreasing critical current. To prevent this the variation of the spectral rf-power has to be done by several resistive meshes located within the quasioptical beam waist. The meshes might consists of series arrays of bicystal junctions, which vary their differential resistance approximately by a factor of 3. A significant insertion loss of rf-power caused by the impedance mismatch of the meshes should be not a problem of the available peak rf-power at the TTF. In summary, a single-bunch measurement requires several components.

1. *Decoupling rf-filter $f_T > 20GHz$:*
   Hilbert spectroscopy requires a constant average voltage $\bar{u}(\tau) = \text{const.}$ and not, as in the case of tunnel junctions, a constant time dependent voltage $u(\tau) = \text{const.}$. Therefore an rf-filter must be placed on the chip to decouple the junction from the voltage source low impedance prevending additional rf-power loss from high frequency loads. The filter is naturally implemented when using rf-dc-SQUIDs.

2. *Limitation of source resistance $R_n N_J < Z_0/4$:*
   For a high frequency signal pickup a two-point measurement of junction is recommended. Signal power can be coupled out from junction by conventional transmission lines. A voltage biasing can be realized for relative high resistances using a series array. The presented rf-dc-SQUIDs are suitable for an operation of small normal-state resistances.

3. *Ultra low-noise signal pickup and biasing $f_M = [50kHz, 4GHz]$, $\sqrt{S}_{U,Amp} < 80pV/\sqrt{Hz}$:*
   The design of an ultra low-noise and broadband signal pickup including biasing is an important feature of a single-bunch measurement. In section C.2, a voltage and current amplifier with excellent performance for different biasing is presented. Alternatively a SQUID amplifier without any U-Φ-characteristic linearization can be used. Using rf-transformers as a current pickup is problematic, because its primary impedance increases the load impedance for voltage biasing. The presented rf-dc-SQUIDs do not have this limitation.

4. *Ultra fast settling of the critical current $\Delta t_I < 5ns$:*
   The settling time of critical current can be improved by increasing the junctions magnetic field sensitivity A_{eff} using flux focussing elements or square washers, well known from superconducting interferometers. Their structural change of rf-coupling on the chip does not effect the measured signal-to-noise ratio when using a regulation.

5. *Fast regulation during rf-adjustment $\Delta t_R < 500ns$:*
   The regulation and junction settling during phase 1 is performed by a DSP (Digital Signal Processor). The time dependent current and flux settlings have to be reordered for a minimum punch through the high frequency readout system.

Indeed the available peak rf-power at the TTF linac must be sufficient enough for a frequency compensation up to frequencies of several THz. According to Fig.4.11 the rf-current at saturation, including the insertion loss of the FFP's, is far lower than the available peak rf-power at the TTF [Gei99].

6.4 Intrinsically increased $I_c R_n$-product of Josephson junctions

Recently the $I_c R_n$-product of bicrystal junctions has been increased by a misorientation of their crystal orientations based on $SrTiO_3$ substrates by a factor of $3 \ldots 5$ [Div02b]. This gain decreasing the measurement time is considered by the parameter ξ in Fig.4.27 and critical current $I_c(0)$ of Eq.4.81. As long as the substrate material is not placed within a replication structure its additional loss should not a problem for the TTF application.

Chapter 7

Summary and outlook

7.1 Summary

In this thesis the method of Hilbert transform spectroscopy has been applied to determine the longitudinal bunch form factor at the TESLA-Test-Facility linac by analyzing coherent far-infrared transition radiation in the sub-millimeter wavelength range using high-T_c Josephson junctions made of $YBa_2Cu_3O_7$ on $LaAlO_3$ substrates. The main results of this work are briefly as follows:

- Theoretically, the detectors dynamic for pulse-type rf-signals within the Focker-Planck formalism has been determined numerically and analytically in first order recurrence outside the Hilbert theory small signal limit. For this a difference recurrence relation scheme has been introduced. For a current biased junction the voltage response and maximum rf-power ratings for monochromatic rf-radiation, single rf-pulse, series of rf-pulses and arbitrary spectral distributions have been determined. Concerning a constant voltage response a decrease of rf-pulse width can be compensated by increasing the rf-pulse peak rf-current within the delta pulse limit. For the rf-pulses repetition rate this is not valid for a unique spectrum reconstruction. The maximum peak rf-power ratings for pulse-type rf-signals are of the same order as for monochromatic rf-radiation.
- Higher order spectral corrections of multi-harmonic mixing effects from several Shapiro steps are determined analytical and are responsible for the lack of current response compensation by the rf-current concerning the repetition rate dependence. For a discrete spectrum these effects are based on its combinatoric spectral distribution.
- In accordance with stochastical and Focker-Planck solutions of the RSJ-model higher order effects reveal a phase dependence of the detectors stationary voltage response from rf-signal. For at least two spectral lines a phase reconstruction has been derived. Recursive algorithms for hardware realizations, which promise a unique spectral reconstruction beyond the Hilbert theory, have been presented. Ghost spectra and its symmetry breaking mechanism for dense spectra have been revealed. This promise a phase reconstruction of rf-radiation far away from validity of Hilbert theory opening a new window for spectroscopy using Josephson junctions.
- The next generation Josephson junction arrays (rf-dc-SQUIDs) for spectroscopy using discrete spectra have been presented. They combine a very low-noise signal pickup, high readout bandwidth and voltage biasing of junctions with small normal-state resistances. The sensor is independent of the junctions parameter spread and has the opportunity for high integration without external regulations. For spectroscopic applications using continuous rf-radiation the sensor offers additional a chopper port, which promises the suppression of all 1/f-noise sources.

- Experimentally, performing broadband spectroscopy with pulsed rf-radiation, the junctions voltage response at maximum rf-power rating reveals as a key feature and limits the measuring bandwidth of the detector. The frequency dependent decrease of the junctions current response limits the detectors dynamic range and requires a frequency domain rf-signal compensation. The maximum current response is estimated for the actual spectrum reconstruction algorithms of about 1% from the junctions I_cR_n-product.
- Several methods to increase the measuring bandwidth has been presented, promising a single rf-pulse measurement at the linar accelerator. The operation of series arrays consisting of up to 200 junctions based on high-T_c Josephson junctions made of $YBa_2Cu_3O_7$ on $LaAlO_3$ substrates has been demonstrated.
- Well defined quasioptical rf-pulse replication structures based on Fabry-Perot interferometers have been investigated with time domain spectroscopy. This render the possibility of a low temperature operation using junctions with high I_cR_n-products and high spectral resolution. Measurements of the actual spectrometer with monochromatic rf-radiation in the low frequency range reveals a high selective transmittance caused from multiple reflections within the sandwiched sample holder structure. These reflections increase the voltage response but do not essentially influence the measured bunch form factors at the linac for a spectrometer operated at liquid nitrogen.
- The dependence of measured bunch form factors of the ps-regime from bunch compressor phase and gun laser power for the TTF linac of repetition rate of 54MHz, macrobunch length of 8μs and 60 box-car samples has been demonstrated. The results are in accordance with simulations. Multiple reflections within the sandwiched sample holder bridge at least a pulse pause of about 20ns. The available voltage resolution within the rough electromagnetic environment of the linac was about 50nV. The concept of narrow band rf-amplifier readout fails, because of the phase correlation of the pulsed voltage response.
- Measurements with a far-infrared laser have proven an operation of the spectrometer at frequencies at least of about 1.19 THz. Josephson self resonances clearly indicate an operation far above this frequency and prove the successful operation of the broadband LP-antenna input coupling structure. The rf-power insertion loss of the spectrometer is mainly caused from the frequency selectivity of the broadband LP-antenna structures. Josephson junctions and series arrays made of $YBa_2Cu_3O_7$ have been prepared for the first time on symmetric 24° $LaAlO_3$ bicrystals with low loss substrate material.

7.2 Outlook

The roadmap for a single-bunch spectrometer is now getting transparent.

- Broadband Hilbert spectroscopy of pulse-type rf-signals requires a frequency domain rf-signal compensation, which can be realized by quasioptical components using transmittive or reflective structures. The regulation of the spectral rf-power can be realized by varying the junctions critical current or the circular current of rf-dc-SQUIDs over external magnetic fields with sufficient dynamic range.
- The rf-power regulation requires a voltage biasing of the detector and an ultra low-noise current rf-amplifier readout, which has already been designed. Josephson junction arrays limit noise contributions from the readout system and have to be investigated for low

temperature operation. Getting independent of the junctions parameter spread and using small normal-state resistances of the junctions, especially rf-dc-SQUIDs arrays have to be investigated. Their circular current pickup has to be realized by a low-noise and high frequency operating SQUID amplifier.

- The measuring time would be reduced by arrays operating at low temperatures overall two decades entering a measuring time of about 100ns below the required bunch pulse pause of the TTF linac. From intrinsically increased I_cR_n-products another decade would be gained entering pulse replication times of about 10ns by using well defined quasioptical delay structures. A normal-state resistance reduction of the array further reduces the measuring time.
- To prevent a high selective transmittance of the spectrometer caused from the actual sample holder structure, the spectrometer completely has to be redesigned with a well defined quasioptical input coupling structure for a low-noise operation. The rf-input coupling system has to be characterized by blackbody radiation, Fourier spectroscopy or THz-spectroscopy.
- To relax the timing situation using a frequency domain rf-signal compensation, a minimum of 7x7 Josephson junction series arrays have to operate at different frequencies simultaneously within the bunch repetition phase.
- The complicated spectrum reconstruction concerning the detectors non-linearity, noise and cutoff effects has to be omitted by using hardware solutions of the RCSJ-model, which promise a further reduction of the measuring time. Focker-Planck calculations including the junctions capacity, have to be investigated. Analytical descriptions of rf-dc-SQUIDs for the seperation of its high frequency properties have to be worked out. The introduced difference recurrence relations suggests a more general validity of the Hilbert theory extended for non RSJ-model type Josephson junctions.
- Concerning a low-noise readout, methods here not presented, using a correlated junction pick up coming below the white noise level have to be investigated. Using the correlation information of the junctions 1/f-noise might also reduce its noise levels.

I pointed out, that a single-bunch measurement based on Hilbert spectroscopy has no essential detector dead time and offers an uncritical synchronization and sampling of bunch pulses of at least a frequency range of 100GHz-3THz. Contrary to Fourier spectroscopy, heterodyn or bolometer receiver, Hilbert spectroscopy based on Josephson junctions offers a high frequency resolution promising a phase reconstruction of the rf-signal. Concerning sub-millimeter spectroscopy we believe, that quasioptical delay structures and low order filters for a compensation using transmittance or reflective structures are easier to realize than complicated sandwiched narrow higher order filters using different element shapes. A reliable time domain reconstruction by the Kramers-Kronig relation should be extended for arbitrary rf-signals by the investigation of phase informations from higher order effects and the intersection range with conventional sampling scopes for an integrated hybrid scope of sub-ps resolution and high sensitivity.

The TESLA-Test-Facility2 with permanent access will be an important coherent transition radiation source for the development of integrated high frequency components in the sub-millimeter range.

Acknowledgements

Without the great support and assistance I was given during the experimental and theoretical phase of my work, this thesis would not have been completed. All my doctoral advisors created the environment to work also on my theoretical preferences despite of the overall experimental expectations.

I would like to thank Prof.Dr.P.Schmüser for his effort and enthusiasm in advising my Ph.D. thesis, for his multidisciplinary interests in Hilbert spectroscopy and for spending his trust in me for guiding the small collaboration.

I would like to thank Prof.Dr.M.Schilling for the longtime trusting, for the uncomplicated teamwork and his never ending experimental knowledge and imaginations.

I would like to thank Prof.Dr.U.Merkt for his support during my scientific career. Thanks him for giving the FIR-laser and the possibility of preparing at the Microstructure Center of Hamburg in a highly motivating environment.

Thanks to Dr.S.Simrock, who is someone who discussed even almost impossible problems leading them to a solution. I mention the pulse replication and his interests in my work.

All my diploma students, J.Menzel, A.Kästner and M.Volk supporting my scientific investigations demonstrated fantastic commitment. My thanks to them. J.Menzel for the design of the spectrometer, construction of sample holder and operation control of the accelerator. Thanks for his software and hardware knowledge, MATLAB spectrum reconstruction sources and spending so much enjoyable night shifts *(twix...)*. A.Kästner for the junction devices, self resonances, proof-reading and countless discussions about models beyond Hilbert spectroscopy. M.Volk for his proof of a successful operation of the spectrometer with a far-infrared laser, MAFIA simulations and many acute discussions inside and outside physics.

I want to mention Priv.Doz.Dr.M.Tonutti for the provision of highly motivated students and for the support of the project. I thank to Priv.Doz.M.Leenen to present my work on international conferences. Dr.M.Kazhan for the time domain sampled FPI measurements at the IAP of the University of Hamburg. H.Gemünd and Dr.E.Kreysa for the mesh characterization at the MPIfR. I want to express my thanks to Priv.Doz.Dr.J.Hansen-Schmidt for his humorous lessions, discussions about electronics and beyond concerning even all problems. Prof.Dr.K.Likharev for many spontaneous private communications. Thanks to Prof.Dr.P.Zerwas for his instructive series of lessions from QFT to SUSY. Thanks for participation of his group and on topics in theoretical physics at the SUSY02 conference. Thanks to Dr.G.Moortgat-Pick for learning about charginos und neutralinos. I would like to thank all members of the TESLA collaboration, especially FDET group, Dr.H.Schlarb, Dr.M.Hüning, Dr.E.Vogel, Dr.M.Geitz and D.Türke for many profound and critical discussions about bunch-length measurements, Dr.S.Krey for longterm friendship inside and outside physics, Dr.H.Bartelmeß *(currrent phase rrelation)*, Dr.H.Burkhardt, Dr.M.Widmann, Dr.A.Richter for funny self made music and friendly atmoshpere, Dr.T.Matsuyama, C.Hinrichs *(...is klar...)*, C.Pels, Lambretta for overcoming countless night shifts and K.Kuchenbrandt for the humorous and pleasant time at the MARCH/IAP. For technical support I want to thank to the members of MHF-P, J.Oentrich and my father from MKK1 for the low distortion power supplies.

For financial support and the possibility to work in an international collaboration I would like to thank the DESY directorate. I want to express my *SPECIAL* ♡ thanks to Bettina, funny Miriam and my parents for their everlasting believe in me and creation of an untroubled environment to work on my scientific preferences.

Bibliography

[AppRF] Application Notes, *RF Transformers Designers Guide*, Mini-Circuits

[AN1022] Application Note AN1022 *Designing Low-Noise Amplifiers for PCS Application*, CEL California Eastern Laboratory, (1997)

[AN1091] Application Note AN1091, *Amplifiers using Low-Noise PHEMTs*, Agilent Technologies

[Ben96] S.P.Benz, C.A.Hamilton, *Pulse-driven Programmable Josephson Voltage Standard*, Appl. Phys. Lett. **68**, 3171, (1996)

[Che97] J.Chen, H.Myoren, K.Nakajima, T.Yamashita, S.Linzen, F.Schmidl, P.Seidel, *Mixing at terahertz frequency band using $YBa_2Cu_3O_3$ Josephson junctions*, Appl. Phys. Lett. **71**, 707 (1997)

[Che99] J.Chen, E.Kobayashi, K.Nakajima, T.Yamashita, S.Linzen, F.Schmidl, P.Seidel, *Response Properties at 2.525THz using High-T_c Josephson Junctions on Silicon Bicrystal Substrates*, IEEE Trans. Appl. Supercond. **9**, 4799 (1999)

[Chr99] A.Chrestin, *Supraströme in Nb/InAs(2DEG)/Nb-Kontakten*, Diploma Thesis, University of Hamburg, (1993)

[Col98] R.E.Collin, *Foundations of Microwave Engineering*, McGraw-Hill Publisher, 2nd edition, (1998)

[Div93] Y.Y.Divin et.al., *Mm-wave response and linewidth of Josephson oscillations in $YBa_2Cu_3O_3$ step-edge junctions*, Appl. Phys. Lett., **62**, 1295 (1993)

[Div02a] Y.Y.Divin, O.Y.Volkov, M.Liatti, V.V.Shirotov, V.V.Pavlovskii, U.Poppe, P.M. Shadrin, K.Urban *Hilbert spectroscopy from gighertz to terahertz frequencies by high-T_c Josephson junctions*, Physica C 327-376, 417 (2002)

[Div02b] Y.Y.Divin, U.Poppe, C.L.Jia, P.M.Shadrin, K.Urban, *Structural and elecrical properties of $YBa_2Cu_3O_3$ [100]-tilt grain boundary Josephson junction on $SrTiO_3$ bicrystals*, Physica C 372-376 , 115 (2002)

[Duh57] R.H.Duhamel, D.E.Isbell, *Broadband logarithmically periodic antenna structures*, IRE. Nat. Cov. Record. **Pt.1**, 199 (1957)

[Gei99] M.A.Geitz, *Inverstigation of the Transverse and Longitudinal Beam Parameters at the TESLA Test Facility Linac*, Ph.D. Thesis, University of Hamburg (1999)

[Gin50] V.L.Ginzburg, L.G.Landau, *On the theory of superconductivity*, Zh. Eksp. Teo. Phys., JETP **20**, 1064 (1950)

[Gin79] V.L.Ginzburg, V.N.Tsychovich, *Several Problems of the Theory of Transition Radiation and Transition Scattering*, Physics Reports **49/1**, (1979)

[Gol98] P.F.Goldsmith, *Quasioptical Systems*, Gaussian Beam Quasioptical Propagation and Application IEEE Press/Chapman and Hall Publishers seires on microwave technology and techniques, (1998)

[Gun92] Meinke-Gundlach, *Taschenbuch der Hochfrequenztechnik*, Springer Verlag, 5th edition, Berlin, (1992)

[Gro95] Grossman, E.N.; Vale, L.R.; Rudman, D.A.; Evenson, K.M.; Zink, L.R., *30 Thz Mixing Experiments on High Temperature Superconducting Josephson Junctions*, IEEE Trans. Appl. Supercond. **5**,3061, (1995)

[Han97] K.Hanke, *Measurement of Picosecond Electron Bunches in a Linear Accelerator*, Ph.D. Thesis, University of Hamburg, (1997)

[Hec89] E.Hecht, *Optics*, Addison-Wesley Publisher, (1989)

[Hei97] J.K.Heinsohn, *Untersuchung des Herstellungsprozesses von Josephson Kontakten aus $YBa_2Cu_3O_3$ mit statistischen Methoden*, Diploma Thesis, University of Hamburg, (1997)

[Hod78] D.T.Hodges, *A Review of Advances in Optically Pumped Far-Infrared Lasers*, Infrared Phys. **18**, 375 (1987)

[Hün01] M.Hüning, *private communication*, (2001)

[Igor] IGOR V4.0, Wavemetrics Inc.

[Jos62] B.D.Josephson, *Possible new effects in superconductive tunneling*, Phys. Lett. **1**, 251 (1962)

[Käs00] A.Kaestner, *Hochfrequenzeigenschaften von Josephson Kontakten aus $YBa_2Cu_3O_3$ auf $LaAlO_3$ Bikristall-Substraten*, Diploma Thesis, University of Hamburg, (2000)

[Keh01] D.Kehrer, W.Simbürger, H.D. Wohlmuth, A.L.Scholz, *Modeling of Monolithic Lumped Planar Transformers up to 20GHz*, IEEE Custom Integrated Circuits Conference CICC2001, San Diego, 401 (2002)

[Kha02] M.Khazan, *Time-domain terahertz spectroscopy and its applications to the study of high-T_c superconductor thin films*, Ph.D. Thesis, University of Hamburg (2002)

[Kos02] E.L.Kosarev, A.Ya.Shul'man, M.A.Tarasov, T.Lindström, *Deconvolution problems and superresolution in Hilbert transform spectroscopy based on the a.c. Josephson effect*, submitted to Physica C (2002)

[Kre99] S.Krey, O.Brügmann, M.Schilling, *Highly sensitive magnetometers based on $YBa_2Cu_3O_3$ Josephson junction arrays*, Appl. Phys. Lett. **74**, 294 (1999)

[Les90] J.C.G.Lesurf, *Millimeter-wave optics, devices and systems*, Adam Hilger Publisher, (1990)

[Lie01] M.Liepe, *Superconducting Multicell Cavities for Linear Collidiers*, Ph.D. Thesis, University of Hamburg, (2001)

[Lil01] L.Lilje, *Experimental Investigations on Superconducting Niobium Cavities at Highest Radiofrequency Fields*, Ph.D. Thesis, University of Hamburg, (2001)

[Lik96] K.K.Likharev, *Dynamics of Josephson Junctions and Circuits*, Gordon and Beach New York, (1996)

[Lud97] F.Ludwig, *Rauschmessungen an dc-SQUID Magnetometern aus* $YBa_2Cu_3O_3$, Diploma Thesis, University of Hamburg, (1997)

[Maf98] *MAFIA Collaboration*, Mafia, T3 - the 3D time domain solver, (1998)

[Mar96] A.Marx, *Niederfrequentes 1/f-Rauschen in Josephson-Stufenkontakten aus Hochtemperatur-Supraleitern*, Shaker Verlag, (1996)

[Mat98] MATLAB V5.2, The MathWorks Inc., *MATLAB Function Reference Volume 1: Language, MATLAB Using SIMULINK*, (1998)

[Men99] J.Menzel, *Nachweis von Übergangsstrahlung mit Josephson-Kontakten*, Dipoma Thesis, Rheinisch-Westfälische Technische Hochchule Aachen, (1999)

[Mura98] H.Murayama, *Probing Physics at Short Distances with Supersymmetry*, hep-ph/ 9801331 v1 17 1998, UCB-PTH-98/05

[Myg99] J.Mygind, V.P.Koshelets, S.V.Shitov, L.V.Filippenko, V.L.Vaks, A.B.Baryshev, W.Luinge and N.Whyborn., *Phase locking of 270-440 GHz Josephson flux flow oscillators*, Superconductor V.P- Science and Technology **12**, 720 (1999)

[Nol92] W.Nolting, *Vielteilchentheorie*, Zimmermann-Neufang Verlag, **Bd.7**, (1992)

[Opp97] J.H. Oppenländer, *Nichtlineare Dynamik raumzeitlicher Muster in Josephson-Kontakt-Netzwerken*, Ph.D. Thesis, Eberhard-Karls-Universität zu Tübingen, (1997)

[Num00] W.H.Press et.al., *Numerical Recepies in C*, Cambridge University Press , 2nd edition, (1992)

[Phi96] J.M.Phillips, *Substrate selection for high-temperature superconducting film thin film*, J. Appl. Phys. **79**, 1829 (1996)

[SPICE] PSPICE Release V8.0, *Simulation with device equations options*, A/D Reference Manual, MicroSim Inc.

[Rie88] M.Rieger, *Mikrowellen-Detektion mit Josephson Elementen*, Ph.D. Thesis, Technische Universität München (1988)

[Ric97] A.Richter, *Supraleitende Quateninterferometer aus* $YBa_2Cu_3O_3$, Diploma Thesis, University of Hamburg, (1997)

[Ris96] H.Risken, *The Focker-Planck Equation*, Springer Verlag, 3rd edition, (1989)

[Rum66] V.H.Rumsey, *Frequency Independent Antennas*, Academic Press, (1966)

[Scha99] R.Scharnberg, *Schwach gekopplete Supraleiter und Josephson Effekte*, lecture script, University of Hamburg, (1999)

[Schi] V.V.Shirotov, *Far-infared broadband measurements with Hibert spectroscopy*, Physica C 372-376, 454 (2002)

[Schl97] H.Schlarb, *Resistive wall wake fields*, Diploma Thesis, University of Hamburg, (1997)

[Schm99] P.Schmüser, *Applications of the Kramers-Kronig-Relation*, internal script lecture, DESY Hamburg, (1999)

[She94] Z.Y.Shen, *High Temperature Superconducting Circuits*, Artech House, (1994)

[Sie86] A.E.Siegman, *Lasers*, University Science Books, (1986)

[Sta95] B.Stasik, *DC-SQUIDSs aus* $YBa_2Cu_3O_7$, Diploma Thesis, University of Hamburg, (1995)

[Tar95] M.A. Tarasov, A.Y. Shul'man, G.V. Prokopenko, V.P. Koshlets, O.Y. Polyanski, I.L. Lapitskaya, A.N. Vystavkin, E.L. Kosarev, *Quasioptical Hilbert Transform Spectrometer*, IEEE Trans. Appl. Supercond. **5**, 2686 (1995)

[Tar01] M.Tarasov, E.Stepantsov, T.Lindström, A.Kalabukhov, H.Chen, L.G.Johansson, Z.Ivanov, *Anisotropy in the transparency of HTS films at millimetre and submillimeter microwave radiation*, IEEE Trans. Appl. Supercond. **11**(1), 1154-1157 (2001)

[TDR01] TESLA collaboration, *Technical Design Report Part II*, DESY Hamburg 2001-011, ECFA 2001-209 (2001)

[Ter72] M.L.Ter-Mikaelian, *High-Energy Electromagnetic Processes in Condensed Media*, Interscience tracts on physics and astronomy, **29**, (1972)

[Tin96] M.Tinkham, *Introduction to Superconductivity*, McGraw-Hill Publisher, (1996)

[Tri] T.Ha.Tri, *Solid State Microwave Amplifier Design*, John-Willey and Sons, Chapter 2

[VC++] MS Visual C++ V5.0, Microsoft Inc.

[Vol00] M.Volk, *Ferninfrarot-Spektroskopie mit Josephson-Kontakten aus* $YBa_2Cu_3O_3$, Diploma Thesis, University of Hamburg, (2000)

[Wei84] T.Weiland, *On the Numerical Solution of Maxwell's Equations ans Applications in the Filed of Accelerator Physics*, Particle Accelerators 12, 245 (1984)

[Zer02] P.M. Zerwas, J.Kalinowski, A.Freitas, G.A.Blair, S.Y.Choi, H.U.Martyn, G.Moortgat-Pick, W.Porod, *Reconstruction of Fundamental SUSY Parameters*, hep-ph/ 0211076 v1 6 Nov 2002, DESY-02-175, ZU-TH 21/02

[Zin86] O.Zinke, H.Brunswik, *Lehrbuch der Hochfrequenztechnik*, Springer Verlag, **Bd.1**, 3rd edition, (1986)

[Zuc97] C.Zuccaro, M.Winter, N.Klein, K.Urban, *Microwave absorption in single crystal of lanthanum aluminate*, J. Appl. Phys. **82**, 5695 (1997)

Appendix A

Mathematical supplement

In this chapter analytic expressions and numerical methods used in this thesis are derived. First of all a review of Hilbert transform spectroscopy is given. Beyond this, numerical methods to solve tridiagonal recurrence relations for arbitrary rf-signals within the FP formalism are presented. For pulse-type rf-signals analytic expressions for the voltage response in first recurrence order are deduced in the time domain. For periodic rf-signals a spectral representation within the FP formalism is presented, as well as higher order mixing and phase effects.

A.1 Definitions

Starting from linear signal theory by using theorems of Fourier transforms from unnormalized pair of time t and frequency f, we yield with Tab.3.1 the following normalized theorems.

$$\begin{aligned}
&\text{Fourier transform} && : && S(\omega) = \mathcal{F}[i_{rf}(\tau)] = \int_{-\infty}^{+\infty} i_{rf}(\tau) e^{i\Omega\tau} d\tau \\
&\text{Inverse Fourier transform} && : && i_{rf}(\tau) = \mathcal{F}^{-1}[S(\Omega)] = \frac{1}{2\pi}\int_{-\infty}^{+\infty} S(\Omega) e^{-i\Omega\tau} d\Omega \\
&\text{Current spectral density} && : && s_i(\Omega) = \lim_{T\to\infty} \frac{1}{2T} \mathcal{F}^*[i_{rf}(\tau)]\mathcal{F}[i_{rf}(\tau)] \\
&\text{Parseval theorem} && : && \lim_{T\to\infty} \frac{1}{2T}\int_{-T}^{+T} i_{rf}^2(\tau) d\tau = \frac{1}{2\pi}\int_{-\infty}^{+\infty} s_i(\Omega) d\Omega
\end{aligned} \tag{A.1}$$

A.2 Hilbert transform spectroscopy excluding noise

This section outlines the theory of Hilbert transform spectroscopy for Josephson junctions using the RSJ-model by the slowly varying phase (SVP) approximation in second order perturbation theory as worked out by several authors [Gei99]. We follow the authors for pointing out, that Hilbert theory is deviated only for continuous rf-radiation.

A.2.1 I-V-characteristic without rf-radiation

A Josephson junction obeying the RSJ model is described by Eq.3.4. For $i_0 > 1$, $d\varphi/d\tau = i_0 - \sin\varphi(\tau) \neq 0$ which can separated $d\varphi/(i_0 - \sin\varphi) = d\tau$. Integration gives with an arbitrary

phase χ the junctions phase φ

$$\varphi(\tau) = 2\arctan\left(\frac{1}{i_0} + \frac{\sqrt{i_0^2-1}}{i_0}\tan(\frac{\sqrt{i_0^2-1}}{2}\tau + \chi)\right). \tag{A.2}$$

The normalized voltage is $u(\tau) = d\varphi(\tau)/d\tau$

$$u(\tau) = (i_0^2-1)\frac{1}{i_0 + \frac{1}{i_0}\left(\cos\left(\sqrt{i_0^2-1}\,\tau + 2\chi\right) + \sqrt{(i_0^2-1)}\sin\left(\sqrt{i_0^2-1}\,\tau + 2\chi\right)\right)}. \tag{A.3}$$

The last expression can be simplified by substituting $\sin\theta = 1/i_0$. Then $\cos\theta = (1-\sin^2\theta)^{1/2} = (i_0^2-1)^{1/2}/i_0$ leads with the constant χ, determined by the initial conditions and choosen such that

$$u(\tau) = \frac{(i_0^2-1)}{i_0 + \sin\left(\sqrt{i_0^2-1}\,\tau + 2\chi + \theta\right)} \quad \rightarrow \quad u(\tau) = \frac{(i_0^2-1)}{i_0 - \cos\left(\sqrt{i_0^2-1}\,\tau\right)}. \tag{A.4}$$

The dc voltage measured across the junction is the time-average of u(τ). The period of oscillation is defined by $\tau_0 = 2\pi/\sqrt{i_0^2-1}$

$$\bar{u} = \frac{1}{\tau_0}\int_0^{\tau_0} \frac{i_0^2-1}{i_0 - \cos\left(\sqrt{i_0^2-1}\,\tau\right)} d\tau = \frac{2}{\tau_0}\left[\arctan\left(\frac{(i_0-1)\tan\left(\sqrt{i_0^2-1}\,\frac{\tau}{2}\right)}{\sqrt{i_0^2-1}}\right)\right]_{\tau=0}^{\tau=\tau_0} \tag{A.5}$$

The argument of the tangent function is zero at the lower boundary and π at the upper boundary. The arctan function advances by π between two successive zeros of its argument. Therefore we obtain the simple formula

$$\bar{u} = \frac{2}{\tau_0}\pi = \sqrt{i_0^2-1} \quad \rightarrow \quad \bar{u} = \begin{cases} 0 & \text{for} \quad |i_0| \leq 1 \\ \sqrt{i_0^2-1} & \text{for} \quad |i_0| > 1 \end{cases} \tag{A.6}$$

A.2.2 I-V-characteristic with rf-radiation

The bias current and phase are expaned into a set of equations for the coefficients a_k,b_k.

$$i = i_0 + \sum_{k=1}^{\infty} a_k i_{rf}^k\,, \quad \varphi = \varphi_0 + \sum_{k=1}^{\infty} b_k i_{rf}^k \tag{A.7}$$

The $\sin\varphi$ term in Eq.3.6 is expanded into a second-order Taylor series

$$\sin\left(\varphi_0 + \sum_{k=1}^{\infty} b_k i_{rf}^k\right) \approx \sin\varphi_0 + b_1\cos\varphi_0\, i_{rf} + \left(b_2\cos\varphi_0 - \frac{b_1^2}{2}\sin\varphi_0\right) i_{rf}^2\,. \tag{A.8}$$

Eq.A.7 and Eq.A.8 are introduced into the differential Eq.3.6. Sorting for powers of i_{rf} we get

$$\frac{d\varphi_0}{d\tau} + \sin\varphi_0 = i_0 \tag{A.9}$$

$$\frac{db_1}{d\tau} + b_1\cos\varphi_0 = a_1 + \sin(\Omega\tau) \qquad \text{for} \quad k=1 \tag{A.10}$$

$$\frac{db_2}{d\tau} + b_2\cos\varphi_0 = a_2 + \frac{b_1^2}{2}\sin\varphi_0 \qquad \text{for} \quad k=2\,. \tag{A.11}$$

Eq.A.9 describes the junction characteristic without radiation and is solved by Eq.A.2. Eq.A.10 and Eq.A.11 are of the form

$$\frac{db_k}{d\tau} + b_k \cos\varphi_0 = f_k(\tau)\,. \tag{A.12}$$

The general solution of this equation is

$$b_k = \exp\left(-\int^\tau \cos\varphi_0\, d\tau'\right)\left(\int^\tau \exp\left(\int^{\tau'} \cos\varphi_0\, d\tau''\right) f_k(\tau')\, d\tau'\right)\,. \tag{A.13}$$

An expression for $\cos\varphi_0$ can be derived from Eq.3.6. Taking the derivative with respect to the normalized time one obtains

$$\frac{d^2\varphi_0}{d\tau^2} + \frac{d\varphi_0}{d\tau}\cos\varphi_0 = 0 \quad\rightarrow\quad \cos\varphi_0 = -\frac{\ddot{\varphi}_0}{\dot{\varphi}_0} = -\frac{d\ln\dot{\varphi}_0}{d\tau}\,. \tag{A.14}$$

Inserting Eq.A.14 into Eq.A.13 the latter equation yields

$$b_k = \dot{\varphi}_0 \int^\tau \frac{f_k(\tau')}{\dot{\varphi}_0(\tau')}\, d\tau'\,. \tag{A.15}$$

We are now looking for the change in the dc current at a fixed value of the time averaged voltage

$$\bar{u} = \overline{\dot{\varphi}_0} + \overline{\dot{b}_1} + \overline{\dot{b}_2} + \ldots\ldots = \overline{\dot{\varphi}_0} \quad \forall \quad \overline{\dot{b}_k} = 0 \quad \text{for all} \quad k > 0\,. \tag{A.16}$$

Therefore the integrand in Eq.A.15 is not allowed to have a dc component. This can be seen as follows. We form the long-term time average of $\dot{b}_k$

$$\overline{\dot{b}_k} = \lim_{T\to\infty}\frac{1}{T}\int_0^T \dot{b}_k d\tau = \lim_{T\to\infty}\frac{1}{T}(b_k(T) - b_k(0))\,. \tag{A.17}$$

Assuming in the integrand in Eq.A.15 a dc component A. Then $b_k(T) - b_k(0)$ would be of the form $A\cdot T$ plus a bounded term due to the ac components of the integrand in Eq.A.15. From the condition $\overline{\dot{b}_k}=0$ follows $A=0$ immediately. The condition $\overline{\dot{b}_1}=0$ implies

$$\overline{(a_1 + \sin(\Omega\tau))\,\dot{\varphi}_0^{-1}} = 0,\ \overline{(a_1 + \sin(\Omega\tau))\,(i_0 - \cos(\bar{u}\tau))} = 0 \tag{A.18}$$

where $f_1(\tau) = a_1 + \sin(\Omega\tau)$ has been inserted. Keeping in mind that a_1 describes a pure dc current component, Eq.A.18 can be solved for a_1

$$a_1 = \frac{1}{i_0}\overline{\sin(\Omega\tau)\cos(\bar{u}\tau)} \quad\rightarrow\quad a_1 = 0, \qquad \Omega \neq \bar{u}\,. \tag{A.19}$$

From Eq.A.19 follows directly that there is no first order dc current component introduced by the small ac current The first order phase correction $b_1(\tau)$ can be calculated from Eq.A.15 setting $a_1=0$.

$$b_1 = \dot{\varphi}_0\int^\tau \frac{\sin(\Omega\tau')}{\dot{\varphi}_0} d\tau' = \frac{1}{i_0 - \cos(\bar{u}\tau)}\int^\tau (i_0 - \cos(\bar{u}\tau'))\sin(\Omega\tau')\, d\tau', \tag{A.20}$$

$$b_1 = -\frac{1}{i_0 - \cos(\bar{u}\tau)}\left(\frac{i_0\cos(\Omega\tau)}{\Omega} - \frac{\cos((\Omega-\bar{u})\,\tau)}{2\,(\Omega-\bar{u})} - \frac{\cos((\Omega+\bar{u})\,\tau)}{2\,(\Omega+\bar{u})}\right)\,. \tag{A.21}$$

The next step is the solution of Eq.A.11 with the condition $\overline{\dot{b}_2}=0$. The absence of a dc component in the integrand in Eq.A.15 means for $k=2$

$$\overline{\left(a_2 + \frac{b_1^2}{2}\sin\varphi_0\right)(i_0 - \cos(\bar{u}\tau))} = 0 \tag{A.22}$$

An expression for $\sin\varphi_0$ can be derived from Eq.A.4,3.6.

$$\dot{\varphi}_0 = \frac{\bar{u}^2}{i_0 - \cos(\bar{u}\tau)} = i_0 - \sin\varphi_0 \quad\rightarrow\quad \sin\varphi_0 = \frac{1 - i_0\cos(\bar{u}\tau)}{i_0 - \cos(\bar{u}\tau)}\,. \tag{A.23}$$

Inserting the latter expression into Eq.A.22 and solving for the second-order correction a_2 of the dc current we find

$$a_2 = -\frac{1}{2i_0}\overline{(1 - i_0\cos(\bar{u}\tau))\, b_1^2}\,. \tag{A.24}$$

Eq.A.21 has to be substituted for b_1 and with the identity

$$\frac{1 - i_0\cos\left(\sqrt{i_0^2-1}\,\tau\right)}{\left(i_0 - \cos\left(\sqrt{i_0^2-1}\,\tau\right)\right)^2} = -2\sum_{k=1}^{\infty}\frac{k\cos\left(k\sqrt{i_0^2-1}\,\tau\right)}{\left(i_0 + \sqrt{i_0^2-1}\right)^k} \tag{A.25}$$

the following expression for the second order dc current is found

$$a_2 = \frac{1}{a_0}\sum_{k=1}^{2}\frac{k\cos\left(k\sqrt{i_0^2-1}\,\tau\right)}{\left(i_0 + \sqrt{i_0^2-1}\right)^k}\overline{\left(\frac{i_0\cos(\Omega\tau)}{\Omega} - \frac{\cos((\Omega-\bar{u})\,\tau)}{2\,(\Omega-\bar{u})} - \frac{\cos((\Omega+\bar{u})\,\tau)}{2\,(\Omega+\bar{u})}\right)^2}\,. \tag{A.26}$$

Note that only the first two terms $k=\{1,2\}$ of the sum are included in taking the time average. Three terms have to be evaluated and integrated leading to

$$T_1 = \frac{1}{\tau}\int^\tau \frac{1}{i_0(i_0+\bar{u})}\left[\frac{-a_0\cos^2(\Omega\tau')\cos^2(\bar{u}\tau')}{\Omega\,(\Omega-\bar{u})}\right] d\tau'$$

$$T_2 = \frac{1}{\tau}\int^\tau \frac{1}{i_0(i_0+\bar{u})}\left[\frac{-a_0\cos^2(\Omega\tau')\cos^2(\bar{u}\tau')}{\Omega\,(\Omega+\bar{u})}\right] d\tau'$$

$$T_3 = \frac{1}{\tau}\int^\tau \frac{2}{i_0\,(i_0+\bar{u})^2}\left[\frac{(\cos^2(\bar{u}\tau')\cos^2(\Omega\tau') - \sin^2(\bar{u}\tau')\sin^2(\Omega\tau'))\,(\cos^2(\bar{u}\tau') - \sin^2(\bar{u}\tau'))}{2\,(\Omega^2-\bar{u}^2)}\right] d\tau'$$

$$a_2 = T_1 + T_2 + T_3 = -\frac{1}{4i_0\,(\Omega^2-\bar{u}^2)}. \tag{A.27}$$

A second order non-zero dc current component remains after the integration. This leads to a resonance type correction of the dc I-V-characteristic from Josephson junction.

$$\Delta i = a_2 i_{rf}^2 = -\frac{i_{rf}^2}{4i_0\,(\Omega^2-\bar{u}^2)} \quad \text{for} \quad \bar{u} \neq \Omega\,. \tag{A.28}$$

A.3 Hilbert transform spectroscopy including noise

According to Eq.3.22 including noise $-\mathcal{K}\mathcal{K} = 1$ is not valid. Only in the limit $\Gamma \to 0$ it reduces to $\mathcal{H}^{-1}\mathcal{H} = 1$. To show this, applying the transform Eq.3.22 two times

$$g(\bar{u}) = \mathcal{K}(s_i(\Omega)) = -\frac{1}{2\pi}\int_{-\infty}^{\infty}\left(\frac{1}{(\Omega-\bar{u})+i\Gamma} + \frac{1}{(\Omega-\bar{u})-i\Gamma}\right) s_i(\Omega)\, d\Omega \tag{A.29}$$

$$s_i(\Omega') = -\mathcal{K}g(\bar{u}) = -\frac{1}{2\pi}\int_{-\infty}^{\infty}\left(\frac{1}{(\Omega'-\bar{u})+i\Gamma} + \frac{1}{(\Omega'-\bar{u})-i\Gamma}\right) g(\bar{u})\, d\bar{u} \tag{A.30}$$

leads for $s_i(\Omega') = -\mathcal{K}\mathcal{K}(s_i(\Omega))$

$$= \frac{1}{4\pi^2}\int_{-\infty}^{\infty} s_i(\Omega)\int_{-\infty}^{\infty}\left(\frac{1}{\Omega'-\bar{u}+i\Gamma}+\frac{1}{\Omega'-\bar{u}-i\Gamma}\right)\left(\frac{1}{\Omega-\bar{u}+i\Gamma}+\frac{1}{\Omega-\bar{u}-i\Gamma}\right)d\bar{u}\;d\Omega \quad (A.31)$$

$$= \frac{1}{4\pi^2}\int_{-\infty}^{\infty} s_i(\Omega)\lim_{\bar{u}'\to\infty}\left[\frac{4\Gamma\arctan\left(\frac{\bar{u}-\Omega'}{\Gamma}\right)}{(\Omega'-\Omega)^2+4\Gamma^2}+\frac{4\Gamma\arctan\left(\frac{\bar{u}-\Omega}{\Gamma}\right)}{(\Omega'-\Omega)^2+4\Gamma^2}\right.$$

$$\left.+\frac{2((\Omega'-\Omega)^2+2\Gamma^2)\log(((\bar{u}-\Omega')^2+\Gamma^2)/(\bar{u}-\Omega)^2+\Gamma^2))}{(\Omega'-\Omega)((\Omega'-\Omega)^2+4\Gamma^2)}\right]\Bigg|_{-\bar{u}'}^{+\bar{u}'} d\bar{u}\;d\Omega \quad (A.32)$$

with the particular case for $\Omega' \to \Omega$ with $z = \Omega' - \Omega$

$$\lim_{z\to 0}\frac{1}{z}\;\frac{(z+\Omega)^2-2(z+\Omega)\bar{u}+\bar{u}^2+\Gamma^2}{\Omega^2-2\Omega\bar{u}+\bar{u}^2+\Gamma^2} = \frac{2(z+\Omega)+2\bar{u}}{\Omega^2-2\Omega\bar{u}+\bar{u}^2+\Gamma^2} = 0 \quad (A.33)$$

finally to

$$s_i(\Omega') = -\mathcal{K}\mathcal{K}(s_i(\Omega)) = \frac{1}{\pi}\int_{-\infty}^{\infty} s_i(\Omega)\frac{2\Gamma}{(\Omega'-\Omega)^2+4\Gamma^2}\,d\Omega. \quad (A.34)$$

Eq.A.34 reduces for $\Gamma \to 0$ with

$$\delta(\Omega-\Omega') = \frac{1}{\pi}\lim_{\Gamma\to 0}\frac{\Gamma}{(\Omega-\Omega')^2+\Gamma^2} \quad (A.35)$$

to the inverse Hilbert transform

$$\lim_{\Gamma\to 0} s_i(\Omega') = -\mathcal{K}\mathcal{K}(s_i(\Omega)) = \int_{-\infty}^{\infty} s_i(\Omega)\delta(\Omega'-\Omega)\,d\Omega = s_i(\Omega') \quad \Rightarrow \quad \mathcal{K}=\mathcal{H}, -\mathcal{K}=\mathcal{H}^{-1}. \quad (A.36)$$

A.4 Various signal spectral densities

• Monochromatic rf-radiation

Starting from the autocorrelation function of the signal $i_{rf}(\tau) = i_{rf}\cos(\Omega\tau)$,

$$R_x(\tau) = \lim_{T\to\infty}\frac{1}{2T}\int_{-T}^{+T} i_{rf}(\tau')i_{rf}(\tau'+\tau)\,d\tau' \quad (A.37)$$

$$= \lim_{T\to\infty}\frac{1}{2T}\int_{-T}^{+T} i_{rf}^2\cos(\Omega\tau')\cos(\Omega(\tau'+\tau))\,d\tau = \lim_{T\to\infty} i_{rf}^2\frac{\cos(\Omega\tau)}{2}\left(1+\frac{\sin(2\Omega T)}{2\Omega T}\right) \quad (A.38)$$

$$= i_{rf}^2\frac{\cos(\Omega\tau)}{2}(1+D(\Omega)) \quad \forall \quad D(\Omega) = \begin{cases} 1 \;\forall\; \Omega = 0 \\ 0 \;\forall\; \Omega \neq 0 \end{cases} \quad (A.39)$$

the current spectral density is given by its Fourier transform of the autocorrelation. The integration over the limited function $D(\Omega)$ vanishes. The result corresponds to the Parseval theorem.

$$s_i(\Omega') = \mathcal{F}[R_x(\tau)] = \frac{\pi}{2}\,i_{rf}^2\,(\delta(\Omega'+\Omega)+\delta(\Omega'-\Omega)) \quad (A.40)$$

• Single rectangular/gaussian rf-pulse

The current spectral density of a single rf-pulse vanish. According to the definition of the spectral density Eq.4.35, this is because a single rf-pulse is time limited. But we can define its power density by using the Fourier transform. Starting from the rectangular rf-pulse with amplitude i_p and width τ_p

$$i_{rf,p}(\tau) = \begin{cases} i_p \;\forall\; |\tau| \le \tau_p/2 \\ 0 \;\forall\; \text{else} \end{cases} \quad \rightleftharpoons \quad \mathcal{F}[i_{rf,p}(\tau)] = i_p\tau_p\,\frac{\sin(\Omega\tau_p/2)}{\Omega\tau_p/2}, \quad (A.41)$$

its spectral power in normalized units results to

$$S_p(\Omega) = |\mathcal{F}[i_{rf,p}(\tau)]|^2 = i_p^2\tau_p^2\left|\frac{\sin(\Omega\tau_p/2)}{\Omega\tau_p/2}\right|^2. \quad (A.42)$$

For a gaussian rf-pulse with normalized width σ_τ, amplitude scaled by peak current i_{ps}

$$i_{rf,ps}(\tau) = i_{ps}\frac{1}{\sqrt{2\pi}\sigma_\tau}\,e^{-\frac{\tau^2}{2\sigma_\tau^2}} \quad \rightleftharpoons \quad \mathcal{F}[i_{rf,ps}(\tau)] = i_{ps}\,e^{-\frac{\sigma_\tau^2\Omega^2}{2}}, \quad (A.43)$$

the gaussian spectral power density is given by

$$S_{ps}(\Omega) = |\mathcal{F}[i_{rf,ps}(\tau)]|^2 = i_{ps}^2\,e^{-\frac{\Omega^2}{2\sigma_\Omega^2}} \quad \text{with} \quad \sigma_\Omega = \frac{1}{\sqrt{2}\sigma_\tau}. \quad (A.44)$$

• Series of rf-pulses

The current spectral density for a time signal results to

$$s_i(\Omega) = \int_{-\infty}^{+\infty}\lim_{T\to\infty}\frac{1}{2T}\int_{-T}^{+T} i_{rf}(\tau')i_{rf}(\tau'+\tau)\,d\tau' e^{-i\Omega\tau}d\tau, \quad S(\Omega) = \mathcal{F}[i_{rf}(\tau)] \quad (A.45)$$

$$= \lim_{T\to\infty}\frac{1}{2T}\int_{-T}^{+T} i_{rf}(\tau')S(\Omega)e^{i\Omega\tau'}\,d\tau' = \lim_{T\to\infty}\frac{1}{2T}S(\Omega)\int_{-\infty}^{+\infty} i_{rf}(\tau')e^{i\Omega\tau'}d\tau' \quad (A.46)$$

$$= \lim_{T\to\infty}\frac{1}{2T}\mathcal{F}^*[i_{rf}(\tau)]\mathcal{F}[i_{rf}(\tau)] \quad \forall \quad i_{rf}(\tau) = i_{rf}(-\tau),\; S(-\Omega) = S^*(\Omega). \quad (A.47)$$

Inserting the series of rf-pulses Eq.4.32, respectively its spectrum into Eq.A.46, the current spectral density becomes by using the definition of the convolution

$$s_i(\Omega) = \lim_{T\to\infty} S^*(\Omega)\,\frac{1}{2T}\sum_n\int_{-T}^{+T}\delta(\tau-n\tau_R) * i_{rf,p}(\tau)\;e^{i\Omega\tau}\,d\tau \quad (A.48)$$

$$= \lim_{T\to\infty} S^*(\Omega)\,\frac{1}{2T}\sum_n\int_{-T}^{+T}\int_{-\infty}^{+\infty} i_{rf,p}(\tau')\delta(\tau-\tau'-n\tau_R)d\tau' e^{i\Omega\tau}d\tau \quad (A.49)$$

$$= \lim_{T\to\infty} S^*(\Omega)\int_{-\infty}^{+\infty} i_{rf,p}(\tau')\lim_{T\to\infty}\frac{1}{2T}\sum_n\int_{-T}^{+T}\delta(\tau-\tau'-n\tau_R)e^{i\Omega\tau}d\tau d\tau' \quad (A.50)$$

$$= \lim_{T\to\infty} S^*(\Omega)\int_{-\infty}^{+\infty} i_{rf,p}(\tau')e^{i\Omega\tau'}d\tau'\lim_{T\to\infty}\frac{1}{2T}\sum_{n\in[-T/\tau_R,+T/\tau_R]} e^{i\Omega n\tau_R} \quad (A.51)$$

$$= \lim_{T\to\infty} S^*(\Omega)\,\frac{1}{\tau_R}\mathcal{F}[i_{rf,p}(\tau)], \quad \text{and proceeding the first term analog} \quad (A.52)$$

$$= \sum_{n=-\infty}^{+\infty} e^{i\Omega n\tau_R}\frac{1}{\tau_R}\mathcal{F}^*[i_{rf,p}(\tau)]\mathcal{F}[i_{rf,p}(\tau)] = \sum_{n=-\infty}^{+\infty}\delta\left(\frac{\tau_R}{\tau}-n\right)\frac{1}{\tau_R}\mathcal{F}^*[i_{rf,p}(\tau)]\mathcal{F}[i_{rf,p}(\tau)] \quad (A.53)$$

$$= \Omega_R\sum_{n=-\infty}^{+\infty}\delta(\Omega-n\Omega_R)\frac{1}{\tau_R}\mathcal{F}^*[i_{rf,p}(\tau)]\mathcal{F}[i_{rf,p}(\tau)]. \quad (A.54)$$

With $\Omega = m\Omega_R$ from delta function in Eq.A.54, the last term of Eq.A.51 reduces to $2T/\tau_R$. By using $\delta(ax) = \delta(x)/|a|$ in Eq.A.54 and $\tau_R = 2\pi/\Omega_R$ we finally yield the current spectral density for a series of rf-pulses with single pulse shape $i_{rf,p}(\tau)$ in normalized units to

$$s_i(\Omega) = \frac{1}{2\pi}\Omega_R^2 \sum_n \delta(\Omega - n\Omega_R) S_p(\Omega). \tag{A.55}$$

The result corresponds to the Parseval theorem.

A.5 Voltage expectation value

According to Eq.4.3 the voltage expectation value Eq.4.5 for a periodic probability density and vanishing noise of ensemble averaging $\langle i_N(\tau)\rangle = 0\rangle$ is given for the ansatz

$$W(\varphi,\tau) = \sum_n c_n(\tau)\sin(\varphi) e^{in(\varphi+\varphi_0)} \tag{A.56}$$

by

$$u(\tau) = \langle i_0 + i_{rf}(\tau) + i_N(\tau) - \sin(\varphi)\rangle = i_0 + i_{rf}(\tau) - \langle\sin(\varphi)\rangle \tag{A.57}$$

$$\langle\sin(\varphi)\rangle = \int_{-\pi}^{+\pi} \sin(\varphi) W(\varphi,\tau) d\varphi = \int_{-\pi}^{+\pi} \sum_n c_n(\tau)\sin(\varphi) e^{in\varphi} e^{in\varphi_0} d\varphi \tag{A.58}$$

$$= \frac{1}{2i}\int_{-\pi}^{+\pi} \sum_n c_n(\tau)\left[e^{i(n+1)\varphi} - e^{i(n-1)\varphi}\right] e^{in\varphi_0} d\varphi \tag{A.59}$$

$$= \frac{1}{2i}\int_{-\pi}^{+\pi} \sum_n \left[c_{n-1}(\tau)e^{-i\varphi_0} - c_{n+1}(\tau)e^{i\varphi_0}\right] e^{in\varphi} e^{in\varphi_0} d\varphi \tag{A.60}$$

$$= -i\pi \sum_n \left[c_{n-1}(\tau)e^{-i\varphi_0} - c_{n+1}(\tau)e^{i\varphi_0}\right]\delta_{n,0} \quad \text{with} \quad c_1(\tau) = c_{-1}^*(\tau) \tag{A.61}$$

$$= -i\pi(c_{-1}(\tau)e^{-i\varphi_0} - c_1(\tau)e^{i\varphi_0}) = -2\pi\left(\mathrm{Re}\left[c_1(\tau)\right]\sin(\varphi_0) + \mathrm{Im}\left[c_1(\tau)\right]\cos(\varphi_0)\right) \tag{A.62}$$

$$u(\tau) = i_0 + i_{rf}(\tau) + 2\pi \mathrm{Im}\left[c_1(\tau)\right] \quad \forall \quad \varphi_0 = 0 \tag{A.63}$$

$$u(\tau) = i_0 + i_{rf}(\tau) + 2\pi \mathrm{Re}\left[c_1(\tau)\right] \quad \forall \quad \varphi_0 = \pi/2. \tag{A.64}$$

The averaged voltage response with ideal measured bandwidth $1/\tau_R$ is given by

$$\bar{u} = i_0 + \frac{1}{\tau_R}\int_0^{\tau_R} i_{rf}(\tau) d\tau + \frac{2\pi}{\tau_R}\int_0^{\tau_R} \mathrm{Im}\left[c_1(\tau)\right] d\tau. \tag{A.65}$$

According to Eq.A.65 the voltage response change at working point i_0 results to

$$\Delta\bar{u} = \frac{1}{\tau_R}\int_0^{\tau_R} \left[i_{rf}(\tau) - i_{rf}(0)\right] d\tau + \frac{2\pi}{\tau_R}\int_0^{\tau_R} \mathrm{Im}\left[\Delta c_1(\tau)\right] d\tau. \tag{A.66}$$

For pure dc-free rf-signals the 1st term vanishes. For rf-pulses this is only guaranteed, if there is no sampling used and the averaging happens over the rf-periode. Furthermore, the complete rf-coupling system has to be in a stationary state.

A.6 Collected power including overlapping effects

In this section I will derive maximum peak current ratings for the series of rf-pulses Eq.4.35 for a sufficient dense spectrum $\Omega_R \ll \Gamma(\Omega)$ based on the Hilbert transform spectroscopy. Inserting Eq.A.55 into Eq.4.31 the maximum current ratings for a series of rf-pulses can given by

$$i_{rf,-3dB}^2(\Omega,\Gamma_0) \geq \frac{1}{\pi}\Omega_R^2 \sum_n \int_{\Omega-\Gamma/2}^{\Omega+\Gamma/2} \delta(\Omega' - n\Omega_R) s_p(\Omega') d\Omega' \tag{A.67}$$

$$\geq \frac{1}{\pi}\Omega_R^2 \sum_n r(\Omega, n\Omega_R) S_p(n\Omega_R) \quad \forall \quad r(\Omega,\Omega') = \begin{cases} 1 \ \forall \ |\Omega'| \leq \Omega + \Gamma/2 \\ 0 \ \forall \ \text{else} \end{cases} \tag{A.68}$$

$$i_{rf,-3dB}^2(\Omega,\Gamma_0) \geq \frac{1}{\pi}\Omega_R^2 \sum_{n\in\left[\frac{(\Omega-\Gamma/2)}{\Omega_R}, \frac{(\Omega+\Gamma/2)}{\Omega_R}\right]} S_p(n\Omega_R) \tag{A.69}$$

For the monochromatic spectral density A.40 the maximum ratings A.69 reduce to the maximum ratings for monochromatic rf-radiation $i_{rf,-3dB}^2(\Omega,\Gamma_0)$ scaled by Ω_R^2. The saturation effect Eq.4.31 dominates in the low frequency range for high Josephson junction linewidths and large amplitudes of pulse-type signals. For the series of rf-pulses Eq.4.35 with sufficient dense spectrum $\Omega_R \ll \Gamma(\Omega)$ the maximum peak current ratings results to

$$i_{rf,-3dB}^2(\Omega,\Gamma_0) \geq \frac{1}{\pi}\Omega_R^2 \sum_{n\in\left[\frac{(\Omega-\Gamma/2)}{\Omega_R}, \frac{(\Omega+\Gamma/2)}{\Omega_R}\right]} i_p^2\tau_p^2 \left|\frac{\sin(\pi n\Omega_R\tau_p)}{\pi n\Omega_R\tau_p}\right|^2 \tag{A.70}$$

$$i_{rf,-3dB}^2(\Omega,\Gamma_0) \geq \frac{1}{\pi}\frac{1}{\tau_R} i_p^2\,\tau_p^2\,\Gamma(\Omega,\Gamma_0) \quad \forall \quad \frac{1}{\tau_R} \ll \Gamma(\Omega,\Gamma_0),\ (\Omega + \Gamma(\Omega,\Gamma_0)/2)\tau_p \ll 1 \tag{A.71}$$

$$i_p^2(\Omega,\Gamma_0,\tau_p,\tau_R) \leq \frac{1}{4\pi}\frac{\tau_R}{\tau_p^2}\frac{i_{rf,-3dB}^2(\Omega,\Gamma_0)}{\Gamma(\Omega,\Gamma_0)}. \tag{A.72}$$

It is obvious, that neighbouring spectral lines convoluted by the Josephson junction noise also produce additional spectral power at a fixed working point. These contributions have to summarize scaled by the spectral power characteristic of Josephson junction for monochromatic rf-radiation. For a series of arbitrary rf-pulses with spectrum $s_i(\Omega)$ we define

$$i_{rf,s_i(\Omega)}^2 = \frac{1}{2\pi}\int_{-\infty}^{+\infty} [(s_\Omega * \gamma_J)(\Omega)]^{1/2}\,[(s_i * \gamma_J)(\Omega)]^{1/2} d\Omega \qquad \text{with} \tag{A.73}$$

$$s_\Omega(\Omega) = \frac{\Omega_R^2}{2\pi}\sum_{\pm m}\delta(\Omega - m\Omega_R)S_p(\Omega),\ (s_\Omega * \gamma_J)(\Omega) = \frac{\Omega_R^2}{2\pi}\sum_{\pm m}\frac{\Gamma}{(\Omega - m\Omega_R)^2 + \Gamma^2} S_p(m\Omega_R) \tag{A.74}$$

$$s_i(\Omega) = \frac{\Omega_R^2}{2\pi}\sum_{n}\delta(\Omega - n\Omega_R)S_p(\Omega),\ (s_\Omega * \gamma_J)(\Omega) = \frac{\Omega_R^2}{2\pi}\sum_{n}\frac{\Gamma}{(\Omega - n\Omega_R)^2 + \Gamma^2}\ S_p(n\Omega_R). \tag{A.75}$$

The rf-radiation spectrum $s_i(\Omega)$ has to be bandlimited, otherwise the collected power is divergent. For monochromatic rf-radiation $n = \pm m$, $s_\Omega(\Omega) = s_i(\Omega)$ and symmetric spectrum $S_p(-m\Omega_R) = S_p(m\Omega_R)$ the collected spectral power, scaled by repetition frequency Ω_R at frequency $m\Omega_R$, results to

$$i_{rf,s_i(\Omega)}^2 = \Omega_R^2 S_p(m\Omega_R)/2\pi. \tag{A.76}$$

A.7 Numerical solution of recurrence relations

A.7.1 I-V-characteristic without radiation

To calculate the I-V-charactristic of a Josephson junction without radiation $i_{rf}(\tau) = 0$ within the FP method, the operator L_{FP} is not explicit time dependent and the probability density can be seperated by making an ansatz for the stationary probability density $W(\varphi)$ with a Fourier expansion of the phase φ and coefficients c_n

$$W(\varphi) = \sum_n c_n\, e^{in\varphi} \qquad \text{with} \qquad c_n = c_{-n}^*. \tag{A.77}$$

For stationary solutions the probability current must be constant leading to $S = (i_0 - \sin\varphi)W(\varphi) - \Gamma_0\partial W(\varphi)/\partial\varphi$. Inserting the ansatz Eq.A.77 into Eq.4.4 one finds the following scalar tridiagonal

recurrence relation.

$$(i_0 - \Gamma_0 in)c_n + \frac{i}{2}(c_{n-1} - c_{n+1}) = S\delta_{n,0} \tag{A.78}$$

For $n = 0$ and $c_1 = c_{-1}^*$ the probability current S is given by $2\pi S = i_0 + 2\pi \mathrm{Im}[c_1]$. Periodic potentials like $\sin(\varphi)$ results also in a periodic probability density $W(\varphi+2\pi) = W(\varphi)$ [Ris96, Rie88], and the averaged voltage drop over Josephson junction depends

$$\bar{u} = \overline{\langle\dot{\varphi}\rangle} = \overline{\langle i_0 - \sin\varphi + i_N(\tau)\rangle} = \langle i_0 - \sin\varphi\rangle \tag{A.79}$$

$$= \int_0^{2\pi} (i_0 - \sin\varphi)W(\varphi)d\varphi = \int_0^{2\pi} S + \Gamma_0 \frac{\partial}{\partial\varphi} W(\varphi)d\varphi = 2\pi S \tag{A.80}$$

on a constant probability current S. Finally we obtain with the probability current S and the solution of the tridiagonal recurrence relation Eq.A.102 with parameters $Q_n^- = i/2$, $Q_n^+ = -i/2$, $Q_n = i_0 - \Gamma_0 in$ the averaged voltage response of a junction including noise. For computational implementation Eq.A.81 is an efficient expression, where its fraction denotes a continued fraction defined by Eq.A.106.

$$\bar{u} = i_0 + 2\pi \mathrm{Im}[c_1] \qquad \text{with} \qquad 2\pi c_1 = 2\sum_{n=1}^{\infty} \frac{1/4}{\lfloor n\Gamma_0 + i\, i_0} \tag{A.81}$$

According to Eq.A.81 the first FP coefficient is mostly negative $c_1 < 0$ for correcting the resistive straight line to the actual I-V-characteristic. In the noisefree limit $\Gamma_0 \to 0$ Eq.A.81 becomes a periodic continued fraction having the value

$$2\pi c_1 = -i\, i_0 + \sqrt{1 - i_0^2}, \qquad 2\pi \mathrm{Re}(c_1)_{\Gamma_0 \to 0} = \begin{cases} \sqrt{1 - i_0^2} & \forall\ |i_0| \le 1 \\ 0 & \forall\ i_0 \ge 1 \end{cases} \tag{A.82}$$

$$2\pi \mathrm{Im}[c_1]_{\Gamma_0 \to 0} = \begin{cases} -i_0 & \forall\ |i_0| \le 1 \\ -i_0 + \sqrt{i_0^2 - 1} & \forall\ i_0 \ge 1 \end{cases} \tag{A.83}$$

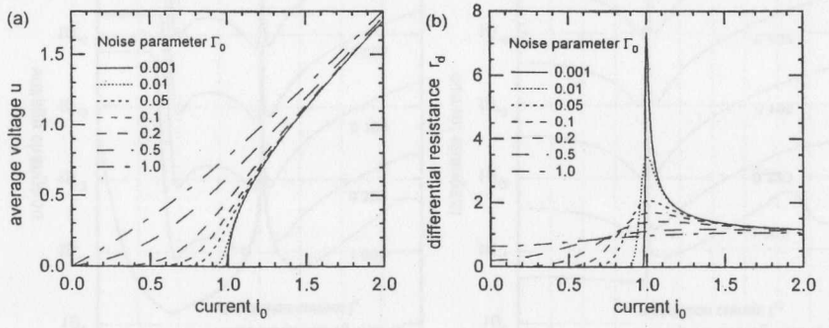

Figure A.1: *Simulated (a) V-I-characteristic and (b) differential resistance $r_d = d\bar{u}/di_0$ of Josephson junction for different noise parameters Γ_0 calculated with the FP method.*

A.7.2 I-V-characteristic with periodic radiation

To calculate the I-V-characteristic of a Josephson junction with discrete radiation spectrum, we introduce its Fourier transform without having any dc component $\tilde{i}_0$

$$i_{rf}(\tau) = \sum_{k=-\infty}^{\infty} \tilde{i}_k e^{-ik\Omega\tau} = \frac{\tilde{i}_0}{2} + \sum_{k=1}^{\infty} \tilde{i}_k \left(e^{ik\Omega\tau} + e^{-ik\Omega\tau}\right), \tag{A.84}$$

where $i_{rf}(\tau + 2\pi/\Omega) = i_{rf}(\tau)$ is periodic. Inserting this and making the ansatz for the probability density with a Fourier expansion in phase and time

$$W(\varphi,\tau) = \sum_{n,m} c_{n,m} e^{in\varphi - im\Omega\tau} \qquad \text{with} \qquad c_{n,m} = c_{-n,-m}^* \tag{A.85}$$

into the time dependent FP equation 4.4 we yield the following scalar recurrence relation.

$$inf_{n,m} - im\Omega\, c_{n,m} = 0 \qquad \text{with} \tag{A.86}$$

$$f_{n,m} = (i_0 - \Gamma_0 in)\, c_{n,m} + \frac{i}{2}(c_{n-1,m} - c_{n+1,m}) + \sum_{k=1}^{\infty} \tilde{i}_k (c_{n,m+k} - c_{n,m-k}) \tag{A.87}$$

To guarantee Eq.A.86, the coefficients must be fulfill $c_{0,m} = 0\ \forall\ n = 0, |m| \ge 1$. The normalization of probability must be valid for all times and results in $\sum_m c_{0,m} exp\ (-im\Omega\tau) = 1/2\pi \to c_{0,m} = \delta_{0,m}/2\pi$ leading to the unperturbated recurrence of I-V-characteristic indexed by n and the perturbated part indexed by m.

$$f_{0,m} = S,\ c_{0,m} = \frac{1}{2\pi}\,\delta_{0,m} \qquad \forall\ n = 0 \tag{A.88}$$

$$(i_0 - \Omega\frac{m}{n} - \Gamma_0 in)\, c_{n,m} + \frac{i}{2}(c_{n-1,m} - c_{n+1,m}) + \sum_{k=1}^{\infty} \tilde{i}_k (c_{n,m+k} - c_{n,m-k}) = 0 \quad \forall\ n \ne 0$$

With the same formalism as needed for Eq.A.81 voltage drop over Josephson junction by using the periodicity of the probability density $W(\varphi + 2\pi, \tau) = W(\varphi,\tau)$, $W(\varphi, \tau + 2\pi/\Omega) = W(\varphi,\tau)$ is given by

$$\bar{u} = i_0 + 2\pi \mathrm{Im}[c_{1,0}]\,. \tag{A.89}$$

In practice the recurrence Eq.A.88 with the indices n, m, k cuts at finite values K, N, M with $K < M$. The convergence of Eq.A.88 is better for lower rf-currents $\tilde{i}_k$ and higher bias point currents i_0, frequency Ω and temperature T, which smoothed out the I-V-characteristic. The poles in the I-V-charateristic for $\Gamma_0 \to 0$, $i_0 \ge 1$ are identified by the vanishing of the diagonal term $(i_0 - \Omega m/n - \Gamma_0 in)$. The recurrence relation Eq.A.88 presents a linear system of equations with band diagonal matrix structure, which is solved numerical for finite size $(N+1)^2 \times (M+1)^2$. Especially for monochromatic rf-radiation we implemented numerical routines for $K = 1$, $N = 40$, $M = 30$, $i_0 \ge 1$, $i_{rf} < 0.1$, $\Omega > 1$ and $T > 8K$.

$$\begin{pmatrix} 1 & & & & & & & & 0 \\ & 1 & & & & & & & \\ & & 1 & & & & & & \\ & & & \ddots & & & & & \\ 0 & & & & 1 & & & & \\ +\frac{i}{2}\cdots\tilde{i}_k & \cdots & \tilde{i}_1 & (i_0 - \Gamma_0 i) & \tilde{i}_1 & \cdots & \tilde{i}_k & \cdots -\frac{i}{2} & 0 \\ & & & & \ddots & & & & \\ & +\frac{i}{2}\cdots\tilde{i}_k & \cdots & \tilde{i}_1 & (i_0 - \Omega m - \Gamma_0 i) & \tilde{i}_1 & \cdots & \tilde{i}_k \cdots -\frac{i}{2} & \\ & & +\frac{i}{2}\cdots\tilde{i}_k & \cdots & \tilde{i}_1 & (i_0 - \Gamma_0 in) & \tilde{i}_1 & \cdots\ \tilde{i}_k \cdots -\frac{i}{2} & \\ & & & & & \ddots & & & \\ 0 & & +\frac{i}{2}\cdots & \tilde{i}_k & \cdots & \tilde{i}_1 & (i_0 - \Omega\frac{m}{n} - \Gamma_0 in)\ \tilde{i}_1 & \cdots\ \tilde{i}_k \cdots -\frac{i}{2} & \end{pmatrix} \cdot \begin{pmatrix} c_{0,0} \\ \vdots \\ c_{0,m} \\ c_{1,0} \\ \vdots \\ c_{1,m} \\ c_{n,0} \\ \vdots \\ c_{n,m} \end{pmatrix} = 0 \tag{A.90}$$

Fig.A.2 show an example for monochromatic rf-radiation. Up to a critical rf-current $i_{rf} \simeq 0.2$ the junction enters the nonlinear region of the response. The voltage response is converted numerically into the current response by rotating the axis of the V-I-characteristic.

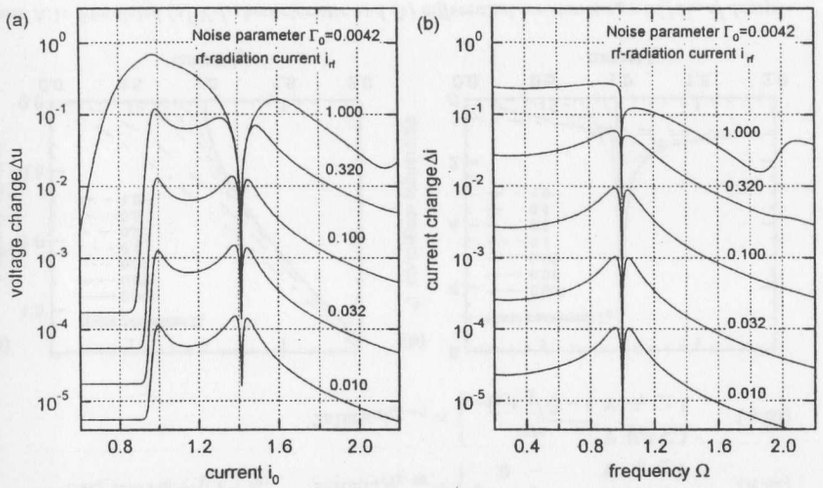

Figure A.2: *FP simulated (a) voltage response $\Delta\bar{u}$ in dependence of bias current i_0 and (b) frequency dependent current response for different rf-currents i_{rf} at noise parameter $\Gamma_0 = 0.0042$.*

A.7.3 I-V-characteristic with arbitrary radiation (1st/2nd order)

To calculate the I-V-characteristic of Josephson junction with arbitrary rf-signals eithin the FP formalism the ansatz of the probability density with time dependent coefficients $c_n(\tau)$ is presented. This ansatz is for pulsed-type radiation more efficient, than the methods performed in the appendix A.7.1,A.7.2 for monochromatic rf-radiation using the Fourier expansion in time.

$$W(\varphi,\tau) = \sum_n c_n(\tau)\, e^{in\varphi} \qquad \text{with} \qquad c_n(\tau) = c^*_{-n}(\tau) \tag{A.91}$$

Inserting Eq.A.91 into the FP equation 4.4 a recurrence relation with time dependent coeffients results to

$$\left(i_0 + i_{rf}(\tau) - \Gamma_0 in - \frac{i}{n}\frac{d}{d\tau}\right) c_n(\tau) + \frac{i}{2}\left(c_{n-1}(\tau) - c_{n+1}(\tau)\right) = 0 \qquad \forall \qquad n \geq 1. \tag{A.92}$$

The normalization of probability density leads again for $n = 0$ to $c_0(\tau) = 1/2\pi$. Using its periodicity with respect to the phase φ one can obtain Eq.A.63 the voltage expectation value $\bar{u}(\tau)$ at time τ or averaged expectation value $\bar{u}$ assuming dc-free rf-signals and vanishing noise contributions averaged over the ensembles.

$$u(\tau) = i_0 + i_{rf}(\tau) + 2\pi \mathrm{Im}\left[c_1(\tau)\right], \tag{A.93}$$

$$\bar{u} = i_0 + 2\pi \lim_{T\to\infty} \frac{1}{2T}\int_{-T}^{T} \mathrm{Im}\left[c_1(\tau)\right] d\tau \quad \text{with} \quad \overline{i_{rf}(\tau)} = 0,\ \langle i_N(\tau)\rangle = 0 \tag{A.94}$$

In the folling we negelect the direct noise contributions $i_N(\tau)$ in Eq.A.93, because we are interested only in the junctions response. Otherwise we would determine the I-V-characteristic better using stochastical methods. Because of the dependencies we laxly call $\bar{u}(\tau)$ the FP 1st order recurrence coefficient, respectively averaged FP 1st order recurrence coefficient. The hierarchy of equations A.92 read explicitly

$$\begin{pmatrix} 1 & & & & 0 \\ +\frac{i}{2} & (i_0 + i_{rf}(\tau) - \Gamma_0 i - i\frac{d}{d\tau}) & -\frac{i}{2} & & \\ & +\frac{i}{2} & (i_0 + i_{rf}(\tau) - 2\Gamma_0 i - \frac{i}{2}\frac{d}{d\tau}) & -\frac{i}{2} & \\ & & \ddots & & \\ 0 & & +\frac{i}{2} & (i_0 + i_{rf}(\tau) - n\Gamma_0 i - \frac{i}{n}\frac{d}{d\tau}) & -\frac{i}{2} \end{pmatrix} \cdot \mathbf{c}(\tau) = 0, \quad \mathbf{c}(\tau) = \begin{pmatrix} c_0(\tau) \\ c_1(\tau) \\ c_2(\tau) \\ \vdots \\ c_n(\tau) \end{pmatrix}. \tag{A.95}$$

Without any radiation the system of equations can be solved by the ansatz $c_n(\tau) = e^{-\lambda\tau}\hat{c}_n$ and reduces to the determination of complex eigenvalues λ [Ris96]. However, we solved Eq.A.92 by a *1st order* differencing scheme in time, similarly the solution of partial differential equations. By using the difference coefficient for the next time step $\tau' = \tau + \Delta\tau$ with $\alpha_n(\tau') = ni(i_0 + i_{rf}(\tau') - n\Gamma_0 i)$, $\beta_n = n/2$, we get

$$\frac{d}{d\tau}\, c_n(\tau) \;\Rightarrow\; \frac{\Delta c_n(\tau)}{\Delta\tau} = \frac{c_n(\tau') - c_n(\tau)}{\Delta\tau} = -\alpha_n(\tau')c_n(\tau') + \beta_n(c_{n-1}(\tau') - c_{n+1}(\tau')), \tag{A.96}$$

which leads to the tridiagonal system with constant coefficients

$$(1 + \Delta\tau\alpha_n(\tau'))c_n(\tau') - \Delta\tau\beta_n(c_{n-1}(\tau') - c_{n+1}(\tau')) = c_n(\tau). \tag{A.97}$$

Eq.A.97 solved iteratively resulting in the time trace of coefficients $c_n(\tau)$ with starting condition $c_n(0)$, which represents the unpertubated coefficients Eq.A.81 without radiation. Especially for continuous broadband spectra Eq.A.97 is a useful approach with acceptable stepping $\Delta\tau$, respectively simulation times. Eq.A.97 is a fully implicit scheme and requires for discrete spectra very small time steps $\Delta\tau$, otherwise the oscillation linewidth of Josephson junction in the high frequency range is broadened. To prevent this, we implemented the *2nd order* accuracy in time by the *Crank-Nicholsen* scheme [Num00]. According to Eq.A.96, we simply form the average of the explicit and implicit scheme resulting in a tridiagonal system

$$\frac{c_n(\tau') - c_n(\tau)}{\Delta\tau} = \frac{1}{1+\eta}\Big[\left(-\alpha_n(\tau')c_n(\tau') + \beta_n(c_{n-1}(\tau') - c_{n+1}(\tau'))\right) + \eta\left(-\alpha_n(\tau)c_n(\tau) + \beta_n(c_{n-1}(\tau) - c_{n+1}(\tau))\right)\Big]. \tag{A.98}$$

or written explicitly with $\gamma = \Delta\tau/(1+\eta)$, as computational implemented [1] for arbitrary rf-radiation

$$\begin{pmatrix} 1 & & & & 0 \\ -\gamma\beta_1 & 1+\gamma\alpha_1(\tau') & \gamma\beta_1 & & \\ & -\gamma\beta_2 & 1+\gamma\alpha_2(\tau') & \gamma\beta_2 & \\ & & \ddots & & \\ 0 & & -\gamma\beta_n & 1+\gamma\alpha_n(\tau') & \gamma\beta_n \end{pmatrix} \cdot \mathbf{c}(\tau') = \begin{pmatrix} 1 & & & & 0 \\ \gamma\eta\beta_1 & 1-\gamma\eta\alpha_1(\tau) & -\gamma\eta\beta_1 & & \\ & \gamma\eta\beta_2 & 1-\gamma\eta\alpha_2(\tau) & -\gamma\eta\beta_2 & \\ & & \ddots & & \\ 0 & & \gamma\eta\beta_n & 1-\gamma\eta\alpha_n(\tau) & -\gamma\eta\beta_n \end{pmatrix} \cdot \mathbf{c}(\tau). \tag{A.99}$$

The mixing parameter η changes slightly from the stable implicit scheme $\eta = 0$ to the accurate scheme $\eta = 1$, or vice versa. According to the *Neumann* stability analysis [Num00], there exists independent solutions or eigenmodes for slowly varying coefficients α_n, β_n in recursion n and

[1] C++ implementation: FOCK_COEFF_RSJ_G_HF 1st, 2nd order accuracy includes Eq.A.97,A.99,A.94

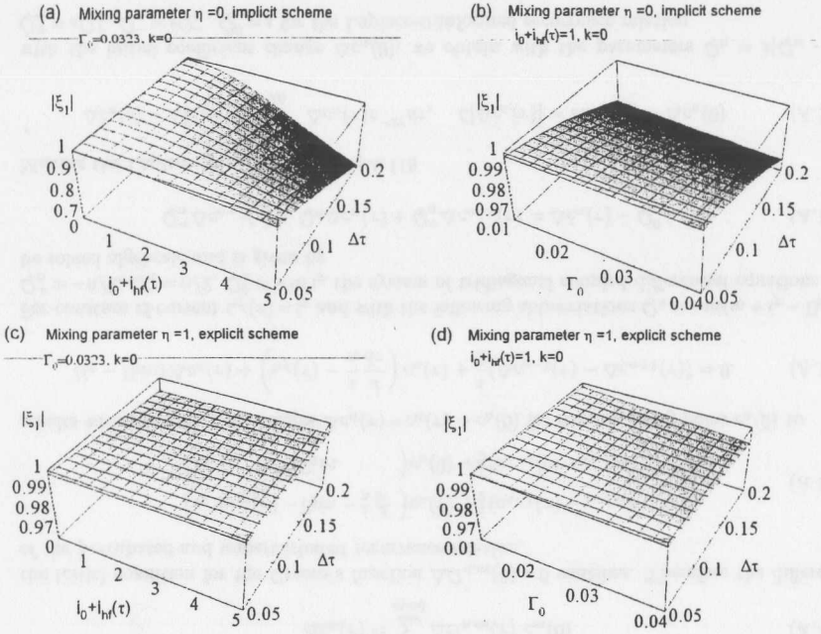

Figure A.3: *Stability analysis of Eq.A.99 for the first recursion coefficient c_1. Amplification factor of (a) the first order scheme $\eta = 0$ in dependence of total current and time step, respectively (b) of noise parameter. The amplification of the second order scheme $\eta = 1$ is much more nearly the unstability condition $|\xi| > 1$ and depends less strongly on (c) total current, (b) noise parameter and time step $\Delta\tau$ than the first order.*

time τ. Here, this is not good fulfilled due to the limitation $\Delta n = 1$ of the recursion coordinate [2]. However the essential behaviour of stability is reflected. As depicted in Fig.A.3a the amplification factor $\xi(k)$ of the first order difference scheme for arbitrary wave number k, total driven current $i_g = i_0 + i_{rf}$ and time stepping $\Delta\tau$ is absolute stable $|\xi| \leq 1$ and is given by

$$|\xi_{n,\eta=0}(k)|^2 = \left| \frac{1}{i(1 + \Delta\tau\alpha_n(i_g, \Gamma_0)) + 2\Delta\tau\beta_n \sin(k)} \right|^2 \leq 1. \tag{A.100}$$

According to Fig.A.3d, the second order scheme is effectively more stable for larger time steps $\Delta\tau$, noise parameter and good recursion conditions. The amplification factor is given by

$$|\xi_{n,\eta=1}(k)|^2 = \left| \frac{i(2 - \Delta\tau\alpha_n(i_g, \Gamma_0)) - 2\Delta\tau\beta_n \sin(k)}{i(2 + \Delta\tau\alpha_n(i_g, \Gamma_0)) + 2\Delta\tau\beta_n \sin(k)} \right|^2 \leq 1. \tag{A.101}$$

For discrete spectra and pulse-type signals with small duty cycles the averaging Eq.A.94 must

[2] This reflects the fact and Fig.A.3d indicates, that the second order scheme Eq.A.99 rarely diverge for poor recursion conditions like zero bias current, no rf-current change, low-noise parameter and small time stepping. One reason might be the absence of the capacity within the model, respectively damping term.

be performed over many periodes. But for pulses with high duty cycles and sufficient high noise parameter we get acceptable short simulation times by the method of time dependent coefficients.

A.8 Analytical solution of recurrence relations

In this section I will deduce solutions of the time independent and time dependent recurrence relations with initial values. By introducing coefficient changes we deduce the voltage changes of the I-V-characteristic in first order for pulse-type signals beyond the small signal approach.

A.8.1 Solution of the time independent coefficients

The tridiagonal recurrence relation can be rewritten with constant coefficients c_n as follows

$$Q_n^- c_{n-1} + Q_n c_n + Q_n^+ c_{n+1} = 0 \tag{A.102}$$

and with $S_n = c_{n+1}/c_n$ we yield from Eq.A.102

$$\frac{Q_n^-}{S_{n-1}} + Q_n + Q_n^+ S_n = 0 \qquad \forall \qquad n \tag{A.103}$$

$$\frac{Q_{n+1}^-}{S_n} + Q_{n+1} + Q_{n+1}^+ S_{n+1} = 0 \qquad \forall \qquad n \to n+1 \tag{A.104}$$

the coefficients S_n.

$$S_n = -\frac{Q_{n+1}^-}{Q_{n+1} + Q_n^+ S_{n+1}} = -\cfrac{Q_{n+1}^-}{Q_{n+1} - \cfrac{Q_{n+1}^+ Q_{n+2}^-}{Q_{n+2} - \cfrac{Q_{n+2}^+ Q_{n+3}^-}{Q_{n+3} - Q_{n+3}^+ \cdots}}} \tag{A.105}$$

$$\equiv -\left\lfloor \frac{Q_{n-1}^-}{Q_{n+1}} \right\rfloor - \left\lfloor \frac{Q_{n+1}^+ Q_{n+2}^-}{Q_{n+2}} \right\rfloor - \left\lfloor \frac{Q_{n+2}^+ Q_{n+3}^-}{Q_{+3}} \right\rfloor \cdots \tag{A.106}$$

The normalization of the probability density results in $c_0 = 1/2\pi$ and the coefficients are given by $c_n = S_{n-1} S_{n-2} \ldots S_0 c_0$.

A.8.2 Solution of the time dependent coefficients with initial value

The time dependent recurrence problem for the coefficients $c_n(\tau)$ with initial values is currently solved with the method of Green's functions [Ris96]

$$Q_n^- c_{n-1}(\tau) + Q_n c_n(\tau) + Q_{n+1}^+ c_{n+1}(\tau) = \dot{c}_n(\tau). \tag{A.107}$$

Here we only summerize the result.

$$c_n(\tau) = \sum_{m=0}^{\infty} G_{n,m}(\tau)\, c_m(0) \quad \text{with} \quad G_{n,m}(\tau) = \mathcal{L}^{-1}[\tilde{G}_{n,m}(s)] \tag{A.108}$$

$$\tilde{G}_{n,m}(s) = \tilde{U}_{n,m}(s)\tilde{G}_{n,m}(s), \quad \tilde{U}_{m,m}(s) = 1, \quad \tilde{G}_{m,m} = [s - Q_m - \tilde{K}_m(s)]^{-1} \tag{A.109}$$

$$\tilde{U}_{m,m}(s) = \tilde{S}_{n-1}^+(s)\tilde{S}_{n-2}^+(s) \ldots \tilde{S}_m^+(s), \quad \forall \quad n \geq m+1 \tag{A.110}$$

$$\tilde{U}_{m,m}(s) = \tilde{S}_{n+1}^-(s)\tilde{S}_{n+2}^-(s) \ldots \tilde{S}_m^-(s), \quad \forall \quad 0 \leq n \leq m-1 \tag{A.111}$$

$$\tilde{S}_m^+(s) = -\cfrac{Q_{m+1}^-}{Q_{m+1}-s} - \cfrac{Q_{m+1}^+Q_{m+2}^-}{Q_{m+2}-s} \cdots - \cfrac{Q_{N-1}^+Q_N^-}{Q_N-s} \tag{A.112}$$

$$\tilde{S}_m^-(s) = -\cfrac{Q_{m-1}^+}{Q_{m-1}-s} - \cfrac{Q_{m-1}^-Q_{m-2}^+}{Q_{m-2}-s} \cdots - \cfrac{Q_1^-Q_0^+}{Q_0-s} \tag{A.113}$$

$$\tilde{K}_m(s) = Q_m^-\tilde{S}_m^-(s) + Q_m^+\tilde{S}_m^+(s) \tag{A.114}$$

A.8.3 Solution of the time dependent coefficient change with initial value

As mentioned in section A.8.2 the time dependent recurrence problem with initial value for the coefficients is currently solved. Here, for the voltage response of the Josephson junction, we are interested in the change of the FP coeffcients $\Delta c_n(\tau)$ for a given initial value $c_1(0)$. For our application the solution differs due to the fact, that the initial values appear as an inhomogeneity in every recurrence equation and with the general solution

$$\Delta c_n(\tau) = \sum_{m=0}^{\infty} \Delta G_{n,m}(\tau)\, c_m(0) \tag{A.115}$$

the initial condition for the Greens's function $\Delta G_{n,m}(0) = 0$ vanishes. Therefore the difference of the pertubated and unperturbated recurrence relation,

$$\begin{aligned} \left(i_0 + i_{rf}(\tau) - \Gamma_0 in - \tfrac{i}{n}\tfrac{d}{d\tau}\right)c_n(\tau) + \tfrac{i}{2}(c_{n-1}(\tau) - c_{n+1}(\tau)) &= 0 \\ \left(i_0 + \qquad - \Gamma_0 in \qquad\right)c_n(0) + \tfrac{i}{2}(c_{n-1}(0) - c_{n+1}(0)) &= 0 \end{aligned} \tag{A.116}$$

results with the cofficient changes $\Delta c_n(\tau) = c_n(\tau) - c_n(0)$ for fixed working point $c_n(0)$ to

$$(i_0 - \Gamma_0 in)\,\Delta c_n(\tau) + \left(i_{rf}(\tau) - \frac{i}{n}\frac{d}{d\tau}\right)c_n(\tau) + \frac{i}{2}(\Delta c_{n-1}(\tau) - \Delta c_{n+1}(\tau)) = 0. \tag{A.117}$$

For constant rf-current $i_{rf}(\tau) = i_p$ and with the following abbreviations $Q_n = -ni(i_0 + i_p - \Gamma_0 in)$, $Q_n^+ = -n/2$, $Q_n^- = n/2$, $Q_n^0 = -ni\,i_p$ the system of tridiagonal coupled differential equations can be solved algebraic and is given by

$$Q_n^-\Delta c_{n-1}(\tau) + Q_n\Delta c_n(\tau) + Q_n^+\Delta c_{n+1}(\tau) = \Delta\dot{c}_n(\tau) - Q_n^0 c_n(0). \tag{A.118}$$

Making the Laplace transform $\mathcal{L}$ of Eq.A.118

$$\Delta\tilde{c}_n(s) = \mathcal{L}[c_n(\tau)] = \int_0^\infty \Delta c_n(\tau)e^{-s\tau}d\tau, \quad \mathcal{L}[\Delta\dot{c}_n(\tau)] = s\Delta\tilde{c}_n(s) - \Delta c_n(0) \tag{A.119}$$

with the initial coefficient change $\Delta c_n(0)$, we obtain with the parameters $\tilde{Q}_n = s(Q_n - s)$, $\tilde{Q}_n^+ = sQ_n^+$, $\tilde{Q}_n^- = sQ_n^-$, $\tilde{Q}^0 = s$ for the Laplace-tranformed recurrence relation

$$\tilde{Q}_n^-\Delta\tilde{c}_{n-1}(s) + \tilde{Q}_n\Delta\tilde{c}_n(s) + Q_n^+\Delta\tilde{c}_{n+1}(s) = -Q_n^0 c_n(0) - \tilde{Q}^0\Delta c_n(0). \tag{A.120}$$

The tridiagonal system of coupled equations A.120 truncates with $c_n(s) = 0\ \forall\ n \geq N+1$ and

reads explicitly

$$\begin{array}{lllll} & \tilde{Q}_0\Delta\tilde{c}_0(s) & + \tilde{Q}_0^+\Delta\tilde{c}_1(s) & = -Q_0^0c_0(0) & - \tilde{Q}^0\Delta c_0(0) \\ \tilde{Q}_1^-\Delta\tilde{c}_0(s) & + \tilde{Q}_1\Delta\tilde{c}_1(s) & + \tilde{Q}_1^+\Delta\tilde{c}_2(s) & = -Q_1^0c_1(0) & - \tilde{Q}^0\Delta c_1(0) \\ \vdots & \vdots & \vdots & \vdots & \vdots \\ \tilde{Q}_{N-1}^-\Delta\tilde{c}_{N-2}(s) & + \tilde{Q}_{N-1}\Delta\tilde{c}_{N-1}(s) & + \tilde{Q}_n^+\Delta\tilde{c}_N(s) & = -Q_{N-1}^0c_{N-1}(0) & - \tilde{Q}^0\Delta c_{N-1}(0) \\ \tilde{Q}_N^-\Delta\tilde{c}_{N-1}(s) & + \tilde{Q}_N\Delta\tilde{c}_N(s) & & = -\tilde{Q}_N^0c_N(0) & - \tilde{Q}^0\Delta c_N(0) \end{array} \tag{A.121}$$

The last equation of Eq.A.121 can be expressed by

$$\Delta\tilde{c}_N(s) = \tilde{S}_{N-1}^+(s)\Delta\tilde{c}_{N-1}(s) + \tilde{a}_N(s) \qquad \text{with} \tag{A.122}$$

$$\tilde{S}_{N-1}^+(s) = -\frac{\tilde{Q}_N^-}{\tilde{Q}_N},\ \tilde{a}_N(s) = -\frac{Q_N^0c_N(0) + \tilde{Q}^0\Delta c_N(0)}{\tilde{Q}_N}. \tag{A.123}$$

Inserting this into the second-last equation of Eq.A.121 we obtain

$$\Delta\tilde{c}_{N-1}(s) = \tilde{S}_{N-2}^+(s)\Delta\tilde{c}_{N-2}(s) + \tilde{a}_{N-1}(s) \qquad \text{with} \tag{A.124}$$

$$\tilde{S}_{N-2}^+(s) = -\frac{\tilde{Q}_{N-1}^-}{\tilde{Q}_{N-1} + \tilde{Q}_{N-1}^+\tilde{S}_{N-1}^+(s)}, \tag{A.125}$$

$$\tilde{a}_{N-1}(s) = -\frac{Q_{N-1}^0c_{N-1}(0) + \tilde{Q}^0\Delta c_{N-1}(0) + \tilde{Q}_{N-1}^+\tilde{a}_N(s)}{\tilde{Q}_{N-1} + \tilde{Q}_{N-1}^+\tilde{S}_{N-1}^+(s)}. \tag{A.126}$$

We proceed in this way until we reach the second equation of Eq.A.121 and finally obtain

$$\Delta\tilde{c}_{n+1}(s) = \tilde{S}_n^+(s)\Delta\tilde{c}_n(s) + \tilde{a}_{n+1}(s) \qquad \text{with} \tag{A.127}$$

$$\tilde{S}_{N-1}^+(s) = -\frac{\tilde{Q}_N^-}{\tilde{Q}_N},\ \tilde{a}_N(s) = -\frac{Q_N^0c_N(0) + \tilde{Q}^0\Delta c_N(0)}{\tilde{Q}_N}, \tag{A.128}$$

$$\tilde{S}_n^+(s) = -\frac{\tilde{Q}_{n+1}^-}{\tilde{Q}_{n+1} + \tilde{Q}_{n+1}^+\tilde{S}_{n+1}^+(s)},\ \tilde{a}_n(s) = -\frac{Q_n^0c_n(0) + \tilde{Q}^0\Delta c_n(0) + \tilde{Q}_n^+\tilde{a}_{n+1}(s)}{\tilde{Q}_n + \tilde{Q}_n^+\tilde{S}_n^+(s)}. \tag{A.129}$$

Inserting the first equation of Eq.A.121 into Eq.A.129 for $n = 0$, the initial solution $\tilde{a}_0$ leads with $\Delta\tilde{c}_1(s) = \tilde{S}_0^+(s)\Delta\tilde{c}_0(s) + \tilde{a}_1(s)$ to

$$\tilde{a}_0(s) = -\frac{-\tilde{Q}_0\Delta\tilde{c}_0(s) - Q_0^+\Delta\tilde{c}_1(s) - \tilde{Q}^0\Delta c_0(0) + \tilde{Q}^0\Delta c_0(0) + \tilde{Q}_0^+\tilde{a}_1(s)}{\tilde{Q}_0 + \tilde{Q}_0^+\tilde{S}_0^+(s)} = \Delta\tilde{c}_0(s). \tag{A.130}$$

As usual, the multiple use of Eq.A.127 on the initial state $\tilde{a}_0$ results to the nth coefficient change $\Delta\tilde{c}_n(s)$. Applying the inverse Laplace transform $\mathcal{L}^{-1}$ the solution of the time dependent recurrence relation Eq.A.118 reads explicitly

$$\begin{array}{lll} \Delta c_n(\tau) = \mathcal{L}^{-1}[\Delta\tilde{c}_n(s)] \quad \text{with} \quad \Delta\tilde{c}_n(s) = & \tilde{S}_{n-1}^+(s)\,\tilde{S}_{n-2}^+(s)\ldots\tilde{S}_1^+(s)\,\tilde{S}_0^+(s) & \tilde{a}_0(s) \\ & + \tilde{S}_{n-1}^+(s)\,\tilde{S}_{n-2}^+(s)\ldots\tilde{S}_1^+(s) & \tilde{a}_1(s) \\ & + \quad\ldots & \\ & + \tilde{S}_{n-1}^+(s)\,\tilde{S}_{n-2}^+(s) & \tilde{a}_{n-2}(s) \\ & + \tilde{S}_{n-1}^+(s) & \tilde{a}_{n-1}(s) \\ & + & \tilde{a}_n(s) \end{array} \tag{A.131}$$

$$\tilde{S}_n^+(s) = -\cfrac{\tilde{Q}_{n+1}^-\rfloor}{\lceil\tilde{Q}_{n+1}} - \cfrac{\tilde{Q}_{n+1}^+\tilde{Q}_{n+2}^-\rfloor}{\lceil\tilde{Q}_{n+2}} \cdots - \cfrac{\tilde{Q}_{N-1}^+\tilde{Q}_N^-\rfloor}{\lceil\tilde{Q}_N} \tag{A.132}$$

A.8.4 Single rf-pulse outside the small signal approach

Now, I will deduce the voltage response change in 1st recurrence order for a single rectangular rf-pulse outside the Hilbert transform spectroscopy within the FP formalism. By solving the difference of the perturbated and unperturbated recurrence relation within the DRR method, the solution of Eq.4.14 for a single non filtered rectangular rf-pulse with peak rf-current i_p and pulse width τ_p

$$i_{rf}(\tau) = \begin{cases} i_p \;\forall \text{ region I} : 0 < \tau < \tau_p \\ 0 \;\forall \text{ region II}: \text{ else} \end{cases} \tag{A.133}$$

by using the continuity at region I/II of the coefficient at time $\tau = 0$ and $\tau = \tau_p$ with $\alpha_1 = i(i_0 - \Gamma_0 i)$ is given by

$$\Delta c_1^I(\tau) = -c_1(0)\frac{i\,i_p}{(\alpha_1 + i\,i_p)}\left(1 - e^{-(\alpha_1 + i\,i_p)\tau}\right). \tag{A.134}$$

$$\Delta c_1^{II}(\tau) = -c_1(0)\frac{i\,i_p}{(\alpha_1 + i\,i_p)}\left(e^{-\alpha_1(\tau-\tau_p)} - e^{-\alpha_1\tau - i\,i_p\tau_p}\right). \tag{A.135}$$

Solutions for higher recurrence order are obtained from the a more general formalism derived in section A.8.3. The result Eq.A.135 is in accordance to the first recurrence order Eq.A.157,Eq.A.159. For a single rf-pulse the expectation value of the voltage response change is given for $\langle i_N(\tau)\rangle = 0$ by

$$\Delta u(\tau) = [i_{rf}(\tau) - i_{rf}(0)] + 2\pi \mathrm{Im}[\Delta c_1^I(\tau) + \Delta c_1^{II}(\tau)]. \tag{A.136}$$

The actual down mixing process of rf-signal components from the rf-region into the hf-region is realized by the readout system transfer function LP, which has typically low-pass filter charateristic consisting of bond-wires, strip-lines and rf-amplifiers.

$$\Delta\bar{u}(\tau) = LP\left[i_{rf}(\tau) - i_{rf}(0)\right] + LP\left[2\pi\mathrm{Im}[\Delta c_1^I(\tau) + \Delta c_1^{II}(\tau)]\right]. \tag{A.137}$$

According to the averaging Eq.A.19 the low-pass characteristic of the system environment is absolute necessary for the frequency selectivity of the Josephson spectrometer. To simplify we replace the readout system transfer function by pure averaging of the voltage response up to the ideal measuring bandwidth $1/\tau_B$, respectively sampling time τ_B, and identify the difference rf-term as a pure averaged dc-shift $i_{dc} = i_p\tau_p/\tau_B$ of working point from rf-pulse duration.

$$\Delta\bar{u} = \frac{1}{\tau_B}\int_0^{\tau_B}[i_{rf}(\tau) - i_{rf}(0)]\,d\tau + \frac{2\pi}{\tau_B}\int_0^{\tau_B}\mathrm{Im}\left[\Delta c_1^I(\tau) + \Delta c_1^{II}(\tau)\right]d\tau. \tag{A.138}$$

$$\Delta\bar{u} = i_{dc} + \frac{2\pi}{\tau_B}\mathrm{Im}\left[\int_0^{\tau_p}\Delta c_1^I(\tau)d\tau + \int_{\tau_p}^{\tau_B}\Delta c_1^{II}(\tau)d\tau\right] \tag{A.139}$$

Due to the fact, that only the difference of noise values before, during and after the rf-pulse, effects the measured voltage change, a two or three point sampling method for the different pulse regions reduces low-frequency noise contributions, which limits the measuring time. Several ideas and szenarios, that have not yet been realized, are discussed in chapter 4.6.. Inserting

Eq.A.134,A.135 into Eq.A.139 we yield

$$\Delta\bar{u} = i_{dc} + \frac{2\pi}{\tau_B}\mathrm{Im}\left[c_1(0)\left(\frac{i_p^2(1-e^{-(\alpha_1+i\,i_p)\tau_p})}{\alpha_1(\alpha_1+i\,i_p)^2} + \frac{i\,i_p\left(e^{-\alpha_1(\tau_p-\tau_B)} - e^{-\alpha_1\tau_B - i\,i_p\tau_p} - \alpha_1\tau_p\right)}{\alpha_1(\alpha_1+i\,i_p)}\right)\right] \tag{A.140}$$

For a down mixing process with low-pass characteristic of readout system compared to the rf-pulse frequencies justifies the approach for long sampling times $\tau_B \gg 1/\Gamma_0$, resulting finally with the working point $c_1(0) = c_1(i_0, \Gamma_0)$ and Eq.A.81 to

$$\Delta\bar{u} = i_{dc} + \frac{2\pi}{\tau_B}\mathrm{Im}\left[c_1(i_0,\Gamma)\left(\frac{i_p^2(1-e^{-(\alpha_1+i\,i_p)\tau_p})}{\alpha_1(\alpha_1+i\,i_p)^2} - \frac{i\,i_p\tau_p}{(\alpha_1+i\,i_p)}\right)\right] \quad \forall \quad \tau_B \gg 1/\Gamma_0 \quad \text{with (A.141)}$$

$$\Delta i \approx -\Delta\bar{u}/r_d(\bar{u},\Gamma_0), \quad \alpha_1 = i(i_0(\bar{u}) - \Gamma_0 i). \tag{A.142}$$

Using broadband spectra with small voltage responses Eq.4.16, especially rf-pulses, the response is transfered into the current response by the differential resistance $r_d(i_0,\Gamma_0)$. In accordance with the Hilbert theory, the response Eq.A.142 fall inversely proportional with the averaging time τ_B in the limit $\tau_B \gg 1/\Gamma_0$. According to Eq.A.82, the real part of the unperturbated first order FP coefficient in the interesting spectral region vanish, and Eq.A.141 simplifies to

$$\Delta\bar{u} = i_{dc} + \frac{2\pi}{\tau_B}\mathrm{Im}\left[c_1(i_0,\Gamma_0)\right]\mathrm{Re}\left[\frac{i_p^2(1-e^{-(\alpha_1+i\,i_p)\tau_p})}{\alpha_1(\alpha_1+i\,i_p)^2} - \frac{i\,i_p\tau_p}{(\alpha_1+i\,i_p)}\right] \;\forall\; \mathrm{Re}[c_1(i_0,\Gamma_0)] \approx 0 \tag{A.143}$$

$$\Delta\bar{u} = i_{dc} + \frac{2\pi}{\tau_B}\mathrm{Im}\left[c_1(i_0,\Gamma_0)\right]\frac{i_p(i_0+i_p)^2}{(i_0^2+\Gamma_0^2)((i_0+i_p)^2+\Gamma_0^2)^2}\times \tag{A.144}$$

$$\left[-\tau_p i_0^2(i_0+i_p) - \frac{1}{(i_0+i_p)}\left(i_p(3i_0+i_p)\Gamma_0 + (2i_0^2+2i_0i_p+i_p^2)\tau_p\Gamma_0^2 + \tau_p\Gamma_0^4\right) + \frac{i_p}{(i_0+i_p)^2}\Gamma_0^3\right.$$
$$\left. + i_p\,e^{-\tau_p\Gamma_0}\left[\Gamma_0\left(\frac{(3i_0+i_p)}{(i_0+i_p)} - \frac{\Gamma_0^2}{(i_0+i_p)^2}\right)\cos[(i_0+i_p)\tau_p] - \left(i_0 - \frac{(3i_0+2i_p)}{(i_0+i_p)^2}\Gamma_0^2\right)\sin[(i_0+i_p)\tau_p)]\right]\right]$$

In the noisefree limit $\Gamma_0 \to 0$ we yield the voltage response from Eq.A.144 as follows

$$\Delta\bar{u} = \Delta\bar{u}_{dc} + \frac{2\pi}{\tau_B}\mathrm{Im}[c_1(i_0,0)]\frac{i_p^2}{i_0(i_0+i_p)}\frac{\sin[(i_0+i_p)\tau_p]}{(i_0+i_p)}, \; 2\pi\mathrm{Im}\left[c_1(i_0,0)\right] = i_0 - \sqrt{i_0^2-1} \tag{A.145}$$

$$\Delta\bar{u}_{dc} = \frac{i_p\tau_p}{\tau_B}\left[1 + 2\pi\mathrm{Im}[c_1(i_0,0)]\frac{1}{(i_0+i_p)}\right] \qquad \forall \quad \tau_B \gg 1/\Gamma_0,\; \Gamma_0 \to 0,\; i_0 \geq 1. \tag{A.146}$$

For a simple working point change $\tau_p = \tau_B$ Eq.A.145, compared to the unperturbated change in the I-V-characteristic $\Delta\bar{u}(i_0 \to i_0 + i_p) = ((i_0+i_p)^2-1)^{1/2} - (i_0^2-1)^{1/2}$, identifies the linear voltage effects $\Delta\bar{u}_{dc}$ as the averaged first order dc-shift of rf-pulse. Now, I will investigate the absolute maximum rf-power ratings for a single rf-pulse. It is easier to consider a filtered rf-pulse with $i_{dc} = 0$ for sufficient long sampling time $\tau_B \gg \tau_p$. In the delta pulse limit $\tau_p \to 0$, while remaining $i_p\tau_p$ constant, the first maxima of Eq.A.145, identified as the previously defined absolute maximum rf-power ratings, results to

$$\frac{\partial\Delta\bar{u}}{\partial i_p} = 0 \implies i_p\tau_p = \frac{\pi}{2} \qquad \forall \quad \tau_B \gg 1/\Gamma_0,\; \tau_p \to 0,\; \Gamma_0 \to 0. \tag{A.147}$$

Analyzing the boundary current values of the nth Shapiro step, so called step boundaries, in the (i_p, i_0)-plane, for a infinite series of rf-pulses in the noisefree case, the maximum ratings Eq.A.147 is, beside a factor of 4, in accordance with the results from the authors [Ben96]

[3]. According to Fig.3.5 the non-linearity between rf-power and first order Shapiro width for small rf-currents, the analysis of step boundaries in the noisefree case is not really helpful for spectroscopy. However, here within the FP formalism, the maximum ratings for the spectroscopic mode of junction operation can be investigated for different noise parameters.

To derive the maximum ratings for a dc-free filtered rf-pulse in the spectroscopic mode of operation, we have to solve the first order recurrence relation with a time dependent rf-current for a filtered single rf-pulse. To simplify we make use of the fact, that according to Eq.A.157, the time dependent solution of the FP coefficients $c_1^I(\tau)$, $c_1^{II}(\tau)$ are invariant against $\tilde{Q}_1^+$, $\tilde{Q}_1^-$ from the appendix A.8.2. Starting from another ansatz for the propabilty density

$$W(\varphi,\tau) = \sum_n c_n(\tau)\, e^{in\varphi}\, e^{in\pi/2} \qquad \text{with} \qquad c_n(\tau) = c^*_{-n}(\tau) \tag{A.148}$$

and inserting this into the FP 4.4 we yield a recurrence relation with time dependent coefficients.

$$\left(i_0 + i_{rf}(\tau) - \Gamma_0 in - \frac{i}{n}\frac{d}{d\tau}\right) c_n(\tau) + \frac{1}{2}(c_{n-1}(\tau) + c_{n+1}(\tau)) = 0 \qquad \forall \qquad n \geq 1 \tag{A.149}$$

In contrary to Eq.A.92 the up and down converting indices have positive sign and the voltage expectation value is evaluated, in analogy to Eq.A.65, from the real part of the first FP coefficient Eq.A.64.

$$\bar{u} = i_0 + \frac{1}{\tau_R}\int_0^{\tau_R} [\langle i_{rf}(\tau)\rangle + \langle i_N(\tau)\rangle] d\tau + \frac{2\pi}{\tau_R}\int_0^{\tau_R} \mathrm{Re}\,[c_1(\tau)]]\, d\tau \tag{A.150}$$

Both representations lead to the same solution for calculations with infinite recurrences. For an early cutoff of the recurrence relation we get different solutions, which represent only different starting conditions, leading to the same solution for the infinite recurrence. According to Eq.A.157, we only analyze the first order FP coefficient, which is independent of the up and down converting indices $\tilde{Q}_1^+$, $\tilde{Q}_1^-$, respectively $\Delta c_2(\tau) = 0$. Therefore, in this case, we find the solution in complete analogy to Eq.A.143, which describes more the spectroscopic mode of operation of the rf-pulse driven Josephson junction.

$$\Delta\bar{u} = i_{dc} - \frac{2\pi}{\tau_B}\mathrm{Im}\,[c_1(i_0,\Gamma_0)]\,\mathrm{Im}\left[\frac{i_p^2(1-e^{-(\alpha_1+ii_p)\tau_p})}{\alpha_1(\alpha_1+i\,i_p)^2} - \frac{ii_p\tau_p}{(\alpha_1+i\,i_p)}\right] \quad \forall \quad \mathrm{Re}[c_1(i_0,\Gamma_0)] \approx 0 \tag{A.151}$$

$$\Delta\bar{u} = i_{dc} - \frac{2\pi}{\tau_B}\mathrm{Im}\,[c_1(i_0,\Gamma_0)]\,\frac{i_p(i_0+i_p)^2}{(i_0^2+\Gamma_0^2)((i_0+i_p)^2+\Gamma_0^2)^2}\times \tag{A.152}$$

$$\left[i_p i_0 - i_0^2\tau_p\Gamma_0 - \frac{1}{(i_0+i_p)^2}\left(i_p(3i_0+2i_p)\Gamma_0^2 + (2i_0^2+2i_0i_p+i_p^2)\tau_p\Gamma_0^3 + \tau_p\Gamma_0^5\right)\right.$$
$$\left. + i_p\, e^{-\tau_p\Gamma_0}\left[\left(-i_0 + \frac{(3i_0+2i_p)}{(i_0+i_p)^2}\Gamma_0^2\right)\cos[(i_0+i_p)\tau_p] + \Gamma_0\left(-\frac{(3i_0+i_p)}{(i_0+i_p)} + \Gamma_0^2\right)\sin[(i_0+i_p)\tau_p)\right]\right]$$

For the noisefree limit $\Gamma_0 \to 0$ we obtain the voltage response from Eq.A.152 as follows

$$\Delta\bar{u} = \frac{\pi}{\tau_B}\mathrm{Im}[c_1(i_0,0)]\,\frac{i_p^2\tau_p^2}{i_0}\left|\frac{\sin[(i_0+i_p)\tau_p/2]}{(i_0+i_p)\tau_p/2}\right|^2, \qquad 2\pi\mathrm{Im}\,[c_1(i_0,0)] = i_0 - \sqrt{i_0^2-1}, \tag{A.153}$$
$$\tau_B \gg 1/\Gamma_0,\ \Gamma_0 \to 0,\ i_0 \geq 1.$$

Now, I will confirm the voltage response change in 1st recurrence order for a single rectangular rf-pulse outside the small signal approach algebraic by the recursive system Eq.A.129.

[3]The authors use a infinite series of rf-pulses and a different rf-current normalization $\tau = \tau_p/2\pi$.

1. *Region I: rf-pulse duration* $0 \leq \tau \leq \tau_p$, $i_p \neq 0$
   For the rf-pulse duration the induced rf-current $i_{rf}(\tau) = i_p$ is assumed to be constant and the coefficient change $\Delta c_1(\tau)$ results from Eq.A.127,A.129 with the unperturbated working point $c_1(0)$, initial coefficients $\Delta c_1(0) = 0$ and $n = N = 1$, $Q_0^0 = \tilde{Q}_0^+ = \tilde{Q}_0^- = 0$, $\tilde{Q}^0 = s$ $\tilde{Q}_0 = -s^2$, $Q_1^0 = -i\,i_p$, $\tilde{Q}_1^+ = -s/2$, $\tilde{Q}_1^- = s/2$, $Q_1 = -i(i_0 + i_p - \Gamma_0 in)$, $\tilde{Q}_1 = s(Q_1 - s)$ to

$$\Delta\tilde{c}_0(s) = \tilde{a}_0(s) = -\frac{Q_0^0 c_0(0) + \tilde{Q}^0\Delta c_0(0) + \tilde{Q}_0^+\tilde{a}_1(s)}{\tilde{Q}_0 + \tilde{Q}_0^+\tilde{S}_0^+(s)} = 0, \tag{A.154}$$

$$\tilde{a}_1(s) = -\frac{Q_1^0 c_1(0) + \tilde{Q}^0\Delta c_1(0)}{\tilde{Q}_1} = -\frac{i\,i_p\; c_1(0)}{s(s-Q_1)} + \frac{\Delta c_1(0)}{(s-Q_1)} \tag{A.155}$$

$$\Delta c_1^I(\tau) = \mathcal{L}^{-1}[\tilde{S}_0^+\Delta\tilde{c}_0(s) + \tilde{a}_1(s)] \tag{A.156}$$

$$\Delta c_1^I(\tau) = -c_1(0)\frac{i_p}{(i_0+i_p-\Gamma_0 i)}\left(1 - e^{-i(i_0+i_p-\Gamma_0 i)\tau}\right) + \Delta c_1(0)\; e^{-i(i_0+i_p-\Gamma_0 i)\tau}. \tag{A.157}$$

   Without any initial change $\Delta c_1(0)$ from working point $c_1(0)$ the result reduces for $\tau = 0$ or without rf-radiation $i_p = 0$ to the working point itself.

2. *Region II: sampling delay* $\tau > \tau_p$, $i_p = 0$
   The solution after rf-pulse duration without rf-radiation $i_p = 0$ reduces from Eq.A.157 with the initial change of coefficient $\Delta c_1(\tau_p)$ shifted with time τ_p to

$$\Delta c_1^{II}(\tau) = \Delta c_1(\tau_p)\; e^{-i(i_0-\Gamma_0 i)\;(\tau-\tau_p)}. \tag{A.158}$$

   The continuity at region I/II of Eq.A.157 $\Delta c_1(\tau_p) = \Delta c_1^I(\tau_p, ip \neq 0, \Delta c_1(0) = 0)$ leads to

$$\Delta c_1^{II}(\tau) = -c_1(0)\frac{i_p}{(i_0+i_p-\Gamma_0 i)}\left(e^{-i(i_0-\Gamma_0 i)\;(\tau-\tau_p)} - e^{-i(i_0-\Gamma_0 i)\tau - i\,i_p\tau_p}\right). \tag{A.159}$$

The complete first order solution of the voltage expectation value Eq.A.140 is given by

$$\Delta\bar{u} = i_{dc} + \frac{2\pi}{\tau_B}\mathrm{Im}[c_1(0)\Delta\tilde{c_1}(i_p,\tau_p,\Gamma_0)] \tag{A.160}$$

$$\Delta\bar{u} = i_{dc} + \frac{2\pi}{\tau_B}\left(\mathrm{Re}[c_1(0)]\mathrm{Im}[\Delta\tilde{c_1}] + \mathrm{Im}[c_1(0)]\mathrm{Re}[\Delta\tilde{c_1}]\right) \tag{A.161}$$

$$\Delta\tilde{c_1} = \left(\frac{i_p^2(1-e^{-(\alpha_1+i\,i_p)\tau_p})}{\alpha_1(\alpha_1+i\,i_p)^2} + \frac{ii_p\left(e^{-\alpha_1(\tau_p-\tau_B)} - e^{-\alpha_1\tau_B - ii_p\tau_p} - \alpha_1\tau_p\right)}{\alpha_1(\alpha_1+i\,i_p)}\right) \tag{A.162}$$

$$\mathrm{Re}[\Delta\tilde{c_1}] = \frac{i_p(i_0+i_p)^2}{(i_0^2+\Gamma_0^2)((i_0+i_p)^2+\Gamma_0^2)^2}\times \tag{A.163}$$

$$\left[-\tau_p i_0^2(i_0+i_p) - \frac{1}{(i_0+i_p)}\left(i_p(3i_0+i_p)\Gamma_0 + (2i_0^2+2i_0i_p+i_p^2)\tau_p\Gamma_0^2 + \tau_p\Gamma_0^4\right) + \frac{i_p}{(i_0+i_p)^2}\Gamma_0^3\right.$$
$$+ i_p\, e^{-\tau_p\Gamma_0}\left[\Gamma_0\left(\frac{(3i_0+i_p)}{(i_0+i_p)} - \frac{\Gamma_0^2}{(i_0+i_p)^2}\right)\cos[(i_0+i_p)\tau_p] - \left(i_0 - \frac{(3i_0+2i_p)}{(i_0+i_p)^2}\Gamma_0^2\right)\sin[(i_0+i_p)\tau_p)\right]$$
$$+ e^{-(\tau_B-\tau_p)\Gamma_0}\left(1+\frac{\Gamma_0^2}{(i_0+i_p)^2}\right)\left[(2i_0+i_p)\cos[i_0(\tau_p-\tau_B)] + \left(i_0(i_0+i_p) - \Gamma_0^2\right)\sin[i_0(\tau_p-\tau_B)]\right]$$
$$\left. + e^{-\tau_B\Gamma_0}\left(1+\frac{\Gamma_0^2}{(i_0+i_p)^2}\right)\left[(2i_0+i_p)\cos[i_p\tau_p + i_0\tau_B)] - \left(i_0(i_0+i_p) - \Gamma_0^2\right)\sin[i_p\tau_p + i_0\tau_B)]\right]\right]$$

$$\mathrm{Im}[\Delta\tilde{c}_1]=\frac{i_p(i_0+i_p)^2}{(i_0^2+\Gamma_0^2)((i_0+i_p)^2+\Gamma_0^2)^2}\times \tag{A.164}$$
$$\left[i_p i_0 - i_0^2\tau_p\Gamma_0 - \frac{1}{(i_0+i_p)^2}\left(i_p(3i_0+2i_p)\Gamma_0^2+(2i_0^2+2i_0i_p+i_p^2)\tau_p\Gamma_0^3+\tau_p\Gamma_0^5\right)\right.$$
$$-i_p\,e^{-\tau_p\Gamma_0}\left[\Gamma_0\left(\frac{(3i_0+i_p)}{(i_0+i_p)}-\frac{\Gamma_0^2}{(i_0+i_p)^2}\right)\sin[(i_0+i_p)\tau_p]+\left(i_0-\frac{(3i_0+2i_p)}{(i_0+i_p)^2}\Gamma_0^2\right)\cos[(i_0+i_p)\tau_p)]\right]$$
$$+e^{-(\tau_B-\tau_p)\Gamma_0}\left(1+\frac{\Gamma_0^2}{(i_0+i_p)^2}\right)\left[(2i_0+i_p)\sin[i_0(\tau_p-\tau_B)]-\left(i_0(i_0+i_p)-\Gamma_0^2\right)\cos[i_0(\tau_p-\tau_B)]\right]$$
$$\left.+e^{-\tau_B\Gamma_0}\left(1+\frac{\Gamma_0^2}{(i_0+i_p)^2}\right)\left[(2i_0+i_p)\sin[i_p\tau_p+i_0\tau_B)]+\left(i_0(i_0+i_p)-\Gamma_0^2\right)\cos[i_p\tau_p+i_0\tau_B)]\right]\right]$$

A.8.5 Series of rf-pulses outside the small signal approach

In this section I will investigate analytical the voltage response of a Josephson junction driven by a series of rf-pulses with pulse width τ_p and pulse pause τ_R. We guarantee a dc-free rf-signal we introduce periodic boundary conditions, which prevent a shift of working point and therefore linear effects in rf-current. A similar derivation of Eq.A.157,A.159 including initial conditions $\Delta c_1(0), \Delta c_1(\tau_p)$ leads to

$$\Delta c_1^I(\tau) = -c_1(0)\frac{i\,i_p^I}{(\alpha_1+i\,i_p^I)}\left(1-e^{-(\alpha_1+i\,i_p^I)\tau}\right)+\Delta c_1(0)e^{-(\alpha_1+i\,i_p^I)\tau} \tag{A.165}$$

$$\Delta c_1^{II}(\tau) = -c_1(0)\frac{i\,i_p^{II}}{(\alpha_1+i\,i_p^{II})}\left(1-e^{-(\alpha_1+i\,i_p^{II})(\tau-\tau_p)}\right)+\Delta c_1(\tau_p)e^{-(\alpha_1+i\,i_p^{II})(\tau-\tau_p)} \quad \text{with (A.166)}$$

$$\Delta c_1(\tau_p)=\Delta c_1^I(\tau_p),\quad \Delta c_1(0)=\Delta c_1^{II}(\tau_R),\qquad i_p^I=i_p\left(1-\frac{\tau_p}{\tau_R}\right),\quad i_p^{II}=-i_p\frac{\tau_p}{\tau_R}. \tag{A.167}$$

Analyzing the periodic boundary conditions we obtain for a sufficient large pulse spacing $\tau_R \gg \tau_p$, respectively vanishing response structure, the stationary start condition for the time dependent coefficients Eq.A.165,A.167

$$\Delta c_1(0)=\Delta c_1^{II}(\tau_R) = -c_1(0)\frac{i\,i_p^{II}}{(\alpha_1+i\,i_p^{II})}\left(1-e^{-(\alpha_1+i\,i_p^{II})(\tau_R-\tau_p)}\right) \tag{A.168}$$
$$+\,e^{-(\alpha_1+i\,i_p^{II})(\tau_R-\tau_p)}\left[-c_1(0)\frac{i\,i_p^I}{(\alpha_1+i\,i_p^I)}\left(1-e^{-(\alpha_1+i\,i_p^I)\tau_p}\right)+\Delta c_1(0)e^{-(\alpha_1+i\,i_p^I)\tau_p}\right]$$

$$\Delta c_1(0) = -c_1(0)\frac{i\,i_p^{II}}{(\alpha_1+i\,i_p^{II})} \qquad \forall \qquad \tau_R \gg \tau_p. \tag{A.169}$$

Again evaluating the voltage response Eq.A.139 by averaging over an rf-periode in the structureless response limit $\tau_R \gg 1/\Gamma_0$, we obtain now no linear voltage effects i_{dc} in rf-current i_p from rf-pulses.

$$\Delta\bar{u}=\frac{2\pi}{\tau_R}\mathrm{Im}\left[c_1(i_0,\Gamma_0)\left(\frac{i_p^2(1-e^{-(\alpha_1+i\,i_p)\tau_p})}{\alpha_1(\alpha_1+i\,i_p)^2}-\frac{i_p^2\tau_p}{\alpha_1(\alpha_1+i\,i_p)}\right)\right] \quad \forall \quad \tau_R \gg 1/\Gamma_0 \tag{A.170}$$

According to the vanishing real part of the unperturbated FP coefficient Eq.A.82 for the low-noise operation, Eq.A.170 simplifies to

$$\Delta\bar{u}=\frac{2\pi}{\tau_R}\mathrm{Im}\left[c_1(i_0,\Gamma_0)\right]\mathrm{Re}\left[\frac{i_p^2(1-e^{-(\alpha_1+ii_p)\tau_p})}{\alpha_1(\alpha_1+i\,i_p)^2}-\frac{i_p^2\tau_p}{\alpha_1(\alpha_1+i\,i_p)}\right] \;\forall\; \mathrm{Re}[c_1(i_0,\Gamma_0)]\approx 0 \tag{A.171}$$

$$\Delta\bar{u}=\frac{2\pi}{\tau_R}\mathrm{Im}\left[c_1(i_0,\Gamma_0)\right]\frac{i_p^2(i_0+i_p)^2}{(i_0^2+\Gamma_0^2)((i_0+i_p)^2+\Gamma_0^2)^2}\times \tag{A.172}$$
$$\left[\tau_p i_0(i_0+i_p)-\frac{1}{(i_0+i_p)}\left((3i_0+i_p)\Gamma_0+i_p\tau_p\Gamma_0^2\right)+\frac{1}{(i_0+i_p)^2}\left(\Gamma_0^3-\tau_p\Gamma_0^4\right)\right.$$
$$\left.+\,e^{-\tau_p\Gamma_0}\left[\Gamma_0\left(\frac{(3i_0+i_p)}{(i_0+i_p)}-\frac{\Gamma_0^2}{(i_0+i_p)^2}\right)\cos[(i_0+i_p)\tau_p]-\left(i_0-\frac{(3i_0+2i_p)}{(i_0+i_p)^2}\Gamma_0^2\right)\sin[(i_0+i_p)\tau_p)]\right]\right]$$

For the noisefree limit $\Gamma_0 \to 0$ we obtain the voltage response from Eq.A.172. As expected, the voltage response has no linear effects in the rf-current dependence.

$$\Delta\bar{u}=\frac{2\pi}{\tau_R}\mathrm{Im}[c_1(i_0,0)]\frac{i_p^2}{i_0(i_0+i_p)}\left[\frac{\sin[(i_0+i_p)\tau_p]}{(i_0+i_p)}-\tau_p\right],\quad 2\pi\mathrm{Im}\left[c_1(i_0,0)\right]=i_0-\sqrt{i_0^2-1}, \tag{A.173}$$
$$\tau_R \gg 1/\Gamma_0,\ \Gamma_0\to 0,\ i_0\geq 1.$$

For the investigation of the spectroscopic mode of operation of the device, we evaluate again the voltage expectation value Eq.A.64 and obtain the same result as Eq.A.153 with $\tau_B \to \tau_R$ for the averaged voltage response.

A.8.6 Discrete spectral distribution outside the small signal approach

I will deduce the voltage change in 1st recurrence order for a nearly non-overlapping equidistant spectrum. Contrary to the linear Hilbert theory, this framework allows us to investigate higher order multi-harmonic mixing and phase effects, which overlap the discrete spectrum of the rf-pulse series causing additional unreal spectral rf-power. Inserting the rf-signal of K spectral lines with phases φ_k

$$i_{rf}(\tau)=\sum_{k=1}^{K}\tilde{i}_k\cos(k\Omega_R\tau+\varphi_k) \qquad \text{with} \quad \mathrm{K}\geq 1 \tag{A.174}$$

into the difference recurrence method Eq.4.13 we yield the time dependent recurrence change

$$c_1(\tau)=e^{-g(\tau)}\left[\mathcal{C}+\alpha_1 c_1(i0,\Gamma_0)\int e^{g(\tau')}d\tau'\right] \text{ with } g(\tau)=\alpha_1\tau+\sum_{k=1}^{K}i\frac{\tilde{i}_k}{k\Omega_R}\sin(k\Omega_R\tau+\varphi_k). \tag{A.175}$$

Using $e^{\pm iz\sin\varphi}=\sum_{n=-\infty}^{\infty}J_n(z)e^{\pm in\varphi}$, $J_{n,k}=J_n\left(\frac{\tilde{i}_k}{k\Omega_R}\right)$ and sort the product (A.176)

$$\exp\left[\sum_{k=1}^{K}i\frac{\tilde{i}_k}{k\Omega_R}\sin(k\Omega_R\tau+\varphi_k)\right]=\prod_{k=1}^{K}\sum_{n=-\infty}^{\infty}J_{n,k}(\Omega_R)e^{in(k\Omega_R\tau+\varphi_k)} \tag{A.177}$$

$$=\lim_{n\to\infty}\prod_{k=1}^{K}\left[\;J_{-n,k}e^{(-n)ki\Omega_R\tau+(-n)i\varphi_k}+J_{-n+1,k}e^{(-n-1)ki\Omega_R\tau+(-n-1)i\varphi_k}+\ldots\right. \tag{A.178}$$
$$\left.\ldots+J_{n-1,k}e^{(n-1)ki\Omega_R\tau+(n-1)i\varphi_k}+J_{n,k}e^{nki\Omega_R\tau+ni\varphi_k}\right]$$

$$=\sum_{\xi=1}^{\infty}a_\xi(\tilde{i}_k,\Omega_R)e^{i\left(\Omega_R b_\xi\tau+c_\xi\varphi_k\right)} \quad \text{with} \tag{A.179}$$

$$a_\xi(\tilde{i}_k,\Omega_R)=\prod_{k=1}^{K} J_{x_k}(\xi)\left(\frac{\tilde{i}_k}{k\Omega_R}\right),\quad b_\xi=\sum_{k=1}^{K}x_k(\xi)k,\quad c_\xi=\sum_{k=1}^{K}x_k(\xi)\varphi_k \tag{A.180}$$

variation and repetition of permutations $(x_1,...,x_k,...,x_K)\in\tilde{V}_K^{(2N+1)}$, one find with $a_\xi = a_\xi(\tilde{i}_k,\Omega_R)$

$$c_1(\tau)=\mathcal{C}\sum_\xi a_\xi e^{-(\alpha_1+i\Omega_R b_\xi)\tau-ic_\xi}+\alpha_1 c_1(i_0,\Gamma_0)\sum_{\xi,\xi'}\frac{a_\xi a_{\xi'}}{\alpha_1+i\Omega_R b_\xi}e^{-i\Omega_R(b_{\xi'}-b_\xi)\tau-i(c_{\xi'}-c_\xi)} \tag{A.181}$$

and continuity of coefficients $c_1(0)=c_1(i_0,\Gamma_0)$ for the determination of $\mathcal{C}$ the FP coefficient change $\Delta c_1(\tau)=c_1(\tau)-c_1(i_0,\Gamma_0)$ for a discrete spectrum.

$$\Delta c_1(\tau)=c_1(i_0,\Gamma)\left[f_1'\sum_\xi a_\xi e^{-(\alpha_1+i\Omega_R b_\xi)\tau-ic_\xi}+\alpha_1\sum_{\xi,\xi'}f'_{\xi,\xi'}e^{-i\Omega_R(b_{\xi'}-b_\xi)\tau}-1\right]\ \text{with} \tag{A.182}$$

$$f_1'=\left[1-\alpha_1\sum_{\xi,\xi'}f'_{\xi,\xi'}\right]\Big/\sum_\xi a_\xi e^{-ic_\xi},\quad f'_{\xi,\xi'}=\frac{a_\xi a_{\xi'}e^{-i(c_{\xi'}-c_\xi)}}{\alpha_1+i\Omega_R b_\xi}. \tag{A.183}$$

Expecting a constant voltage response for the stationary solution $\tau_B\to\infty$ with vanishing transient effects $1/(\tau_B\Gamma_0)\gg 1$ and dc-free rf-signals, we yield with

$$\Delta\bar{u}=\lim_{\tau_B\to\infty}\frac{2\pi}{\tau_B}\mathrm{Im}\int_0^{\tau_B}\Delta c_1(\tau)d\tau \tag{A.184}$$

only contributions and a constant coefficient change after evaluating Eq.A.184 for the

$$\text{stationary voltage response}\quad\Longleftrightarrow\quad b_\xi=b_{\xi'}. \tag{A.185}$$

Eq.A.185 represents the invariance of the voltage response against an rf-signal translation caused from analyzing the junctions stationary voltage response. In other words, averaging over the junctions response for a given measuring time τ_B, the rf-signal phases, respectively shape can only be reconstructed without its translation information within the measuring time. This is, what we expected without using trigger signals or analyzing transient effects from the Josephson junction. However, consequently we find for the Shapiro order index n cutted at finite N and permutation element $x_k(\xi)\in[-N,+N]$

$$\Delta\bar{u}=2\pi\mathrm{Im}\left[c_1(i_0,\Gamma_0)\left((i_0-\Gamma_0 i)\sum_{\xi=1,\xi'=1,b_\xi=b_{\xi'}}^{(2N+1)^K}\frac{a_\xi(\tilde{i}_k,\Omega_R)a_{\xi'}(\tilde{i}_k,\Omega_R)e^{-i(c_{\xi'}-c_\xi)}}{i_0+\Omega_R b_\xi-\Gamma_0 i}-1\right)\right]. \tag{A.186}$$

This expression involves higher order Shapiro steps, phase effects as well as multi-harmonic mixing effects. Without rf-radiation $\tilde{i}_k=0$ the response vanishes exactly with $J_0(0)=1$ guaranteed by the recurrence difference scheme Eq.4.13. In the limit of non-overlapping Shapiro steps, preferable for small noise parameter $\Gamma_0\to 0$, main contributions to Eq.A.186 are given approximately for $b_\xi=-k$ at frequency $i_0\approx k'\Omega_R\pm\Gamma$, respectively $i_0\gg 1$. For this case, the maximum voltage response $\Delta\bar{u}_{max}=\Delta\bar{u}^+-\Delta\bar{u}^-$ of a single Shapiro step results with Eq.A.186 to

$$\Delta\bar{u}^\pm\approx 2\pi\mathrm{Im}\left[c_1(i_0,\Gamma_0)\left((k'\Omega_R\pm\Gamma-\Gamma_0 i)\sum_{\substack{\xi=1,\xi'=1,\\ b_\xi=b_{\xi'}=-k'}}^{(2N+1)^K}\frac{a_\xi(\tilde{i}_k,\Omega_R)a_{\xi'}(\tilde{i}_k,\Omega_R)e^{-i(c_{\xi'}-c_\xi)}}{\pm\Gamma-\Gamma_0 i}-1\right)\right] \tag{A.187}$$

$$\Delta\bar{u}_{max}=2\pi\mathrm{Im}\left[c_1(i_0,\Gamma_0)k'\Omega_R\frac{2\Gamma}{\Gamma^2+\Gamma_0^2}\gamma_{k'}\right]\ \text{with}\ \gamma_{k'}=\sum_{\substack{\xi=1,\xi'=1,\\ b_\xi=b_{\xi'}=-k'}}^{(2N+1)^K}a_\xi(\tilde{i}_k,\Omega_R)a_{\xi'}(\tilde{i}_k,\Omega_R)e^{-i(c_{\xi'}-c_\xi)}. \tag{A.188}$$

The double summation of Eq.A.188 is performed over multi-harmonic mixing effects for $\xi=\xi'$ and phase effects for $\xi\neq\xi'$. Sum contributions with exchanged ξ,ξ' leads with $a_\xi a_{\xi'}=a_{\xi'}a_\xi$ and $2\cos(c_{\xi'}-c_\xi)=\exp(-i(c_{\xi'}-c_\xi))+\exp(-i(c_\xi-c_{\xi'}))$ to

$$\gamma_{k'}=\sum_{\substack{\xi=1,\\ b_\xi=-k'}}^{(2N+1)^K}a_\xi^2(\tilde{i}_k,\Omega_R)+\sum_{\substack{\xi=1,\xi'=1,\xi<\xi',\\ b_\xi=b_{\xi'}=-k'}}^{(2N+1)^K}2a_\xi(\tilde{i}_k,\Omega_R)a_{\xi'}(\tilde{i}_k,\Omega_R)\cos(c_{\xi'}-c_\xi). \tag{A.189}$$

The voltage response is converted into the current response by $\Delta\bar{u}_{max}\approx r_d(i_0,\Gamma_0)\Delta i_{max}$ resulting with $\mathrm{Re}[\gamma_{k'}]=0$, Eq.A.82, Eq.4.27 and the low rf-power adjustment to the Hilbert transform theory from section 4.3.3 using the replacement $\eta_1(k'\Omega_R,\Gamma)\to\tilde{\eta_1}(k'\Omega_R,\Gamma)$ finally to

$$\Delta i_{max}=\gamma_{k'}\tilde{\eta_1}(k'\Omega_R,\Gamma)\quad\text{with}\quad\gamma_{k'}=\sum_{\substack{\xi=1,\\ b_\xi=-k'}}^{(2N+1)^K}a_\xi^2(\tilde{i}_k,\Omega_R)+\sum_{\substack{\xi=1,\xi'=1,\xi<\xi',\\ b_\xi=b_{\xi'}=-k'}}^{(2N+1)^K}2a_\xi(\tilde{i}_k,\Omega_R)a_{\xi'}(\tilde{i}_k,\Omega_R)\cos(c_{\xi'}-c_\xi). \tag{A.190}$$

Eq.A.190 is restricted to adequate noise parameter caused by analyzing only the first recurrence order. Furthermore the small signal adjustment using the Hilbert transform theory, based on Eq.3.10, is not a good approximation for the noiseless operation $\Gamma_0=0$ using adequate rf-power, as depicted in Fig.4.7. However, for non operlapping Shapiro steps and a noiseless operation the $\eta_1(\Omega,\Gamma)$ function can be determined numerically, expecting an rf-power dependence and a linear rf-current dependence of the current response of Eq.A.190, as depicted in Fig.3.5. In this case the quadratic dependence of the Besselfunctions within RSJ-model deviates from the FP predictions. However, as procceded for the mixing corrections from Eq.4.50 to Eq.4.51 the single Shapiro step, respectively Bessel function dependencies are substituted. The summation and indexing of the harmonics Eq.A.174, respectively its permutations, can be reduced to non vanishing spectral lines $\tilde{i}_k\neq 0$. This can be performed, because contributions to the current change Eq.A.186 vanish with Eq.A.180 and $J_{x_k(\xi)}(\tilde{i}_k=0)=0$ for permutation elements $x_k(\xi)\neq 0$. Whereas for $x_k(\xi)=0$ with $J_0(\tilde{i}_k=0)=1$ contributions occur, but without changing the parameter b_ξ, c_ξ, respectively the selection of permutations $b_\xi=b_{\xi'}=-k'$. For monochromatic rf-radiation Eq.A.186 reduces to

$$\Delta\bar{u}=2\pi\mathrm{Im}\left[c_1(i_0,\Gamma_0)\left((i_0-\Gamma_0 i)\sum_{n=-\infty}^{\infty}\frac{J_n^2\left(\frac{\tilde{i}_1}{\Omega_R}\right)}{i_0+n\Omega_R-\Gamma_0 i}-1\right)\right]. \tag{A.191}$$

In the noiseless limit $\Gamma_0\to 0$ Eq.A.186 reduces with Eq.A.83 to

$$\Delta\bar{u}=\begin{cases}i_0\eta & \forall\ |i_0|\le 1\\ \left(i_0-\sqrt{i_0^2-1}\right)\eta & \forall\ i_0\ge 1\end{cases},\quad\text{with}\quad\eta=\sum_{\xi=1}^{(2N+1)^K}\frac{a_\xi^2(\tilde{i}_k,\Omega_R)}{i_0+\Omega_R b_\xi}-1 \tag{A.192}$$

The current change at frequency $k'\Omega_R$, caused from biharmonic effects from two spectral lines at frequency $k_1\Omega_R$, $k_2\Omega_R$ with $k_2\Omega_R>k_1\Omega_R$ in 1st recurrence and Bessel order $N=1$ can be analyzed.

• Biharmonic mixing effects: $\xi=\xi'$

As depicted in Fig.4.16 no degeneracy of $b_\xi=b_{\xi'}=-k'$ with $\xi\neq\xi'$ is found at frequency

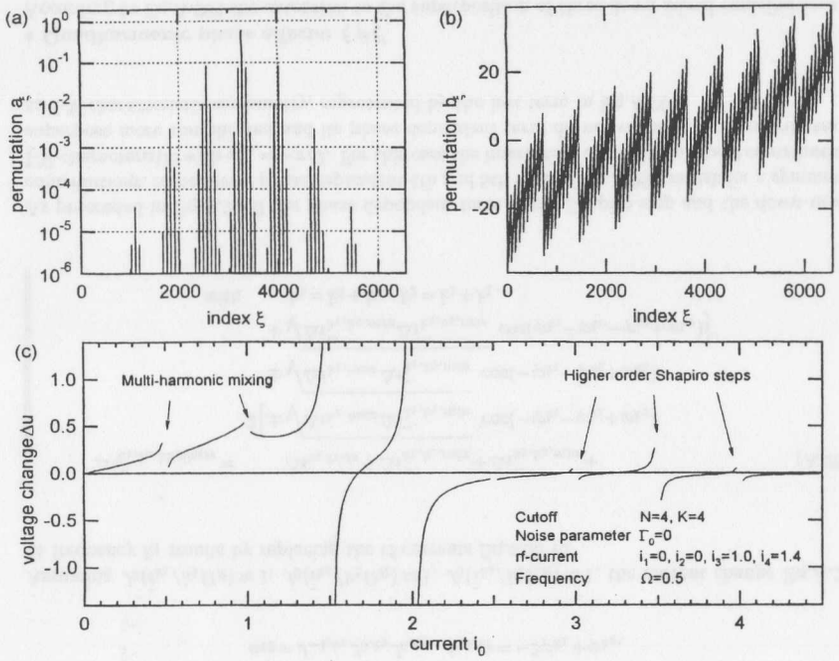

Figure A.4: *Multi-harmonic mixing and higher order Shapiro effects using Eq.A.192.*

$k'\Omega_R$. The current change results with the notation of Eq.A.176 and permutations $\xi \in \{5,8\}$, which represent with $(x_{k_1}, x_{k_2}) \in \{(-1,-1),(1,-1)\}$ at up, respectively down mixed frequency $k' = k_2 \pm k_1$, to

$$\Delta i^{+}_{k_1,k_2,mix} = a_5^2 \tilde{\eta}_1(k'\Omega_R, \Gamma_0) \quad \text{with} \quad a_5 = J_{-1,k_1} J_{-1,k_2},\ k_2 = k' - k_1 \tag{A.193}$$

$$\Delta i^{-}_{k_1,k_2,mix} = a_8^2 \tilde{\eta}_1(k'\Omega_R, \Gamma_0) \quad \text{with} \quad a_8 = J_{1\ ,k_1} J_{-1,k_2},\ k_2 = k' + k_1. \tag{A.194}$$

Using $J_n(x) = (-1)^n J_{-n}(x)$ and replacing the rf-currents from a single spectral line Eq.4.30 the current change at up, respectively down mixed frequency is given by

$$\Delta i^{\pm}_{k_1,k_2,mix} = \left(\frac{\tilde{\eta}_1(k'\Omega_R,\Gamma)}{\tilde{\eta}_1(k_1\Omega_R,\Gamma)\ \tilde{\eta}_1(k_2\Omega_R,\Gamma)} \right) \Delta i_{k_1,max} \Delta i_{k_2,max} \quad \text{with} \quad k' = k_2 \pm k_1, \tag{A.195}$$

$$k_2 > k_1,\ \Delta i_{k',max} = 0.$$

• Biharmonic phase effects: $\xi \neq \xi'$

According to Fig.4.21 dominant phase effects are present if the down mixed frequency $k' = k_2 - k_1$ coincide with the frequency k_1 itsself resulting in $k_2 = 2k_1$. In this case a degeneracy of $b_\xi = b_{\xi'} = -k'$ with $\xi \neq \xi'$ can be found for the permutations $\xi \in \{4,8\}$ and $(x_{k_1}, x_{k_2}) \in \{(-1,0),(1,-1)\}$. Using the translation invariance condition Eq.A.185 $k_1(x_{k_1}(\xi') - x_{k_1}(\xi)) = -k_2(x_{k_2}(\xi') - x_{k_2}(\xi))$,

the phase argument $\alpha_{\xi,\xi'} = c_{\xi'} - c_\xi$ is given with $(x_{k_1}(\xi') - x_{k_1}(\xi)) = -2$ from Fig.4.21 by

$$\alpha_{\xi,\xi'} = \varphi_{k_1}(x_{k_1}(\xi') - x_{k_1}(\xi)) + \varphi_{k_2}(x_{k_2}(\xi') - x_{k_2}(\xi)) = \left(\varphi_{k_1} - \varphi_{k_2} \frac{k_1}{k_2} \right) (x_{k_1}(\xi') - x_{k_1}(\xi)), \tag{A.196}$$

leading at frequency k_1 to the phase dependent current change

$$\Delta i^{-}_{k_1,k_2,phase} = \Big[\overbrace{a_4^2}^{k_1 \text{ Shapiro step}} \quad \overbrace{+a_8^2 + 2a_4 a_8 \cos(\alpha_{4,8})}^{k_1,k_2-k_1 \text{ interaction}} \Big] \tilde{\eta}_1(k_1\Omega_R, \Gamma) \tag{A.197}$$

$$\text{with} \quad a_4 = J_{-1,k_1} J_{0,k_2},\ a_8 = J_{1,k_1} J_{-1,k_2},\ \alpha_{4,8} = \varphi_{k_2} - 2\varphi_{k_1},\ k_2 = 2k_1.$$

By performing an unlimited averaging of the junctions voltage response, the rf-signal phases can only be determined beside its translation. Therefore one phase can be given, for example $\varphi_{k_1} = 0$. Assuming $\tilde{i}_{k_2} \ll 1$ with $J_0(\tilde{i}_{k_2}/k_2\Omega_R) \approx 1$, the current change Eq.A.197, respectively phase, results by using Eq.A.195 analyzed at frequency $k' = k_1$ and replacing the rf-currents Eq.4.30 to

$$\Delta i^{-}_{k_1,k_2,phase} = \Delta i_{k_1,max} + \Delta i^{-}_{k_1,k_2,mix} \pm 2\sqrt{\Delta i_{k_1,max} \Delta i^{-}_{k_1,k_2,mix}}\ \cos(\varphi_{k_2} - 2\varphi_{k_1}) \quad \text{with} \quad k_2 = 2k_1. \tag{A.198}$$

According to Eq.A.198 the current change is determined by the Shapiro steps itsself, biharmonic mixing and a phase dependent term. Analyzing working points i_0 from the negative branch of the I-V-characteristic with $b_\xi = k'$, the factor a_4 gets asymmetric and the phase dependent contribution becomes negative. The rf-signal is determined for $\varphi_{k_1} = 0$ by Eq.A.174

$$i_{rf}(\tau) = \tilde{i}_{k_1} \cos(k_1\Omega_R\tau) + \tilde{i}_{k_2} \cos(k_2\Omega_R\tau + \varphi_{k_2}) \tag{A.199}$$

The symmetry of the I-V-characteristic is given under the transformation $b'_\xi = -b_\xi$, respectively permutation elements $x'_k(\xi) = -x_k(\xi)$, by the factor $a'_\xi \neq a_{\xi'}$ with $J_{x_k(\xi)}(x) = (-1)^{x_k(\xi)} J_{-x_k(\xi)}(x)$ of the phase dependent term in Eq.A.198. Considering an rf-signal with arbitrary translation τ_0 and symmetric I-V-characteristic

$$i_{rf}(\tau) = \tilde{i}_{k_1} \sin(k_1\Omega_R(\tau - \tau_0)) + \tilde{i}_{k_2} \sin(k_2\Omega_R(\tau - \tau_0)), \tag{A.200}$$

$$i_{rf}(\tau) = \tilde{i}_{k_1} \cos(k_1\Omega_R\tau + \varphi_{k_1}) + \tilde{i}_{k_2} \cos(k_2\Omega_R\tau + \varphi_{k_2}) \quad \text{with} \quad \varphi_{k_1} = k_1\Omega_R\tau_0 - \pi/2, \tag{A.201}$$

$$\varphi_{k_2} = k_2\Omega_R\tau_0 - \pi/2$$

the phase dependent term Eq.A.196 $\cos(\alpha_{\xi,\xi'}) = \cos(\pi - \pi k_1/k_2) = 0$ is independent of the rf-signal translation and vanishes for $k_2 = 2k_1$, as expected. We conclude, that for vanishing rf-phases of the ansatz Eq.A.200 the Shapiro step and the down mixed frequency component simply superpose without any phase effects and I-V-characteristic asymmetry. Using the translation invariance of an rf-pulse series, especially for a symmetric rf-pulse Eq.4.33 with $\tau_0 = -\tau_p/2$ and $\varphi_{k_n} = -\pi/2$, an asymmetry of the I-V-characteristic and phase effects are unexpected still present. This indicates other interaction effects within a highly degenerated spectrum.

• Triharmonic phase effects: $\xi \neq \xi'$

The superposition of a Shapiro acting at frequency k_1 and down mixed contributions of frequen-

cies $k_1 = k_3 - k_2 = k_2 - k_1$ are given for the first order Besselfunctions by

$$\begin{array}{lllll} \xi & x_1\,k_1 & x_2\,k_2 & x_3\,k_3 & b_\xi \quad \text{Type} \\ 7: & 0\,k_1 + & 1\,k_2 - & 1\,k_3 = -k_1, & \text{0th order multi-harmonic mixing } k_3, k_2 \\ 11: & 1\,k_1 - & 1\,k_2 + & 0\,k_3 = -k_1, & \text{0th order multi-harmonic mixing } k_2, k_1 \\ 12: & -1\,k_1 - & 0\,k_2 + & 0\,k_3 = -k_1, & \text{1st order Shapiro step } k_1, \end{array} \tag{A.202}$$

respectively three degenerated permutations $\xi \in \{7, 11, 12\}$ with $(x_{k_1}, x_{k_2}, x_{k_3}) \in \{(0.1,-1),(1,-1,0),(-1,0,0)\}$ leading at frequency k_1 to the phase dependent current change

$$\begin{aligned} \Delta i^-_{k_1,k_2,k_3,phase} = \Big[& \overbrace{a_{12}^2}^{k_1 \text{ Shapiro step}} + \overbrace{2a_7 a_{11}\cos(\alpha_{7,11})}^{k_3-k_2,k_2-k_1 \text{ interaction}} \\ & + \underbrace{a_7^2 + 2a_7 a_{12}\cos(\alpha_{7,12})}_{k_1,k_3-k_2 \text{ interaction}} + \underbrace{a_{11}^2 + 2a_{11}a_{12}\cos(\alpha_{11,12})}_{k_1,k_2-k_1 \text{ interaction}} \Big] \tilde{\eta}_1(k_1\Omega_R, \Gamma) \end{aligned} \tag{A.203}$$

$$\begin{aligned} \text{with} \quad & a_{\,7} = J_{0,k_1} J_{1,k_2} J_{-1,k_3},\ \alpha_{7,11} = \varphi_{k_1} - 2\varphi_{k_2} + \varphi_{k_3},\quad k_3 = k_2 + k_1, \\ & a_{11} = J_{1,k_1} J_{-1,k_2} J_{0,k_3},\ \alpha_{7,12} = -\varphi_{k_1} - \varphi_{k_2} + \varphi_{k_3},\quad k_2 = k_1 + k_1, \\ & a_{12} = J_{-1,k_1} J_{0,k_2} J_{0,k_3},\ \alpha_{11,12} = -2\varphi_{k_1} + \varphi_{k_2}. \end{aligned}$$

Assuming $J_0(\tilde{i}_{k_1}/k_1\Omega_R) \approx 1$, $J_0(\tilde{i}_{k_2}/k_2\Omega_R) \approx 1$, $J_0(\tilde{i}_{k_3}/k_3\Omega_R) \approx 1$, the current change Eq.A.203 at frequency k_1 results by replacing the rf-currents Eq.4.30 to

$$\begin{aligned} \Delta i^-_{k_1,k_2,k3,phase} = \quad & \Delta i_{k_1,max} + \Delta i^-_{k_1,k_2,mix} + \Delta i^-_{k_2,k_3,mix} + \\ & 2\Big[\pm\sqrt{\Delta i_{k_1,max}\Delta i^-_{k_1,k_2,mix}}\,\cos(-\varphi_{k_1} - \varphi_{k_1} + \varphi_{k_2}) \\ & \pm\sqrt{\Delta i_{k_1,max}\Delta i^-_{k_2,k_3,mix}}\,\cos(-\varphi_{k_1} - \varphi_{k_2} + \varphi_{k_3}) \\ & + \sqrt{\Delta i^-_{k_1,k_2,mix}\Delta i^-_{k_2,k_3,mix}}\,\cos(\varphi_{k_1} - \varphi_{k_2} - \varphi_{k_2} + \varphi_{k_3})\Big] \\ \text{with} \quad & k_3 = k_2 + k_1,\ k_2 = k_1 + k_1. \end{aligned} \tag{A.204}$$

As procceded in Eq.A.200ff the phase dependent term of the Shapiro step and the down mixed contributions, respectively phase dependent 4th and 5th term of Eq.A.204 vanish for a symmetric I-V-characteristic with $\varphi_{k_n} = -\pi/2$. For this case the interaction of the down mixed contributions superpose more complicated and its phase dependent term do *not* vanishes, nor contributes to an I-V-characteristic asymmetry, represented by the last term in Eq.A.204.

• **Quadharmonic phase effects:** $\xi \neq \xi'$

According to Eq.A.204 the extension to the superposition of three down mixed contributions at frequencies $k' = k_4 - k_3 = k_3 - k_2 = k_2 - k_1$ without any Shapiro step interaction is straightforward and given for the first order Besselfunctions by

$$\begin{aligned} \Delta i^-_{k_1,k_2,k3.k4,phase} = \quad & \Delta i^-_{k_1,k_2,mix} + \Delta i^-_{k_2,k_3,mix} + \Delta i^-_{k_3,k_4,mix} + \\ & 2\Big[\sqrt{\Delta i^-_{k_2,k_3,mix}\Delta i^-_{k_3,k_4,mix}}\,\cos(\varphi_{k_2} - \varphi_{k_3} - \varphi_{k_3} + \varphi_{k_4}) \\ & + \sqrt{\Delta i^-_{k_1,k_2,mix}\Delta i^-_{k_2,k_3,mix}}\,\cos(\varphi_{k_1} - \varphi_{k_2} - \varphi_{k_2} + \varphi_{k_3}) \\ & + \sqrt{\Delta i^-_{k_1,k_2,mix}\Delta i^-_{k_3,k_4,mix}}\,\cos(\varphi_{k_1} - \varphi_{k_2} - \varphi_{k_3} + \varphi_{k_4})\Big] \\ \text{with} \quad & k_4 = k_3 + k',\ k_3 = k_2 + k',\ k_2 = k_1 + k', \Delta i_{k',max} = 0. \end{aligned} \tag{A.205}$$

A.8.7 Mixing and scaling effects from finite recurrence cutoff

In this section, I will show, that a finite cutoff of recurrence order using the exact unperturbated I-V-charateristic within the DRR method does not effect the voltage response in the frequency dimension. Contrary, using an unperturbated I-V-characteristic based on finite cutoff recurrence order scaling and mixing effects are produced. Now we introduce with the parameter β a generalized difference scheme. For $\beta = 1/2c_0$ and $c_2(\tau) = 0, c_2(0) = 0$ the scheme reduces to the method depicted in Fig.4.2 with changed unperturbated I-V-characteristic from finite recurrence cutoff.

$$\frac{d}{d\tau} c_1(\tau) + i\,(i_0 + i_{rf}(\tau) - \Gamma_0 i)\,c_1(\tau) = \beta \tag{A.206}$$

Solving Eq.A.206 we yield with $\Delta c_1(\tau) = c_1(\tau) - c_1(\tau, i_p = 0)$, $c_1^I(0) = c_1(0)$, $c_1^{II}(\tau_p) = c_1^I(\tau_p)$, $c_1^I(i_p = 0) = c_1^{II}(\tau_p) = c_1(0)$ for a single rf-pulse driven junction

$$\Delta c_1^I(\tau) = e^{-(\alpha_1 + i i_p)\tau}\left(c_1(0) - \frac{\beta}{(\alpha_1 + i i_p)}\right) - e^{-\alpha_1\tau}\left(c_1(0) - \frac{\beta}{\alpha_1}\right) - \gamma \text{ with } \gamma = \frac{\beta i i_p}{\alpha_1(\alpha_1 + i i_p)} \tag{A.207}$$

$$\Delta c_1^{II}(\tau) = e^{-\alpha_1\tau + i i_p \tau_p}\left(c_1(0) - \frac{\beta}{(\alpha_1 + i i_p)}\right) + \gamma\left(e^{-\alpha_1(\tau - \tau_p)} - 1\right) + e^{-\alpha_1\tau}\left(c_1(0) - \frac{\beta}{\alpha_1}\right) \tag{A.208}$$

the voltage response analog to the deviation of Eq.A.153 of the junctions spectroscopic mode of operation in the noisefree limit $\Gamma_0 \to 0$

$$\Delta\tilde{u} = \frac{\pi}{\tau_B}\left(\mathrm{Re}[\beta] + \mathrm{Im}[c_1(i_0, 0)]\,(i_0 + i_p)\right)\frac{i_p \tau_p^2}{i_0}\left|\frac{\sin[(i_0 + i_p)\tau_p/2]}{(i_0 + i_p)\tau_p/2}\right|^2, \quad \tau_B \gg 1/\Gamma_0,\ \Gamma_0 \to 0,\ i_0 \geq 1. \tag{A.209}$$

For $\beta = \alpha_1 c_1(i_0, \Gamma_0)$, respectively $\mathrm{Re}[\alpha_1 c_1(i_0, 0)] = -i_0 \mathrm{Im}[i_0, 0]$ Eq.A.209 reduces to Eq.A.153 from the introduced DRR method. We conclude, that analytic expressions with low recurrence cutoffs are reliable for spectroscopy applications, when using the DRR method. Performing the same procedure for a periodic spectrum with $\Delta c_1(\tau) = \Delta c_1(\tau) - \Delta c_1(\tau, \tilde{i}_k = 0)$ we yield the following expression, which also reduces for $\beta = \alpha_1 c_1(i_0, \Gamma_0)$ to Eq.A.191.

$$\Delta c_1(\tau) = f_1 \sum_\xi a_\xi e^{-(\alpha_1 + i\Omega_R b_\xi)\tau} + \beta \sum_{\xi,\xi'} f_{\xi,\xi'} e^{-i\Omega_R(b_{\xi'} - b_\xi)\tau} - \left[c_1(i_0, \Gamma_0) - \frac{\beta}{\alpha_1}\right] e^{-\alpha_1\tau} - \frac{\beta}{\alpha_1}, \tag{A.210}$$

$$f_1 = \left[c_1(i_0, \Gamma_0) - \beta \sum_{\xi,\xi'} f_{\xi,\xi'}\right] \Big/ \sum_\xi a_\xi, \quad f_{\xi,\xi'} = \frac{a_\xi a'_\xi}{\alpha_1 + i\Omega_R b_\xi} \tag{A.211}$$

$$\Delta\tilde{u} = 2\pi \mathrm{Im}\left[\frac{\beta}{i}\left(\sum_{\xi=1}^{(2N+1)^K} \frac{a_\xi^2(\tilde{i}_k, \Omega_R)}{i_0 + \Omega_R b_\xi - \Gamma_0 i} - \frac{1}{i_0 - \Gamma_0 i}\right)\right]. \tag{A.212}$$

A.9 Quasioptical Fabry-Perot interferometers

The transmission line matrix approach is widely used in the design of integrated microwave circuits [Col98] and in quasioptical systems [Gol98]. The method is very convenient for calculating the frequency and time domain response of systems composed of cascaded elements including layers of different dielectric constants and planar geometries. The quasioptical propagation is assumed to be in only one scattering channel and the quasioptical components effect only the complex amplitude of the transmitted wave. In this case we can use the transmission line matrix approach to describe the behaviour of the field components of the plane wave or gaussian beam. The transmission line matrix approach automatically includes the dependencies of system phase shifts or round trip phases with frequency. In ABCD representation the input and output voltages and currents at a two port element device are related by the ABCD matrix. Especially for quasioptical components, like distances, capacities, inductivities, crosses, tripoles grids and shunted elements equivalent circuits and there ABCD matrices have been developed. For integrated microwave circuits also many descriptions for transmission lines, waveguides, coupled striplines and coplanar lines have been developed. Discontinuities, like steps, T-junctions, networks-ports, open-ends, gaps and nothes are represented in this formalism. Also for active elements, like Schottky-barries, point contacts, bipolar transistors, MESFET's, Pin, Gunn and Impatt diodes equivalent circuits have been developed. Here, for quasioptical components the input power reflection $|r_{in}|^2$ and power transmission $|t|^2$ coefficients of a Z_s sourced and Z_l loaded ABCD element is given by

$$\begin{pmatrix} V_{in} \\ I_{in} \end{pmatrix} = \begin{pmatrix} A & B \\ C & D \end{pmatrix} \cdot \begin{pmatrix} V_{out} \\ I_{out} \end{pmatrix}, \tag{A.213}$$

$$|r_{in}|^2 = \left|\frac{AZ_l - DZ_s + B - CZ_lZ_s}{AZ_l + DZ_s + B + CZ_lZ_s}\right|, \quad |t|^2 = \left|\frac{1}{G}\right|^2 \text{ with } G = \frac{AZ_l + DZ_s + B + CZ_lZ_s}{2Z_l} \tag{A.214}$$

$$\tilde{t} = \frac{1}{\mathrm{Re}[G] + i\ \mathrm{Im}[G]}, \quad |\tilde{t}|^2 = \frac{1}{\mathrm{Re}[G]^2 + \mathrm{Im}[G]^2}. \tag{A.215}$$

The transmission line matrix for some basic elements are given by [Gol98]

$$\text{Material distance} \quad M = \begin{bmatrix} \cosh\gamma d & Z\sinh\gamma d \\ \frac{1}{Z}\sinh\gamma d & \cosh\gamma d \end{bmatrix} \quad \text{with} \quad \gamma = i\frac{2\pi n}{\lambda_0}\cos\theta, \tag{A.216}$$

$$\text{Lossless distance} \quad M = \begin{bmatrix} \cos\ \beta d & iZ\sin\ \beta d \\ \frac{i}{Z}\sin\ \beta d & \cos\ \beta d \end{bmatrix} \quad \text{with} \quad \beta = 2\pi f/c, \tag{A.217}$$

$$\text{Shunt element of admittance} \quad M = \begin{bmatrix} 1 & 0 \\ Y & 0 \end{bmatrix}, \tag{A.218}$$

$$\text{Series element of impedance} \quad M = \begin{bmatrix} 1 & Z \\ 0 & 1 \end{bmatrix}, \tag{A.219}$$

where $n = \sqrt{\epsilon} = \sqrt{\epsilon_r}(1 - i\tan\delta/2)$ is the complex index of refraction of the material and θ is the propagation angle relative to normal incidence in this material. For an efficient rf-pulse repetition we are interested in the time domain impulse response of the delaying system. The following formula can be easily extended to on chip integrated microwave delaying structures by replacing the ideal transmission lines by stripline matrices. To simplify, we introduce the following normalized loss admitance $Y_R = Z_0/R$, grid $Y_X = Z_0/X_g$ admittance and phases $\varphi_i = \beta d_i$ for different grid distances, where $Z_0 = 120\pi$ is the vacuum resistance. The transmission matrix

for a lossy grid $\mathbf{X}$, respectively the ith delay line $\mathbf{D}_i$ is given by

$$\mathbf{X} = \begin{bmatrix} 1 & 0 \\ Y_g & 1 \end{bmatrix}, \quad \mathbf{D}_i = \begin{bmatrix} \cos\varphi_1 & iZ_0\sin\varphi_i \\ \frac{i}{Z_0}\sin\varphi_i & \cos\varphi_i \end{bmatrix} \quad \text{with } Y_g = \frac{1}{Z_0}\left(\frac{1}{Y_R} + \frac{i}{Y_X}\right)^{-1}. \tag{A.220}$$

- **2 grid interferometer including lossy grids**

$$\mathbf{M} = \mathbf{X}\cdot\mathbf{D}_1\cdot\mathbf{X} \tag{A.221}$$

$$\mathbf{M} = \begin{bmatrix} \cos\varphi_1 + i\frac{\sin\varphi_1}{\left(\frac{1}{Y_R}+\frac{i}{Y_X}\right)} & iZ_0\sin\varphi_1 \\ \frac{2\cos\varphi_1}{Z_0\left(\frac{1}{Y_R}+\frac{i}{Y_X}\right)} + i\frac{\sin\varphi_1}{Z_0\left(\frac{1}{Y_R}+\frac{i}{Y_X}\right)^2} + i\frac{\sin\varphi_1}{Z_0} & \cos\varphi_1 + i\frac{\sin\varphi_1}{\left(\frac{1}{Y_R}+\frac{i}{Y_X}\right)}) \end{bmatrix} \tag{A.222}$$

$$\mathrm{Re}[G] = \frac{1}{4(Y_R^2+Y_X^2)^2}\left[Y_R^2((Y_R+1)+1)\ ((Y_R^2+Y_X^2)\cos(\varphi_1)+Y_R^2Y_X\sin(\varphi_1))\right] \tag{A.223}$$

$$\mathrm{Im}[G] = \frac{1}{4(Y_R^2+Y_X^2)^2}\Big[-2Y_R^2Y_X(Y_R^2+Y_X^2)\cos(\varphi_1) + (2Y_R^4 - Y_R^2Y_X^2(Y_R(Y_R-2)-4)Y_X^4(Y_R(Y_R+2)+2))\sin(\varphi_1)\Big] \tag{A.224}$$

The fringe spacing Δf in frequency domain is given for an FPI including dielectric material $\varepsilon_r, tan\delta \ll 1$ by $\Delta f = c/2d\sqrt{\varepsilon_r}$, impedance $Z_0 \to Z_0/\sqrt{\varepsilon_r}$ and time delay $\Delta T/2$ of 1st, respectively ΔT 2nd, 3rd... rf-pulses by $\Delta T = 1/\Delta f$. Without any loss, but different grids the transfer function of Eq.A.223,A.224 reduces to

$$\tilde{t} = \left[\cos\varphi_1 + \frac{1}{2}(Y_{X1}+Y_{X2})\sin\varphi_1 + i\left(\frac{\sin\varphi_1}{2}(2 - Y_{X1}Y_{X2}) - \frac{1}{2}(Y_{X1}+Y_{X2})\cos\varphi_1\right)\right]^{-1} \tag{A.225}$$

- **3 grid interferometer including lossy grids**

$$\mathbf{M} = \mathbf{X}\cdot\mathbf{D}_1\cdot\mathbf{X}\cdot\mathbf{D}_2\cdot\mathbf{X} \tag{A.226}$$

$$\mathrm{Re}[G] = \frac{1}{4(Y_R^2+Y_X^2)^3}\times \tag{A.227}$$

$$\begin{bmatrix} (2Y_R^6Y_X^2 + 3Y_R^5Y_X^4 - Y_R^2Y_X^6(Y_R+1)) & \cos(\varphi_1-\varphi_2) \\ +(4Y_R^6 - 2Y_R^4Y_X^2(Y_R(Y_R-3)-6) + Y_X^6(Y_R(Y_R(Y_R+2)+6)+4)) & \cos(\varphi_1+\varphi_2) \\ -3Y_R^2Y_X^4(Y_R^3 - 4Y_R - 4) & \cos(\varphi_1+\varphi_2) \\ +2Y_R^2Y_X(Y_R^2+Y_X^2(4Y_R+3)) & \sin(\varphi_1+\varphi_2)\end{bmatrix}$$

$$\mathrm{Im}[G] = \frac{1}{4(Y_R^2+Y_X^2)^3}\times \tag{A.228}$$

$$\begin{bmatrix} (Y_R^3Y_X^5(3Y_R+4) - Y_R^5Y_X^3(Y_R-4)) & \cos(\varphi_1-\varphi_2) \\ -(6Y_R^6Y_X + Y_X^5Y_R^2(Y_R(3Y_R+4)+6) - Y_X^3Y_R^4(Y_R+2)(Y_R-6)) & \cos(\varphi_1+\varphi_2) \\ +(4Y_R^6 + 2Y_X^6(Y_R(2Y_R+3)+2) + 12Y_X^4Y_R^2(Y_R+1) - 2Y_R^4Y_X^2(Y_R(2Y_R-3)-6)) & \sin(\varphi_1+\varphi_2)\end{bmatrix}$$

Appendix B

Noise-correlation measurements

According to Eq.4.47 the symmetry of the unperturbated I-V-characteristic, respectively differential resistance, might be explained by the autocorrelation spectrum of the Josephson junctions intrinsic and external noise sources. For spectroscopy the investigation of the correlation spectrum in the frequency domain is of interest. A more detailed discussion is given by the following paper concerning 1/f-noise correlation measurements.

Noise-correlation measurements of $YBa_2Cu_3O_7$ Josephson junctions in the time and frequency domain

F. Ludwig, C. Hinnrichs and M. Schilling

Institut für Angewandte Physik und Zentrum für Mikrostrukturforschung, Universität Hamburg, Jungiusstraße 11, D-20355 Hamburg, Germany

March 7, 1998

Abstract

The correlation of critical current and normal-state resistance fluctuations is determined on $YBa_2Cu_3O_7$ step-edge grain-boundary Josephson junctions. The results are in correspondence to the intrinsically shunted junction (ISJ) model. We observe a bias current dependent decay of a frequency independent correlation coefficient. With novel precision measurements of the correlation coefficient in the frequency domain, we can exclude aliasing effects, contributions from white noise and the voltage dependence of the characteristic quasi-particle times to explain the observed bias current dependence of the correlation coefficient. A detailed analysis of the spectral density redistribution by chopping of noise signals in the frequency domain with regard to the correlation coefficient is presented.

PACS Numbers: 74.50.+r, 74.40.+k, 73.50.Td

1 Introduction

Noise and correlation measurements are able to identify the sources of physical noise phenomena and represent a powerful instrument to clarify the charge transport mechanism in Josephson junctions. Whether the Josephson current in junctions is restricted to narrow superconducting filaments in a weakly superconducting medium [1] or passes through a dielectric barrier containing a high density of localized defect states [2, 3] is still under discussion. Voltage noise power spectra from Josephson junctions consist of contributions from white noise and $1/f$-noise at low frequencies with a voltage noise spectral density of $S(f) \sim 1/f^{\alpha}$ for $\alpha \simeq 1$. Within the ISJ-model $1/f$-noise is explained to arise from trapping and release of charge carriers in localized states, which result in fluctuations of the local barrier height [4, 5, 6]. An individual trapping center can be characterized by two characteristic times τ_u and τ_o for the unoccupied and the occupied state, respectively. A single trapping center is characterized by the characteristic frequency $1/\tau_{eff} = 1/\tau_u + 1/\tau_o$ and contributes, with exponentially distributed τ_u and τ_o, a Lorentzian type power spectrum. The total power spectrum is obtained for a proper distribution of characteristic frequencies of the individual trapping centers [7, 8]. For a time independent spatial separation of the Cooper-pair and quasi-particle current uncorrelated voltage noise is expected, and thus contradicts the observed correlation between both current contributions. Marx et al.[6] have determined the noise-correlation on bicrystal grain-boundary Josephson junctions for different bias currents and temperatures. They find exclusive positive correlation coefficients between critical current fluctuations δI_c and normal-state resistance fluctuations δR_n, which strongly suggests a tunneling transport mechanism for both Cooper-pairs and quasi-particles. The correlation for same bias current was determined as $C(0) = 0.7$ instead of $C(0) = 1$, as theoretically expected. They interpret these deviations as resulting from bias-current depended characteristic times of the occupation of the localized states [6].

2 Noise measurements

Noise and correlation measurements have been done with an ultra low noise inductively coupled voltage amplifier with a sensistivity of $150pV/\sqrt{Hz}$ in a bandwidth between $10Hz$ and $30kHz$. The input inductance of the room-temperature amplifier is 200Ω at frequency $f = 10Hz$. The Josephson junction circuit is decoupled from the transformer with a large balancing capacitor of $C_k = 22mF$. For

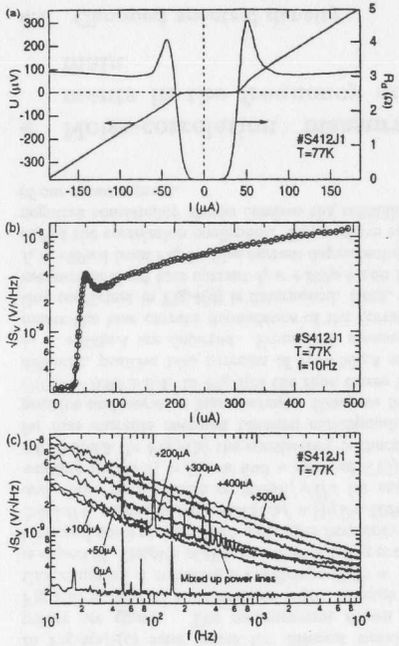

Figure 1: *Grain boundary Josephson junction #S412J1: (a) Current-voltage curve and Differential resistance at a temperature of $T=77K$. (b) Voltage noise vs. bias current at $f=10Hz$. (c) Voltage noise spectra for different static bias currents. Short circuit noise from measurement system is not subtracted.*

the noise measurements we use the spectrum analyzer HP35665A or a lock-in-amplifier (LIA) SR350. The current noise in the measuring bandwidth of the current source is $40pA/\sqrt{Hz}$ for noise measurements and $4pA/\sqrt{Hz}$ for correlation measurements. Transport and noise measurements have been performed on a $YBa_2Cu_3O_7$ step-edge grain-boundary Josephson junction in four-probe arrangement at a temperature of $T=77K$ in a well electromagnetically shielded environment. A typical current-voltage curve is depicted in Fig.1(a).

In correspondence with the differential resistance $R_d=\frac{\delta U}{\delta I}\ (I)$ from Fig.1(a) we find a peak of the voltage noise $\sqrt{S_V(f)}$ at $f=10Hz$ from Fig.1(b) close to the noise-rounded critical current $I_c=30\mu A$ of the Josephson junction. The dependence of $1/f$-voltage noise on the bias current based on model of a intrinsically and capacitively shunted junctions (RCSJ) is the result of a superposition of a decreasing noise component from critical current fluctuations δI_c and an increasing noise component from normal-state resistance fluctuations δR_n [9, 10]. The noise contribution from contact, and cable resistances ($\approx 100pV/\sqrt{Hz}$) and the pre-amplifier ($\approx 150pV/\sqrt{Hz}$) resulted in $200pV/\sqrt{Hz}$ according to the spectrum in the superconducting state of the Josephson junction shown in Fig.1(c). White voltage noise from Josephson junction resistance R_n and the current noise from the unchopped current source ($\approx 40pA/\sqrt{Hz}$) is transformed by the differential resistance into the voltage noise level, which is determined above the corner frequency of $1/f$-noise, of approximately $180pV/\sqrt{Hz}$. External disturbances of the power lines are mixed up by nonlinear differential resistance for the bias currents close to the critical current and produce higher harmonics.

Noise measurements with modulated bias current are shown in Fig.2. Contrary to noise reduction techniques with chopped polarity of bias currents in dc-SQUIDs [11] and Josephson junctions [12, 13], we switch the bias current between the voltage-carrying state at I_1 and superconducting state with $U(I_2)=0$. For the noise this is equivalent to its multiplication with the unit rectangle function or a convolution in the frequency domain. Therefore the complete noise information of the Josephson junction is convoluted around the chopper frequency f_c. It can be readout after the compensation of the rectangular signal at the working point for fixed bias current with standard demodulation technique. As expected, the $1/f$-noise from the amplifier is completely suppressed down to lowest frequencies, as depicted in the chopped measurement for $U(I_2)=0$ in Fig.2.

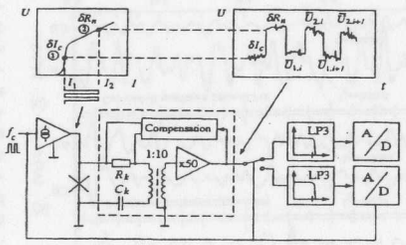

Figure 2: *Chopped noise measurements with one superconducting state in comparision with static direct noise measurements. As expected, the $1/f$-noise from amplifier in the chopped measurement is completely suppressed down to lowest frequency range. Deviations for $f>300Hz$ are due to the limited chopper frequency f_c.*

3 Noise-correlation measurements in the time domain

3.1 Measurement principle

To determine the correlation coefficient between critical current fluctuations δI_c and normal-state resistance fluctuations δR_n we switch the bias current I at frequency f_c between two values $I_1 \approx I_c$, where I_c fluctuations dominate, and $I_2 \gg I_c$, where R_n fluctuations dominate. We record the voltage fluctuations $\overline{U}^{1,i}$, $\overline{U}^{2,i}$ for the lower and upper working point, respectively, by sampling with a data-aquisition system, as depicted in Fig.3.

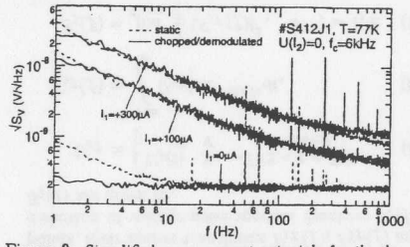

Figure 3: *Simplified measurement principle for the determination of the correlation coefficient in the time domain from Josephson junctions with a low noise, wideband and inductively coupled voltage amplifier. A regulated compensation of static working points at the input circuit avoids the saturation of amplifier. A low pass filter minimizes aliasing effects from the sampling process. For synchronized data readout we use a data-aquisation system and for unsynchonized data readout a storage oscillograph.*

To get a sufficient input sensitivity of the spectrum analyzer to detect the voltage noise signals and to avoid the saturation of the amplifier, we compensate the rectangular signal from static working points at the input circuit by the voltage drop from a resistance $R_k \simeq 0.8\Omega$ in series with the inductively coupled amplifier. For the compensation, we detect the rectangular components from the chopped signal and coupled the regulated compensation signal into the input circuit. Analyzing only frequencies in the measuring bandwidth Δf of the sampled time traces, we obtain the correlation coefficient $C(0)$ with the discret representation of the cross correlation [6] in the time domain for $k=0$:

$$C(\tau_k)=\frac{\sum_{i=1}^{N}\overline{U}_{1,i}\overline{U}_{2,i+k}}{\sqrt{\sum_{j=1}^{N}\overline{U}_{1,j}{}^2}\sqrt{\sum_{l=1}^{N}\overline{U}_{2,l}{}^2}}\quad\forall\ \tau_k=k\Delta T \qquad (1)$$

With the above normalization of the correlation coefficient and the fact, that anti-correlated critical current δI_c and resistance fluctuations δR_n produce correlated voltage fluctuations [6], and vice versa, we get the correlation coefficient:

$$C(0)=\begin{cases}-1 & \forall & I_c,R_n & \text{correlated}\\ 0 & \forall & \text{"} & \text{uncorrelated}\\ +1 & \forall & \text{"} & \text{anti-correlated}\end{cases} \qquad (2)$$

Depending on the correlation coefficient measured between both working points, the responding voltage noise signal from the Josephson junction contains different contributions. For $C(0)=+1$ it consists of low frequency fluctuations from inphase fluctuations in both working points. For $C(0)=-1$ it contains fluctuations mixed up around the chopper frequency f_c and their harmonics resulting from out-of-phase fluctuations in the working points. To determine the correlation coefficient in the time domain we conclude, that a wide bandwidth, low noise voltage amplifier with an upper cutoff frequency f_U must transfer the low frequency and high frequency fluctuations f_c, $3f_c$, $5f_c$, $7f_c < f_U$. For the upper cutoff frequency $f_U \simeq 30kHz$ of our voltage amplifier we have chosen our chopper frequency of $f_c=2.85kHz$. The analysis within the measuring bandwidth $\Delta f=[10Hz, 50Hz]$ of the correlation coefficient is limited by the lower cutoff frequency of the amplifier of about $f_L \simeq 10Hz$.

3.2 Aliasing effects

Because of the bias current switching and voltage sampling process, correlation measurements with a finite chopper frequency contain aliasing effects [14], which reduce the correlation coefficient. To eliminate aliasing effects from the sampling process an anti-aliasing filter with cutoff frequency of a half of the chopper frequency before the sampling process or signal separation is required. But with such filtering no high frequency fluctuations for the determination of the correlation coefficient in the time domain can be transferred. To suppress the mixing of very high frequency fluctuations, much higher than the chopper frequency f_c, down into the low frequency spectrum, we use for every signal line an anti-aliasing butterworth low pass filter of third order after the sampling process. Aliasing effects from bias current switching have more general character and depend on the voltage noise spectral density of the Josephson junction near the chopper frequency f_c and the correlation coefficient itself. To avoid these aliasing effects under consideration of the sampling theorem, the minimum chopper frequency f_c must be twice of the maximum frequency f_{noise}, where we have still noise power

from the Josephson junction. Thus, white noise contributions from the junction resistance R_n reduce the correlation coefficient. To minimize aliasing effects from bias current switching, the chopper frequency f_c should be higher than the corner frequency of the $1/f$-noise spectrum for both working points. Short circuit noise from the final stage of the current source ($\approx 4pA/\sqrt{Hz}$), amplifier ($\approx 150pV/\sqrt{Hz}$) and the measurement system ($\approx 100pV/\sqrt{Hz}$) are present in both working points and therefore increase the correlation coefficient. A limited bandwidth of the voltage amplifier reduces contributions from out-of-phase fluctuations contained in the higher harmonics and also increases the coefficient. The aliasing effects and the noise from our compensation circuit decrease the correlation coefficient. The latter contributions on the correlation coefficient in our measurements are only very small, and can be estimated from the consistency checks, as described below.

3.3 Results

In Fig.4(a)-(c) time traces for different working points are shown. The measurement shown in Fig.4(a) is used as a consistency check, because in this situation a correlation coefficient $C(0) = +1$ is expected. Despite of the described aliasing problems and noise sources, with a chopper frequency of $2.85kHz$, analyzed bandwidth $\Delta f = [10Hz, 50Hz]$ and short circuit noise of $200pV/\sqrt{Hz}$ for same working points $I_1 = I_2$, we find a value of $C(0) = +0.93 \pm 0.3$. In Fig.4(b) the consistency is checked for bias currents chopped between corresponding positive and negative bias currents. Here, we find $C(0) = -0.96 \pm 0.4$. In Fig.4(c) the time traces for different, positive bias currents of $I_1 = 50\mu A$ and $I_2 = +300\mu A$ are depicted. From such measurements the bias current dependence of the correlation coefficient in Fig.4(d) is determined. Here, we measure at fixed bias current $I_1 = +300\mu A$ and for $I_1 = +50\mu A$ from Fig.5 a bias current dependent decay of the correlation coefficient. The positive and negative consistency checks confirm the reliability of our measurement.

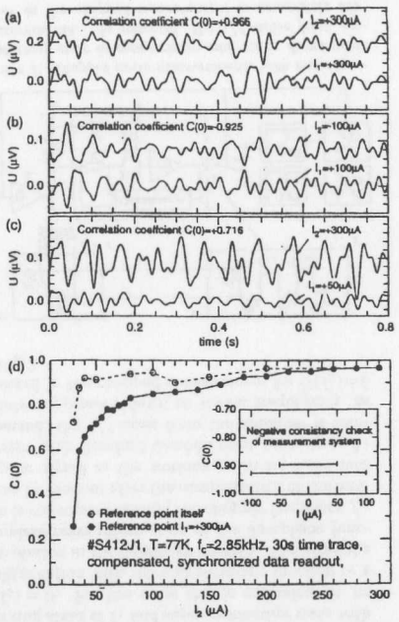

Figure 4: *(a), (b), (c) Section from 30sec. measured time traces for different working points, as given in the figures. The voltage offset is given for clarity. (d) Averaged correlation coefficient in the measuring bandwidth $\Delta f = [10Hz, 50Hz]$ vs. bias current with the synchronized data readout. The inset and coefficents with same working points confirms the reliability of measured data. We observe a current dependent decay of correlation coefficient between critical current δI_c and normal-state resistance fluctuations R_n.*

4 Noise-correlation measurements in the frequency domain

4.1 Chopped spectral density

Due to the aliasing problems from sampling process the measuring method in the time domain is limited to low frequencies. The analyzed bandwidth $\Delta f = [10Hz, 50Hz]$ of the correlation coefficient is in comparison to the required bandwidth $10Hz - 30kHz$ of the voltage amplifier very small. The correlation coefficient can alternatively be determined from voltage noise spectral densities in the frequency domain. For $C(0) = +1$ low frequency inphase voltage fluctuations of the chopped noise signal stay in the low frequency range and for $C(0) = -1$ high frequency out-of-phase voltage fluctuations are modulated around the chopper frequency f_c and their harmonics. For this, we determine the spectrum $F_{12T}(f)$ and spectral density $S_{12}(f)$ of the chopped voltage noise signal $U_{12}(t)$ from the Josephson junction. With the periodic unit rectangle function $r(t)$ of frequency f_c,

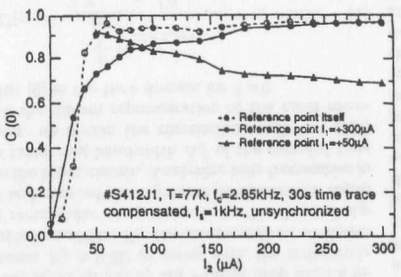

Figure 5: *Averaged correlation coefficient in the measuring bandwidth $\Delta f = [10Hz, 50Hz]$ vs. bias current with the unsynchronized data readout for different reference points.*

its fourier representation $R(f)$ with delta function $\delta(f)$, development coefficients R_n,

$$r(t) = \begin{cases} 1 & \forall \quad I(t) = I_1 \\ 0 & \forall \quad I(t) = I_2 \end{cases}, \tag{3}$$

$$R(f) = \sum_{n=-\infty}^{+\infty} R_n \delta(f - nf_c), R_n = \frac{1}{\pi n} \sin\left(\frac{\pi}{2} n\right), \tag{4}$$

the noise time traces $U_1(t)$, $U_2(t)$ for both working points, their fourier transforms $F_{1T}(f)$, $F_{2T}(f)$ and definition of voltage noise spectral densities $S_1(f)$, $S_2(f)$ are given as,

$$U_{jT} = \begin{cases} U_j(t) & \forall \quad -T/2 < t < T/2 \\ 0 & \forall \quad \text{otherwise} \end{cases}, \tag{5}$$

$$F_{jT}(f) = \int_{-\infty}^{+\infty} U_{jT}(t) e^{-i2\pi ft} dt, \tag{6}$$

$$S_j(f) = \lim_{T\to\infty} \frac{1}{T} |F_{jT}(f)|^2, \quad \forall \quad j = 1, 2. \tag{7}$$

We obtain the fourier transform $F_{12T}(f)$ of the chopped signal $U_{12}(t) = r(t)U_1(t) + (1 - r(t))U_2(t)$ with the fourier transformation F_T as:

$$F_{12T}(f) = F_T\Big(r(t)(U_1(t) - U_2(t))\Big) + F_{2T}(f) \tag{8}$$

$$= R(f) * \Big(F_{1T}(f) - F_{2T}(f)\Big) + F_{2T}(f) \tag{9}$$

$$= \sum_{n=-\infty}^{+\infty} R_n \delta(f - nf_c) * \Big(F_{1T}(f) - F_{2T}(f)\Big) + F_{2T}(f) \tag{10}$$

After the convolution for $n = 0$ with $R_0 = 1/2$ is done and using the property $\delta(f) * F_T = F_T$ of the delta function, the resulting expression is sorted by the development coefficients R_n. We obtained the spectrum and spectral density with their definition of the chopped voltage noise:

$$S_{12}(f) = \lim_{T\to\infty} \frac{1}{T} |F_{12T}(f)|^2, \tag{11}$$

$$F_{12T}(f) = \frac{1}{2}\Big(F_{1T}(f) + F_{2T}(f)\Big) \tag{12}$$

$$+ \frac{1}{\pi}\Big(\delta(f - f_c) + \delta(f + f_c)\Big) * \Big[F_{1T}(f) - F_{2T}(f)\Big]$$

$$+ \sum_{n\geq 2}^{+\infty}\Big(R_n \delta(f - nf_c) + R_{-n}\delta(f + nf_c)\Big) * \Big[F_{1T}(f) - F_{2T}(f)\Big]$$

The inphase fluctuations with $C(0) = +1$ from the time domain are called the correlated components, while the anti-correlated with $C(0) = -1$ components are called out-of-phase fluctuations. The first term of Eq.(13) describes the inphase fluctuations in the low frequency range and the other terms with $n \geq 1$ describes the out-of-phase fluctuations, which are modulated around the chopper frequency f_c and its harmonics. Corresponding measurements of the spectral density $S_{12}(f)$ of the chopped voltage noise from the Josephson junction #S412J1 for various working points I_1, I_2 are shown in Fig.6. In correspondence with Eq.(13) we recognize that only out-of-phase, anti-correlated voltage fluctuations are modulated around the chopper frequency f_c and its harmonics. As long as the chopper frequency is chosen high enough, no aliasing effects between the spectrum with in- and out-of-phase fluctuations occur and the out-of-phase fluctuations are missing completely in the low frequency range.

In Fig.6(a) for the case of $I_1 = I_2$ with $S_1(f) = S_2(f)$ only inphase voltage fluctuations with $C(0) = +1$, as in Fig.4(a) are present in the chopped signal. The signal is completely correlated with itself. In Fig.6(b) for the case of $I_1 = -I_2$ with $S_1(f) = S_2(f)$ and $C(0) = -1$ only out-of-phase voltage fluctuations are present, so that a pure amplitude-modulation of the noise occurs. Under the condition that the signal has no inphase fluctuations with $C(0) = -1$, we observe essentially no noise power in the low frequency range. White noise results from the amplifier and the Josephson junction. In Fig.6(c) the signal containing the superconducting state for $S_1(f) = 0$ and $S_2(f) \neq 0$ can be described as a superposition of the inphase (Fig.6(a)) and out-of-phase (Fig.6(b)) signals of half of the amplitude. In chopped signals, containing the superconducting state the complete noise information of one working point $S_2(f)$ is modulated around the chopper frequency f_c, so that modulated noise measurements with conventional modulation techniques are available. A signal containing one superconducting working point has a correlation coefficient of $C(0) = 0$, the same as two uncorrelated time

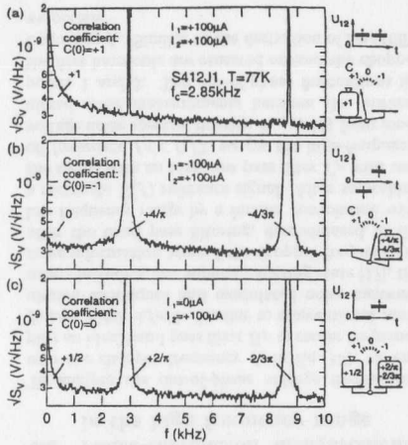

Figure 6: *Measured chopped voltage noise for different working points I_1, I_2. The modulated noise power around the chopper frequency f_c depends on the static voltage noise spectral density $S_1(f)$, $S_2(f)$ of the working points and on the correlation coefficient $C(0)$ itself. With the chopped time signals $U_{12}(t)$ and corresponding fluctuations of the working points we recognize, that only out-of-phase fluctuations modulate around the chopper frequency. Furthermore the correlation coefficient is measured from balancing the spectral densities of inphase and out-of-phase fluctuations.*

signals.

4.2 Noise-correlation measurements in the low frequency range

The correlation coefficient can be also determined from spectral densities of the voltage noise in the frequency domain. We measure the low-frequency voltage noise $S_{12,IP}(f)$ for $f < f_c/2$. If we assume, that for a sufficient high chopper frequency f_c no aliasing effects occur and $F_{1T}(f) = F_{2T}(f) = 0 \;\forall\; |f| > f_c/2$ is valid, we can negelect the out-of-phase fluctuation terms and mixed terms in Eq.(13). We use the definition of cross spectral density $\underline{W}_{12}(f)$ and the complex coherence function $\underline{\gamma}(f)$ [15]

$$\underline{W}_{12}(f) = \lim_{T\to\infty} \frac{1}{T}(F^*_{1T}(f)F_{2T}(f)), \qquad (13)$$

$$\underline{\gamma}(f) = \frac{\underline{W}_{12}(f)}{\sqrt{S_1(f)}\,\sqrt{S_2(f)}} \qquad (14)$$

Finally, we obtain the voltage noise spectral density of the inphase fluctuations $S_{12,IP}(f)$ from the low frequency part of $F_{12T}(f)$:

$$S_{12,IP}(f) = \lim_{T\to\infty} \frac{1}{T}\left|\frac{1}{2}\Big(F_{1T}(f)+F_{2T}(f)\Big)\right|^2 \qquad (15)$$

for $f < f_c/2$, and no aliasing (16)

$$= \frac{1}{4}\left(S_1(f)+S_2(f)+2Re\Big(\lim_{T\to\infty}\frac{1}{T}(F^*_{1T}(f)F_{2T}(f))\Big)\right) \qquad (17)$$

$$= \frac{1}{4}\left(S_1(f)+S_2(f)+2Re\Big(\underline{W}_{12}(f)\Big)\right), \underline{W}_{12} = \underline{W}^*_{21} \qquad (18)$$

$$= \frac{1}{4}\Big(S_1(f)+S_2(f)+2Re\Big(\underline{\gamma}(f)\sqrt{S_1(f)}\sqrt{S_2(f)}\Big)\Big) \qquad (19)$$

$$S_{12,IP}(f) = \frac{1}{4}\Big(S_1(f)+S_2(f)+2\gamma(f)\sqrt{S_1(f)}\sqrt{S_2(f)}\Big) \qquad (20)$$

We define $S_{1,IP}(f) = S_1(f)$ and $S_{2,IP}(f) = S_2(f)$ as the low-frequency voltage noise spectral density of the working points 1 and 2, which are known from static unchopped noise measurements. If the physical origin of the $1/f$-noise does not change between the static noise and correlation measurements, the spectral densities $S_{1,IP}(f)$, $S_{2,IP}(f)$ can be supposed as parameters. From Eq.(20) we obtain the frequency dependent correlation coefficient.

$$\gamma(f) = \frac{4S_{12,IP}(f) - (S_{1,IP}(f) + S_{2,IP}(f))}{2\sqrt{S_{1,IP}(f)}\,\sqrt{S_{2,IP}(f)}} \qquad (21)$$

for $n = 0$, $f < f_c/2$, no aliasing

Apart from different noise mechanism in the working points, no superconducting state of the physical system for the determination of the correlation is required. As long as the chopper frequency f_c is high enough to suppress aliasing effects with $S_{1,IP}(f) = S_{2,IP}(f) = 0 \;\forall\; f > f_c/2$, the correlation coefficient $\gamma(f)$ between both working points is completely determined by the voltage noise $S_{12,IP}(f)$ of the chopped signal $U_{12}(t)$ and the static voltage noise $S_{1,IP}(f)$, $S_{2,IP}(f)$ of the working points 1 and 2. The determination of the correlation coefficient in the frequency domain in comparison to the method in the time domain has some advantages.

i.) The frequency dependence of the correlation coefficient $\gamma(f)$ is obtained.

ii.) Aliasing effects from the sampling process do not exist.

iii.). The amplifier does not have to transfer the high frequency out-of-phase fluctuations around the frequencies f_c, $3f_c$, $5f_c$, ... With an upper cutoff frequency $f_U < f_c/2$ the amplifier only transfers the low frequency inphase fluctuations. With an extremly high chopper frequency f_c aliasing effects from the bias current switching process can be effectively suppressed.

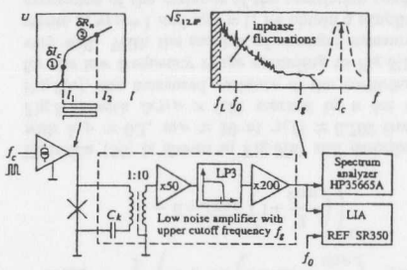

Figure 7: *Measurement principle for the determination of the frequency dependent correlation coefficient $\gamma(f)$ in the low frequency range from Josephson junctions with a low noise voltage amplifier with upper cutoff frequency f_U. A high frequency rectangle current source with chopper frequency $f_c \gg 2f_U$ transport the out-of-phase fluctuations out of the measuring bandwidth $\Delta f = [f_L, f_g]$ of the amplifer. Therefore the correlation coefficients are fully determined by the spectral densities of the inphase fluctuations in the low frequency range. A complicated compensation of the static rectangle voltages of the working points is not necessary with an low pass filter higher order with cutoff frequency f_g after the first amplifier stage.*

iv.) The short circuit noise of the measurement system can be subtracted in $S_{1,IP}(f)$, $S_{2,IP}(f)$ and the measured noise spectrum can be corrected before the correlation coefficient is determined.

v.) No compensation, signal separation, filtering and complicated data analysis are required.

The measurement principle for the low frequency range is shown in Fig.7. To avoid the saturation of amplifier from the static current-voltage curve of the Josephson junction and to get a sufficent high input voltage noise sensitivity of the spectrum analyzer, we used a low pass filter (LP3) of the third order with an cutoff frequency of $f_g < f_c/2$.
In Fig.8(a) the measured voltage noise spectral densities $S_{1,IP}$, $S_{2,IP}$, $S_{12,IP}$ in the low frequency range for different bias currents in the regimes of critical current fluctuations δI_c and resistance fluctuations δR_n of the Josephson junction #S412J1 are shown. For spectral densities with chopped bias current we used a chopper frequency of $f_c = 50kHz$. In Fig.8(b) the frequency independent correlation coefficient is depicted, which is determined from the above measurement using Eq.(21). In comparison to the correlation coefficient determined by the time method from Fig.4(c) in the measuring range $\Delta f = [10Hz, 50Hz]$ an averaging of the frequency dependent correlation coefficient with the normalization factors η_1, η_2 is given by [16]

$$C(0) = \frac{1}{\eta_1\eta_2}\int_{\Delta f} Re\Big(\underline{W}_{12}(f)\Big)\,df \qquad (22)$$

$$\eta_1 = \left[\int_{\Delta f} S_{1,IP}(f)df\right]^{1/2}, \eta_2 = \left[\int_{\Delta f} S_{2,IP}(f)df\right]^{1/2} \qquad (23)$$

and with Eq.(18) to Eq.(21)

$$C(0) = \frac{1}{\eta_1\eta_2}\int_{\Delta f}\gamma(f)\sqrt{S_{1,IP}(f)}\sqrt{S_{2,IP}(f)}df \qquad (24)$$

$$= \frac{1}{\eta_1\eta_2}\frac{1}{2}\int_{\Delta f}\Big(4S_{12,IP}(f) - (S_{1,IP}(f)+S_{2,IP}(f))\Big)df \qquad (25)$$

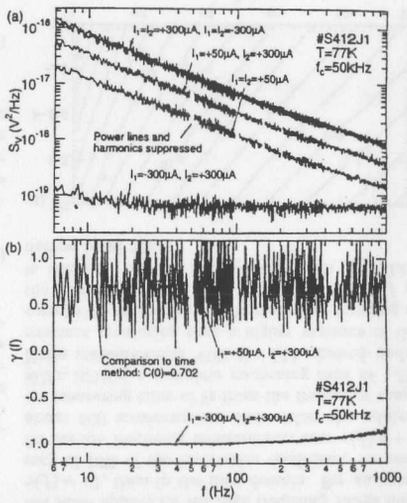

Figure 8: *(a) Measured static $S_{1,IP}(f)$, $S_{1,IP}(f)$ and chopped $S_{12,IP}(f)$ noise spectra for different working points I_1, I_2 in the low frequency range. With an high end cutoff frequency f_U of amplifier and sufficient high chopper frequency $f_c \gg 2f_U$ out-of-phase fluctuations are transported out of the measuring bandwidth and aliasing effects are effectively suppressed. Aliasing effects and white noise sources reveals as remaining spectral density for working points with $I_1 = -I_2$, $S_{1,IP}(f) = S_{2,IP}(f)$ and $\gamma(f) = -1$ in the low frequency range. (b) Correlation coefficient $\gamma(f)$ vs. frequency between critical current δI_c and normal-state resistance fluctuations δR_n. In comparision to the time method an averaging of the correlation coefficients by Eq.(24) in the measuring range $\Delta f = [10Hz, 50Hz]$ reveal with $\gamma(f) = 0.702$ in excellent agreement.*

reveals with $C(0) = 0.702$ in excellent agreement. With longer measuring times for the frequency method, we get a smoother spectrum of correlation coefficients $\gamma(f)$, which are not automatically averaged in the measuring range Δf as in the time method. The positive consistency check for same working points $I_1 = I_2$ of the frequency method is trivial, because $S_{12,IP}(f) = S_{1,IP}(f) = S_{2,IP}(f)$ results in $\gamma(f) = +1$. The negative consistency check for opposite working points $I_1 = -I_2$ is more demanding, since the spectral densities $S_{12,IP}(f)$, $S_{1,IP}(f)$, $S_{2,IP}(f)$ with chopping of bias current have to be measured. The determined coefficients of -0.98 ± 0.02 up to $100Hz$ confirms the high reliability of the frequency method.

Reversely, for a correlation coefficient $\gamma(f) = -1$ and $S_{1,IP}(f) = S_{2,IP}(f)$, aliasing effects or white noise sources reveal as remaining chopped voltage noise $S_{12,IP}(f)$ for opposite working points $I_1 = -I_2$ in the low frequency range, as shown in Fig.8(a). A further increase of the chopper frequency f_c up to $200kHz$ resulted in no decrease of the voltage noise $S_{12,IP}(f)$ for opposite working points in the low frequency range, so that aliasing effects are effectively suppressed. The origin of the remaining voltage noise can be caused, in correspondence with Fig.1(c), from white noise sources of the Josephson junction resistance R_n, and, according to Fig.1(a), from the current source transformed by the differential resistance R_d.

4.3 Noise-correlation measurements in the high frequency range

To analyse the out-of-phase voltage fluctuations near the chopper frequency f_c in Eq.(13), we employ an ideal band pass filter B_P of center frequency f_c and width $\pm fc/2$. Similar to conventional modulation techniques and modulated noise measurements including one superconducting state [17], the noise information around the chopper frequency is, after the band pass filtering, demodulated to the low frequency range by a further convolution with a rectangle $R(f)$ reference signal. After smoothing the signal with an ideal low pass filter T_P with cut-off frequency $fg < f_c/2$, we get the high-frequency voltage noise spectral density $S_{12,OP}(f)$ from modulated noise measurements between the working points 1 and 2. The out-of-phase fluctuations for the first harmonic are centered around the chopper frequency f_c. Similar to the derivation of Eq.(16ff), we obtain:

$$S_{12,OP}(f) = \lim_{T\to\infty} \frac{1}{T} \left| T_P\Big(R(f) * B_P\Big(F_{12T}(f)\Big)\Big)\right|^2 \quad (26)$$

$$= \lim_{T\to\infty} \frac{1}{T} \left| \left(\frac{1}{\pi}\right)\left(\frac{2}{\pi}\right)\Big(F_{1T}(f) - F_{2T}(f)\Big)\right|^2 \quad (27)$$

$$\text{for } f < f_c/2, \text{ no aliasing} \quad (28)$$

$$= \left(\frac{1}{\pi}\right)^2\left(\frac{2}{\pi}\right)^2\Big(S_1(f) + S_2(f) - 2\gamma(f)\sqrt{S_1(f)}\sqrt{S_2(f)}\Big) \quad (29)$$

As shown in Fig.2, the voltage noise spectral densities of the working point $S_1(f)$ can also be determined by chopped noise measurements containing a superconducting state $I_2 = 0$, where $S_{1,OP}(f) = (1/\pi)^2(2/\pi)^2\, S_1(f)$ with $S_2(f) = 0$ and $\gamma(f) = 0$ is known. Seperately, $S_{2,OP}(f) = (1/\pi)^2(2/\pi)^2 S_2(f)$ with $S_1(f) = 0$ and $\gamma(f) = 0$ is determined. If the physical origin of the $1/f$-noise does not change between the modulated noise measurements $S_{1,OP}(f)$, $S_{2,OP}(f)$ and the modulated correlation measurement $S_{12,OP}(f)$, we can substitute these into Eq.(29) and obtain the correlation coefficient from modulated noise measurements with a sufficient high chopper frequency f_c for every harmonics without aliasing effects as:

$$\gamma(f) = \frac{S_{1,OP}(f) + S_{2,OP}(f) - S_{12,OP}(f)}{2\sqrt{S_{1,OP}(f)}\sqrt{S_{2,OP}(f)}} \quad (30)$$

$$\text{for } n = 1, 2, 3\ldots,\ f < f_c/2, \text{ no aliasing} \quad (31)$$

If the physical system has no superconducting state, the adjustment and measuring of the spectral densities $S_1(f)$, $S_2(f)$ are also possible for $\gamma(f) = -1$ with $S_1(f) = S_2(f)$ for opposite working points $I_1 = -I_2$. In this case we obtain a similar expression to Eq.(21) with the substitution $\gamma \to -\gamma$ for the correlation coefficient determined by spectral densities from modulated noise measurements. However, especially in the very low frequency range $\Delta f = [0.01Hz, 10kHz]$ the correlation coefficient can also determined with the advantages of conventional modulation techniques, working at room temperature with an amplifier noise with less than $50pV/\sqrt{Hz}$, so that a complicated low-T_c-SQUID measuring system is not necessary.

4.4 Variance of the correlation coefficient

According to Fig.8(b) variations of the correlation coefficients depend on the coefficient itself and on the variance of the measured voltage noise spectral densities $S_{12,IP}(f)$, $S_{1,IP}(f)$, $S_{2,IP}(f)$ caused by the averaging process of spectrum analyzer due to the limited measuring time. Starting from Eq.(21) with the partial derivatives and the law of error propagation, we obtain the variance of the correlation coefficient as follows:

$$\Delta\gamma^2 = \Delta S_{12,IP}^2\left(\frac{\partial\gamma}{\partial S_{12,IP}}\right)^2 + \Delta S_{1,IP}^2\left(\frac{\partial\gamma}{\partial S_{1,IP}}\right)^2 + \Delta S_{2,IP}^2\left(\frac{\partial\gamma}{\partial S_{2,IP}}\right)^2 \quad (32)$$

$$\Delta\gamma^2 = \Delta S_{12,IP}^2\left(\frac{4}{S_{1,IP}S_{2,IP}}\right) + \frac{\Delta S_{1,IP}^2}{16}\left(\frac{1}{\sqrt{S_{1,IP}S_{2,IP}}} + \frac{(4S_{12,IP} - S_{2,IP})}{S_{1,IP}\sqrt{S_{1,IP}S_{2,IP}}}\right)^2 + \frac{\Delta S_{2,IP}^2}{16}\left(\frac{1}{\sqrt{S_{1,IP}S_{2,IP}}} + \frac{(4S_{12,IP} - S_{1,IP})}{S_{2,IP}\sqrt{S_{1,IP}S_{2,IP}}}\right)^2 \quad (33)$$

With the assumption, that all voltage noise spectral densities are measured within the same measuring time, and resulted from n averages by the spectrum analyzer [14], we get with $k_{IP} = 1/\sqrt{n} = \Delta S_{1,IP}/S_{1,IP} = \Delta S_{2,IP}/S_{2,IP} = \Delta S_{12,IP}/S_{12,IP}$ and $v_{IP} = S_{1,IP}(f)/S_{2,IP}(f)$ the variance of correlation coefficient for the low frequency range.

$$\Delta\gamma^2 = \frac{k_{IP}^2}{S_{1,IP}S_{2,IP}}\left[6S_{12,IP}^2 + \frac{1}{8}\left(S_{1,IP} - S_{2,IP}\right)^2\right] \quad (34)$$

After the substitution of Eq.(21) and a similar derivation with Eq.(31) and $k_{OP} = 1/\sqrt{n} = \Delta S_{1,OP}/S_{1,OP} = \Delta S_{2,OP}/S_{2,OP} = \Delta S_{12,OP}/S_{12,OP}$, $v_{OP} = S_{1,OP}(f)/S_{2,OP}(f)$, we obtain the variance of the correlation coefficient for the low and high frequency range.

$$\Delta\gamma_{IP} = \frac{k_{IP}}{2}\left(6\gamma^2 + 2\left(1 + v_{IP} + \frac{1}{v_{IP}}\right) + 6\gamma\sqrt{v_{IP}}\left(1 + \frac{1}{v_{IP}}\right)\right)^{1/2} \quad (35)$$

$$\Delta\gamma_{OP} = \frac{k_{OP}}{2}\left(6\gamma^2 + 2\left(1 + v_{OP} + \frac{1}{v_{OP}}\right) - 6\gamma\sqrt{v_{OP}}\left(1 + \frac{1}{v_{OP}}\right)\right)^{1/2} \quad (36)$$

Equation (36) is shown in Fig.9(a) and describes with $k_{IP} \simeq 0.1$, $v_{IP} \simeq 10$ at $\gamma(f) \simeq 0.702$ from Fig.8(a) with $\Delta\gamma_{IP} \simeq 0.31$ marked by a dot in Fig.9(a), the measured variance of the coefficient for the low frequency range according to Fig.8(b) very well. With the number of averaged measurements n, $v_{IP} = 1$ and $v_{OP} = 1$, we obtain a simplier expression of the variance of the correlation coefficient for the low and high frequency measurement.

$$\Delta\gamma_{IP} = \frac{1}{2}\sqrt{\frac{6}{n}}(1+\gamma),\ n = \frac{3}{2\Delta\gamma_{IP}^2}(1+\gamma)^2 \quad (37)$$

$$\Delta\gamma_{OP} = \frac{1}{2}\sqrt{\frac{6}{n}}(1-\gamma),\ n = \frac{3}{2\Delta\gamma_{OP}^2}(1-\gamma)^2 \quad (38)$$

Surprisingly, the calculated fluctuations of the correlation coefficient for the high frequency measurement $n = 1, 2, 3\ldots$ from Eq.(37) are very small at $\gamma(f) = +1$, contrary to the low frequency measurement according to Fig.9. The measurement in the frequency domain of Fig.8(b) is much more precisely for the low frequency range near $\gamma(f)! = -1$, the same applies for the high frequency range near $\gamma(f) = +1$, than in the time domain. For an accuracy of 10% of the correlation coefficient, we need for the low frequency measurement near $\gamma(f) = +1$, about 600 measurements and within the analyzers measuring time of 8s from the frequency range $[0Hz, 100Hz]$ a complete measuring time of 1.3h. Noise measurements with the LIA showed under constant measuring time a higher variance of the correlation coefficient $\Delta\gamma$, because an averaging of the coefficient in the measuring bandwidth Δf as in the time domain is impossible with the LIA's narrow band filter.

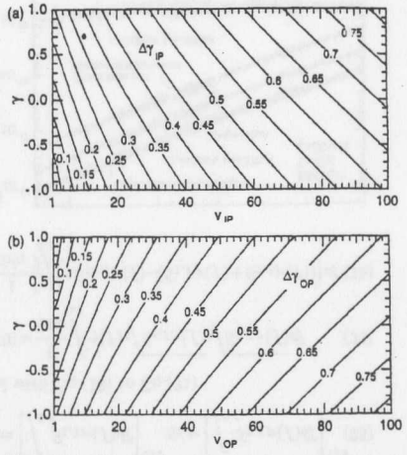

Figure 9: *Calculated variance of the correlation coefficient $\Delta\gamma_{IP}$ vs. the ratio v_{IP} of static spectral densities of the working points and the correlation coefficient γ with $k_{IP} = 0.1$ for inphase (a) and out-of-phase (b) fluctuations.*

5 Chopped characteristic quasi-particle times

Apart from aliasing effects due to the remaining voltage noise spectral density from an $1/f$-noise spectrum of the Josephson junction at finite chopper frequency f_c, the switching of the characteristic quasi-particle times $\tau_{eff}(U)$ and their voltage dependence [6] does not influence the correlation coefficient for a sufficient high chopper frequency with $f_c \gg 1/\tau_{eff}$ of both working points. To show this, we determine the spectrum of a single trapping center biased between two working points with chopper frequency f_c. The conditional probability $P_{o,u}(t)$, that the resistance will stay after an initial jump to that state, is given for a time dependent and exponentially distributed lifetime $\tau_{o,u}(t)$ for the occupied, respectively unoccupied state as:

$$P_{o,u}(t) = \exp\left(-\int_0^t \frac{1}{\tau_{o,u}(t')}\,dt'\right) \qquad (39)$$

The trapping center is characterized at each time by a Lorentzian type power spectrum with characteristic frequency $1/\tau_{eff1} = 1/\tau_{u1} + 1/\tau_{o1}$ and exponentially distributed lifetimes for the occupied $P_{o1}(t) = \exp(-t/\tau_{o1})$ and unoccupied state $P_{u1}(t) = \exp(-t/\tau_{u1})$ at working point 1, respectively working point 2. For a sufficient high chopper frequency f_c with $f_c \gg 1/\tau_{eff1}, 1/\tau_{eff2}$ we get from Eq. (39) the probabilty $P_o(t)$, that the electron will stay in the occupied, respectively for the unoccupied state as:

$$P_o(t) = (P_{o1}(t)\ P_{o2}(t))^{1/2} \ \forall\ f_c \gg \frac{1}{\tau_{eff1}}, \frac{1}{\tau_{eff2}} \qquad (40)$$

$$P_u(t) = (P_{u1}(t)\ P_{u2}(t))^{1/2}$$

The probability $P_o(t)$ reduces for the unswitched case with $P_{o1}(t) = P_{o2}(t)$ to the probability $P_{o1}(t)$, respectively $P_u(t)$. After the substitution of the individual probabilities into Eq.(40), we define an effective characteristic lifetime for the occupied τ_o and unoccupied τ_u state of both working points.

$$P_o(t) = e^{-t/\tau_o}, \quad \frac{1}{\tau_o} = \frac{1}{2}\left(\frac{1}{\tau_{o1}} + \frac{1}{\tau_{o2}}\right) \qquad (41)$$

$$P_u(t) = e^{-t/\tau_u}, \quad \frac{1}{\tau_u} = \frac{1}{2}\left(\frac{1}{\tau_{u1}} + \frac{1}{\tau_{u2}}\right) \qquad (42)$$

Using the same derivation of Machlup [18] we obtain for a sufficient high chopper frequency f_c also a Lorentzian type power spectrum $S^{LS}_{12,R}(f)$ for a single trapping center with an effective charateristic lifetime τ_{eff} for both working points.

$$S^{LS}_{12,R}(f) = \delta R^2\ \frac{\tau^2_{eff}}{\tau_o + \tau_u}\ \frac{\tau_{eff}}{1 + (2\pi f \tau_{eff})^2} \qquad (43)$$

$$\text{for}\quad \frac{1}{\tau_{eff}} = \frac{1}{\tau_o} + \frac{1}{\tau_u},\ f_c \gg \frac{1}{\tau_{eff}}$$

Numerical generated time traces of a single trap are shown for different chopper frequencies in Fig.10(a). In Fig.10(b) the resulting distribution of lifetimes are depicted. The approach for a constant quasi-particle lifetime τ_{eff} from Eq.(44) resulting in a Lorentzian type power spectrum for switched life-

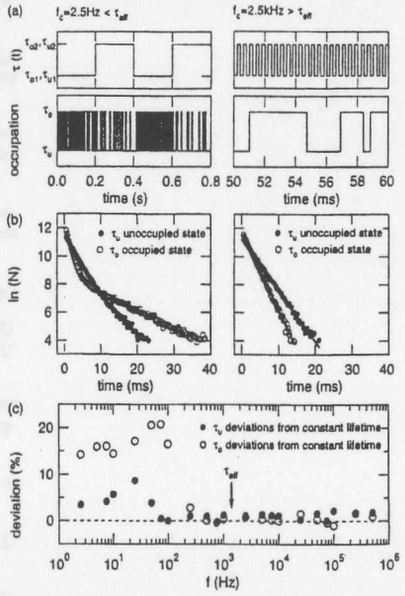

Figure 10: *Random telegraph noise for a two-level switching process with exponentially distributed, chopped characteristic lifetimes for $\tau_{o1} = 2ms$, $\tau_{u1} = 1ms$, $\tau_{o2} = 4ms$, $\tau_{u2} = 8ms$ in the low frequency $f_c \ll 1/\tau_{eff}$ and high frequency $f_c \gg 1/\tau_{eff}$ limit. (a) Switched lifetimes $\tau(t)$ and simulated occupation for a single trap. (b) Semi-log plot of the times spent in the high and low resistance state. (c) Percentage deviations of the statistically determined quasi-particle lifetimes τ_o, τ_u from the expected lifetimes in the high frequency limit determined by Eq.(41,42) vs. chopper frequency f_c. The approach of the multiplication of the inidividual probabilities from Eq.(40) resulting in a constant effective lifetime τ_{eff} is valid for chopper frequencies with $f_c > 1/\tau_{eff}$.*

times is only valid for chopper frequencies with $f_c > 1/\tau_{eff}$, as depicted in Fig.10(c). The superposition of independent traps with $g(\tau_{eff}) \propto 1/\tau_{eff}$ distribution of effective lifetimes results in an $1/f$-noise spectrum for the resistance fluctuations.

$$S_{12,R}(f) = \int_0^\infty g(\tau_{eff}) S^{LS}_{12,R}(f, \tau_{eff})\, d\tau_{eff} \propto \frac{1}{f} \qquad (44)$$

Therefore, the voltage dependence of the characteristic quasi-particle times [6] can be neglected in the determination of the correlation coefficient due to the sampling of one physical origin - namely the $1/f$-noise spectrum from resistance fluctuations of Eq.(44) - as long as the chopper frequency f_c is greater than the inverse of all contributing effective lifetimes τ_{eff} or the corner frequencies of the $1/f$-noise spectrums of the working points.

6 Discussion and Conclusions

For working points with $S_1(f) = S_2(f)$ and correlation coefficients of $\gamma(f) = -1$, no inphase voltage fluctuations exist and no $1/f$-noise power from Josephson junction is present in the low frequency range. Only aliasing effects and contributions from white noise sources reveal as remaining chopped voltage noise $S_{12,IP}(f)$ in the low frequency range. The voltage dependence of the characteristic quasi-particle times [6] underly, with a finite chopper frequency f_c, the sampling theorem and also reveal as an aliasing effect. We obtain the possible systematic deviation of the correlation coefficient due to aliasing and white noise sources with the spectral densities at $f = 10Hz$ from Fig.8(a) with $\Delta S = 0.9 \cdot 10^{-19} V^2/Hz$ for $I_1 = -300\mu A$, $I_2 = +300\mu A$ and $S_{1,IP} = 1.1 \cdot 10^{-17} V^2/Hz$ for $I_1 = +50\mu A$. We find without the variance due to the limited measuring time with $k_{IP} = \Delta S/S_{1,IP} \simeq 8.2 \cdot 10^{-3}$, $v_{IP} \simeq 10$ at $\gamma_{IP}(f) \simeq 0.702$ from Eq.(36) a deviation of $\Delta\gamma_{IP}(f) = 0.026$. Therefore, aliasing effects, the voltage dependence of characteristic times of quasi-particles and white noise sources cannot explain the current dependent decay of correlation coefficient of about $\Delta\gamma = 1 - 0.702 = 0.298$. Furthermore fluctuations with characteristic times of the inverse of the maximum corner frequency $f_{noise} \simeq 10kHz$ with $\tau_{eff} \simeq 100\mu s$ of the $1/f$-noise from Fig.1(d) are detected by the used chopper frequency of up to $fc = 200kHz$ with sampling times of $5\mu s$ and result in no further decrease of correlation coefficient. Even with a smaller chopper frequency and aliasing effects, a noticeable decrease of the correlation coefficient can only be observed, when the chopped voltage noise for opposite working points in the low frequency range have nearly the same spectral density as the static unchopped voltage noise $S_{1,IP}$ or $S_{2,IP}$ for $I_1 = +50\mu A$ and $I_2 = +300\mu A$. But, actually the static unchopped voltage noise is of the order of $10^3 \ldots 10^1$ higher than the chopped spectral density for working points with opposite polarity of bias currents in the low frequency range at $f = 10Hz$.

The exclusive measured positive correlation coefficients $\gamma(f)$ between critical current fluctuations δI_c and normal-state resistance fluctuations δR_n are describable by a statistically variing spatial separation of the transport of Cooper-pairs and quasi-particles with differently noise signatures, where the actual fluctuation mechanism is caused from localized states in the insulating grain-boundary barrier of the Josephson junction. The Coulomb barriers due to occupied localized states with quasi-particles act as a spatial restricted barrier or barrier with finite tunnel probability for the following Cooper-pairs. In correspondence with the observed current dependent decay of correlation coefficient from Fig.4(a), the higher the current in the resistive part of the static current-voltage curve against the reference point is chosen, the more charge carriers occupy the localized states and force the following Cooper-pairs and quasi-particles on statistically different, spatial seperated, channels and noise signatures to decrease the correlation coefficient. The continuity of the current dependent decay and the frequency independence of the correlation coefficient suggest a high density of localized states in the insulating boundary barrier. With the given formulas for the adjustment without switching into a superconducting state, the described noise-correlation measurement can be used in every physical system.

This work was supported by the Bundesministerium für Bildung, Wissenschaft, Forschung und Technologie, Federal Republic of Germany under Contract No. 13N6734-0.

References

[1] B.H. Moeckly, D.K. Lathrop, R.A. Buhrmann, Phys. Rev. B **47**, 400 (1993)

[2] R. Gross, B. Mayer, Physica C **180**, 235 (1991)

[3] R. Gross, *Grain Boundary Josephson Junctions in the High Temperature Superconductors in Interfaces in Superconducting Systems*, Springer Verlag, New York (1992), Chapter 6

[4] R.H. Koch. Elsevier Science Publishers B.V. **36**, 377 (1983)

[5] C.T. Rogers, R.A. Buhrman, Phys. Rev. Lett. **53**, no.13, 1272 (1984)

[6] A. Marx, U. Fath, L. Alff, R. Gross, Appl. Phys. Lett. **67**, 1929 (1995)

[7] P. Dutta, P.M. Horn, Rev. Mod. Phys. **53**, no.3, 497 (1981)

[8] C.T. Rogers, R.A. Buhrman, IEEE Transactions on magnetics **MAG-23**, no.2, 1658

[9] A. Marx, U. Fath, W. Ludwig, R. Gross, T. Amrein, Phys. Rev. B **51**, 6735 (1995)

[10] M. Kawasaki, P. Chaudhari, A. Gupta, Phys. Rev. Lett. **68**, 1065 (1992)

[11] O. Doessel, B. David, M. Fuchs, W.H. Kullmann, K.M. Luedecke, IEEE Transactions on magnetics **27**, 2797 (1991)

[12] S.G. Hammond, Y. He, C.M. Muirhead, M.S. Colclough, K. Char, Cryogenics **32**, 715 (1992)

[13] A.H,. Miklich, J. Clarke, M.S. Colclough, K. Char, Appl. Phys. Lett. **60**, 1899 (1992)

[14] H.G. Natke, *Einführung in Theorie und Praxis der Zeitreihen- und Modalanalyse*, Vieweg Verlag Wiesbaden (1992)

[15] F. Landstorfer, H. Graf, *Rauschprobleme der Nachrichtentechnik*, R. Oldenbourg Verlag München Wien (1981)

[16] R. Müller, W. Heywang, *Halbleiter-Elektronik Rauschen*, Springer Verlag, New York (1979), Chapter 2.4

[17] V. Foglietti, W.J. Gallagher, M.B. Ketchen, A.W. Kleinsasser, R.H. Koch, S.I. Raider, R.L. Sandstrom Appl. Phys. Lett. **49**, 1393 (1986)

[18] S. Machlup, J. Appl. Phys. **25**, 341 (1954)

Appendix C

Technical data

C.1 Mask layouts

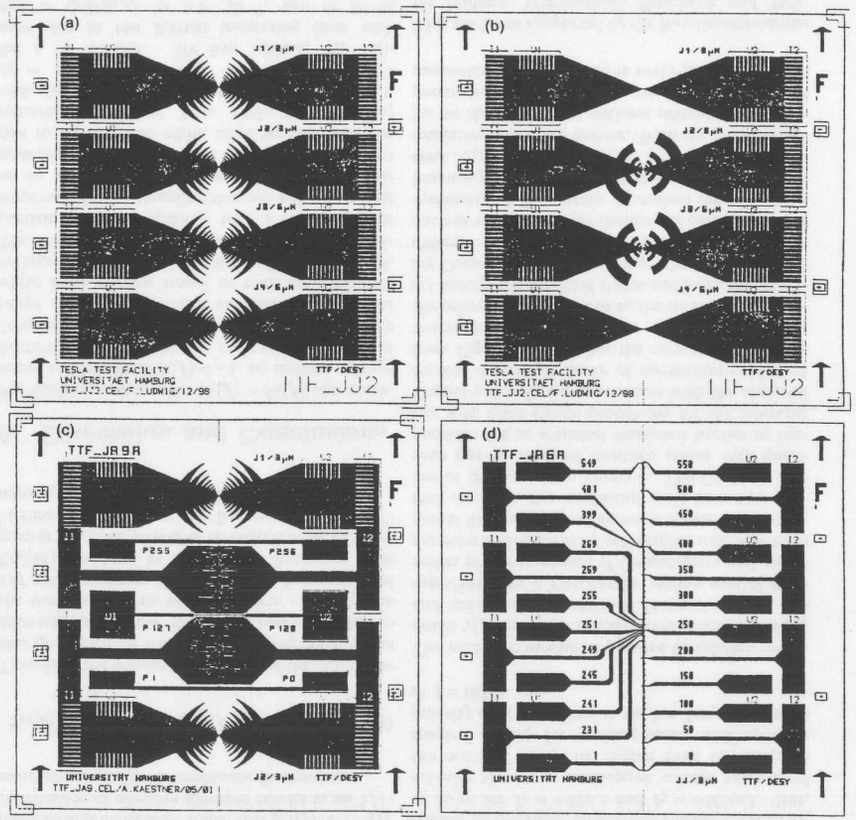

Figure C.1: *Chrom masks for the lithography process of bicrystal junctions including (a) BD-LP-antenna and (b) RA-LP-antenna and Bow-tie type antenna. (c) Two 1-dimensional series array consisting of 128 junctions coupled to a fin antenna biased by a BD-LP-antenna. (d) one-dimensional series array with 550 grain boundary junctions.*

C.2 Design of ultra low-noise components

Ultra low-noise voltage, respectively current pickup and biasing and fast a readout of the junction is absolute neccessary for Hilbert spectroscopy using pulsed rf-sources for a single-bunch operation. In this section we will design a pickup and biasing with less than $80pV/\sqrt{Hz}$ equivalent input voltage noise in the frequency range of [1MHz,4GHz].

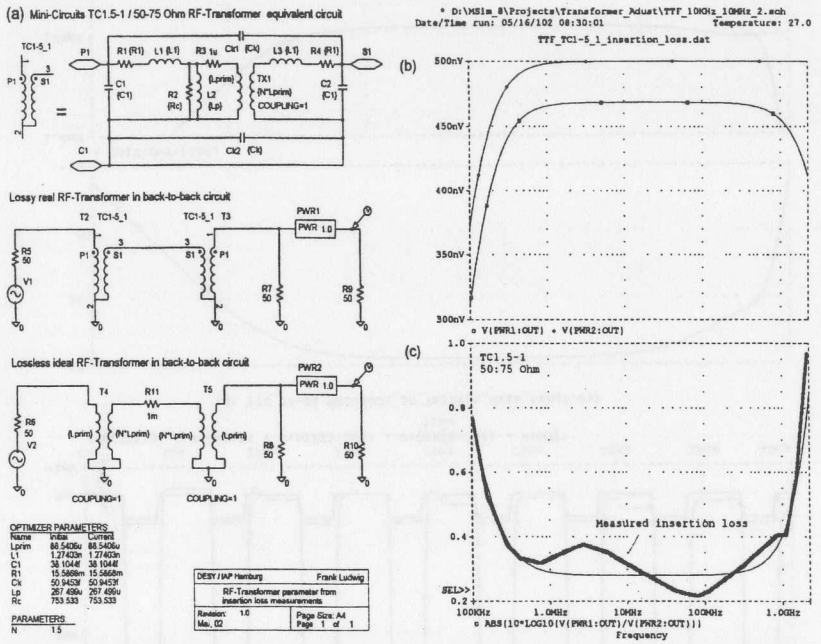

Figure C.2: *(a) PSPICE optimized determination of rf-transformer equivalent circuit parameters from insertion loss measurements. (b),(c) Appropriate lossy and lossless transfer function with insertion loss.*

The design and realization of rf-circuits operating at wavelengths smaller than its dimensions requires replacement circuits of transmission structures, rf-devices and geometries including material properties. S-parameter representations and Smith-Digramms are widely used for characterization of active and passive devices in the frequency domain [Col98]. For transient analysis several simulators like PSPICE, HPEesof, SUPERMIX etc. are widely used by solving the circuit as a network of coupled differential equations with matrix methods and time domain difference schemes [SPICE]. The design of low-noise rf-amplifiers reduces to the problem of finding coupling networks preparing the optimum input and output impedances for all amplifier stages over a specified frequency range for a given specification [Tri, AN1022, AN1091, Col98, Gun92]. There exist several optimizers and tools for finding networks, which provide matching for given source and load impedances. Broadband characteristics can be achieved by detuning several resonator stage or using the concept of traveling amplifier [Gun92]. We focus on a rf-amplifier stage and biasing of the junction for an rf-pulse series duration from FPI in the ns regime.

C.3 RF-transformer pickup and (SQUID) rf-amplifier design

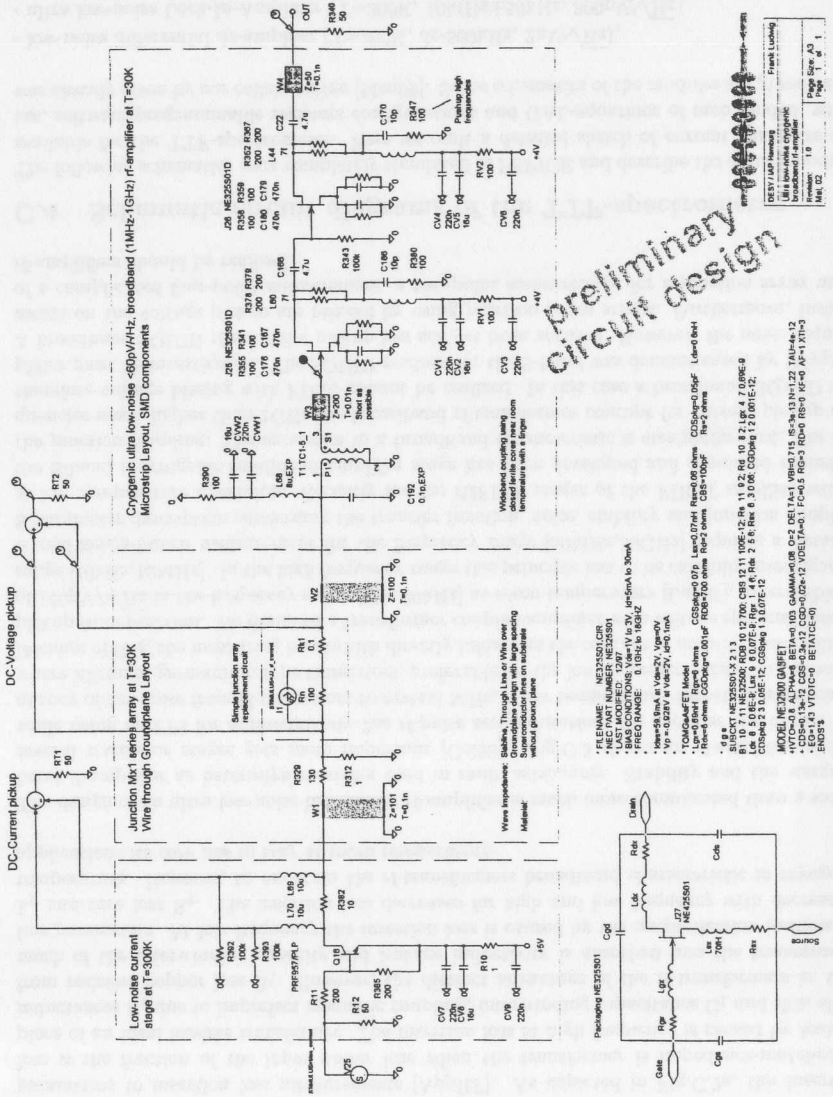

Figure C.3: *Ultra low-noise cryogenic broadband rf-amplifier with equivalent input voltage noise of $\sqrt{S_{U,AMP}} < 80pV/\sqrt{Hz}$ and frequency range $[1MHz, 1GHz]$. The junction series array is modeled by its normal-state resistance $N_J R_n$ and biased by a discrete low-noise rf-stage with low impedance for voltage biasing. The current response pickup can be realized by a rf-transformer or a broadband SQUID amplifier. Several other types of InP HEMT's, HJ FET's or GaAs-FET's transistors might be used like Fujitsu FHC40LG, NEC334S01 etc.*

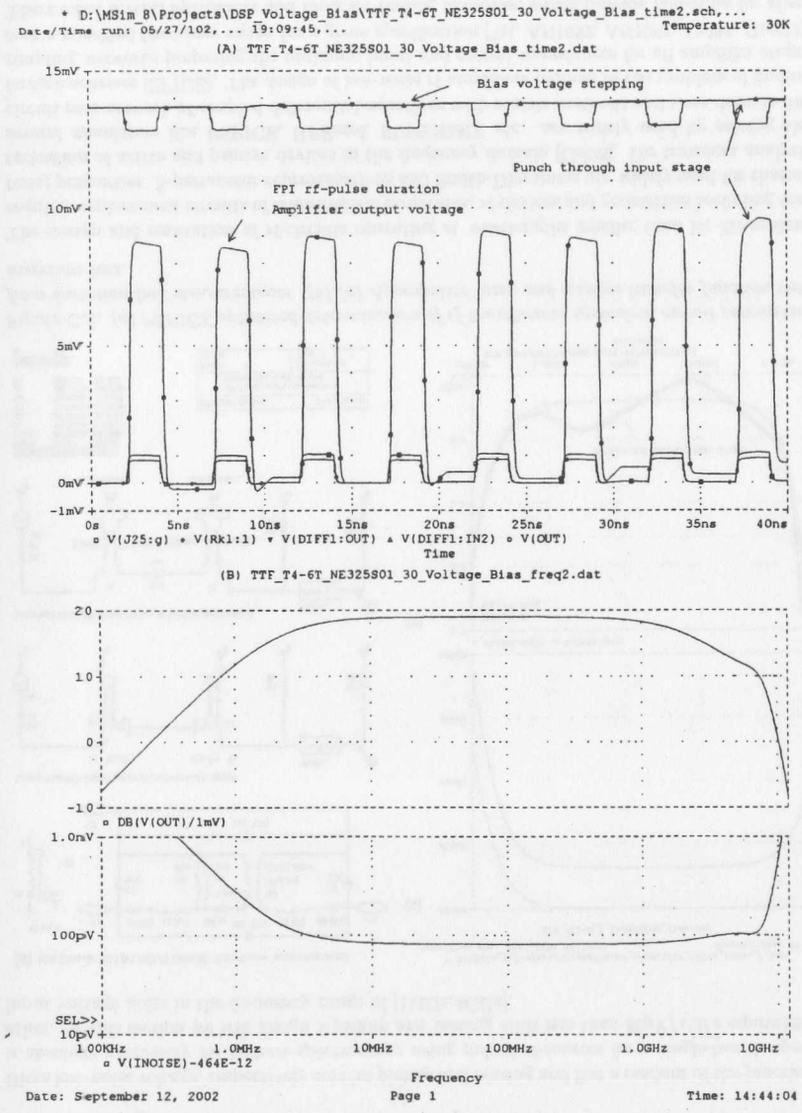

Figure C.4: *PSPICE simulated (a) time traces of a 2ns rf-pulse series duration from junction array while stepping the biasing voltage. (b) Transfer function and input voltage noise spectral density of $80pV/\sqrt{Hz}$. A low-T_c SQUID system operating at $T = 4K$ has approximately $20pV/\sqrt{Hz}$ [Lud97].*

As we will see, a transformer pickup is a key feature of a voltage biased series array of Josephson junctions. To simulate a reliable rf-transformer characteristic, we optimize its equivalent circuit parameters to insertion loss measurements [AppRF]. As depicted in Fig.C.2a, the insertion loss is the fraction of the input power loss when the transformer is impedance-matched in place of an ideal lossless transformer. The insertion loss at high frequency is caused by leakage inductances L_1 due to imperfect magnetic coupling, interwinding capacitance C_1 and skin effect from resistive copper loss R_1. However, the distinct advantage of the rf-transformers is, that much of the interwinding capacity and leakage inductivity is absorbed into the transmission line parameters. At low frequency the insertion loss is caused by the magnetization inductance L_p and core loss R_c. The insertion loss decreases for high and low frequency with decreasing temperature. However, to maintain the rf-transformers broadband characteristic in cryogenic applications its core has to stay at room temperature.

The design of an ultra low-noise broadband rf-amplifier is much more complicated than a small-band if-amplifier as heterodyn receivers used in radio astronomy. Stability and the usage of several transistor stages gets more important [Col98]. Fig.C.3 shows an rf-amplifier pickup while using an FPI for approximately 2ns rf-pulse series duration. To decrease the corner frequency of 1/f-noise from rf-transistors to several MHz, a low temperature operation is required, where silicon or germanium type transistors, preferable for the low frequency range, do not work. Because of this, the measuring bandwidth directly influences the concept of amplifier and voltage pickup from junction. We designed a transformer coupled amplifier with voltage spectral density of $140pV/\sqrt{Hz}$ in the frequency range [1Hz,20kHz] at room temperature [Lud97], extendable to range [10kHz,10MHz]. In the high frequency range this principle has to be carefully investigated. A real single-bunch measurement for the frequency range [50MHz,50GHz] requires a detailed S-parameter description concerning the transfer function, noise, stability and junction coupling at low temperature operation. Recently for the HIFI IF stages of the FIRST satellite within the S-band a cyrogenic smallband amplifier stage has been developed and simulated including the junction coupling. The extension to a broadband characteristic is straightforward. For frequencies much higher than 1GHz the broadband rf-transformer concept for current pickup and therefore voltage biasing with FDSC cannot be realized. In this case a broadband SQUID amplifier must be investigated. The SQUID readout for the S-band was demonstrated by [Myg99]. A broadband SQUID rf-amplifier pickup has not yet been realized. However, the noise requirements on the voltage pickup are relaxed by using junction series arrays. Furthermore, instead of a complicated four-point measurement, a two-point measurement for a junction array using rf-amplifiers should be realized.

C.4 Schematic circuit diagrams of the TTF-spectrometer

The following schematics were completely simulated in PSPICE and describe the actual modules available for the TTF-spectrometer. Here we omit a detailed sketch of current hardware status, software programmable registers configurations and GAL-equations of each modul, which was already given by our collaboration [Men99]. Some schematics of the modules are given below

- low-noise differential dc-amplfier (T=300K, dc-500kHz, $2nV/\sqrt{Hz}$),
- ultra low-noise Lock-In-Amplifier (T=300K, 10MHz±50kHz, $300pV/\sqrt{Hz}$),
- ultra low-noise rf-broadband amplifier (T=300K, 10kHz-1GHz, $380pV/\sqrt{Hz}$),
- ultra low-noise broadband ac-amplifier (T=300K, 1Hz-20kHz, 10kHz-10MHz, $140pV/\sqrt{Hz}$),
- ultra low-noise high speed matched current source (16Bit, 500kHz) with bunch timing,
- 10MHz phase shifter, TTF timing adapter and isolation for VME crayds.

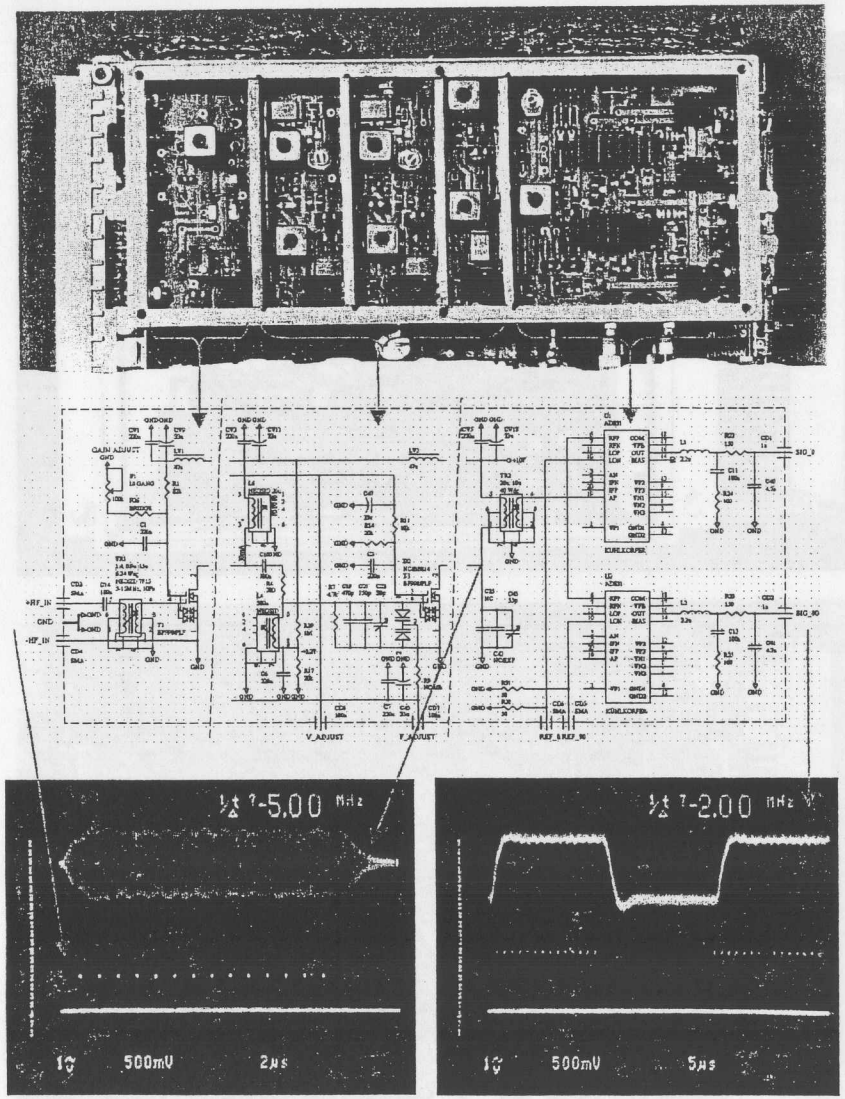

Figure C.5: *Voltage response of a series of 15 pulses of width Δt=10ns, peak voltage ΔU=100μV (input signal was scaled down) with distance ΔT=1μs. The Lock-In-Amplifier operates with an amplification of $v=3\cdot10^5$ at center frequency f=10MHz$\pm$50kHz. Pulses pushes filters and produce a continuous frequency, which is down modulated by a phase shifter controlled from TTF timing. The measurement fits quite well to PSPICE simulations.*

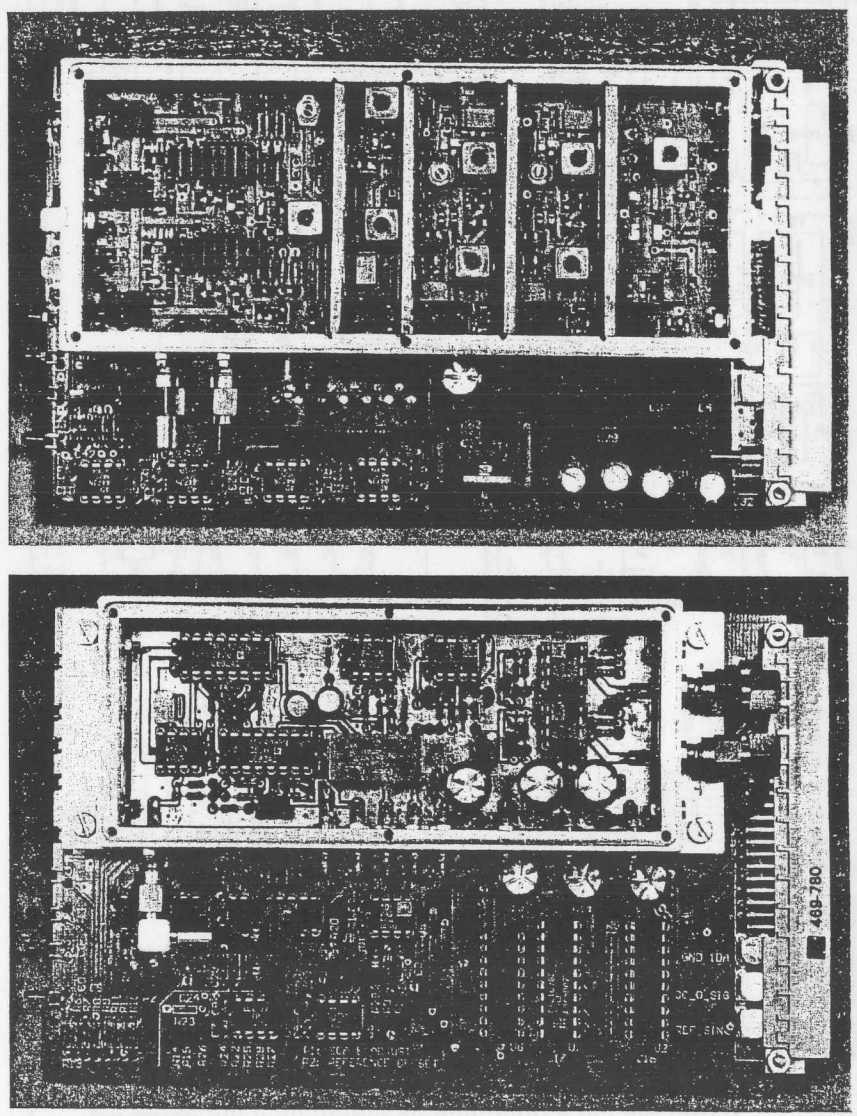

Figure C.6: *(a) Ultra low-noise 10MHz Lock-In-Amplifier and (b) Low-noise dc-differential amplifier for voltage pickup.*

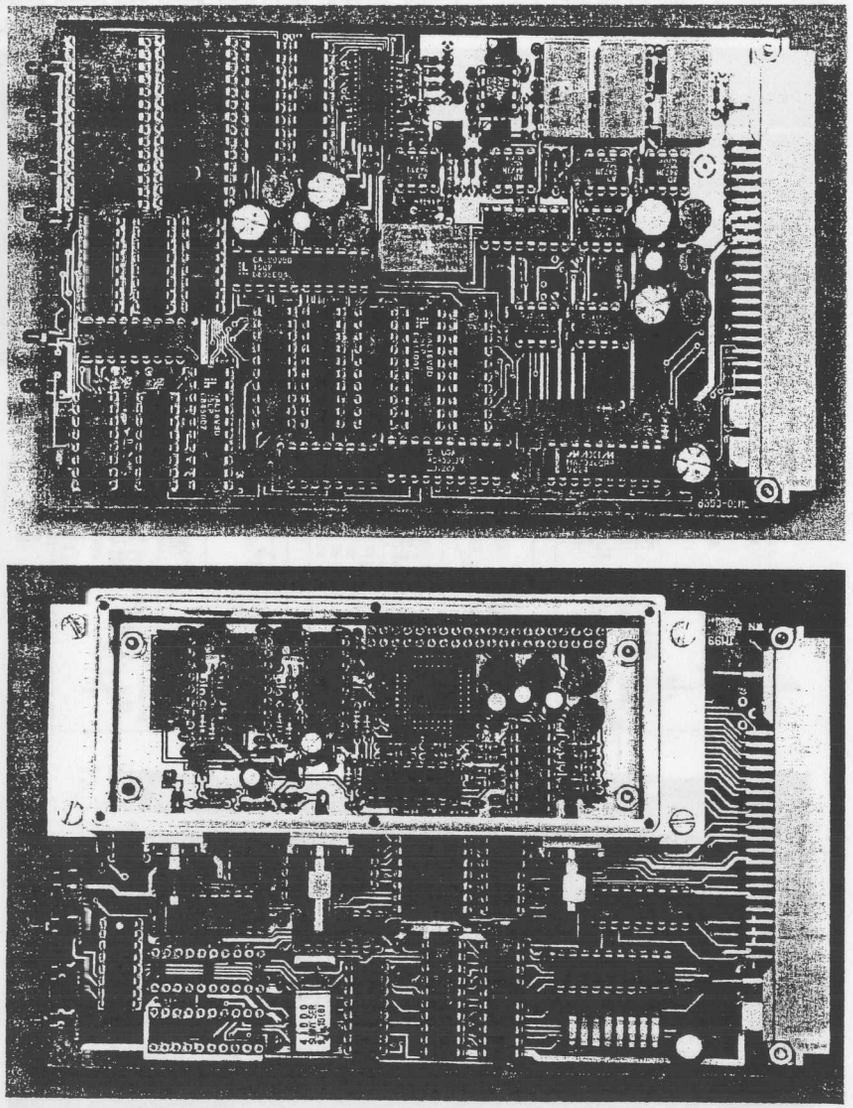

Figure C.7: *(a) Ultra low-noise chopped current source with programable timing. (b) Timing modul including programable 10MHz phase shifter in ECL logic.*

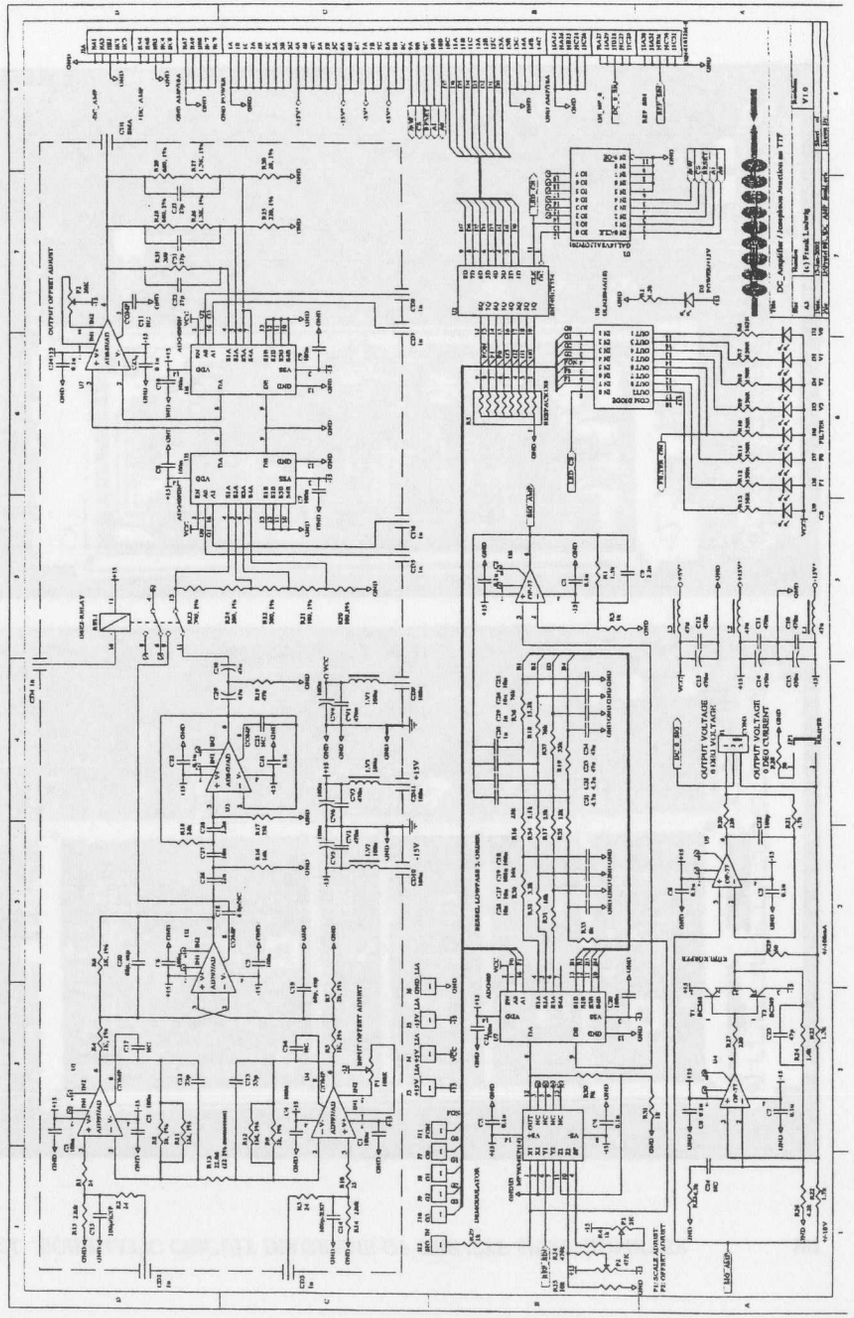

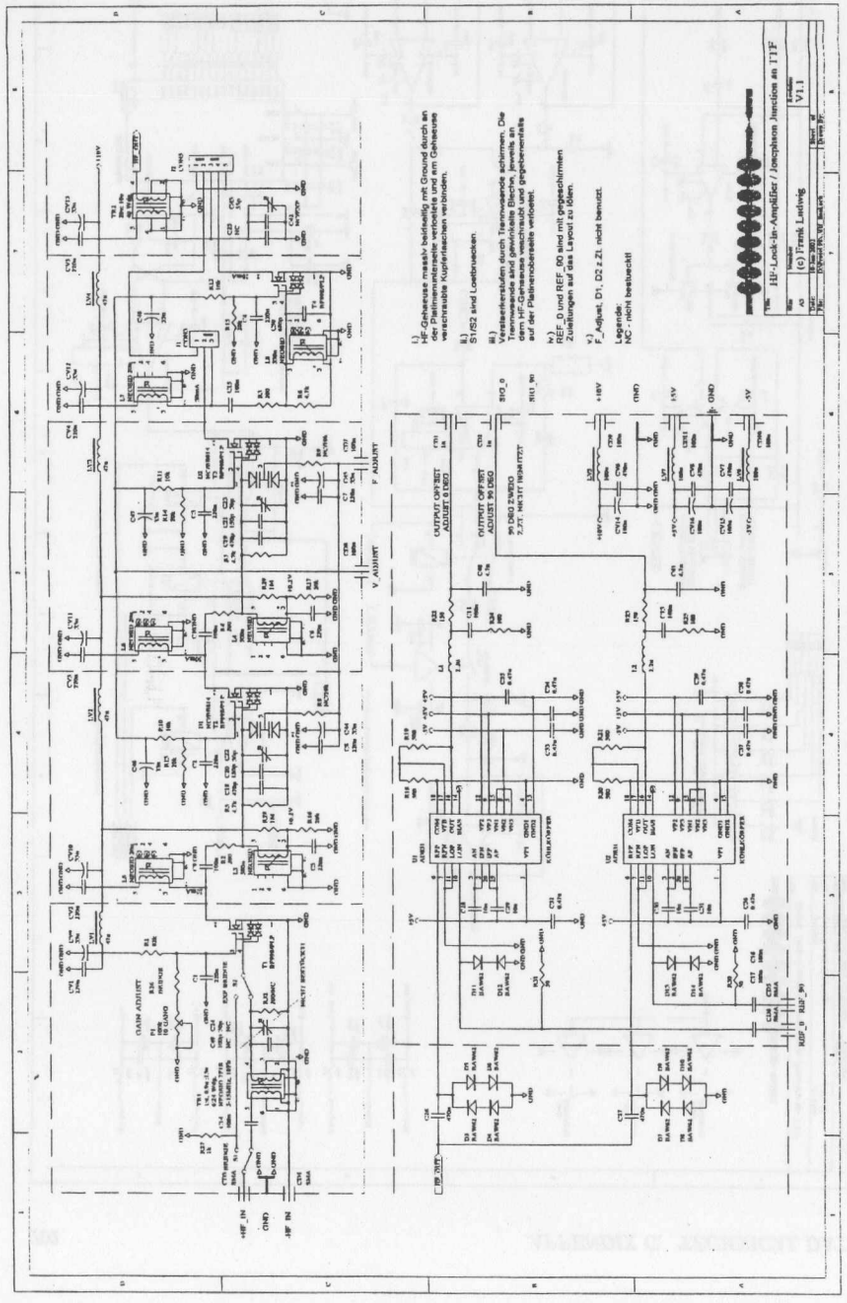
HF-Lock-in-Amplifier / Josephson Junction an TTF
(c) Frank Ludwig
V1.1
i.)
HF-Gehäuse muss/ sollte beidseitig mit Ground durch an der Platinenunterseite verlötete und am Gehäuse verschraubte Kupferfasen verbinden.
ii.)
S1/S2 sind Lötbrücken.
iii.)
Versteinerkreisen durch Transparente schirmen. Die Transparente sind durch Durchkontaktierungen mit dem HF-Gehäuses verschraubt und gegebenenfalls auf der Platinenoberseite verlötet.
iv.)
REF_0 und REF_90 sind mit gegeschirmten Zuleitungen auf das Layout zu führen.
v.)
F_Adjust, D1, D2 z.Zt. nicht benutzt.
Legende:
NC - nicht beabsicht
OUTPUT OFFSET ADJUST 0 DEG
OUTPUT OFFSET ADJUST 90 DEG
90 DEG PHASE
Z.ZT. NICHT INSTALLIERT
F ADJUST
V_ADJUST
GAIN ADJUST
HF_IN
HF IN

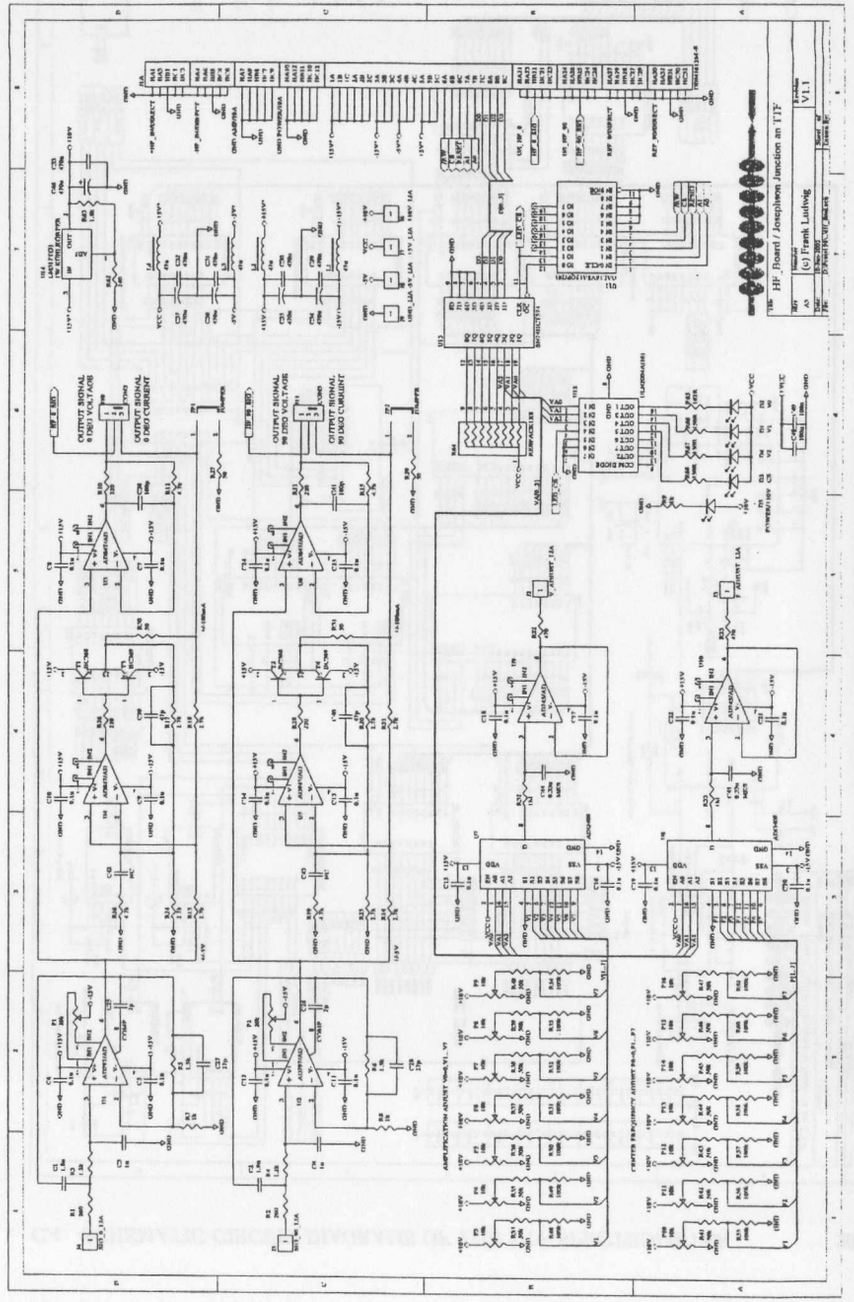
HF Board / Josephson Junction an TTF
(c) Frank Ludwig
V1.1
OUTPUT SIGNAL 0 DEG VOLTAGE
OUTPUT SIGNAL 0 DEG CURRENT
OUTPUT SIGNAL 90 DEG VOLTAGE
OUTPUT SIGNAL 90 DEG CURRENT
AMPLIFICATION ADJUST
CENTER FREQUENCY ADJUST

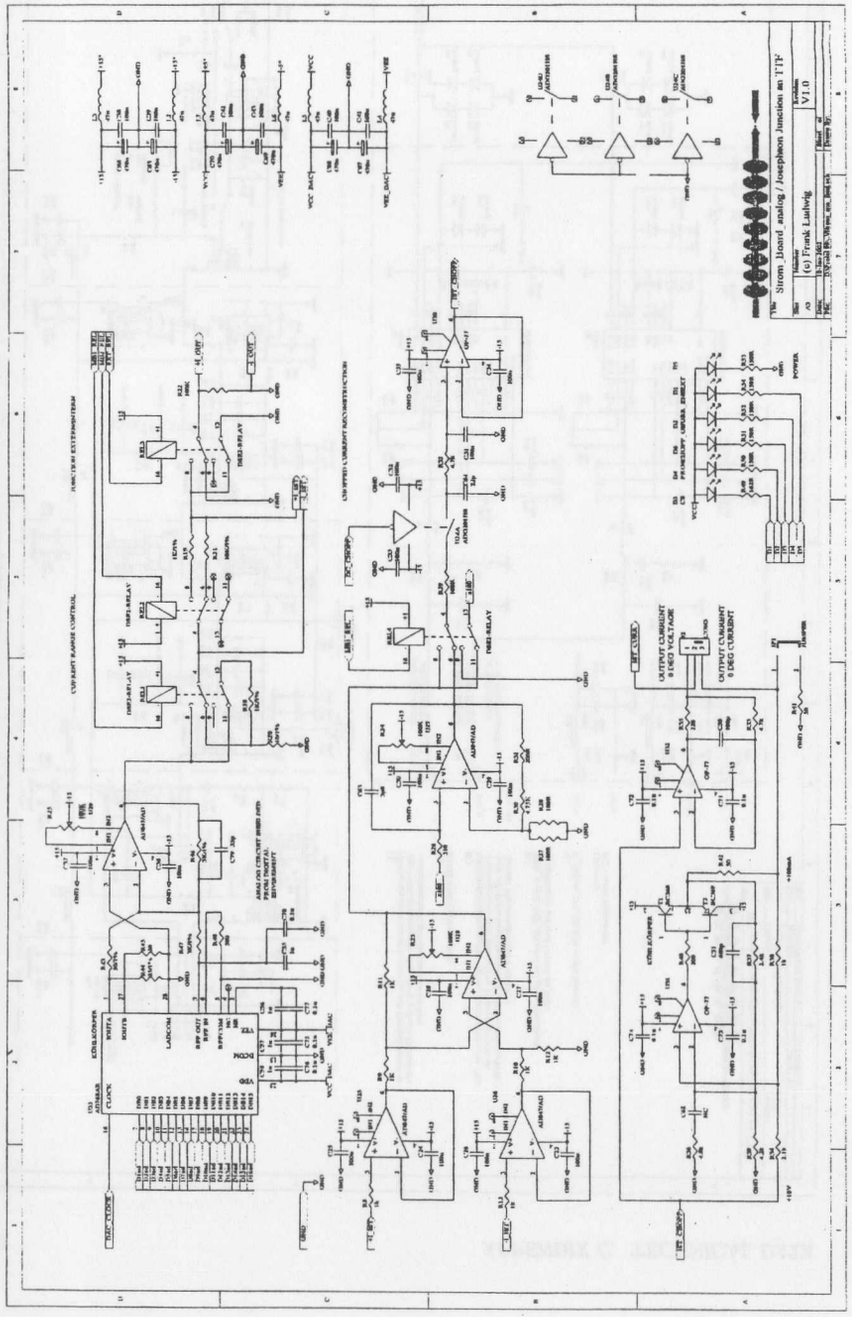
Strom_Board_analog / Josephson Junction an TTF
(c) Frank Ludwig
V1.0

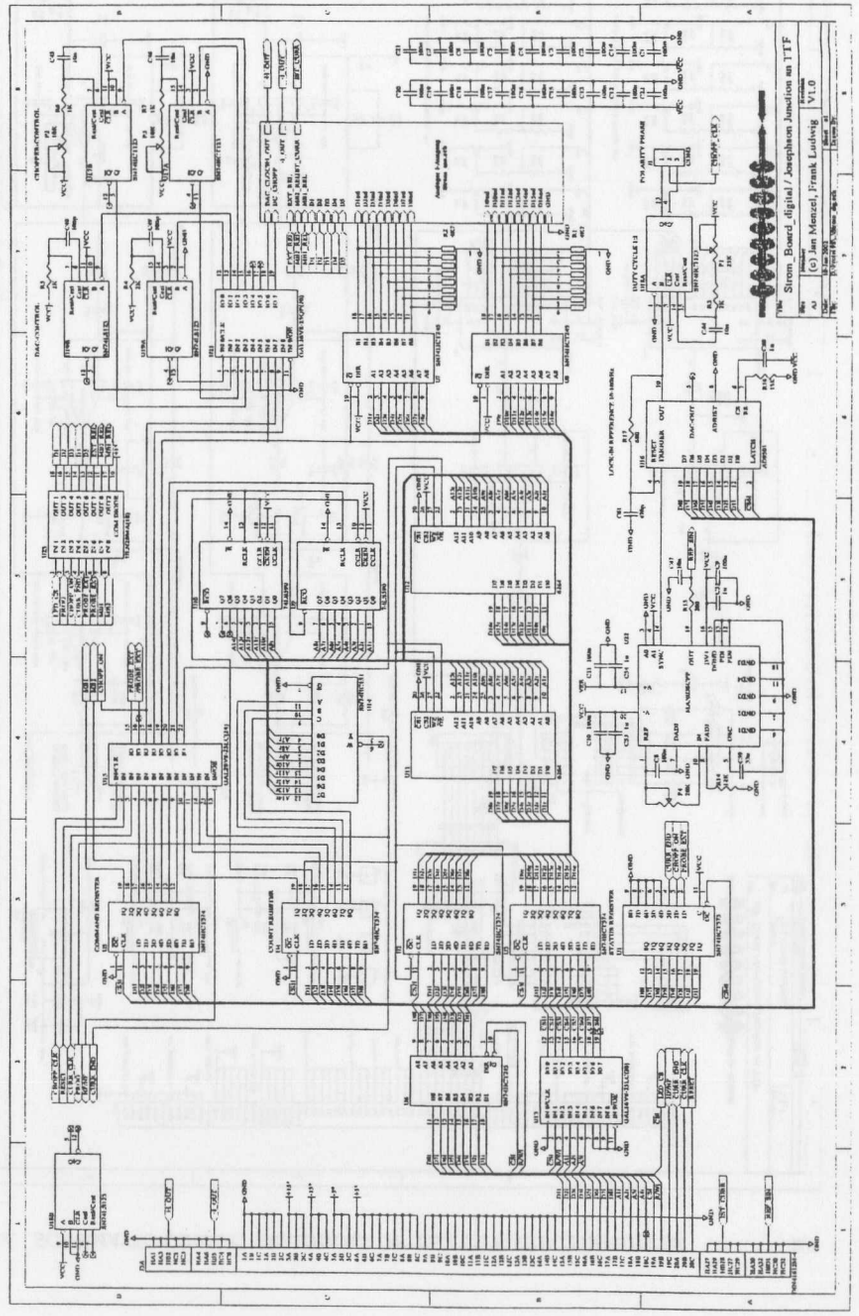
Strom_Board_digital / Josephson Junction an TTF
(c) Jan Menzel, Frank Ludwig
V1.0

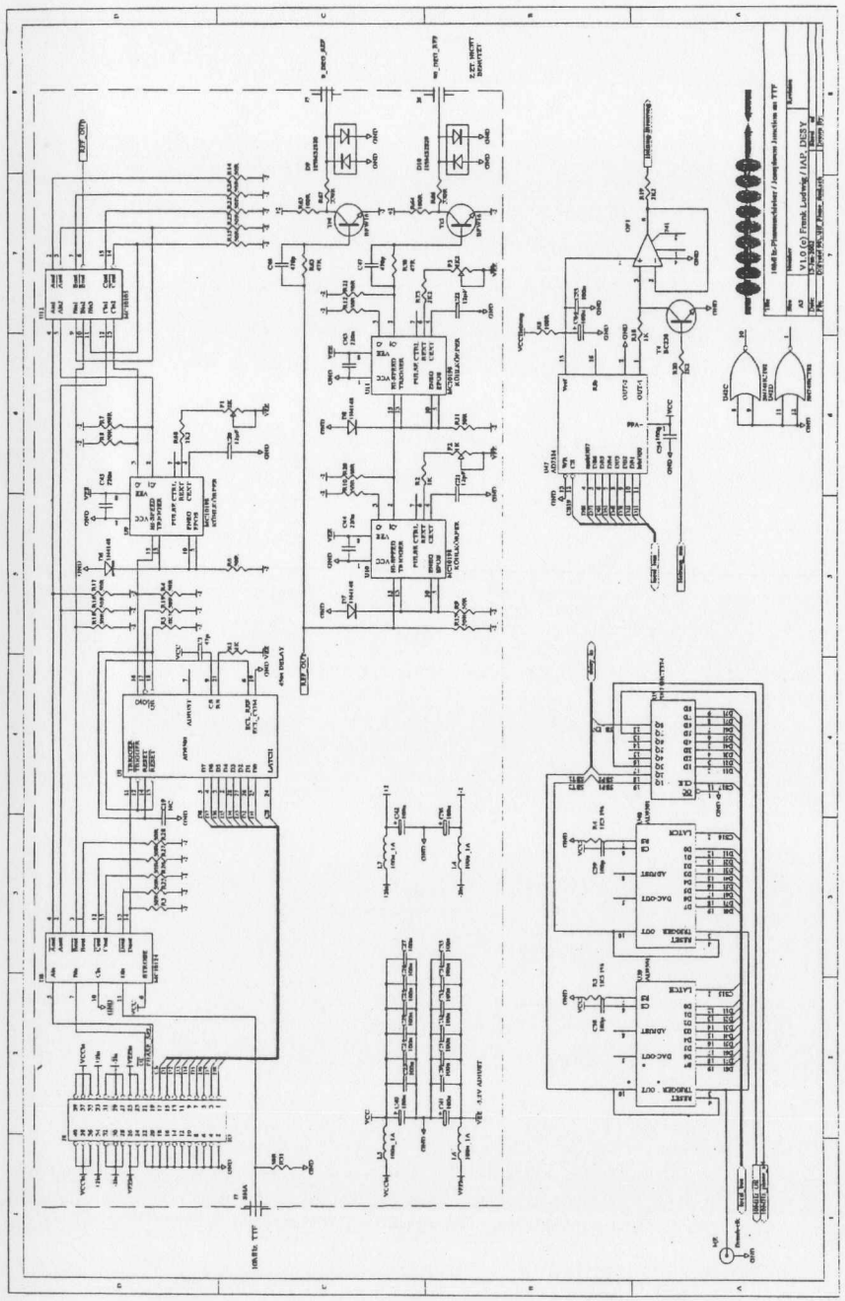

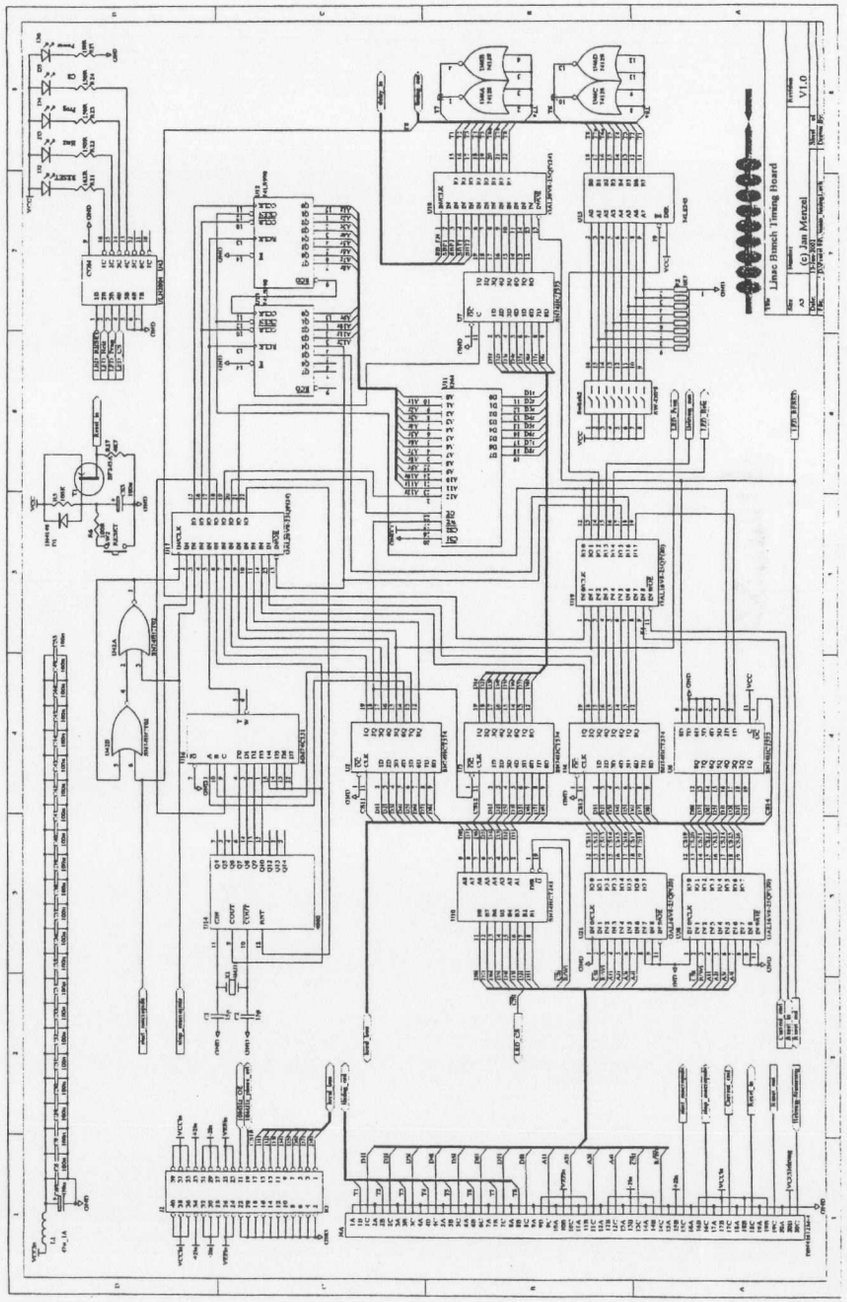
Linac Bunch Timing Board
(c) Jan Menzel
V1.0